2006

Topology Optimization of Engine Exhaust-Washed Structures

Mark A. Haney
Wright State University

TOPOLOGY OPTIMIZATION OF ENGINE EXHAUST-WASHED STRUCTURES

A dissertation submitted in partial fulfillment of the
requirements for the degree of
Doctor of Philosophy

By

Mark A. Haney
B.S., Arkansas State University, 1991
M.S., University of Illinois, 1994

2006
Wright State University

WRIGHT STATE UNIVERSITY

SCHOOL OF GRADUATE STUDIES

November 7, 2006

I HEREBY RECOMMEND THAT THE DISSERTATION PREPARED UNDER MY SUPERVISION BY Mark A. Haney ENTITLED Topology Optimization of Engine Exhaust-Washed Structures BE ACCEPTED IN PARTIAL FULFILLMENT OF THE REQUIREMENTS FOR THE DEGREE OF Doctor of Philosophy.

Ramana V. Grandhi, Ph.D.
Dissertation Director

Ramana V. Grandhi, Ph.D.
Director, Ph.D. Program

Joseph F. Thomas, Jr., Ph.D.
Dean, School of Graduate Studies

Committee on Final Examination

Ramana V. Grandhi, Ph.D.,WSU

Ravinder Chona, Ph.D.,WPAFB

David F. Thompson, Ph.D.,UC

Kenneth Cornelius, Ph.D.,WSU

Ravi Penmetsa, Ph.D.,WSU

ABSTRACT

Haney, Mark, Ph.D., Department of Mechanical and Materials Engineering, College of Engineering and Computer Science, 2006. Topology Optimization of Engine Exhaust-Washed Structures.

Aircraft structure subjected to elevated temperature and acoustic loading present a challenging design environment. Thermal stress in a structural component has typically been alleviated by allowing thermal expansion. However, very little work has been done which directly addresses the situation where such a prescription is not possible. When a structural component has failed due to thermally-induced tensile stresses, the answer to the question of how best to stiffen the structure is far from trivial. In this work, we demonstrate that conventional stiffening techniques, for example, those which add material to the thickness of a failing panel, may actually increase the rate of damage as well as increasing load into sub- and surrounding structure. The typical compliance minimization topology optimization formulation is applied to a thermally-loaded panel resulting in extremely non-optimal configurations. To generate successful thermal stress designs where the objectives are to lower the tensile stresses while simultaneously limiting the amount of additional load into sub- and surrounding structures, a well-known characteristic of topology optimization for a single-load case mechanical loading is exploited which by construction limits additional load into surrounding structure. Acoustic loading is also a major concern as exhaust gases with random frequency content impinge on aircraft structure in the vicinity of

the engines. An evolutionary structural optimization algorithm is developed which addresses both the maximum von-Mises stress and minimum natural frequency for a generic thermal protection system. The similarities between the two approaches are demonstrated.

Table of Contents

List of Figures

Acknowledgments

I would like to take this opportunity to thank all the people who have given up so much to allow me the opportunity to fulfill my dreams. First and foremost, I want to thank my wife Jennifer who has been there to support me in every way possible. She has kept our family running the last few years while "Daddy was busy." I will spend the rest of my life making up for the sacrifices she has made. To my two children, Taylor and Sara, thank you for understanding when Dad couldn't give you all the time you deserved and for the many times you both cut the grass so Dad could work. I want to thank my father, Terry, for being an incredible inspiration to me. Anyone who has pursued an advanced degree in engineering has, at some point, entertained the thought of quitting. When these thoughts entered my mind, my father's example of toughness and persistence have given me the strength to persevere. Thanks also to my mother, Margaret, for all the years of unconditional love and support. I would also like to thank my father and mother-in-law, Bill and Paula, for their love and faith in me.

A special thanks must be given to my advisor, Dr. Ramana Grandhi. Dr. Grandhi has demonstrated great patience over the last three years in accommodating my busy work schedule at the Air Force Research Lab. I want to thank him especially for his encouraging words that have, on many occasions, reassured me that I am "Ph.D. Material." As a world-renown researcher, Dr. Grandhi has afforded me, as well as his other students, opportunities that do not exist but to an elite few. The opportunity to publish with Dr. Grandhi has been

one of my proudest achievements and I look forward to continuing the tradition of high quality publications as a product of Dr. Grandhi's research circle. Thanks are also extended to my co-advisor, Dr. Ravinder Chona. Dr. Chona, as the leader of the Structural Sciences Center of the Air Force Research Lab, has constantly provided me excellent career advice as well as encouragement throughout this endeavor. His greetings of "Dr. Haney" have been an affirmation of his belief in my ability and I look forward to years of service in the Structural Sciences Center, under Dr. Chona, as we produce the technologies that will enable the U.S. Air Force to meet the challenges of the future. I would also like to thank the other members of my committee, Drs. Penmetsa, Cornelius and Thompson for their participation in the Ph.D. candidacy process as well as the review of this manuscript. Having been involved in several Masters students' theses, I appreciate the commitment made by all the members of my committee.

I now want to take this opportunity to thank the Air Force Research Lab Air Vehicles Directorate and in particular the Structures Division for their commitment to this process. I would never have been able to accomplish this task without being given the time by my management to focus almost solely on this work. Dr. Kristina Langer, Chief of the Analytical Structural Mechanics Branch, has played a very important role in my success at AFRL. Dr. Langer was first to involve the Structures Division in the root cause analysis of the B-2 aft deck. I am thankful that I was chosen as a member of that award-winning team as that difficult problem became the inspiration for much of this work. Dr. Langer has been

a good friend to me and has given me countless encouraging words along with any tool needed to complete this work. She never hesitated in pulling whatever strings were needed to assure that I had adequate time to achieve this goal. I also want to take this opportunity to thank Mr. Michael Camden. Mike served as the technical leader in thermal structures for several years in the Structures Division. I had the great opportunity of working with Mike and having him serve as my mentor over the past two years. Mike has been a constant source of encouragement to me and without his initiative, I would not have completed this work. Mike petitioned our management to pay more than lip service to the time commitment necessary for this undertaking. He was successful and I am the benefactor. I also want to thank Mr. John Bowlus, Chief of the Structures Division. As many who know me are aware, my personality rarely allows me to say "no" when presented with exciting work. Mr. Bowlus took on this responsibility for me. He reassigned people to take on my other responsibilities and supported me in countless other ways. I would also like to thank AFRL/VAS Division for providing my salary as I completed this work.

I want to acknowledge a few of my co-workers who have contributed to this work by being excellent sounding boards for my ideas. In particular, I want to thank Dr. Thomas Eason for his advice and encouragement over the past year. Special thanks also goes to Mr. Brett Hauber who has provided many insights into thermal structures from his propulsion perspective. I would also like to thank Dr. Steven Spottswood for our interesting conversations and for his willingness to provide insights into acoustic response of structures.

I also want to thank Dr. Anthony Ingraffea of Cornell University for his career advice and for the rounds of golf that provided a much needed distraction. Thanks also goes to Dr. Joseph Hollkamp for our discussions of panel buckling and dynamic response. I would also like to express my appreciation to Mr. Robert Gordon for his many insights into dynamic and acoustic response of thin panels. And lastly, I want to thank Dr. Larry Byrd. Larry has been a great friend for the last 17 years. So many of the world's problems have been solved on our lunchtime walks. Larry has seen me through the lows and highs of the Ph.D. Process. He has taught me patience and endurance. About three years ago, Larry faced a debilitating disease which left much of this body paralyzed. I visited Larry in the hospital and witnessed his relentless fight to recover. When he could only move his arms, he moved them continuously. He refused to surrender to the effects of this disease. Larry's struggle and subsequent victory over this condition have been a tremendous source of encouragement to me and have given me strength. Larry recently shared with me a quote from The Alchemist, "if you pursue your dreams, the whole universe conspires in helping you achieve it."[**1**] There is no better quote to sum up the experiences of my life.

CHAPTER 1

Introduction

1.1. Motivation

The age-old adage "necessity is the mother of invention" is appropriate in describing the genesis of this work. Over the past three years the author along with other members of the Air Force Research Lab Structures Division (AFRL/VA) have been involved in the root cause investigation of premature cracking of the aft deck of the B-2 Stealth Bomber. The aft deck is comprised of a large sheet of a high temperature titanium alloy which is doubly curved in order to match the outer mold line (OML) of the aircraft and is located directly behind the engines (Figure 1.1). Stealth aircraft like the B-2 rely on low observability (LO) from both radar cross section and

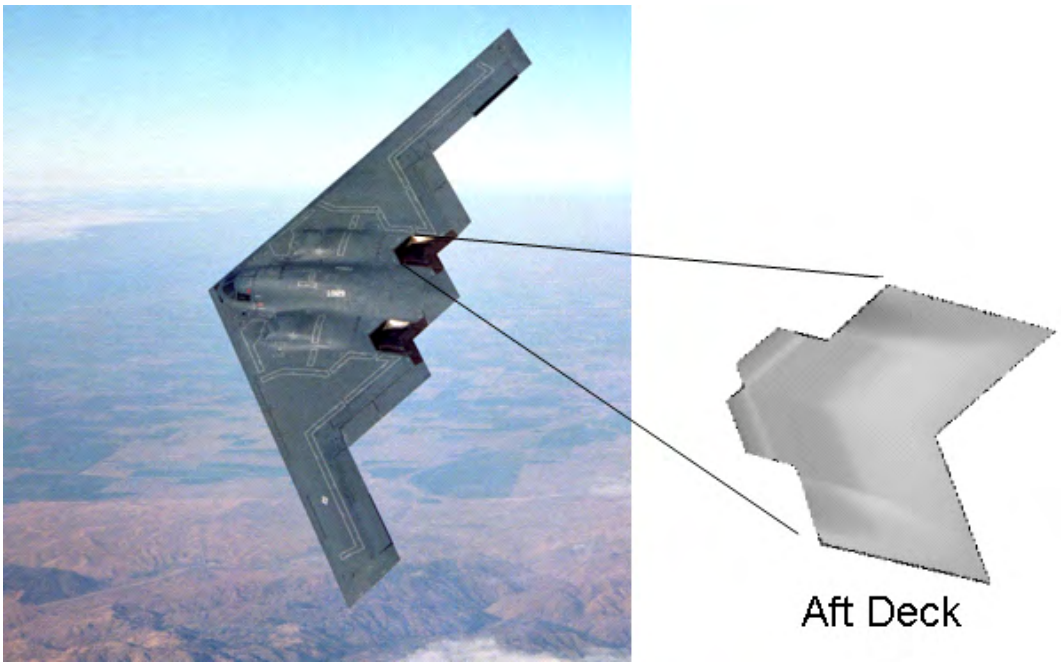

Figure 1.1. Location of aft deck structure relative to B-2 aircraft.

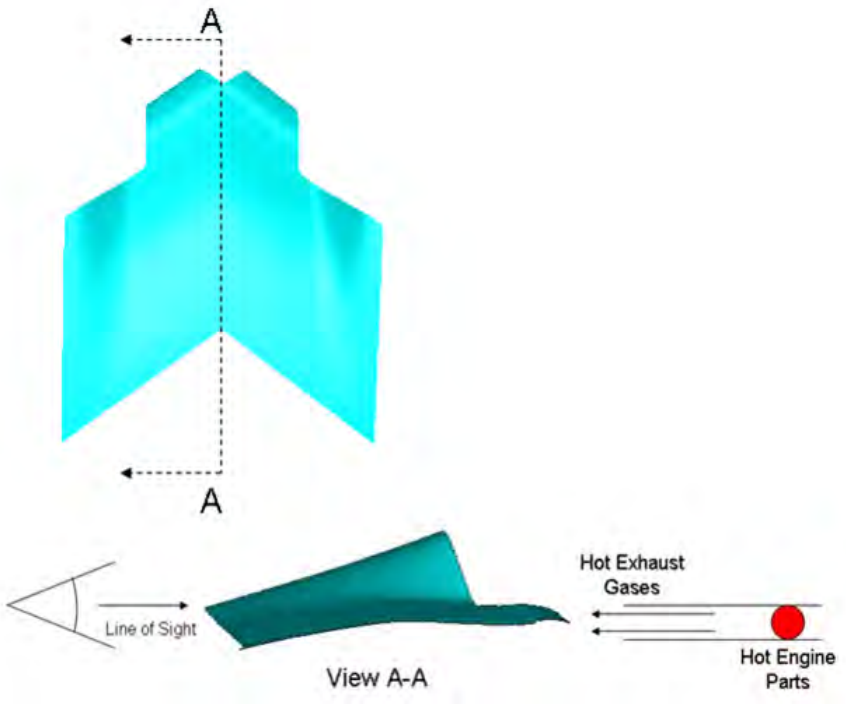

Figure 1.2. Side view of aft deck curvature

infrared detection standpoints for full mission capability. The concept of embedding engines inside the airframe to prevent enemy detection has become a common characteristic of stealth aircraft. A path for the expulsion of exhaust gases must be directed such that the thrust is maintained and line of sight into the hot components of the engine is prevented. One important purpose of an aft deck structure is to prevent direct line of sight into the high temperature regions of the engine (Figure 1.2). Therefore, the aft deck, in effect, denies a target which is very amenable to infrared detection. In peforming its function, this structure is exposed to an extreme, combined thermal-acoustic loading generating a very challenging design environment.

The root cause investigation determined that the premature cracking was due to excessive stress generated at the "fixed" interfaces to sub- and surrounding structure due to thermal expansion. This out-of-plane deformation was several times the thickness of the aft deck and hence required nonlinear analysis. The original models

were analyzed using MSC/Nastran linear static analysis and therefore did not predict the failure condition. As cracks formed and grew to appreciable lengths, the natural frequency of the structure decreased. With wide-band random noise impinging on the structure from the engine exhaust, this frequency drop resulted in additional high cycle fatigue damage which accelerated the crack growth rate.

The traditional approach to the design of thermal structures typically includes a prescription for allowing thermal expansion. Thermal stresses result when this expansion is inhibited. Aerospace examples of this approach to hot structures can be found in engine liners, tailpipes and the well-known example of the fuel system of the SR-71 [**1**]. This concept is not, however, unique to the aerospace industry as very familiar examples are found in expansion joints in concrete sections and in the slotted attachment of vinyl siding for home exterior.

An approach that allowed for thermal expansion was investigated for the long-term solution of the engine exhaust-washed structure (EEWS) of the B-2. There were several considerations that made this solution unworkable. Firstly, the aft deck, while not being in the primary flight load path, does, in fact, carry a small but significant share of the flight loads. Removing the attachment to surrounding structure and implementing a "floating" design which was free to expand would, indeed, reduce the aft deck thermal stress; however, flight load would be reacted in structure not designed for this purpose. Secondly, a concern was raised with respect to an increase in radar cross section. An expansion joint would introduce a discontinuity in the outer mold line of the aircraft and could potentially impact the mission capability of the plane. A cover seal that is used at other junctures of the plane to conceal stationary gaps was investigated as a potential solution. These knife-edge seals (Figure 1.3) were found to be inadequate for a sliding interface due to potential curling of the edges resulting from the stick-slip nature of frictional contact. A cavity similar to that shown in

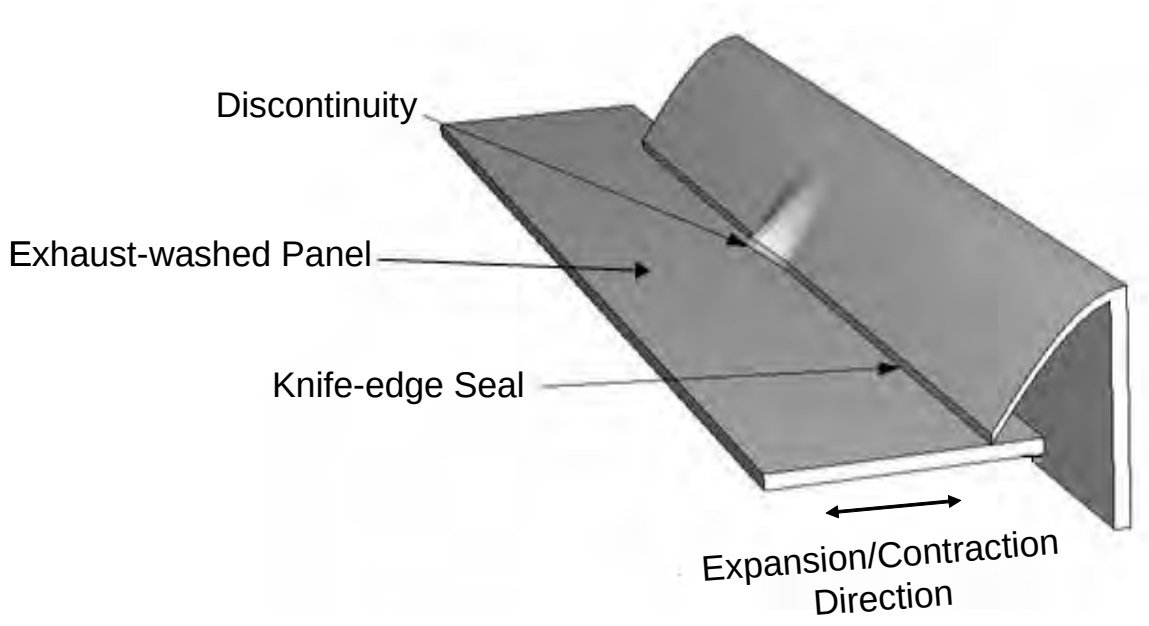

Figure 1.3. Discontinuity formation due to sliding at exhaust-washed panel – knife-edge seal interface.

Figure 1.3 could result in an increase in radar signature due to loss of smoothness [**2**].

Figure 1.4 provides a detailed description of the damage location and representative substructure that provides the relative fixity with respect to the aft deck skin. The transient and subsequent steady state thermal reponse results from the engine exhaust gases transferring energy to the upper surface of the aft deck through convection. Radiation and conduction heat transfer mechanisms transmit the heat down through the supporting structure. Thermal stresses result from both the through-thickness gradient in temperature as well as the pure volumetric expansive effects. With relatively little cooling supplied to the cavity, the stress field is dominated by the gradient contribution early in the heat up. As the thermal response approaches steady state, the volumetric effects increase and eventually dominate the stress response producing large loads into surrounding structure. Two spars (named the

trailing edge and tunnel spar (Figure 1.4)) provide resistance to the thermal expansion of the aft deck skin with respect to both displacement and rotation. Since the structure can be considered a shell with large but finite radii of curvature, several modes of deformation are possible. The deck can respond linearly for low temperature and small gradient regimes. If the maximum temperature and/or gradient is increased, nonlinear geometric effects become important and out-of-plane bowing results. Depending on the level of fixity provided by the surrounding structure and in-plane and through thickness temperature gradients, the skin can become unstable as buckling and post-buckling behavior is possible. The damage locations are consistent with a clamped boundary with the cracks initiating on the bottom surface at the location where the deformed radius of curvature is maximum. Section B-B depicts a recent crack location where repair was required. However, since no allowance has been made to relieve thermal stress, and constraint is provided by a series of spars and ribs, cracks are possible at a multitude of locations.

Since traditional methods of relieving this thermal stress condition proved problematic, another approach was needed. A stiffening approach which employed conventional stiffening members (e.g., T- and I- shaped beams) was investigated. While this approach would suffice in a mechanically-loaded environment in which the loading is independent of the stiffeners, a thermal environment necessarily requires participation of the additional stiffening structure as loads into surrounding structure. Hence, when a clamped boundary assumption is made (which is conservative from a loads perspective), an enormous increase in loads and moments is observed at the clamped boundary. While a truly clamped boundary is difficult to observe in a physical system, it provides a reasonable metric for comparison of design alternatives. This increase in load is attributable to two factors. Firstly, the decrease in out-of-plane

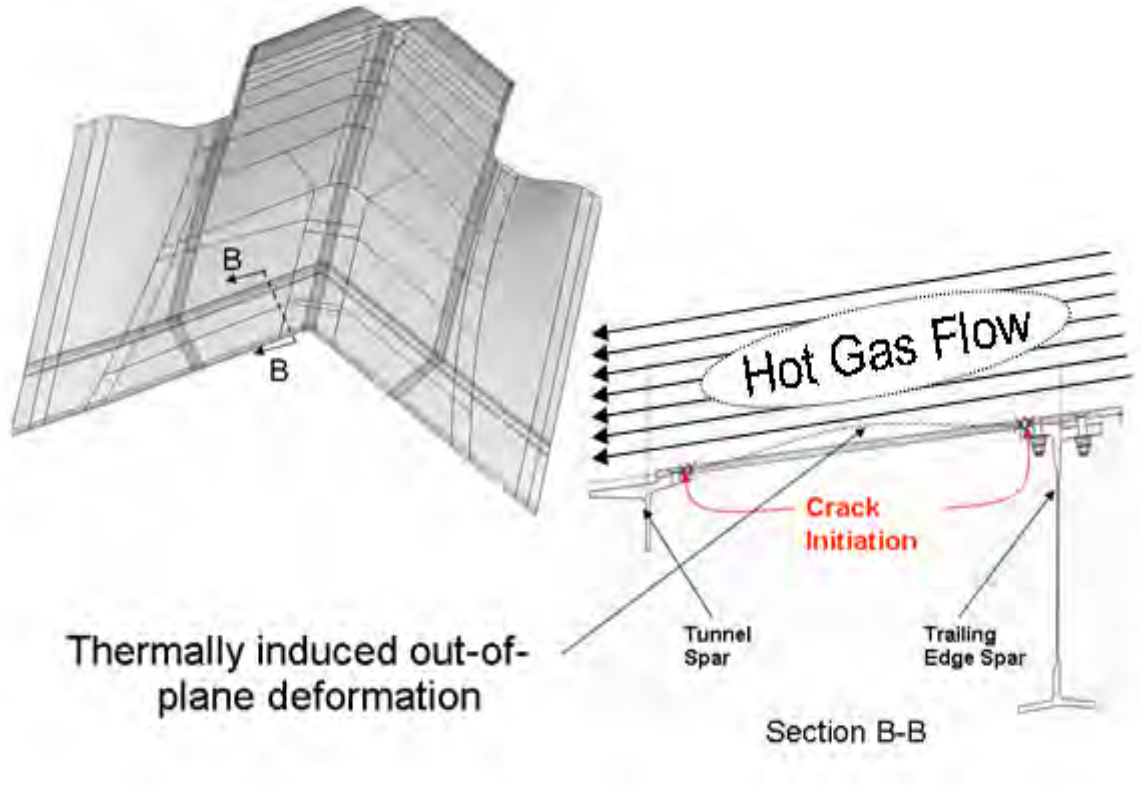

Figure 1.4. B-2 aft deck detailed damage location

bowing of the curved skin structure will result in additional load as the bending moment reacted at the boundary is exchanged for in-plane compression. The second factor and the primary focus of this work, is the additional load that results from the thermal participation of the stiffening structure. An obvious trade space emerged which seeks to balance the need for additional out-of-plane stiffening with increase in load at the boundary. A tool which provided for the greatest exploitation of the design space was desired. Topology optimization was chosen as this tool to investigate an "optimal" stiffener that would prevent cracking in the skin while giving consideration to additional load into surrounding structure.

1.2. Research Objectives

It should be emphasized that while a recent failure investigation provided the motivation for this work, the implications are much broader. When possible, traditional methods of alleviating thermal stress should be employed, namely, permitting the expansion to take place. For example in the B-2 aft deck investigation, in the regions where damage was observed initially, the stresses could be practically eliminated if a few hundreths of an inch expansion were permitted over length scales of 10 to 12 inches. However, any situation which does not permit the alleviation of thermal stress by expansion can benefit from the concepts revealed in this dissertation. Hence, future stealth aircraft with embedded engines will undoubtable encounter similiar design difficulties. Therefore, this work addresses a class of problems where design solutions will continue to be extremely important to the long-term vision of the Air Force. Since the exact geometry of future aircraft will differ from that encountered on the B-2, without loss of generality, simple, single-curved shells and beam strips are used in this work to demonstrate the salient features of the tools developed in this dissertation.

The research objectives in this work are threefold. The first is to identify the non-intuitive nature of the problem being addressed. Examples will be presented which demonstrate how the structural analyst, who is familiar with the design of mechanically-loaded structures, must use extreme caution when applying this "room temperature" mentality to constrained thermal structures. Secondly, well-established topology methods will be utilized to evolve a structure which balances the two objectives of stress reduction in the skin and load into surrounding strucuture by taking advantage of a deficiency in the classical, minimum compliance topology optimization formulation. And lastly, a novel evolutionary structural optimization (ESO) method is developed which simultaneously addresses von-Mises stress and frequency for the

more general application of thermal protection systems. Since the environment under consideration contains acoustic as well as thermal energy, maintaining fundamental frequency at high levels reduces the potential damage from acoustic loading.

1.3. Chapter Outline

This work begins with a review of previous efforts relevant to this development. Chapter 2 is a review of thermal structures relevant to this development. Since plane stress shells are used to model the skin response and are the focus of the failure location, the thermal structures chapter provides a literature review which includes a survey of previous work in thermally loaded shell geometries. The nature of the difficulty in stiffening thermally loaded structures is illustrated by a series of simple, but revealing, examples. These results provide additional motivation for the current work as well as demonstrating the necessity of advanced analysis and optimization tools for robust designs in this environment. With topology optimization being a primary focus of this work, Chapter 3 is devoted to providing an historical perspective of this subject beginning with the discrete nature of the problem and the mathematical ill-posedness of the formulation. Relaxation methods such as homogenization and the widely used SIMP (Simple Isotropic Material with Penalization) are introduced to overcome the difficulties associated with '0-1' nature of the integer programming problem. A less mathematically rigorous topology formulation known as evolutionary structural optimization (ESO) is then introduced which does address the discrete problem directly through a slow process of finite element removal. The ESO method provides the framework for the topology formulation in Chapter 4 which simultaneously treats thermal stress and fundamental frequency. And lastly, a relative new-comer to the world of topology optimization formulations is briefly discussed in the Level-Set method.

Topology optimization began as a tool exclusively applied to solid mechanics. Since that time, many formulations have evolved which apply topology optimization to the energy equation [**3**], Stoke's flow [**4**], and multi-physics applications [**5**]. In this work, the focus is exclusive to solid mechanics so the review provided begins with the minimum compliance formulation for mechanically-loaded structures and eventually narrows the focus to nonlinear thermoelasticity.

In Chapter 4, conventional minimum compliance topology optimization is applied to the stiffening of a thin, shallow shell geometry in an elevated temperature environment by taking advantage of a known deficiency in topology optimization associated with single load case *mechanical* loadings. A novel multi-objective ESO topology method which seeks to minimize thermal stress while simultaneously increasing the fundamental frequency of a thermal protection system (TPS) panel is developed in Chapter 5. Chapter 5 provides paths for future work including a formulation which directly addresses the reaction force vs out-of-plane deformation trade space.

CHAPTER 2

Thermal Structures Review

2.1. Historical Perspective

When one begins a study of thermal structures and thermal stress response, two classic texts on the topic should be thoroughly reviewed. The first, Boley and Weiner [**6**], provides a very rigorous mathematical treatment of the subject matter for linear thermoelasticity. The coupled treatment of both the energy equation and elastic equilibrium is developed. Guidelines for when the equations must be solved in a coupled fashion and when a sequential, weak coupling of the thermal and structural solutions is adequate are presented. Linear buckling of plates is addressed and solutions for various boundary conditions are provided. The inclusion of nonlinear strain coupling between the membrane and bending effects is developed and an analytical solution is provided for the unrestrained condition. Many of the analytical solutions presented in [**6**] examine the unconstrained case in which stresses result from in-plane and through-thickness temperature gradients. The stresses generated from this type of loading are, in practice, smaller than those observed when overall volumetric expansion of prevented, i.e., clamped boundaries, except in the case of thermal shock where very localized heating takes place.

The second text, which has a slightly more applied flavor, in particular, to the aerospace industry, is the text by Gatewood [**7**]. Analytical and semi-analytical solutions are presented for skin-stringer combinations and other familiar aerospace constructs. Common to both references is the treatment of both transient and steady state effects. Gatewood provides a more thorough treatment of temperature

dependent material properties which over large temperature ranges, can be quite pronounced and if neglected can lead to misleading results.

The impetus for our ability to simulate the response of structures to thermal loading began in the early 1950's with the breaking of the sound barrier in the X-1A experimental aircraft program. Compressible gas dynamics predicts that large temperature increases can accompany frictional effects from the conversion of kinetic energy in the flowstream to internal energy (in the form of heat) at the fluid-structure interface. The generated heat flux inpinges on the surface of the vehicle and causes an accompanying temperature increase. The second mechanism associated with supersonic flight which can potentially generate very high temperatures in localized areas is that of shock wave generation. Shocks are typically produced when supersonic flow is reduced to subsonic flow at a point of stagnation such as a leading edge of a wing or other control surface on the vehicle. The first vehicle on which aerothermal heating was studied was the X-1B [**8**]. The X-1B was a more sophisticated version of Captain Charles E. Yeager's initial supersonic vehicle. Mach numbers reached by the X-1B were just under Mach 2. The aerodynamic heating effects for the given air velocity and altitude resulted in skin temperatures of approximately 200^0F. Conventional aluminum airframes were capable of surviving this environment, however, higher temperature material systems would be vital to enable higher speed vehicles. As technology advanced in propulsion systems, supersonic speeds increased rapidly, and aerodynamic heating effects began to dominate the designs. The challenges of managing the thermal environment and the associated difficulties became known as the *thermal barrier* [**1**].

The X-2 was the first aircraft designed in which aerodynamic heating effects were given full consideration [**9**]. Up to this point, speeds had not been large enough for aerodynamic heating to adversely affect the aircraft performance. In 1956, the X-2

achieved a Mach number of 2.5. This capability was realized through high temperature material systems. The fuselage was constructed from K-Monel with the skins consisting of stainless steel. These heavier materials systems were a penalty from a payload and performance perspective when compared with aluminum. However, they were an enabling component of high speed flight. This trade-off between payload and thermal protection continues to be an important trade space. These efforts are well documented in [**10**].

The next significant achievement in the realm of thermal structures occured with the establishment of the X-15 program. One of the many X planes that furthered American aviation supremacy, the X-15 consisted of a thick-skinned vehicle made of high temperature, nickel-based alloys (Inconel-X). The flights were short in duration typically lasting from 10 to 12 minutes [**11**]. The maximum temperature reached on the vehicle occured at one of the primary stagnation points (the wing leading edges) and exceeded 1300^0F. One of the principal events of the twentieth century with respect to the so-called *race to space* was the success of the Sputnik I program After the Soviets successfully orbited the world's first man-made satellite (Sputnik I), the X-15 program became a very important national priority with regard to the undestanding of aerothermal structures. The X-15 made many significant contributions to the understanding of hypersonic flight including the design of thermal structures.

The success of Sputnik forced United States hypersonic flight research to change focus and to make space access its number one priority. Along with this change of focus, came an even more challenging thermal-structural environment. With Mach numbers approaching twenty, the maximum temperatures predicted on the lifting bodies were in excess of 3000^0F. Two approaches were taken to mitigate this extreme environment. The *cool structures* approach sought to insulate the primary load bearing structure from the intense heat by means of a thermal shield. These

barriers were made of high temperature metals, ceramic or ablative material and carried virtually no flight load. Hence, their weight was parasitic, penalizing the mission payload. These type of systems are designed for transient thermal loads that are associated with re-entry. The insulation layer is designed such that the low-temperature airframe never reaches some specified critical temperature. If no active cooling is provided, these structures cannot operate at a steady state condtion as the backing structure would eventually reach a temperature above its usage. This *cool structures* approach has been somewhat successfully demonstrated on the space shuttle, but the fragililty of the thermal protection system (TPS) has resulted in costly losses including loss of life in the case of the Columbia tragedy.

An alternative approach to successful operation in the elevated temperature environment is often referred to as *hot structures.* Hot structures are designed to operate at or near the skin temperature. Hot structures are intended to participate in the load path reaction and are integral to the airframe. The obvious advantage of hot structure is that its weight is non-parasitic. This benefit can potentially reduce the cost to achieve lower earth orbit (LEO) with a payload. The challenges associated with this approach make this area an active research field. The material systems that can tolerate the high temperature environment are inherently brittle and have low damage tolerance. Therefore, to use these materials as load carrying structure is extremely challenging. The material science community has attempted to incorporate acceptable damage tolerance characteristics into ceramic-like material systems by resorting to high-temperature composites. The combination of ceramic fibers with a damage tolerant matrix has generated some success. Another approach to mitigating the risk associated with these materials is to employ structural health monitoring (SHM). Since small cracks in brittle materials can cause catastrophic failure, embedded sensors to detect damage before it becomes critical are being pursued to mitigate

this risk. SHM is an active area of research and is one of the primary foci of research funding of the Department of Defense and the Air Force Research Lab.

Engine exhaust-washed structures can be categorized as hot structure given that they are exposed directly to a high temperature environment absent a thermal barrier coating or insulation. Since the EEWS is expected to operate continuously for long periods of time, a low-conductivity coating would only succeed in smoothing out the early transients and delaying the heat transfer through the thickness. After a period of time, the skin EEWS would come up to temperature as steady state conditions dominate. While much of the work in hot structures assumes the high temperature environment is a result of aerodynamic heating and Chapter 5 of this work examines this case, an additional high temperature environment exists due to exhaust wash from embedded engines in low-observable aircraft. And hence, the structure is exposed to overall sound pressure levels (OSPL) that can potentially result in acoustic excitation and additional damage accumulation.

2.2. Plates and Shells

Since the structure considered here can best be idealized as a shell, [**12**] is useful in studying the past work in themal-mechancial response of plate and shell structures. Plates and shells exposed to thermal energy can respond in several different ways depending on the in-plane temperature variation, through-thickness temperature gradient, and essential boundary conditions. Depending on these inputs, the panel may continuously deform out-of-plane (bowing); however, under appropriate conditions, buckling and subsequent post-buckling response does occur. When studying flat plates subjected to thermal loading, buckling is the primary response and occurs at relatively low temperatures. As initial curvature is introduced into the geometry, a shell geometry results and the buckling temperature increases [**12**]. This result

is intuitive as buckling occurs due to instability which forces the structure to follow bifurcated equlibrium paths. If the structure contains intial curvature, a smooth equilibrium path may exist independent of buckling which allows for thermal expansion albeit out-of-plane.

2.2.1. Flat Plate Response

Plates and shells can be categorized more broadly as plane stress structural elements. In plane stress, the deformation is assumed to be a function of the in-plane coordinates only. As the name implies, a plane state of stress exists such that the transverse components of stress are assumed to be zero. Plane stress is identified with thin sheets where the smallest in-plane dimension is much larger than the thickness. Figure 2.1 details the rectangular geometry of a perfectly flat plate with thickness h and dimensions $2a$ x $2b$. The thermo-elastic equations for plane elasticity are given by Eqs. 2.1-2.4 with respective stresses given by σ_x, σ_y, and τ_{xy}. $\phi(x, y)$ is defined as the Airy stress function which satisfies the inhomogeneous compatibility Eq. 2.4 and the prescribed boundary conditions. The inhomogeneous term is comprised of E, the modulus of elasticity, α, the coefficient of thermal expansion, and $T(x, y)$, a spatially-dependent temperature field.

$$\sigma_x = \frac{\partial^2 \phi}{\partial y^2} \tag{2.1}$$

$$\sigma_y = \frac{\partial^2 \phi}{\partial x^2} \tag{2.2}$$

$$\tau_{xy} = -\frac{\partial^2 \phi}{\partial x \partial y} \tag{2.3}$$

$$\nabla^4 \phi = -E\alpha\nabla^2 T \tag{2.4}$$

Note that the inhomogeneity in the compatibility equation vanishes if the temperature field satisfies the steady state heat conduction equation ($\nabla^2 T = 0$) and the Airy

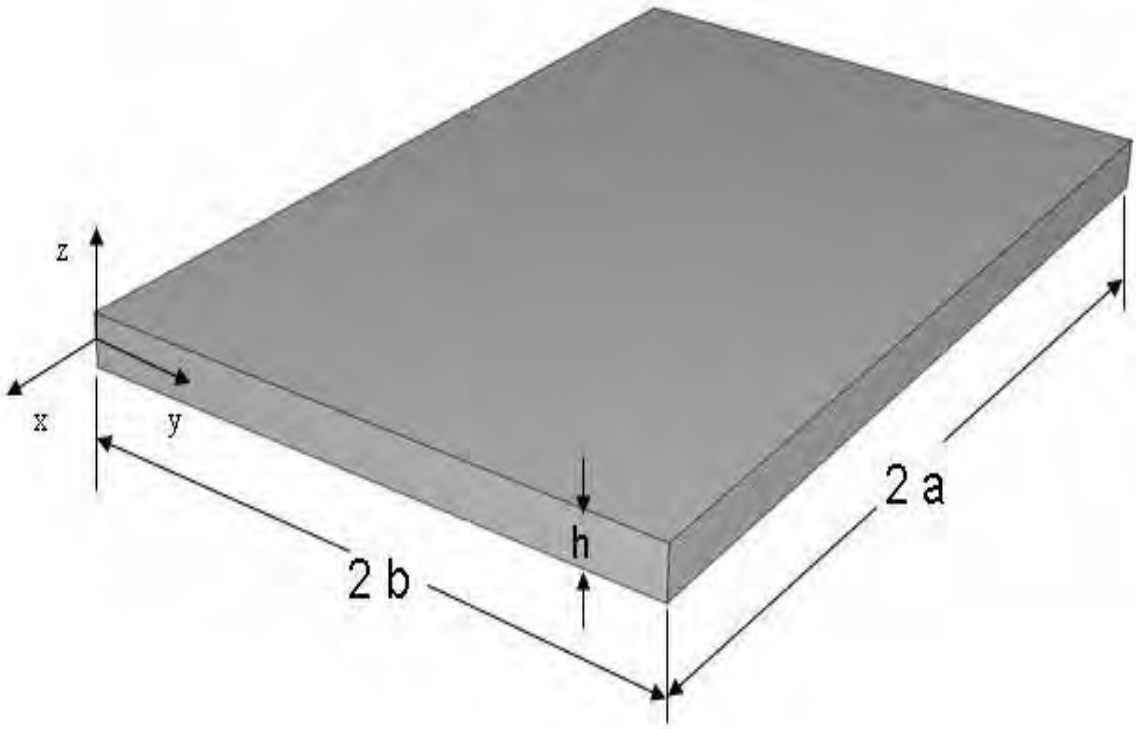

Figure 2.1. Rectangular plate of dimensions 2a x 2b

stress function takes the form of a third-order polynomial in x and y. Eqs. 2.1-2.4 provide the in-plane response, however, because the plate is assumed perfectly flat, no out-of-plane deformation is predicted. To determine the critical buckling temperature, a small out-of-plane displacement $w(x, y)$ must be assumed. The displacement $w(x, y)$ of the buckled plate is governed by the linear differential transverse equilibrium equation

$$D\nabla^4 w = N_x \frac{\partial^2 w}{\partial x^2} + 2N_{xy} \frac{\partial^2 w}{\partial x \partial y} + N_y \frac{\partial^2 w}{\partial y^2} \tag{2.5}$$

where D is the flexural rigidity given by $Eh^3/12(1-\nu^2)$ and N_x, N_y, N_{xy} are the in-plane stress resultants obtained by multiplying the stresses by the plate thickness h. These resultants are often referred to as *running loads* ($\frac{force}{length}$) in design engineering parlance. A solution to Eq. 2.5 is provided in [**13**] with simply-supported boundary

conditions and is given by

$$N_x \frac{m^2\pi^2}{(2a)^2} + N_y \frac{n^2\pi^2}{(2b)^2} = D\left(\frac{m^2\pi^2}{(2a)^2} + \frac{n^2\pi^2}{(2b)^2}\right)^2 \tag{2.6}$$

where m and n represent the number of waves in the x and y directions, respectively. For a $2a$ x $2b$ flat plate, the in-plane running loads for the uniform thermal loading, ΔT, are given by

$$N_x = N_y = \frac{\alpha\ \Delta T\ E\ h}{(1-\nu)} \tag{2.7}$$

Substituting these force expressions into Eq. 2.6 along with the expression for D, and using the minimum values of m and n (=1), the critical buckling temperature change is given by

$$\Delta T_{cr} = \frac{\pi^2 h^2}{48(1+\nu)\alpha}\left(\frac{1}{a^2} + \frac{1}{b^2}\right) \tag{2.8}$$

One important conclusion drawn from Eq. 2.8 is the independence of modulus of elasticity. This is unique to thermal buckling as buckling caused by mechanical loading is a function of material stiffness [**13**]. Eq. 2.8 predicts extremely small buckling temperature changes. For example, an aluminum plate with $a = 18$ in, $b = 12$ in, and $h = 0.25$ in with $\alpha = 13.0\ \mu$ in/in$-^\circ F$ buckles at a temperature change above room temperature of $7.5^\circ F$. The most obvious parameter to increase if thermal buckling is a concern is the thickness. This quadratic dependence increases the buckling temperature by a factor four each time the thickness is doubled. Also note that the buckling dependence is inversely proportional the coefficient of thermal expansion (CTE). Therefore, if several materials are being considered for a high temperature application, the material with the lowest CTE should be chosen provided the material properties remain stable at the desired operational temperature. The

dimensional aspects also play a crucial role in buckling studies. The aspect ratio, a/b, of the plate influences the buckling characteristics and is a parameter in almost all plate buckling studies [**14**]. The aspect ratio of a panel is usually dictated by the substructure of the aircraft. However, the introduction of stiffeners can be used to alter the aspect ratio and hence the critical value of the buckling temperature.

While Eq. 2.8 provides a good estimate of the onset of buckling, no allowance is made for the change of in-plane stress components with respect to the deformation. The linear equations above assume the deformed and the undeformed configuration coincide. The first work to investigate thermal post-buckling of plates was done in [**15**]. The above equations assume no coupling between the in-plane and out-of-plane deformation. Therefore, they can be solved independently. In reality, when the transverse deflection of a plate becomes large (typically on the order of one plate thickness) lengthening of the middle surface occurs and the membrane forces change. This coupling requires simultaneous solution of both the stress function and the transverse displacement. The set of equations which include these nonlinear effects is attributed to von Karman. The complete development of these equations can be found in [**6**].

$$h\nabla^4\phi = Eh\left[\left(\frac{\partial^2 w}{\partial x\partial y}\right)^2 - \frac{\partial^2 w}{\partial x^2}\frac{\partial^2 w}{\partial y^2}\right] - \nabla^2 N_T \tag{2.9}$$

$$D\nabla^4 w = h\left[\frac{\partial^2\phi}{\partial y^2}\frac{\partial^2 w}{\partial x^2} - 2\frac{\partial^2\phi}{\partial x\partial y}\frac{\partial^2 w}{\partial x\partial y} + \frac{\partial^2\phi}{\partial x^2}\frac{\partial^2 w}{\partial y^2}\right] - \frac{1}{(1-\nu)}\nabla^2 M_T \tag{2.10}$$

where the thermal force per unit length is given by

$$N_T = E\alpha\int_{-\frac{h}{2}}^{\frac{h}{2}} T(x,y,z)dz \tag{2.11}$$

and the thermal moment per unit length is given by

$$M_T = E\alpha \int_{-\frac{h}{2}}^{\frac{h}{2}} T(x,y,z) z dz \tag{2.12}$$

Insight may be gained into Eqs. 2.11-2.12 by considering a temperature field independent of the normal coordinate z. Being an even function, the thermal force has a contribution to the solution, whereas, the thermal moment vanishes identically. While the boundary conditions are not explicity stated in the above formulation, it is understood that the functions ϕ and w, must satisfy the prescribed essential and/or natural boundary conditions. Most thermal stress problems of interest are associated with constraint of the expansion, in fact, for a steady state temperature field in an isotropic body with an unconstrained boundary, no thermal stress exists [**7**]. This, however, does not hold true for arbritary temperature fields.

2.2.2. Simply-Supported Finite Stiffness Boundary

Because thermal stress is a function of restrained thermal expansion, the thermoelastic response is highly dependent on the boundary conditions. As was stated previously, for certain temperature distributions, the thermal stress response is zero if the body is unconstrained. As the level of constraint is increased, the potential for higher stresses and larger reaction loads into surrounding structure exists. An investigation of the effects of varying boundary stiffnesses on thermally loaded, simple-supported flat plates was conducted in [**16**]. Figure 2.2 illustrates the boundary stiffnesses in the x and y directions supporting a flat plate in the plane. For a flat plate, elastic tensile stresses capable of producing failure can only be generated if panel buckling occurs. The critical buckling temperature which incorporates the boundary stiffnesses is given

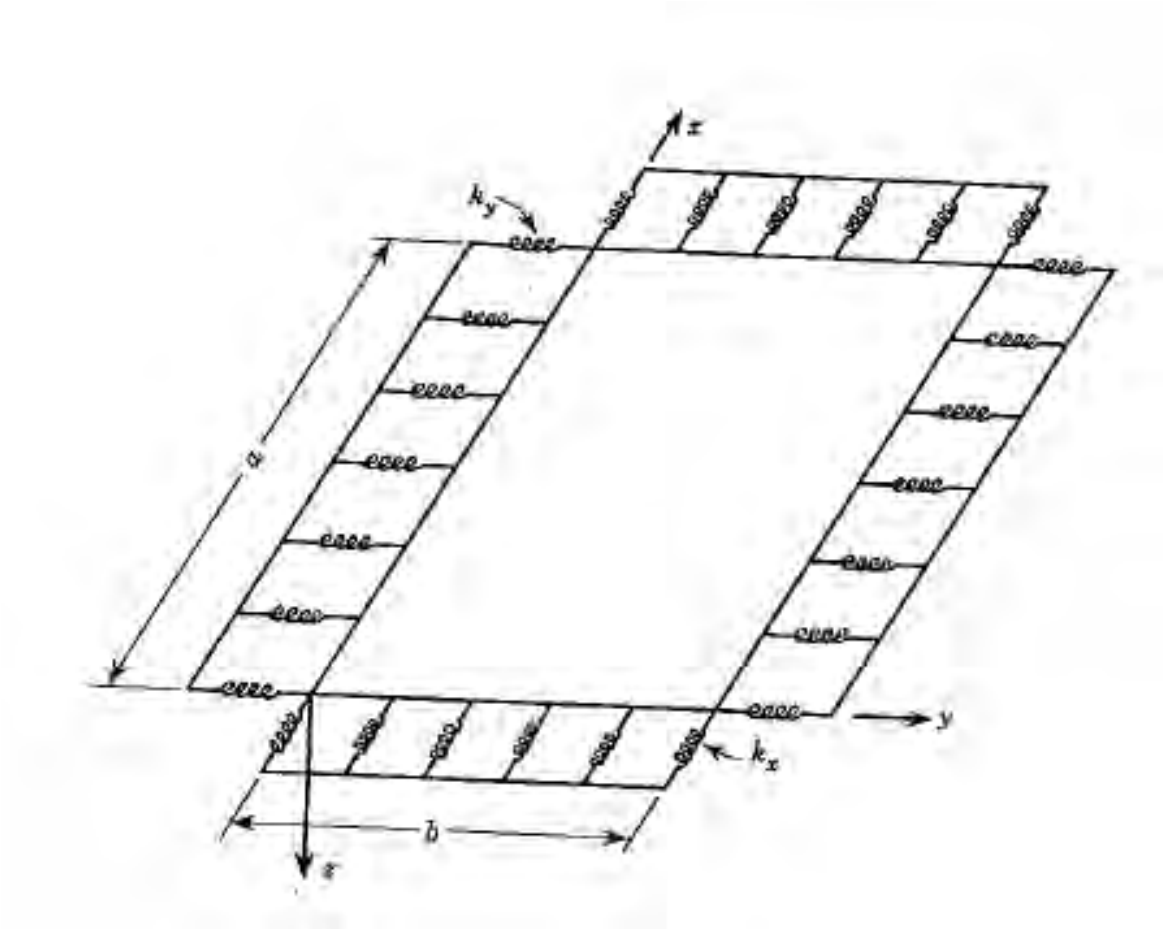

Figure 2.2. Rectangular Plate with Edge Restraint in Plane of Plate [**16**]

by

$$(\alpha\Delta T)_{cr} = \frac{\frac{\pi^2}{12(1-\nu^2)}\left(\frac{h}{a}\right)^2\left[1+\left(\frac{a}{b}\right)^2\right]^2\left[\left(1+\frac{2E}{k_x a}\right)\left(1+\frac{2E}{k_y b}\right)-\nu^2\right]}{\left[1+\left(\frac{a}{b}\right)^2\right][1+\nu]+\left(\frac{2E}{k_y b}\right)+\left(\frac{a}{b}\right)^2\left(\frac{2E}{k_x a}\right)} \tag{2.13}$$

Eq. 2.13 is developed by solving the nonlinear von Karman plate equations. As the boundary stiffnesses (k_x and k_y) approach ∞, the modulus dependence is eliminated similar to Eq. 2.8. However, for small and intermediate values of boundary stiffness, the modulus plays a significant role. As the boundary stiffnesses approach zero, the buckling temperature approaches ∞ for a uniform temperature field. With small boundary stiffness, no potential is available to generate large in-plane loads which

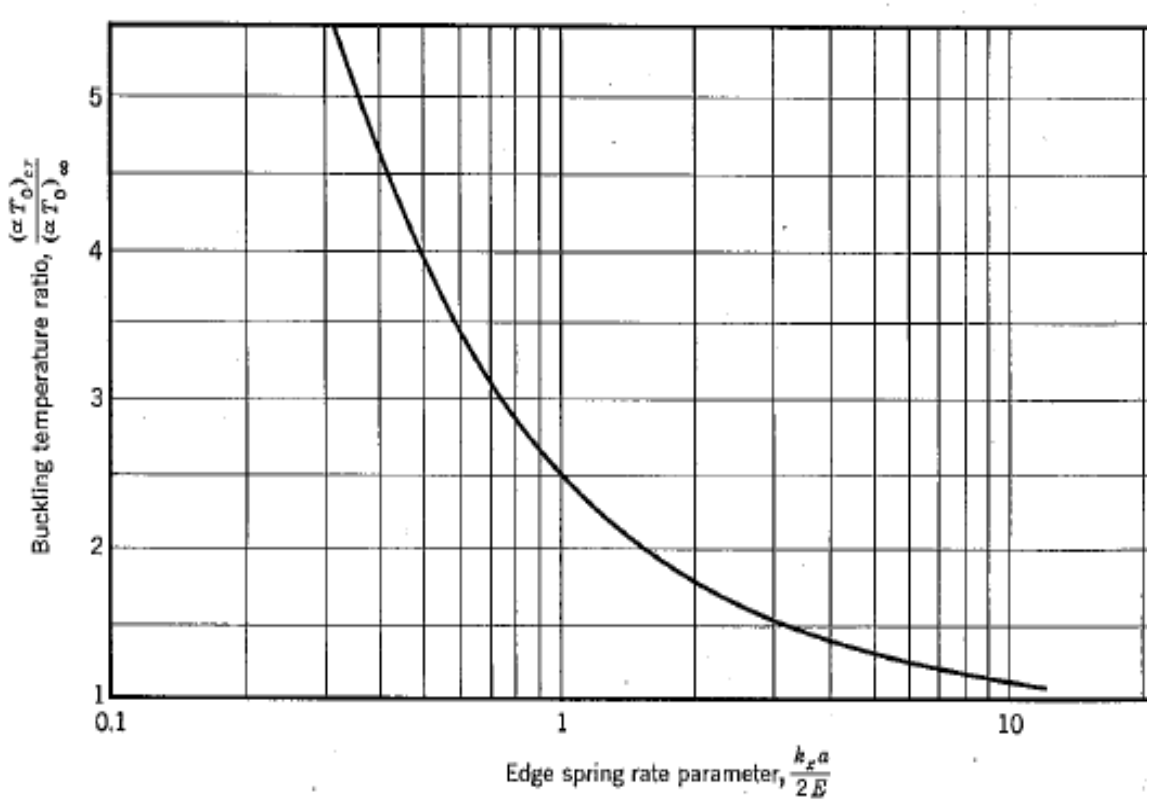

Figure 2.3. Spring stiffness vs buckling temperature ratio [**16**]

are required to buckle the plate. Figure 2.3 demonstrates that as the edge stiffness increases, the buckling temperature ratio (where the subscript ∞ denotes infinite stiffness) approaches unity. The stiffness ratio, $\frac{k_x a}{2E}$, is a key parameter which provides a measure of the relative stiffness between the plate and the boundary. For example, with a stiffness ratio value of 10.0, the buckling temperature ratio is approximately 1.145. Therefore, the actual buckling temperature is only 14.5% above the minimum (k_∞ condition). Of design importance is the infinite stiffness condition (which is difficult to implement practically) but provides a conservative estimate of any real, simply-supported flat plate. For problems in which the thermal moment M_T and/or a transverse load are nonzero and does not vary spatially over the entire domain, the plate experiences transverse deflection w immediately upon loading, and bifurcation buckling *does not* result [**17**]. Therefore, in many practical scenarios where the

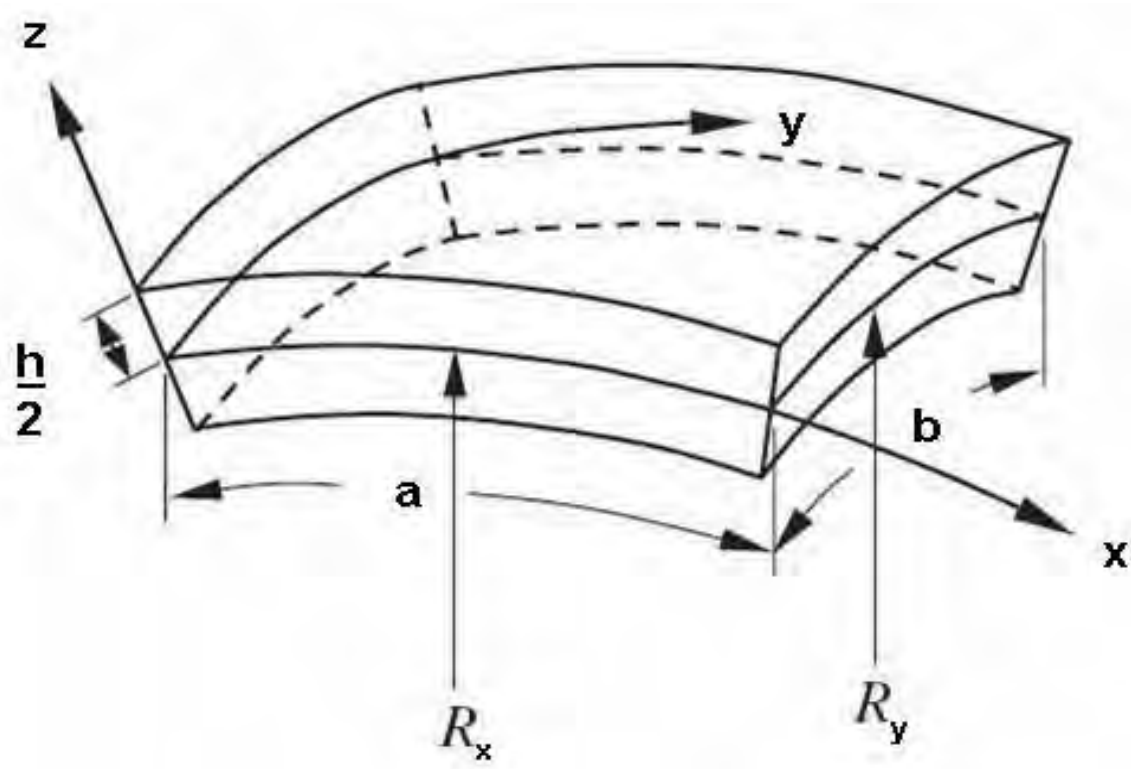

Figure 2.4. Geometry and coordinates of a typical doubly-curved shell.

thermal loading involves a transient heat up, a through thickness gradient exists. Hence, a thermal moment is observed which causes bowing in the plate and allows a smooth transition to out-of-plane deformation for originally flat plates.

2.2.3. Curved Shell Response

While the analytical solution for the response of flat plates provides an important academic contribution to the study of thermally-loaded plane stress members, a more general approach was needed and was realized with shell theory. Since no structural member is truly planar, shells provided a more general geometric framework for more realistic response prediction of engineering structures. A generic shell structure is shown is Figure 2.4. While a shell's curvatures ($\frac{1}{R_x}$ & $\frac{1}{R_y}$) can vary continuously, the two radii of curvature of most practical shells are constant due to manufacturing

constraints. As both radii approach infinity, the flat plate solution is recovered. Moreover, as a single radius is increased, the geometry approaches that of a cylinder. The nonlinear equations for the response of the shell are more complicated than that of the flat plate due to the presence of the initial curvature. The compatibility and transverse equilibrium equations for a thermally loaded shell are given by Eqs. 2.14 and 2.15, respectively.

$$\frac{1}{Eh}\nabla^4\phi = \left(\frac{\partial^2 w}{\partial x \partial y}\right)^2 - \frac{\partial^2 w}{\partial x^2}\cdot\frac{\partial^2 w}{\partial y^2} - \frac{1}{R_x}\frac{\partial^2 w}{\partial y^2} - \frac{1}{R_y}\frac{\partial^2 w}{\partial x^2} - \frac{1}{Eh}\nabla^2 N_T \tag{2.14}$$

$$D\nabla^4 w = \frac{\partial^2 w}{\partial x^2}\cdot\frac{\partial^2 \phi}{\partial y^2} + \frac{\partial^2 w}{\partial y^2}\cdot\frac{\partial^2 \phi}{\partial x^2} - 2\frac{\partial^2 \phi}{\partial x \partial y}\cdot\frac{\partial^2 w}{\partial x \partial y} + \frac{1}{R_x}\frac{\partial^2 \phi}{\partial y^2} + \frac{1}{R_y}\frac{\partial^2 \phi}{\partial x^2} - \frac{1}{(1-\nu)}\nabla^2 M_T \tag{2.15}$$

The Airy stress function, ϕ, as well as N_T and M_T are identical to that employed in the flat plate equations. Many texts and articles exist which address the formulation and solution of shell equations for mechanical, transverse loading. Some of the earliest works can be found in [**18**],[**19**],[**20**],[**21**],and [**22**]. However, with respect to thermal loading, the number of publications is more limited. The text by Langhaar [**23**] is one of the few which includes the thermal load terms in the development of the equations for shell theory. Most references to thermally loaded structures which include instabilities are found in articles. Some of the first publications which addressed thermoelastic response and stability of shells are found in the works by Hoff [**24**], [**25**], and [**26**]. In these articles, geometric symmetry is used to reduce the computational burden as the solution domains are chosen to be cylindrical and conical.

2.2.3.1. In-plane Temperature Gradient. More applicable to the current work with respect to geometry is the article by Mahayni [**27**]. Mahayni investigated the thermal stability of isotropic nonlinear shallow shells subjected to an in-plane temperature gradient. A sinusoidal solution is assumed for the transverse displacement, w, which satisfies the zero displacement condition. A stress function is proposed which satisfies Eq. 2.14 exactly. The transverse equilibrium Eq. 2.15 is then solved by employing a Galerkin method to approximate the solution. R_x in Figure 2.4 is chosen to be ∞, so that the shell panel is singly-curved. Mahayni's geometry differs slightly from that in Figure 2.4 in that the origin of the coordinate axes are located at the center of the figure with domain described by $-a/2 \leq x \leq a/2$, $-b/2 \leq y \leq b/2$, and $-h/2 \leq z \leq h/2$. The positive direction of z is also reversed such that it points toward the center of curvature. With u, v, and w as the displacement components of a point on the middle surface, the internal forces can be represented by integrating the stresses through the thickness,

$$N_x = \int_{-h/2}^{h/2} \sigma_x dz = [\frac{Eh}{1-\nu^2}\frac{\partial u}{\partial x} - k_x w + \frac{1}{2}(\frac{\partial w}{\partial x})^2 + \nu\left\{\frac{\partial v}{\partial y} - k_y w + \frac{1}{2}(\frac{\partial w}{\partial y})^2\right\}] - \frac{N_T}{1-\nu} \tag{2.16}$$

$$N_y = \int_{-h/2}^{h/2} \sigma_y dz = [\frac{Eh}{1-\nu^2}\frac{\partial v}{\partial y} - k_y w + \frac{1}{2}(\frac{\partial w}{\partial y})^2 + \nu\left\{\frac{\partial u}{\partial x} - k_x w + \frac{1}{2}(\frac{\partial w}{\partial x})^2\right\}] - \frac{N_T}{1-\nu} \tag{2.17}$$

$$N_{xy} = \int_{-h/2}^{h/2} \sigma_{xy} dz = \frac{Eh}{2(1+\nu)}\left[\frac{\partial u}{\partial y} + \frac{\partial v}{\partial x} + \frac{\partial w}{\partial x}\frac{\partial w}{\partial y}\right] \tag{2.18}$$

and

$$M_x = -D\left(\frac{\partial^2 w}{\partial x^2} + \nu\frac{\partial^2 w}{\partial y^2}\right) - \frac{M_T}{(1-\nu)} \tag{2.19}$$

$$M_y = -D\left(\frac{\partial^2 w}{\partial y^2} + \nu\frac{\partial^2 w}{\partial x^2}\right) - \frac{M_T}{(1-\nu)} \tag{2.20}$$

$$M_{xy} = (1-\nu)D\frac{\partial^2 w}{\partial x \partial y} \tag{2.21}$$

The temperature distribution is assumed constant through the thickness and circumferential directions but varies parabolically from $x = 0$ to a such that

$$T = [f + k(x-a)^2] \tag{2.22}$$

where

$$k = \frac{e-f}{a^2} = \frac{\Delta T}{a^2}$$

$$\Delta T = \text{Temperature difference}$$

$$f = T_{x=a}$$

$$e = T_{x=0}$$

A solution for the transverse displacement which satisfies the prescribed boundary condition is given by

$$w = \sum_{n=1,2,3,\ldots}^{\infty} A_n(\cos\frac{\pi x}{a}\cos\frac{\pi y}{b})^n = \sum_{n=1,2,3,\ldots}^{\infty} A_n\ \mathbf{\Psi}_n \tag{2.23}$$

where A_n are undetermined coefficients. The solution of equation 2.14 with $R_x \to \infty$ and $R_y = R$, is given by

$$(2.24) \quad \phi = Eh\left(\frac{\pi^2}{ab}\right)^2\left(\frac{-A_1}{2}\right)\left\{\frac{\cos\frac{2\pi x}{a}}{\left(\frac{2\pi}{a}\right)^4}+\frac{\cos\frac{2\pi y}{b}}{\left(\frac{2\pi}{b}\right)^4}\right\} + \frac{Eh}{R}\left(\frac{\pi}{a}\right)^2 A_1\left\{\frac{\cos\frac{\pi x}{a}\cos\frac{\pi y}{b}}{\left[\left(\frac{\pi}{a}\right)^2+\left(\frac{\pi}{b}\right)^2\right]^2}\right\} - \frac{\alpha\ y^2}{2} - \frac{\beta\ x^2}{2} - \frac{Ehck}{12}x^4$$

The solution presented in Mahayni contains a 24 in the denominator of the last term instead of the 12 used in this work. In fact, the stress function in [**27**] does not satisfy equation 2.14. Therefore the equations derived from this point forward in this development will differ from that found in [**27**]. Also, note that α is used in this section to denote a reaction force as opposed its typical use as coefficient of thermal expansion. The variables used in this section were employed to permit the interested reader to most easily compare results with the original work

The Galerkin method is used to determine the unknown coefficient, A_1. A residual equation is formed from the transverse equilibrium equation, 2.15, by rearranging such that the right hand side of the equation is zero. Denoting this residual by Q, the error is minimized by determining A_1 such that

$$(2.25) \qquad \int_{-a/2}^{a/2}\int_{-b/2}^{b/2} Q\ \mathbf{\Psi}_n\ dx\ dy = 0$$

The following dimensionless quantities are defined to facilitate the solution,

$$(2.26) \qquad K_y = \frac{b^2}{R\ h}, \qquad \lambda = \frac{a}{b}, \qquad Z_1 = \frac{A_1}{h}$$
$$\overline{K} = \frac{a^2b^2}{h^2}ck, \quad P_x = \frac{\alpha b^2}{Eh^3}, \quad and \quad P_y = \frac{\beta a^2}{Eh^3}$$

where c is the coefficient of thermal expansion

Upon completing the integration in Eq. 2.25, and incorporating the non-dimensional quantities Eq. 2.26, a cubic equation in Z_1 is obtained.

(2.27)

$$\left[3\pi^8(1+\lambda^2)^2(1+\lambda^4)\right] Z_1^3 - \left[32\ K_y\pi^4\lambda^4(17+2\lambda^2+\lambda^4)\right] Z_1^2 + [-\frac{4\pi^8(1+\lambda^2)^4}{(\nu^2-1)}$$

$$+48\ K_y^2\pi^4\lambda^4 + 24\ \overline{K}\,\pi^4\lambda^4 - 4\pi^6(12\ P_x + 12\ P_y + \overline{K}\,\lambda^2)(\lambda+\lambda^3)^2]\ Z_1$$

$$-1536\ \overline{K}\,K_y\lambda^4(1+\lambda^2)^2 + 192\ K_y\pi^2(4\ Py + \overline{K}\,\lambda^2)(\lambda+\lambda^3)^2 = 0$$

It should be noted here that the non-dimensional quantities for P_x and P_y again differ from that published in [**27**]. In this work, both P_x and P_y contain an additional power of h in their definition making the quantities dimensionless. Without this definition of dimensionless force, Eq. 2.27 would contain both dimensionless and dimensional quantities (e.g., h). These discrepancies do alter the results presented in [**27**] and are therefore presented in this work for completeness.

The first case to be analyzed allows free in-plane expansion. The non-dimensional reactions, P_x and P_y, will be zero. Substituting these values into Eq. 2.27 provides a relationship between the non-dimensional temperature difference, $\overline{K}$, and Z_1, the maximum value of w scaled by the thickness, h. The response of the shell is best described by plotting $\overline{K}$ vs Z_1 for various values of curvature, K_y and aspect ratio, λ. Figure 2.5 displays results for several values of curvature. Since positive Z_1 is directed toward the center of curvature, the unbifurcated paths are left of the $Z_1 = 0$ axis. As the spatial temperature difference increases, the potential exists to "snap" to another equilibrium position to the right of $Z_1 = 0$. The plot reveals that as $K_y \to \infty$ ($R \to 0$), ever-increasing temperature differences are required to cause bifurcation. An important revelation of Eq. 2.27 with $P_x = P_y = 0$ is that the temperature only enters the equations through $\overline{K}$ which is a measure of spatial

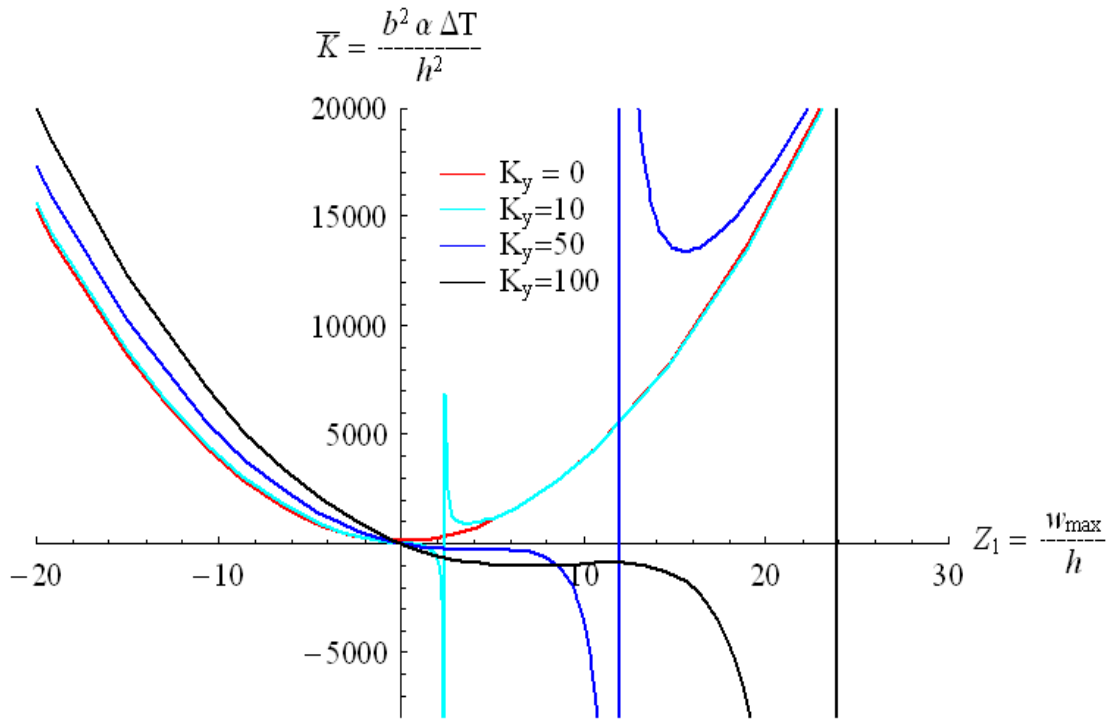

Figure 2.5. Load deflection curve for $\nu = .30$, $\lambda = 1$, and $P_x = P_y = 0$.

temperature difference. Therefore, if a constant temperature of any magnitude is prescribed, buckling is *not* predicted for this set of boundary conditions for finite values of b. As mentioned earlier, the aspect ratio also plays an important role in buckling studies. Figure 2.6 shows load vs maximum deflection for three values of λ. Note that for an aspect ratio of three or greater, the response converges to a single curve.

While the results are presented as non-dimensional quantities and allow application to any isotropic material system, it is instructive to examine what physical temperature difference is required for a prospective high temperature material. Using Titanium 6-2-4-2 material properties [**28**], with $\lambda = 1, h = .125$ in. and $K_y = 5$, Figure 2.7 displays the critical buckling temperature difference vs the circumferential distance. To arrive at this relation, the equation for $\bar{K}$ in Eq. 2.26 is solved for ΔT

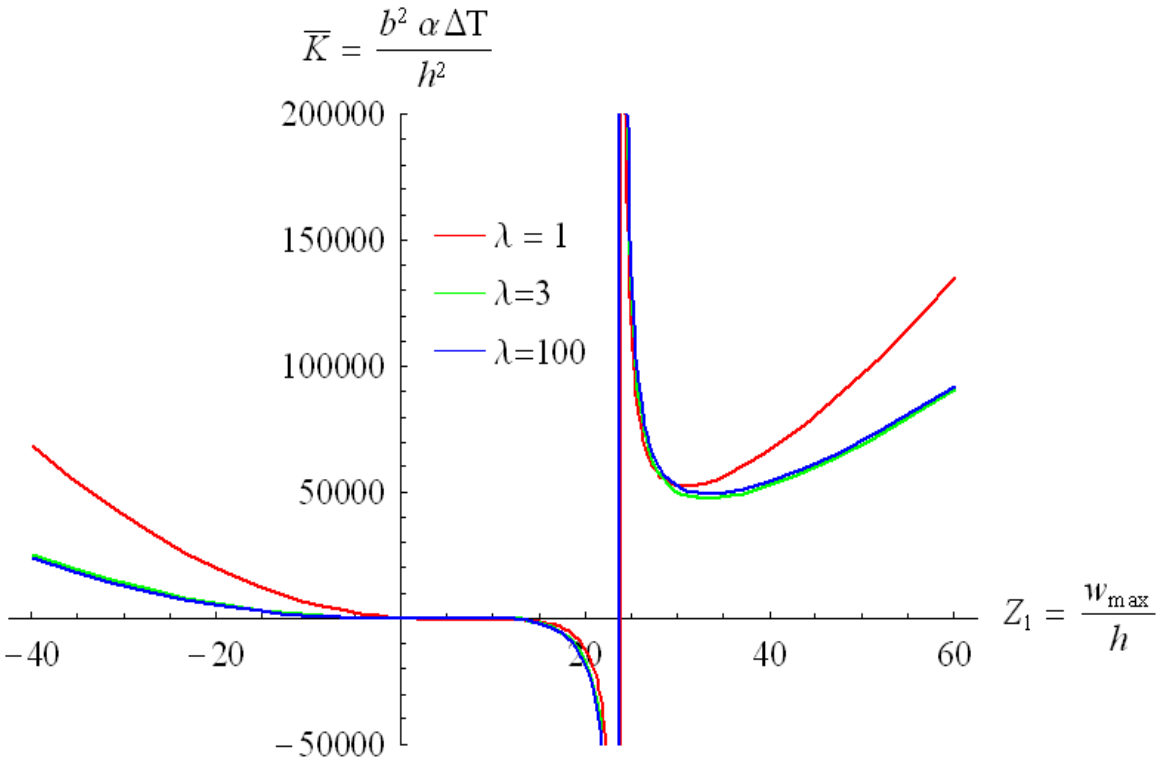

Figure 2.6. Load-deflection curve for $\nu = .30$, $K_y = 100$ and $P_x = P_y = 0$.

with $a = b$. We can see that as $b \to \infty$, $(\Delta T)_{cr} \to 0$, but for finite values of b, a non-zero value of ΔT is required for buckling. At the other extreme, small values of b ($\simeq$10 in), $(\Delta T)_{cr}$ is well above the usage temperature of the material ($\simeq$20,000°F). Using Mahayni's values, a non-dimensional curvature (K_y) of 200 would be required to produce similar results. Hence, his values greatly *underestimate* the value of in-plane temperature gradient necessary to produce buckling in a curved panel with boundary conditions that allow in-plane motion.

The second case of shallow shell buckling response examined is that of a simply-supported boundary. Rotations at the boundary are allowed but no deflection (in-plane or transverse) is permitted. The average displacement of the middle surface in

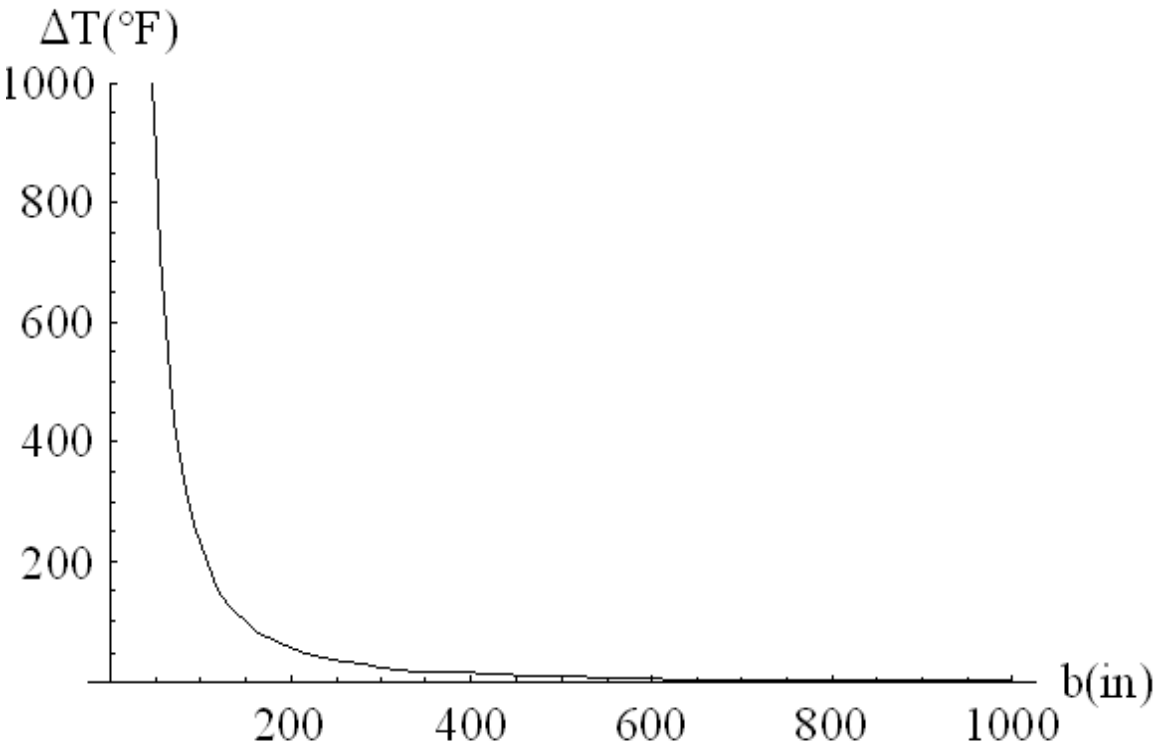

Figure 2.7. Critical spatial temperature difference ΔT vs circumferential distance b for titanium alloy with K_y=5 and $\lambda = 1$

the x-direction is given by the integral

$$e_x = -\frac{1}{a}\int_{-a/2}^{a/2} \frac{\partial u}{\partial x} dx \tag{2.28}$$

However, this average varies in the y-direction. Hence, the integral average over the y-coordinate is

$$\bar{e}_x = \frac{1}{b}\int_{-b/2}^{b/2} e_x dy \tag{2.29}$$

The constitutive equation provides a relation between $\frac{\partial u}{\partial x}$ and the dependent variables (equation 2.30).

$$\frac{\partial u}{\partial x} = \frac{1}{Eh}\left(\frac{\partial^2 \phi}{\partial y^2} - \nu \frac{\partial^2 \phi}{\partial x^2}\right) - \frac{1}{2}\left(\frac{\partial w}{\partial x}\right)^2 + cT \tag{2.30}$$

Carrying out the integrations in Eqs. 2.28 and 2.29, and equating $\bar{e}_x = 0$, an equation containing P_x and P_y is generated. This process is similarly carried out for $\bar{e}_y = 0$ resulting in a second equation containing P_x and P_y. This system is solved for P_x and P_y and substituted into Eq. 2.27. The governing equation for the panel with restrained edges is given by

$$
\begin{aligned}
(2.31) \qquad & 3\pi^8(1+\lambda^2)^2(-3-4\lambda^2\nu+\nu^2+\nu^4(-3+\nu^2))Z_1^3+ \\
& 32\ K_y\pi^4\lambda^2(3\nu+\lambda^2(8+6\nu-5\nu^2)+\lambda^4(8+3\nu-2\nu^2)-\lambda^6(-4+\nu^2))Z_1^2+ \\
& (-4\pi^8(1+\lambda^2)^4+48\ \bar{f}\ \pi^6(1+\lambda^2)^3(1+\nu)+52\ \bar{K}\pi^6\lambda^2(1+\lambda^2)^3(1+\nu)- \\
& 3072\ K_y^2\lambda^4(\nu^2-1)+48\ K_y^2\pi^4\lambda^4(\nu^2-1)+24\ \bar{K}\pi^4\lambda^2(\lambda+\lambda^3)^2(\nu^2-1))Z_1- \\
& 768\ \bar{f}\ K_y\pi^2\lambda^2(1+\lambda^2)^2(1+\nu)-1536\ \bar{K}\ K_y\lambda^4(1+\lambda^2)^2(\nu^2-1)+ \\
& 64\ \bar{K}\ K_y\pi^2\lambda^4(1+\lambda^2)^2(-15-13\nu+2\nu^2)=0
\end{aligned}
$$

where

$$\bar{f} = \frac{cfa^2}{h^2}$$

The response of the shell with restrained edges is shown in Figures 2.8 and 2.6 for various values of curvature and aspect ratio. The values of $\bar{\mathrm{K}}$ shown in Figures 2.8 and 2.9 are two orders of magnitude lower than those presented in [**27**]. Mahayni predicts buckling of simply-supported curved panels to occur for only for very small values of curvature (< 20) in the practical temperature of the material. The results computed in this work using the correct stress function reveal that simply-supported panels are more likely to buckle due to in-plane temperature gradients than the unsupported panels. Mahayni reached the opposite conclusion.

With such a large discrepancy between the results presented here and those published earlier, it is important that verification of the results be carried out. One

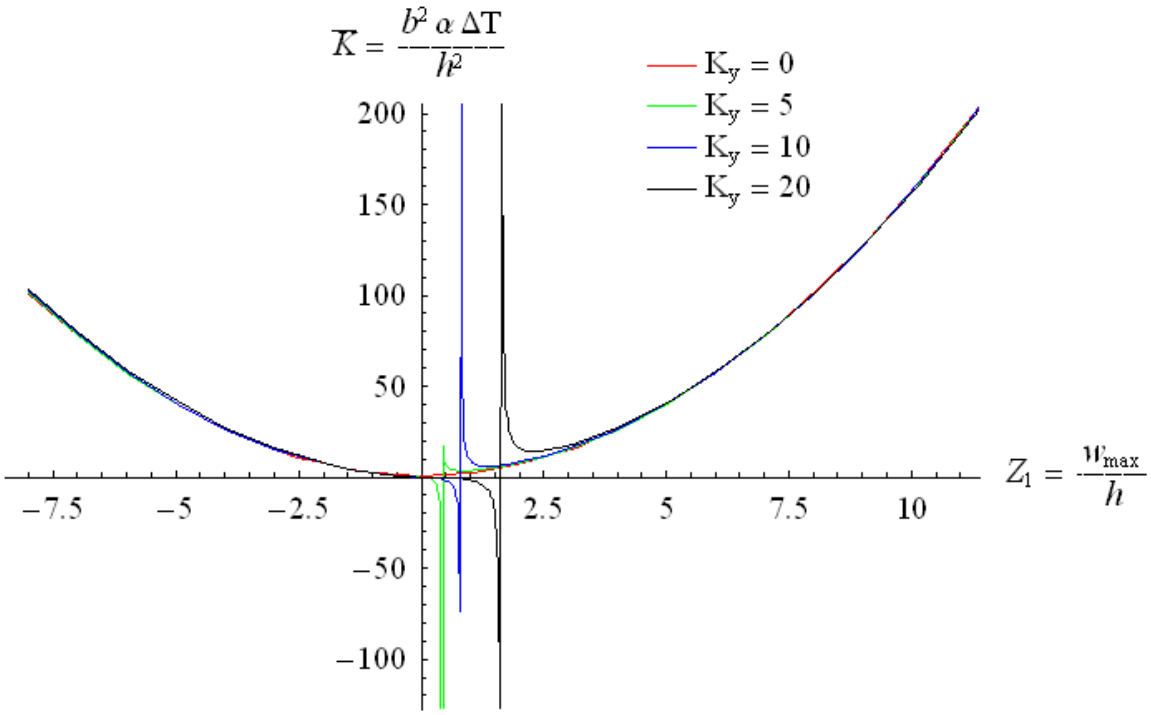

Figure 2.8. Load-deflection curve for $\nu = 0.3$, $\lambda = 1$, $\bar{f} = 0$, and $\bar{e}_x = \bar{e}_y = 0$.

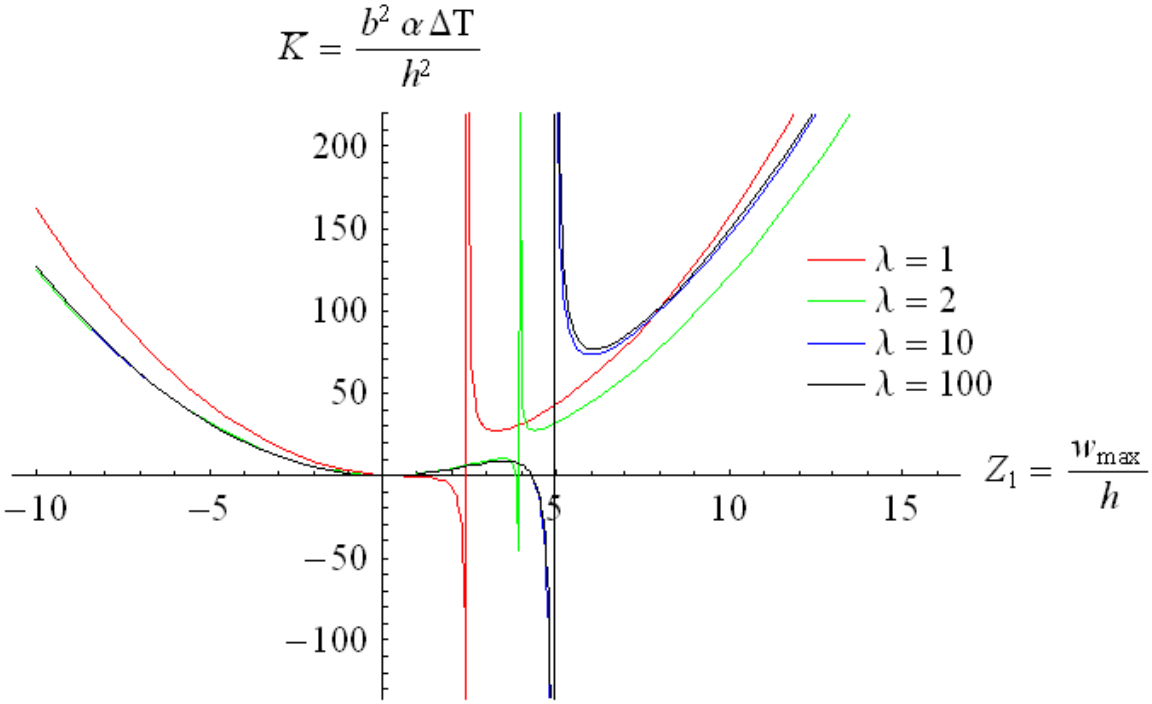

Figure 2.9. Load-deflection curve for $\nu = 0.3$, $K_y = 30$, $\bar{f} = 0$ and $e_x = e_y = 0$.

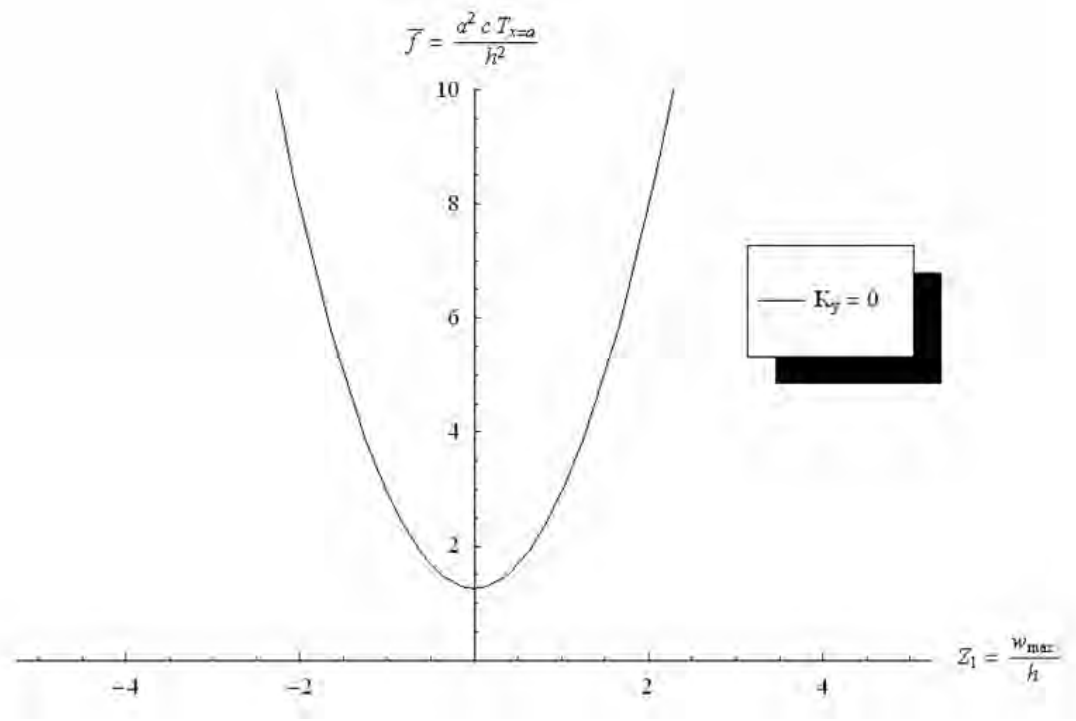

Figure 2.10. Load-deflection curve for $\lambda = 1$, $\nu = 0.3$, $K_y = 0$, $K = 0$, and $\bar{e}_x = \bar{e}_y = 0$.

important difference between the unrestrained and simply-supported conditions is the presence of $\bar{f}$. Since $\bar{f}$ contains an explicit reference to the temperature, buckling can occur devoid of an in-plane temperature gradient. Since other, independent analytical solutions exist for constant temperature buckling solutions of simply-supported flat plates, the solution developed in this section will be verified independently. Setting $\bar{K} = 0$, $K_y = 0$, and $\lambda = 1$, the response of $\bar{f}$ vs Z_1 is given in Figure 2.10. Since $\bar{f} = \frac{cfa^2}{h^2}$, the critical buckling temperature of the shell is given by $f = (\frac{h^2}{ca^2})\ \bar{f}$. This minimum value of $\bar{f}$ $(\simeq 1.265)$ from Figure 2.10 occurs as $Z_1 \rightarrow 0$. The corresponding critical value of f above the reference state for a 12 in x 12 in x 0.125 in Titanium 6-2-4-2 plate is 27.46 $^\circ F$. Eq. 2.13 can be adapted to provide the necessary independent verification. As the spring boundary stiffness terms approach infinity, Eq. 2.13 predicts a critical buckling temperature for the given titanium plate to be

T =27.46 $^{\circ}F$. Therefore, the equations derived in this section reduce to the classical flat plate buckling solution and provide a measure of verification.

The major conclusions that can be deduced from this study are (i) as initial curvature increases, larger spatial gradients and/or higher temperatures are required to initiate buckling for both cases; (ii) much larger temperature differences are required to initiate buckling in the unrestrained case than in the simply-supported scenario, and (iii) the aspect ratio influences the response to a much greater degree in the simply-supported case.

While the previous study provides insight into the onset of buckling and post-buckling response of a curved panel, stresses obtained from such a model are highly inaccurate. The one-term approximation of the transverse displacement is not sufficient to resolve stresses accurately. Even though deflections may be fairly accurate, the second derivatives of the approximate deflections may deviate widely from their proper values. Consequently, when deflections are used to calculate stresses, a high degree of accuracy may be required [**23**]. This is not unlike the displacement finite element formulation where higher mesh density and/or higher order polynomials are needed for stress convergence [**29**]. Since two and three-dimensional nonlinear problems typically require approximate methods like the Galerkin method used above, in the next section a one-dimensional nonlinear model is solved to gain insight into the stress behavior of thermally-loaded shell structures and the boundary loads generated from employing common stiffening methods.

2.3. Straight Beam Model

2.3.1. Fixed End Conditions

A unit width strip model (Figure 2.11), will be used to demonstrate the non-intuitive nature of stiffening in an elevated temperature thermoelastic environment. The strip

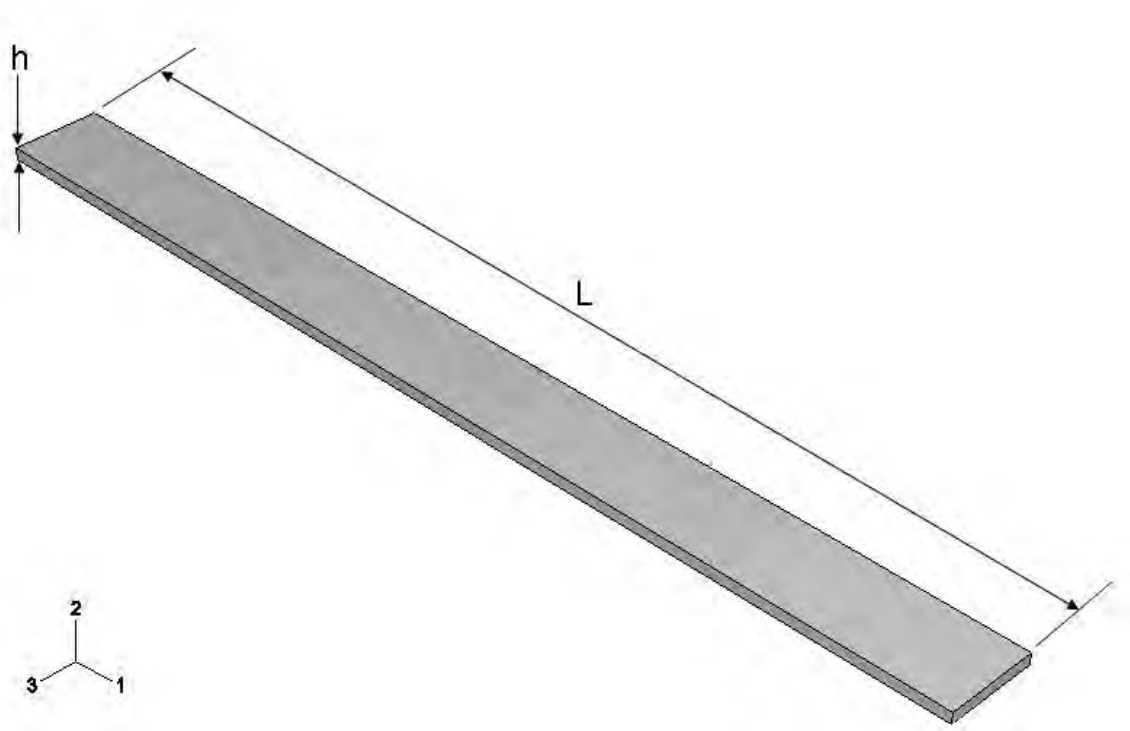

Figure 2.11. Unit width strip beam model

model permits the use of a simplified nonlinear beam theory to demonstrate the essential characteristics of cylindirical bending of a semi-infinite shell. Following an approach similar to that employed in [**30**],[**31**],[**32**], and [**33**] a planar two-point boundary value problem is solved for the post-buckling response of a clamped-clamped, thermally-loaded beam by employing the so-called "shooting" method for nonlinear ordinary differential equations. Figure 2.12 illustrates the undeformed and deformed states of an initially straight beam. The material points in the undeformed configuration are described by the pair (X, Y) with $X \epsilon [0, L]$ and $Y \equiv 0$. Hence, the material points, $(X, 0)$ transform to points $(X + u, w)$ when the beam configuration corresponds to a buckled state. An undeformed differential element, $\boldsymbol{dS}$, is mapped into the stretched and rotated differential element $\boldsymbol{ds}$ in the current (or deformed) configuration. The deformations are restricted to lie in the X-Y plane and symmetry

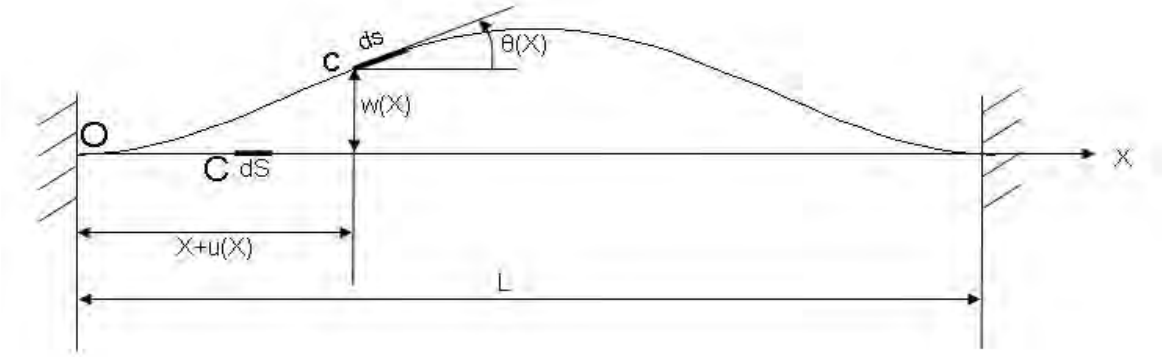

Figure 2.12. Undeformed and deformed configuration of thermally loaded, clamped-clamped beam.

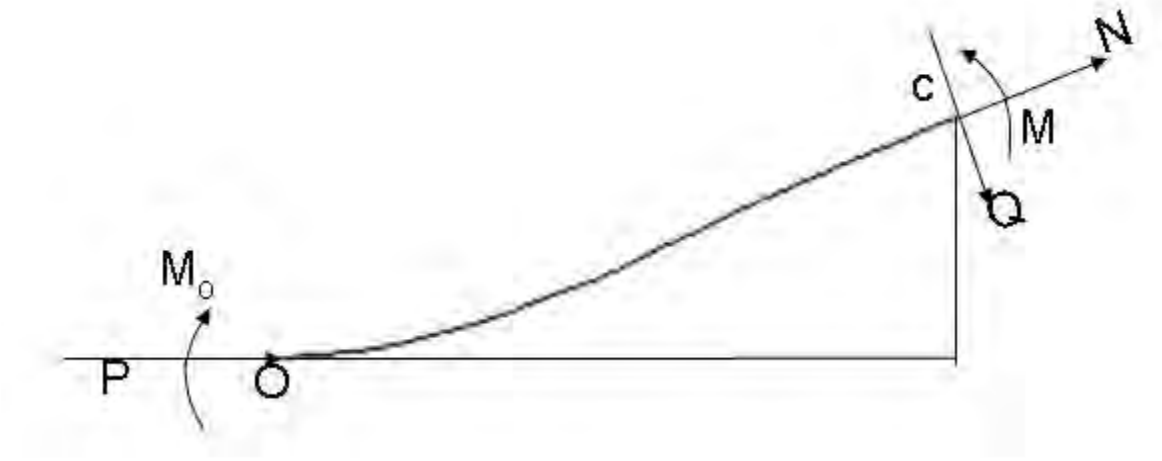

Figure 2.13. Free-body diagram of deformed configuration

about $X = L/2$ is assumed. Equilbrium in the deformed configuration is illustrated in Figure 2.13.

Symbolically, the mapping from the original to current configuration can be expressed by

$$\boldsymbol{ds} = \boldsymbol{F}\, \boldsymbol{dS} \tag{2.32}$$

where $\boldsymbol{F}$ is the deformation tensor [**34**]. In terms of the displacement gradient, $\boldsymbol{F}$ can be expressed as

$$\boldsymbol{F} = \boldsymbol{I} + \nabla_X \boldsymbol{u}(X) \tag{2.33}$$

where ∇_X represents the gradient operator with respect to the material (or Lagrangian) configuration. From Eqs. 2.32-2.33, the following geometric relations are obtained (with dependent variables suppressed).

$$\frac{|\boldsymbol{ds}|}{|\boldsymbol{dS}|} = \frac{ds}{dX} = r, \quad \frac{du}{dX} = r\cos\theta - 1, \quad \frac{dw}{dX} = r\sin\theta \tag{2.34}$$

The strain and curvatures can be expressed in terms of r and θ by

$$\varepsilon = r - 1, \qquad \kappa = \frac{1}{r}\frac{d\theta}{dX} \tag{2.35}$$

The thermoelastic constitutive equations are given by

$$N = EA\ (\varepsilon - \alpha\ \Delta T), \quad M = EI\ \kappa \tag{2.36}$$

Summing the forces and moments at point "c" results in the equilibrium equations,

$$N + P\cos\theta = 0, \quad M + Pw = M_o \tag{2.37}$$

$$r = -\frac{P}{EA}\cos\theta + \alpha\ \Delta T + 1 \tag{2.38}$$

where $s(X)$ is the arc length of the deflected curve, $r(X)$ is the stretch ratio of the axial line, and $\theta(X)$ is the cross-section rotation; $N(X)$ is the axial internal force, and $M(X)$ is the internal bending moment; P is the constraint reaction force at the clamped boundary; M_O is the reaction moment at the constrained ends; E is the Young's modulus; α is the linear thermal expansion coefficient; A is the cross-sectional area; I is the second moment of area of the cross-section and ΔT is the change in temperature of the uniform field. For this study, the material properties will be assumed independent of the temperature.

For solution convenience, the following dimensionless variables will be used,

$$(\xi, \widehat{s}, \widehat{u}, \widehat{w}, \widehat{h}) = \frac{1}{L}(X, s, u, w, h), \qquad \tau = \gamma^2 \alpha \ \Delta T, \tag{2.39}$$

$$\gamma = L\sqrt{\frac{A}{I}}, \quad p = \frac{PL^2}{EI}, \quad m = \frac{M_O L}{EI} \tag{2.40}$$

the nonlinear system of dimensionless equations are given by

$$\widehat{s}^{\,\prime}(\xi) = r, \quad \widehat{u}^{\,\prime}(\xi) = r \ \cos\theta - 1, \tag{2.41}$$

$$\widehat{w}^{\,\prime}(\xi) = r \ \sin\theta, \quad \theta^{\,\prime}(\xi) = r \ (m - p\widehat{w}) \tag{2.42}$$

$$p'(\xi) = m'(\xi) = 0 \tag{2.43}$$

where $r = (-p\cos\theta + \tau)/\gamma^2 + 1$ along with the following symmetric boundary conditions,

$$\widehat{s}(0) = \widehat{u}(0) = \widehat{w}(0) = \theta(0) = 0 \tag{2.44}$$

$$\widehat{u}(\frac{1}{2}) = \theta(\frac{1}{2}) = 0 \tag{2.45}$$

The dimensionless temperature τ is treated as a prescribed parameter in the solution process. For values of τ greater than $4\pi^2$, buckling occurs. To compute the large displacement, out-of-plane deformation, a shooting method for solving nonlinear ordinary differential equations is utilized to solve the system of equations. Symbolically, the system can be expressed as

$$\frac{d\boldsymbol{Y}(\xi)}{d\xi} = \boldsymbol{H}(\xi, \boldsymbol{Y};\ \tau) \qquad (0 < \xi \ < \frac{1}{2}) \tag{2.46}$$

$$\boldsymbol{B}_1\boldsymbol{Y}(0) = \{0 \ \ 0 \ \ 0 \ \ 0\}^T, \quad \boldsymbol{B}_2\boldsymbol{Y}(\frac{1}{2}) = \{0 \ \ 0\}^T$$

$$\boldsymbol{Y} = \{y_1 \ \ y_2 \ \ y_3 \ \ y_4 \ \ y_5 \ \ y_6\}^T = \{\widehat{s} \ \ \widehat{u} \ \ \widehat{w} \ \ \theta \ \ m \ \ p\}^T$$

$$\boldsymbol{H} = \{r \quad r\cos y_4 - 1 \quad r\sin y_4 \quad r(y_5 - \ y_3 y_6) \quad 0 \quad 0\}^T$$

$$\boldsymbol{B}_1 = \begin{bmatrix} 1 & 0 & 0 & 0 & 0 & 0 \\ 0 & 1 & 0 & 0 & 0 & 0 \\ 0 & 0 & 1 & 0 & 0 & 0 \\ 0 & 0 & 0 & 1 & 0 & 0 \end{bmatrix}, \boldsymbol{B}_2 = \begin{bmatrix} 0 & 1 & 0 & 0 & 0 & 0 \\ 0 & 0 & 0 & 1 & 0 & 0 \end{bmatrix}$$

In actuality, m and p are problem parameters. These load parameters are treated as unknown functions of ξ forming a standard problem statement for accomodating nonlinear boundary value problems with multiple parameters [**35**].

The shooting method for the solution of nonlinear ordinary differential equations involves reformulating the problem in terms of an initial value problem.

$$\begin{aligned} \frac{d\widetilde{\boldsymbol{Y}}(\xi)}{d\xi} &= \boldsymbol{H}(\xi, \widetilde{\boldsymbol{Y}};\ \tau) \qquad (0 < \xi \ < \frac{1}{2}) \\ \widetilde{\boldsymbol{Y}}(0) &= \{0 \ \ 0 \ \ 0 \ \ 0 \ \ m(0) \ \ p(0)\}^T \end{aligned} \tag{2.47}$$

The initial value problem is iteratively solved using an appropriate integrator (i.e., 4^{th}-order Runka-Kutta) until the conditions at $\xi = 1/2$, match the prescribed values. This problem can be treated as an optimization problem with the objective being satisfaction of the end conditions while the unprescribed values at $\xi = 0$, $m(0) = p(0)$, are treated as design variables. If we define the design variable vector $\boldsymbol{d}^T = \{y_5(0) \ \ y_6(0)\}$, then the current estimate of the initial value problem can be treated as a function of the design variables,

$$\begin{aligned} \frac{d\widetilde{\boldsymbol{Y}}(\xi, \boldsymbol{d})}{d\xi} &= \boldsymbol{H}(\xi, \widetilde{\boldsymbol{Y}}(\xi, \boldsymbol{d});\ \tau) \\ \widetilde{\boldsymbol{Y}}(0) &= \{0 \ \ 0 \ \ 0 \ \ 0 \ \ d_1 \ \ d_2\}^T \end{aligned} \tag{2.48}$$

The primal problem can be differentiated to compute analytical sensitivities of the response with respect to the design variables. This direct differentiation method is given by the two following *pseudo* problems.

$$\begin{aligned} \left(\frac{d\widetilde{\boldsymbol{Y}}(\xi, \boldsymbol{d})}{d\xi}\right)_{,d_1} &= \boldsymbol{H}_{,\widetilde{\boldsymbol{Y}}}(\boldsymbol{\xi}, \widetilde{\boldsymbol{Y}}(\boldsymbol{\xi}, \boldsymbol{d});\ \tau)\ \widetilde{\boldsymbol{Y}}_{,d_1} \\ \widetilde{\boldsymbol{Y}}_{,d_1}(0) &= \{0 \ \ 0 \ \ 0 \ \ 0 \ \ 1 \ \ 0\}^T \end{aligned} \tag{2.49}$$

$$\begin{aligned} \left(\frac{d\widetilde{\boldsymbol{Y}}(\xi, \boldsymbol{d})}{d\xi}\right)_{,d_2} &= \boldsymbol{H}_{,\widetilde{\boldsymbol{Y}}}(\xi, \widetilde{\boldsymbol{Y}}(\xi, \boldsymbol{d});\ \tau)\ \widetilde{\boldsymbol{Y}}_{,d_2} \\ \widetilde{\boldsymbol{Y}}_{,d_2}(0) &= \{0 \ \ 0 \ \ 0 \ \ 0 \ \ 0 \ \ 1\}^T \end{aligned} \tag{2.50}$$

The residual system of equations to be solved is expressed by

$$\mathbf{\Pi}(\boldsymbol{d}^*) = \left(\widetilde{\boldsymbol{Y}}(\boldsymbol{\xi}, \boldsymbol{d}^*) - \boldsymbol{B}_2 \boldsymbol{Y}(\xi) \right)_{\xi=\frac{1}{2}} = \mathbf{0} \tag{2.51}$$

where $\boldsymbol{d}^*$ denotes the optimal value of $\boldsymbol{d}$. Expanding Eq. 2.51 in a first-order Taylor series expansion,

$$\mathbf{\Pi}(\boldsymbol{d}^*) = \mathbf{\Pi}(\boldsymbol{d}^i) + \left(\frac{\partial \mathbf{\Pi}(\boldsymbol{d})}{\partial \boldsymbol{d}} \right)_{\boldsymbol{d}=\boldsymbol{d}^i} \Delta \boldsymbol{d}^i \approx \mathbf{0} \tag{2.52}$$

$$\Delta \boldsymbol{d}^i \approx - \left(\frac{\partial \mathbf{\Pi}(\boldsymbol{d})}{\partial \boldsymbol{d}} \right)^{-1}_{\boldsymbol{d}=\boldsymbol{d}^i} \mathbf{\Pi}(\boldsymbol{d}^i) \tag{2.53}$$

$$\boldsymbol{d}^{i+1} = \boldsymbol{d}^i + \Delta \boldsymbol{d}^i \tag{2.54}$$

facilitates application of Newton's method for the solution of the nonlinear system with $\boldsymbol{d}^i$ the current estimate of the design variables.

Thermally buckled configurations are shown in Figure 2.14 for various values of τ. For a clamped-clamped isotropic beam, the maximum tensile stress will occur at the clamped edge at the outermost fibers opposite the displacement. Hence for the case under consideration, the maximum stress occurs at point "O" (Figure 2.13) on the bottom side of the beam. One of the most common approaches to alleviating thermal buckling is to increase the thickness of the panel. The minimal value of τ for which buckling occurs is computed by solution of the linearized eigenvalue problem in Eq. 2.46. The critical value of τ at which buckling occurs is $4\pi^2$. From Eq. 2.39, with $\tau = 4\pi^2 = \gamma^2 \alpha \ (\Delta T)_{cr}$ a decrease in γ increases the temperature change required for buckling to occur. The non-dimensional thickness is related to γ^2 by

$$\gamma^2 = L^2 \frac{A}{I} = L^2 \left(\frac{h}{\frac{1}{12} h^3} \right) = \frac{12}{\left(\frac{h^2}{L^2} \right)} = \frac{12}{\widehat{h}^2} \tag{2.55}$$

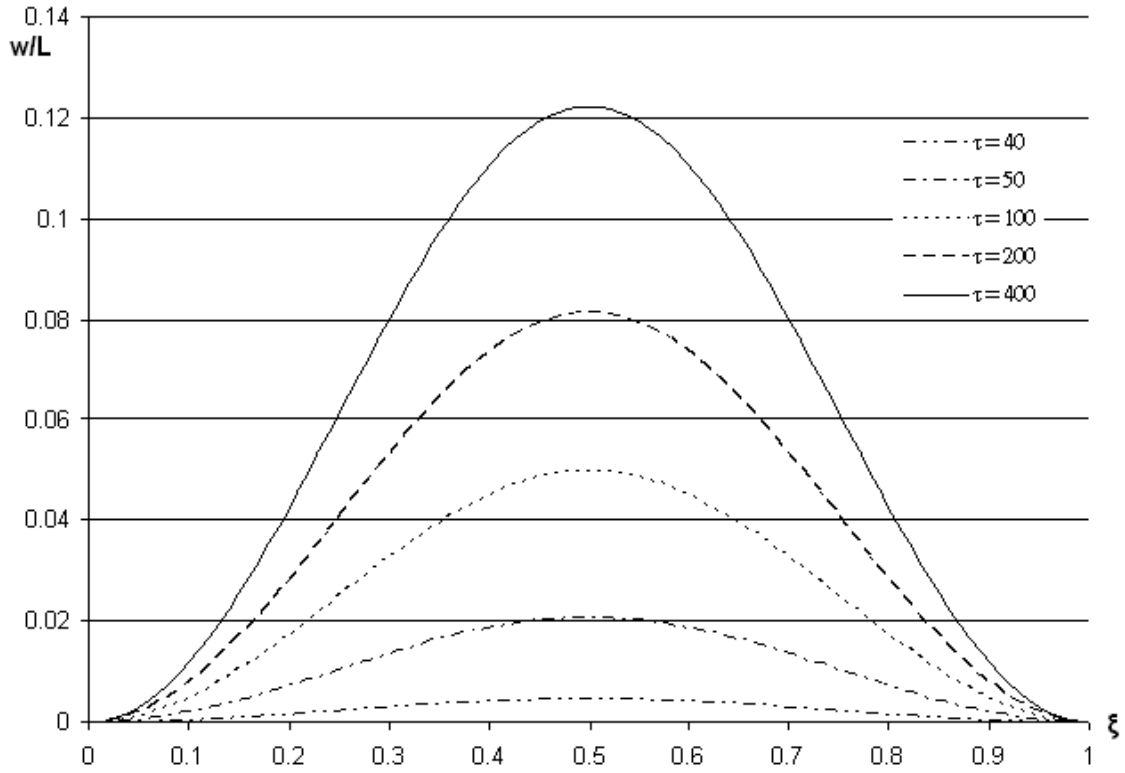

Figure 2.14. Post-buckled configurations for various values of τ.

Therefore, a factor two increase in thickness increases the critical buckling temperature by a factor of four. While this *is* an efficient means to increase buckling temperature, the increased load due to participation of the additional thermal mass, must be reacted by the surrounding structure. So, care must be taken to ensure the structural integrity of sub- and surrounding structure. Additionally, if an attempt is made to prohibit buckling, and due to model uncertainty (e.g., boundary conditions, material properties, etc.), the desired buckling temperature is under predicted, an *increase* in tensile stress can be observed in the skin. Figure 2.15 presents the results of a study examining the influence of plate thickness on maximum *mechanical* strain. Note the parabolic behavior of the strain response with thickness. For a given material and temperature change, there exists a maximum strain condition corresponding to a particular value of non-dimensional thickness. This result differs dramatically

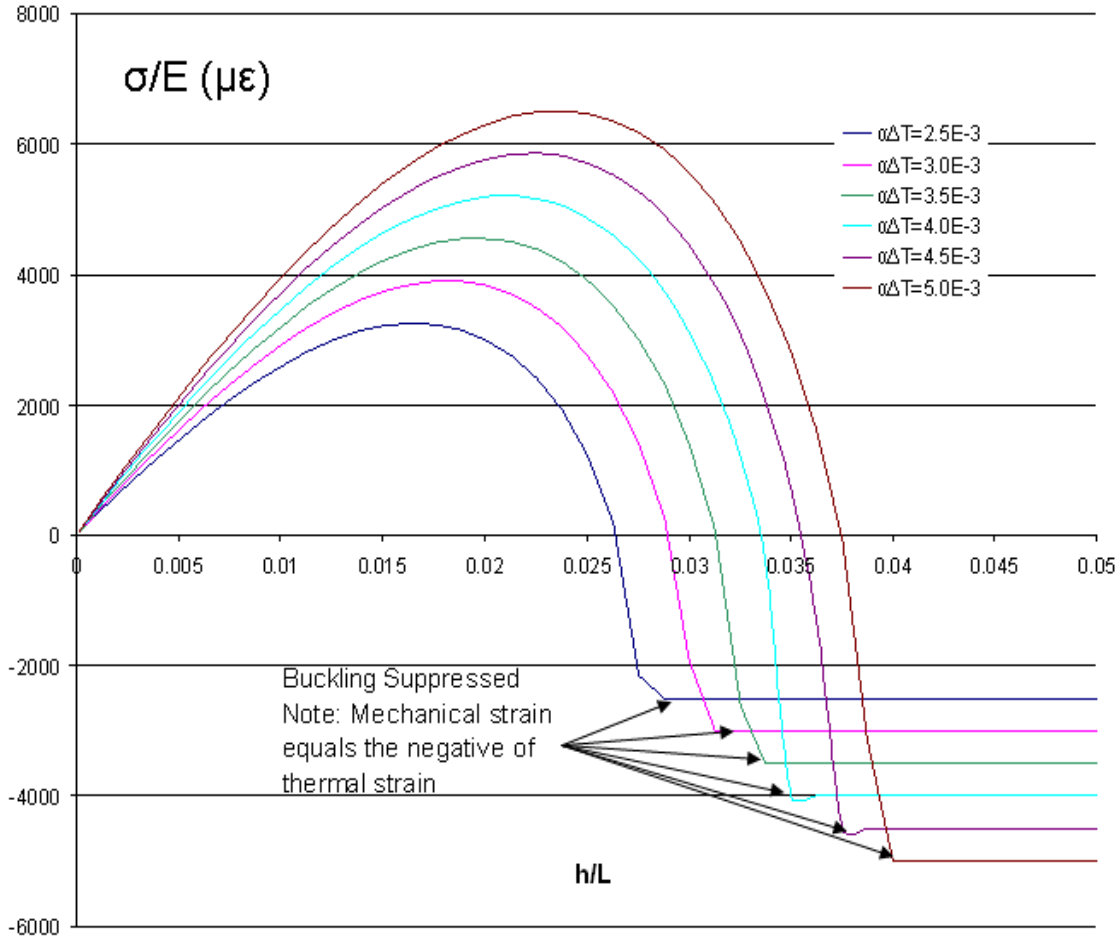

Figure 2.15. Maximum mechanical strain vs normalized thickness for various values of $\alpha\Delta T$.

from typical mechanically-loaded cases where increases in thickness decrease the stress monotonically. In fact, if geometric nonlinearity is ignored, a monotonic decrease in stress is also observed in the thermoelastic problem for realistic values of thickness [**36**].

Figure 2.15 demonstrates that increasing thickness does not necessarily lower the stress and can, in many circumstances, increase the stress levels. Another important consideration is the additional load that is transferred to the fixed boundary. The fixed boundary assumption provides an upper bound on the potential load that can be generated. From Eq. 2.40, with $\alpha\Delta T = .005$, the increase in load, P, is proportional

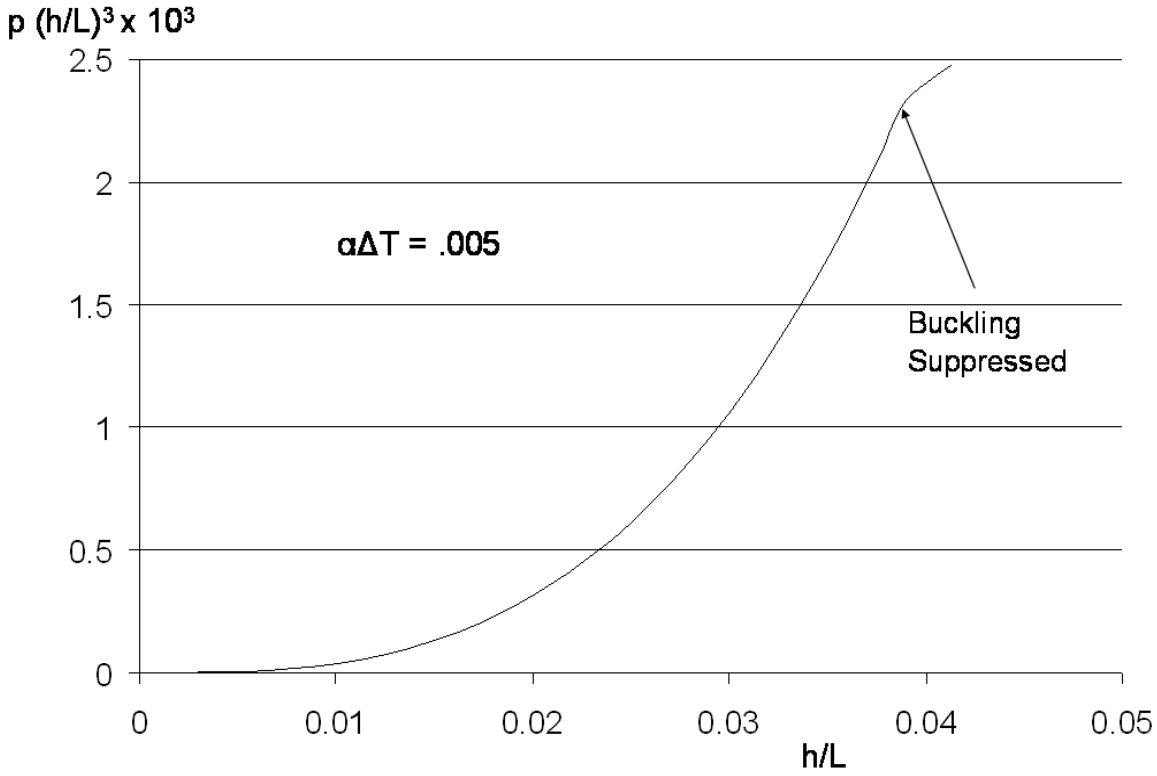

Figure 2.16. Effect of increasing thickness on non-dimensional load factor.

to the non-dimensional load, p, and the cube of the non-dimensional thickness, $\widehat{h}^3$,

$$P \sim p(\widehat{h})\widehat{h}^3 \tag{2.56}$$

The non-dimensional load, $p(\widehat{h})$, is very nearly constant over the range of $\widehat{h}$ up to the point where buckling is suppressed (Figure 2.16). Hence, in this region, the $\widehat{h}^3$term dominates the relation. At thicknesses at which buckling is suppressed and greater, a constant linear increase in reaction load at the boundary is observed. Since the load for an unbuckled, unit width, flat rectangular beam is given by $P = AE\alpha\Delta T = (E\alpha\Delta T)h$, these results are consistent. The slope of the load curve is greatest just below the buckling suppression point. Therefore, if an attempt is made to suppress buckling by increasing thickness and this point is missed due to model inadequacy, a large increase in load is observed for even very small increases in thickness. This

behavior is similar to what was observed in the strain verses thickness behavior. The primary conclusion to be drawn is that an increase in thickness results in a monotonic increase in load to the boundary which, in a realistic structure, will be reacted by sub- and surrounding structure. So material, being used to stiffen a structure in a thermal environment, should be used sparingly and judicously to accomplish the two objectives of minimal boundary load increase and stress reduction.

2.3.2. Elastic End Conditions

In the previous section, fixed end conditions were exclusively considered. In this section the influence of flexibility at the boundary will be addressed. With flexible end conditions, the possibility exists that the results of the previous section could be called into question. However, one indication that the conclusions reached in the fixed end condition case will remain valid is given by the curve in Figure 2.3. Note that at large values of relative spring stiffness, the curve is rather flat. This implies that decreases in relative spring stiffness between the panel and the boundary have little effect on the buckling temperature when the boundary stiffnesses are large. Therefore, as the stiffness of the panel is increased (e.g., increasing thickness) relative to the boundary stiffness, the initial indication is that stresses may not be reduced until a given ratio of stiffness is obtained. This phenomenon is investigated in this section.

Since the damage location of interest is coincident with the boundary, edge rotations will again be suppressed, however, finite edge displacements will be permitted as thermal expansion takes place. Figure 2.17 illustrates the geometry in which linear springs are placed at $X = 0$ and $X = L$. This choice of placement maintains symmetry in the problem formulation. In [**33**], Vaz and Solano introduce a spring at $X = 0$ but maintain a simple-supported boundary at $X = L$ which destroys symmetry in

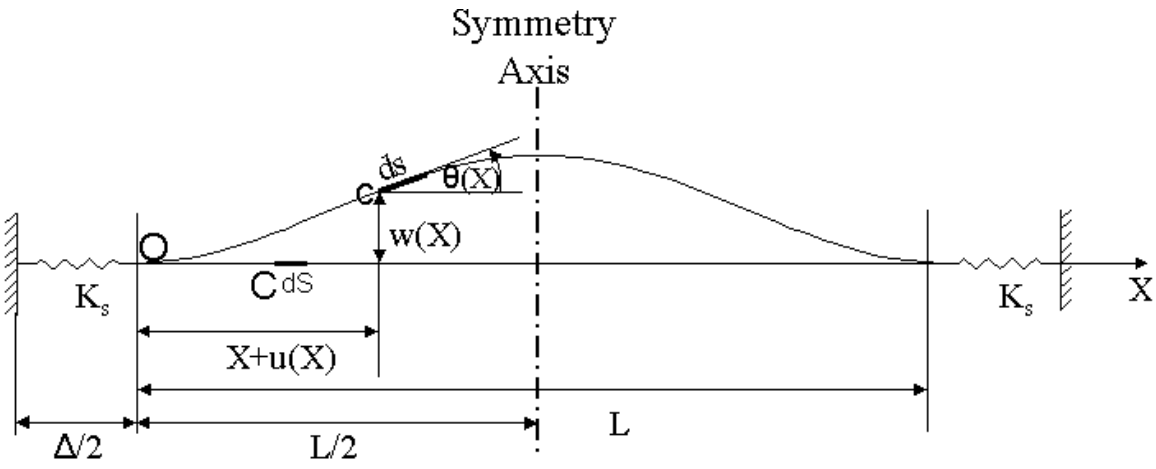

Figure 2.17. Undeformed and deformed configuration of thermally loaded beam with spring supports.

the undeformed configuration. However, Vaz and Solano overcome this difficulty by expressing the deformation gradient derivatives with respect to deformed variables.

The commerical nonlinear finite element code Abaqus is used to conduct a parametric study of the influence of the edge spring stiffness. A linear thermal buckling analysis is initially performed. The first buckled shape is then used to seed the nonlinear analysis with an small imperfection. Since the thickness is changed in each analysis run, the initial imperfection is scaled to be 5% of the current thickness for each analysis performed. A study was performed to ensure that the results were independent of the perturbation size and did not influence the desired responses. A temperature of $900°F$ was applied to the beam with a thermal expansion coefficient of $5.0{\cdot}10^{-6}/°F$. A constant, *at-temperature* value of Young's modulus of $10.0{\cdot}10^{6} lb_f/in^2$ was used. A mesh convergence study was conducted and a mesh size of 0.1 inches was found to be adequate to predict the buckling temperature difference. Since the potential exists for large out-of-plane displacement, nonlinear geometric effects were included in all analyses.

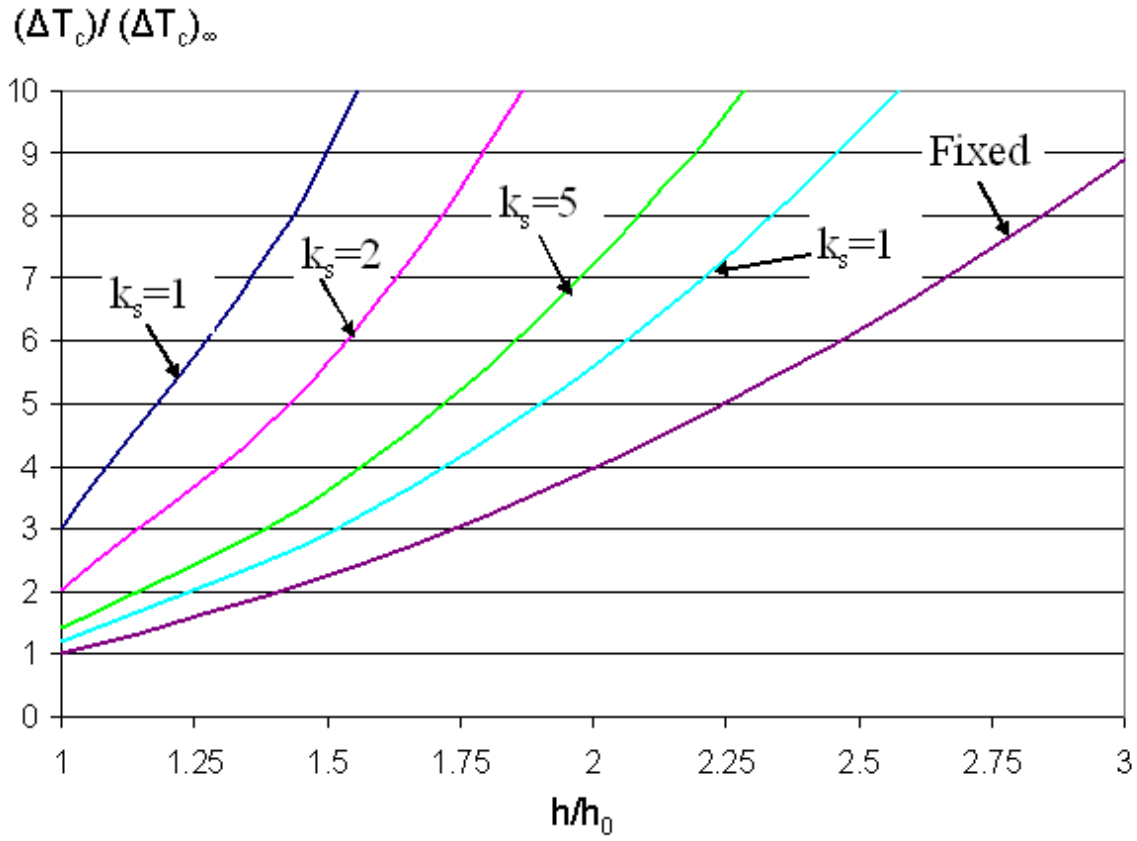

Figure 2.18. Buckling temperature ratio vs h/h_0 for various values of end spring stiffnesses.

Along with the non-dimensional quantities used in the previous section, an additional variable is introduced which represents the relative stiffness of the strip to that of the boundary spring, K_s.

$$k_s = \frac{K_s}{EA/L} \tag{2.57}$$

While this ratio differs from the non-dimensionalization necessary for problem independent solutions (e.g., [**33**]), scaling by the familiar beam stiffness, EA/L, provides greater insight for physical systems. Figure 2.18 details the influence on critical buckling temperature ratio as the thickness of the titanium panel is increased. The y-axis in Figure 2.18 is the ratio of the current value of ΔT necessary to buckle the

panel of thickness h to the value of ΔT with fixed boundary conditions and a thickness of h_0. This graph is useful is analyzing a possible repair scenario in which the repair consists of adding material to the thickness of the failing panel. If we examine the figure at a thickness ratio of 2 (which corresponds to doubling the thickness), the buckling temperature increases by a factor 4 for the infinite edge stiffness condition. If we consider a finite stiffness ratio of 10, the buckling temperature ratio approaches 6. Therefore, if the operating temperature is greater than a factor 6 above the original buckling temperature, the panel could continue to buckle. Hence, as was shown in the fixed edge case, the possibility exists that the post-buckled state of the thicker panel could produce higher stresses than the post-buckled state of the thin, failing panel. Another important observation that can be gleaned from the above results is as the initial boundary stiffness ratio decreases (i.e, weaker springs), adding thickness to the panel has an ever increasing influence on the magnitude of buckling temperature. This fact is reflected in the average slope of each curve. As k_s decreases, the slope increases. If the original boundary stiffness were non-existent (free-edge), then the buckling temperature, as well as the slope of the $k_s = 0$ curve, would approach infinity. Small values of k_s are of little interest due to the fact that failures of the original structure (thickness h) would be much less likely to occur. Since the quantitative behavior varies widely with boundary stiffness, a premium is placed on the accuracy to which the boundary stiffness is determined. For example, if the boundary stiffness is underestimated, adding thickness could appear to be a very feasible solution from a stress reduction viewpoint.

As was discussed in the fully clamped case, the additional load transferred into the boundary must also be considered for the flexible end case. Both the increase in reaction force and moment are of concern as these additional loads must be reacted by sub- and surrounding structure. Furthermore, the surrounding structure may

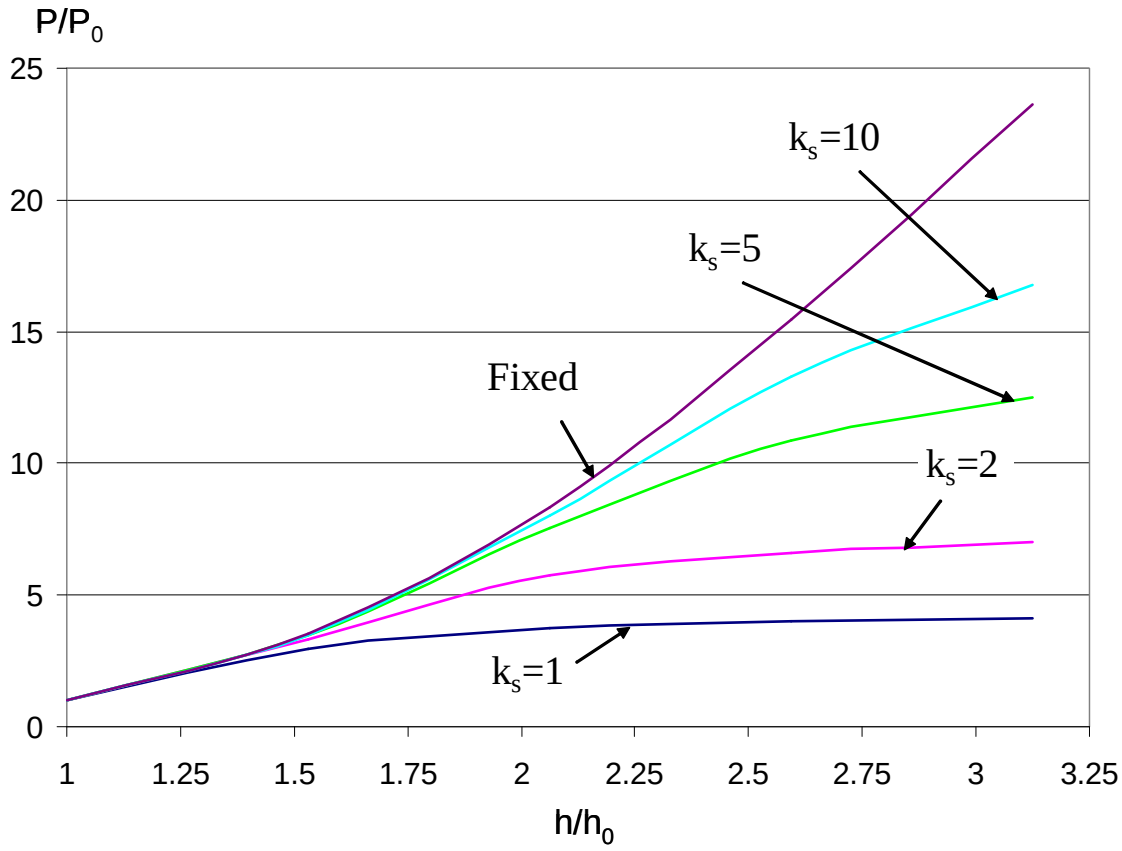

Figure 2.19. Reaction force increase vs thickness increase for various stiffness ratios.

have little or no margin for carrying this additional load if the thickness increase is part of a repair. Figures 2.19 and 2.20 provide an illustration of the reaction force and moment increases, respectively, for associated increases in thickness. Examining Figure 2.19, we see that for small values of boundary stiffness, only small increases in reaction force are possible. For large values of boundary stiffness ratio, the loads increase very rapidly with the infinite stiffness condition providing an upper bound. Note that up to approximately two times the original thickness, the stiffness ratios of 5 and 10 are both approximated well by the fixed condition. As the thickness continues to increase, the infinite stiffness condition provides an upper bound and can be used as a conservative design point. Another important bound can be deduced if we examine the spring stiffness of the boundary and imagine the skin expanding freely. This free

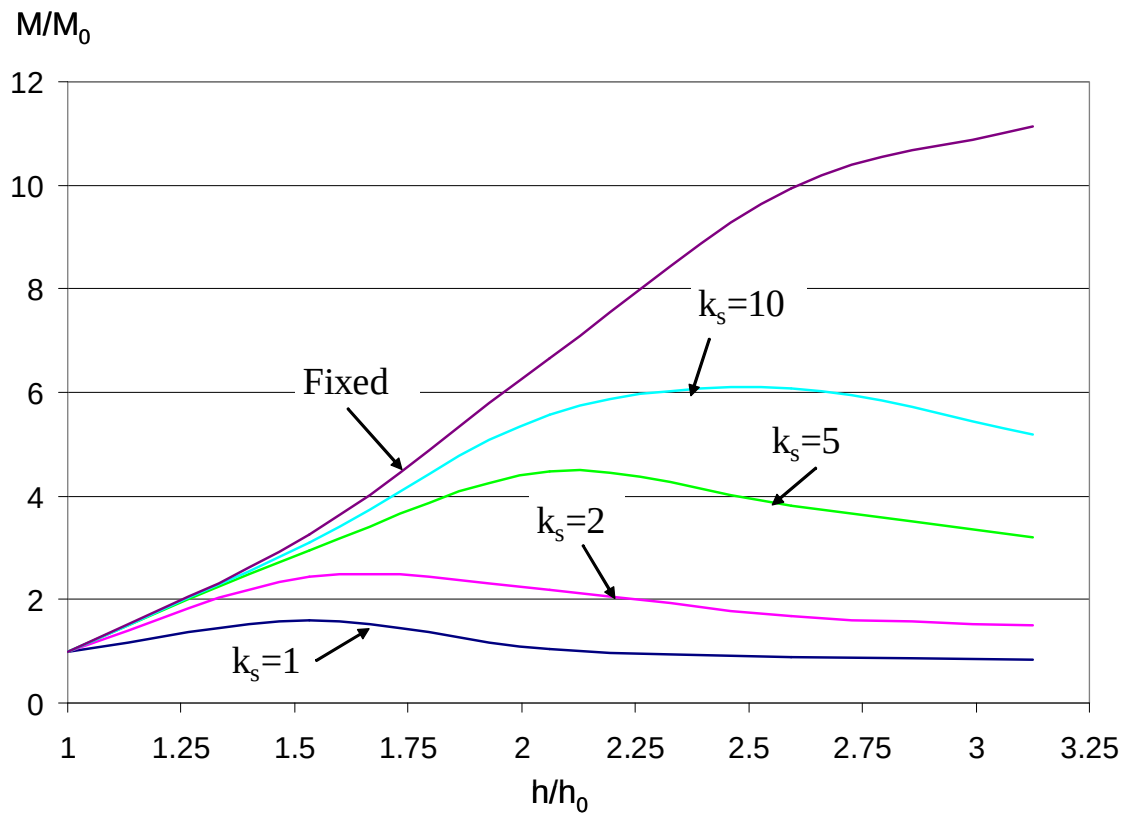

Figure 2.20. Moment increase vs thickness increase for various stiffness ratios

in-plane expansion multiplied by the spring stiffness provides an upper bound on the reaction force produced. While this load is not theoretically possible since the skin is not free to expand unabated, it does provide a useful metric for comparison if the boundary stiffness ratio is available to the analysis.

The moment curves in Figure 2.20 demonstrate similar behavior to that found in the previous clamped beam study. The moment initially increases with increasing thickness, reaches a maximum and then tails off as out-of-plane deformation is eventually suppressed due to the buckling temperature exceeding the operation temperature. Again we notice that as the boundary stiffness is reduced, less potential exists for generating large moments. And as in the reaction force, the infinite stiffness case provides an upper bound on possible moment increases. Also, the stiffness ratio of 10 is sufficiently approximated by the fixed case up to thickness ratios of 2.

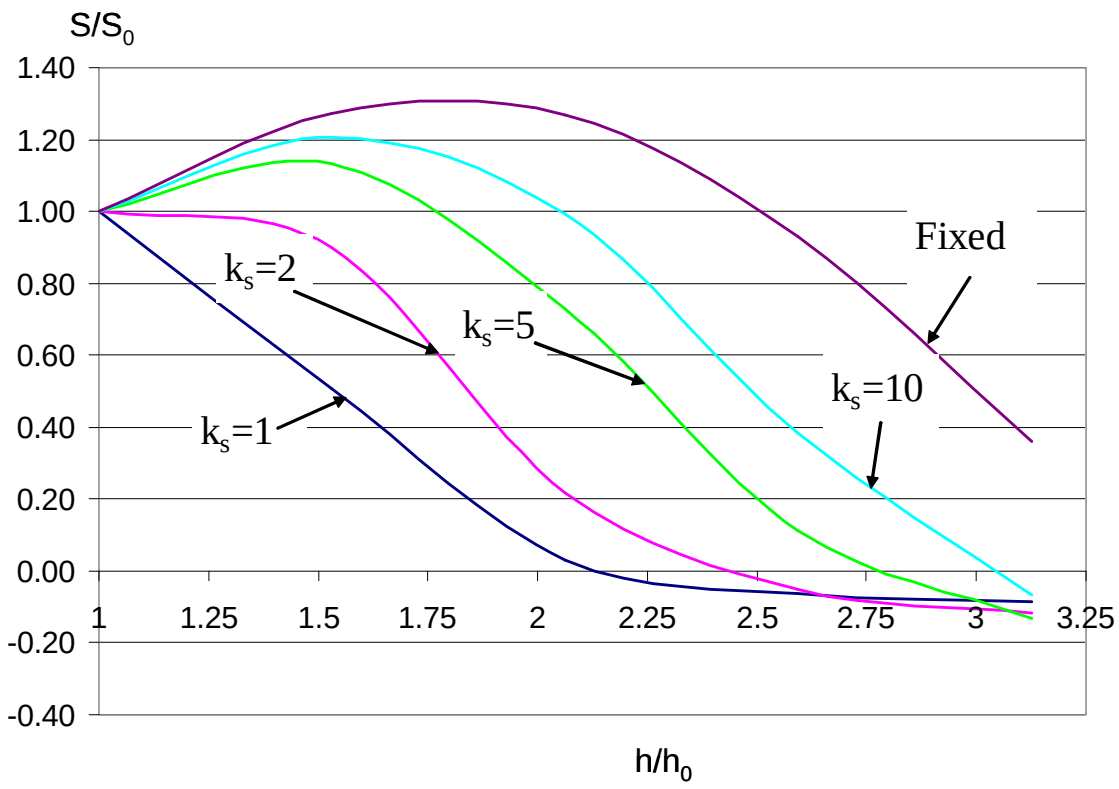

Figure 2.21. Stress ratio vs thickness ratio for various values of spring stiffness ratio

While the additional loads into surrounding structure are of the utmost importance, the stress response also reveals the importance of knowledge about the stiffness of the boundary. Axial stresses generated by the combination of in-plane load and bending moment are shown in Figure 2.21. This graph is very revealing in that it demonstrates that while the goal of adding material was to decrease the stress in the panel, in fact, the stresses can increase for large values of boundary stiffness as material is added. If we examine closely the k_s=10 curve at double the original thickness, while we have dramatically increased the loads into the boundary, the stress is virtually the same as the unstiffened panel. In the case of a crack repair, if the doubler plate is placed over the crack on the high stress side opposite the deformation, the outer-most fibers of the doubler plate would replace the single-thickness skin as the location of highest stress. While this action would retard additional damage of the

original panel since the crack would be located at the neutral axis of the new configuration, new cracking would appear in the doubler plate. Therefore, this approach would provide a temporary fix and would require routine inspection and replacement of the doubler. If, however, the crack has grown completely through the panel and the repair consists of placing the doubler on the side opposite the maximum stress location, the cracking can accelerate. The author observed this phenomena when a doubler plate was placed over a severe crack in the B-2 aft deck on the outer mold line. The crack growth rate on the underside of the skin (initial crack location) actually increased. Much of the motivation for this study was provided by this observation.

This study confirms the findings in the clamped case investigation and further demonstrates that the addition of material in a thermal environment must be approached with extreme caution and with careful consideration given to the trade space of load and stress reduction.

2.4. Curved Beam Model

While the study in the previous section applied a small perburtation to the initially flat beam to provide a smooth equilibrium path for out-of-plane deflection, the focus of this section is to quantify the effect of initial curvature on the problem at hand. A study was conducted employing the widely used preliminary design text by Roark [**36**] and comparing these results with finite element computations performed using both ABAQUS linear and nonlinear static analyses. Again, the strip (or beam) model (Figure 2.22) is utilized for a uniform temperature field over the entire span, where δ is the initial out-of-plane distance at the center of the beam. Reaction forces and moments at each end of the beam as well as relevant cross section dimensions are also shown in Figure 2.22. Assuming a fixed boundary, the effect of the thickness ratio, d/δ, on maximum strain, ϵ, will be analyzed. For the geometries being considered,

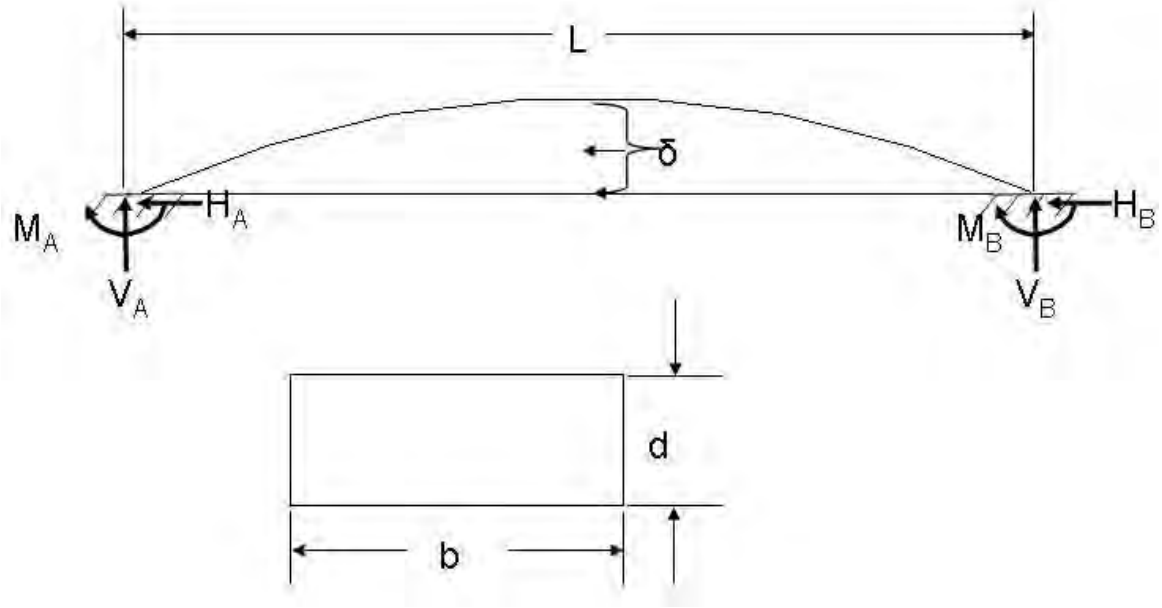

Figure 2.22. Curved beam geometry and reaction forces.

the maximum strain will again occur at the clamped edges. With $L = 12$ inches (and the values of δ also in inches), Figures 2.23 - 2.26 detail the results of the investigation for various values of an initial out-of-plane curvature of the panel which is described by the δ/L ratio. The linear finite element solution and the Roark solution coincide precisely. To achieve this agreement, a mesh density of 0.01 inches was required (~1200 two-noded linear elements). For very small values of δ (Figures 2.25 - 2.26) there are large differences between the linear solution (Roark's or linear FEA) and the nonlinear finite element solution. The linear solutions make no distinction between the deformed and undeformed configuration. Therefore, as the two configurations diverge, nonlinear geometric effects must be included. The out-of-plane deformation in these two cases is greater than the thickness and hence requires nonlinear analyses. As the initial out-of-plane distance of the curved panel is increased (Figures 2.23 - 2.24), the out-of-plane deformation decreases which results in coalescence of the linear and nonlinear solutions. Another important observation is that the maximum

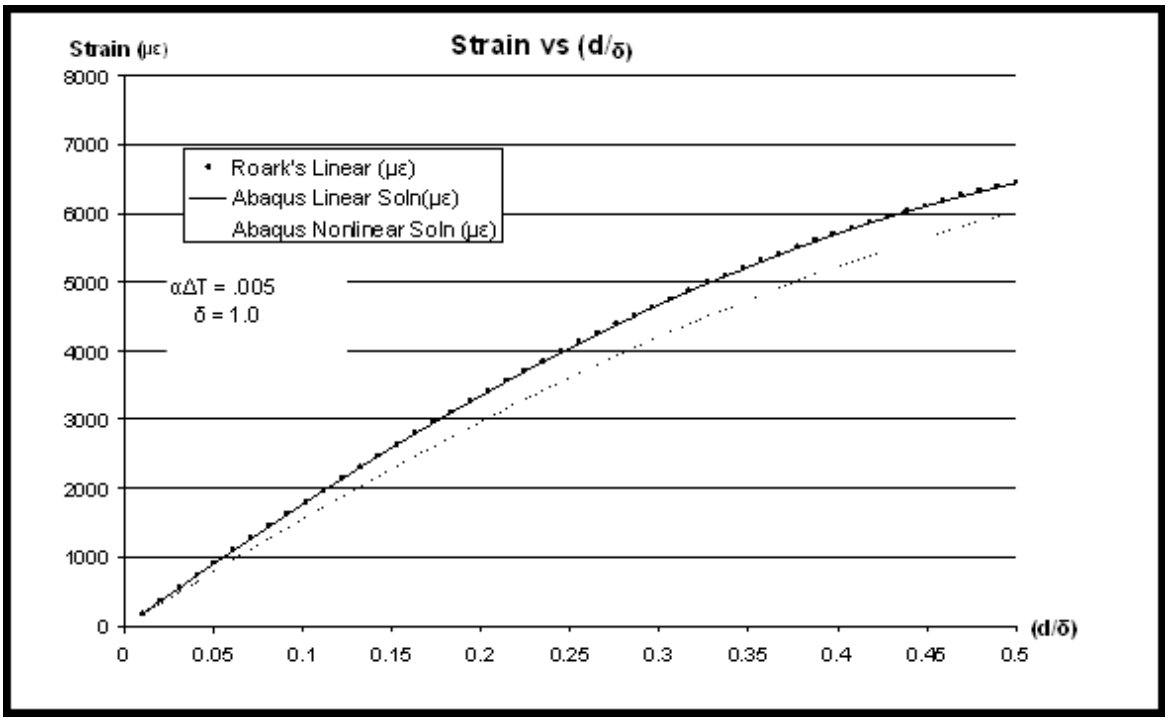

Figure 2.23. Strain vs d/δ for $\delta/L = 0.083$.

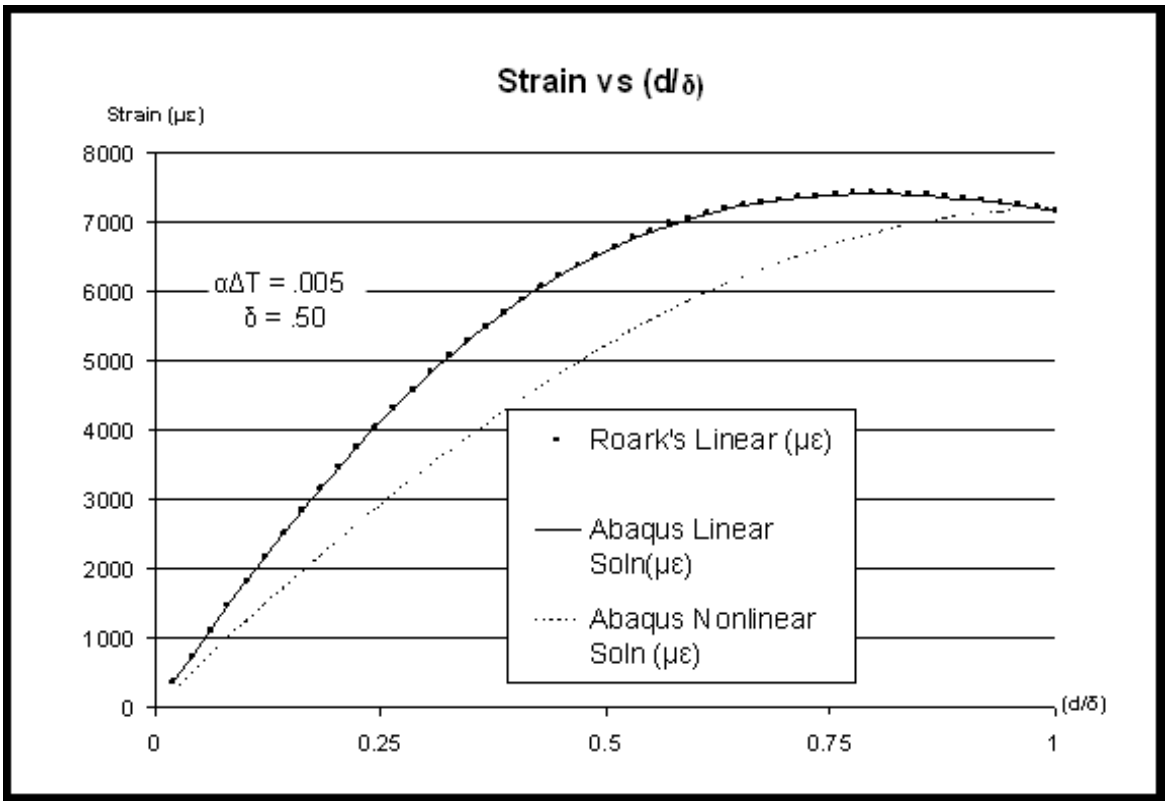

Figure 2.24. Strain vs d/δ for $\delta/L = .042$

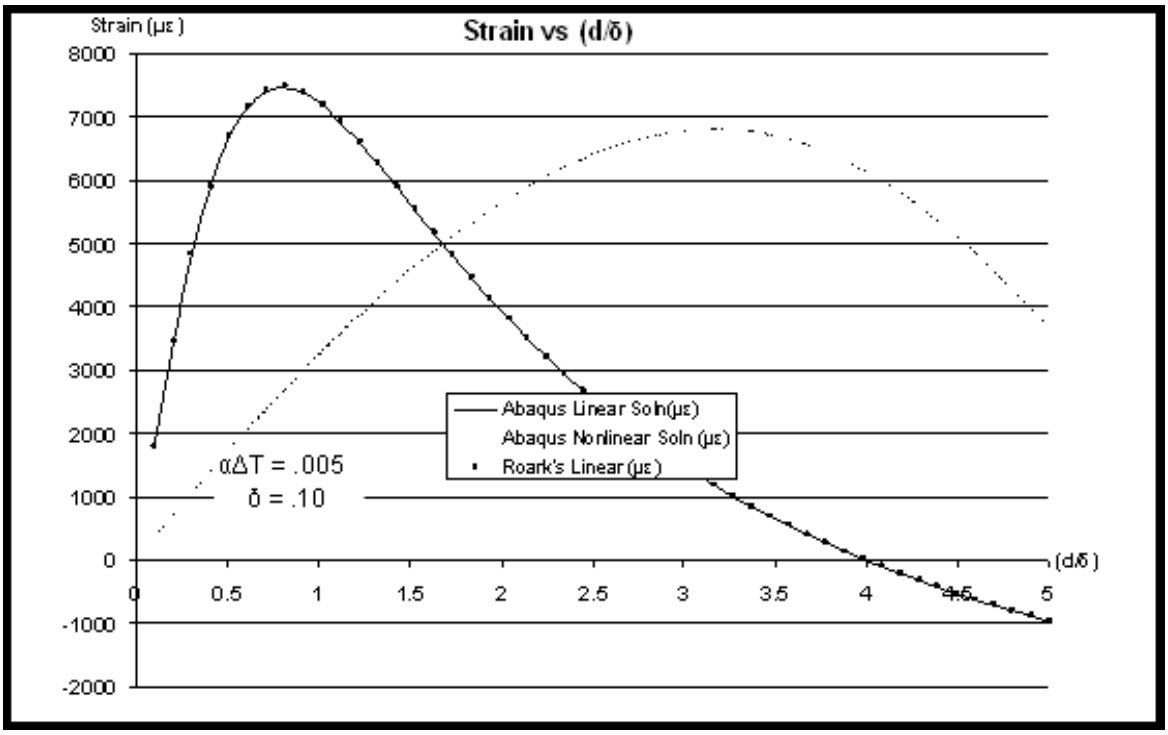

Figure 2.25. Strain vs d/δ for $\delta/L = 0.0083$.

tensile strain, for a given thickness, d, as δ increases, is greatly reduced. Figure 2.27 shows the values of mechanical strain for different values of δ with thickness held constant at 0.125 inches. Therefore, a small decrease in radius of curvature can provide a substantial reduction in stress and can increase the life of the curved hot structure. As the in-plane load for various values of thickness was examined in the flat beam scenarios of the previous sections, so too are the results presented for additional reaction load in the initially curved beams. Figure 2.28 shows the added bonus of reducing the radius of curvature. The graph demonstrates that as the initial out-of-plane distance is increased, the loads are reduced with thickness increases. The design engineering concept of applying generous radii to corners to alleviate mechanical stress is a useful notion in this environment, albeit, for very different reasons.

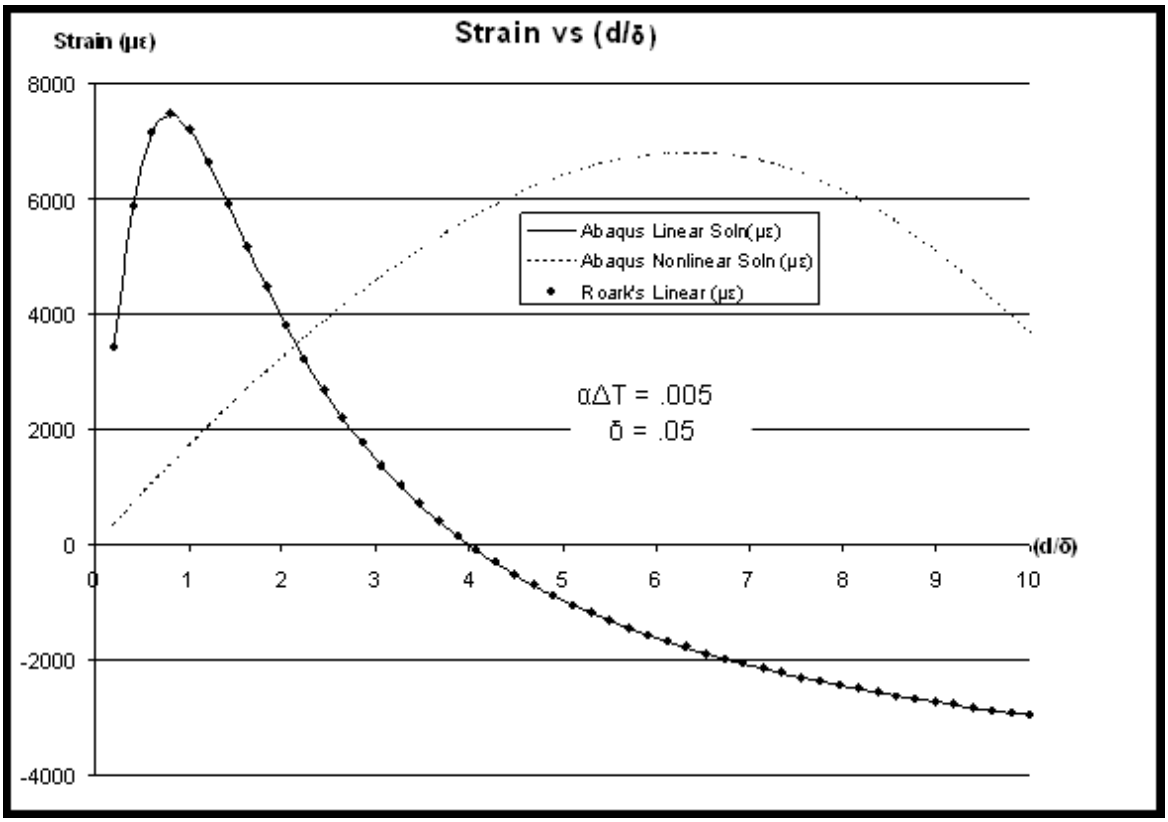

Figure 2.26. Strain vs d/δ for $\delta/L = 0.0042$

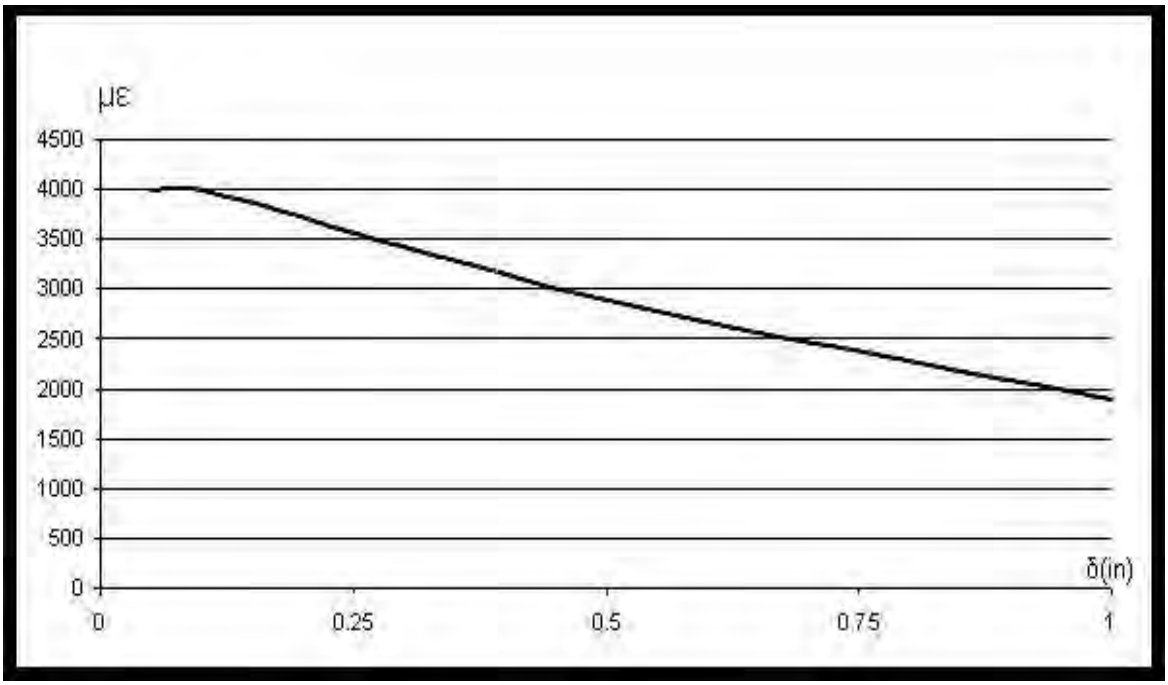

Figure 2.27. Maximum strain vs initial out-of-plane distance δ.

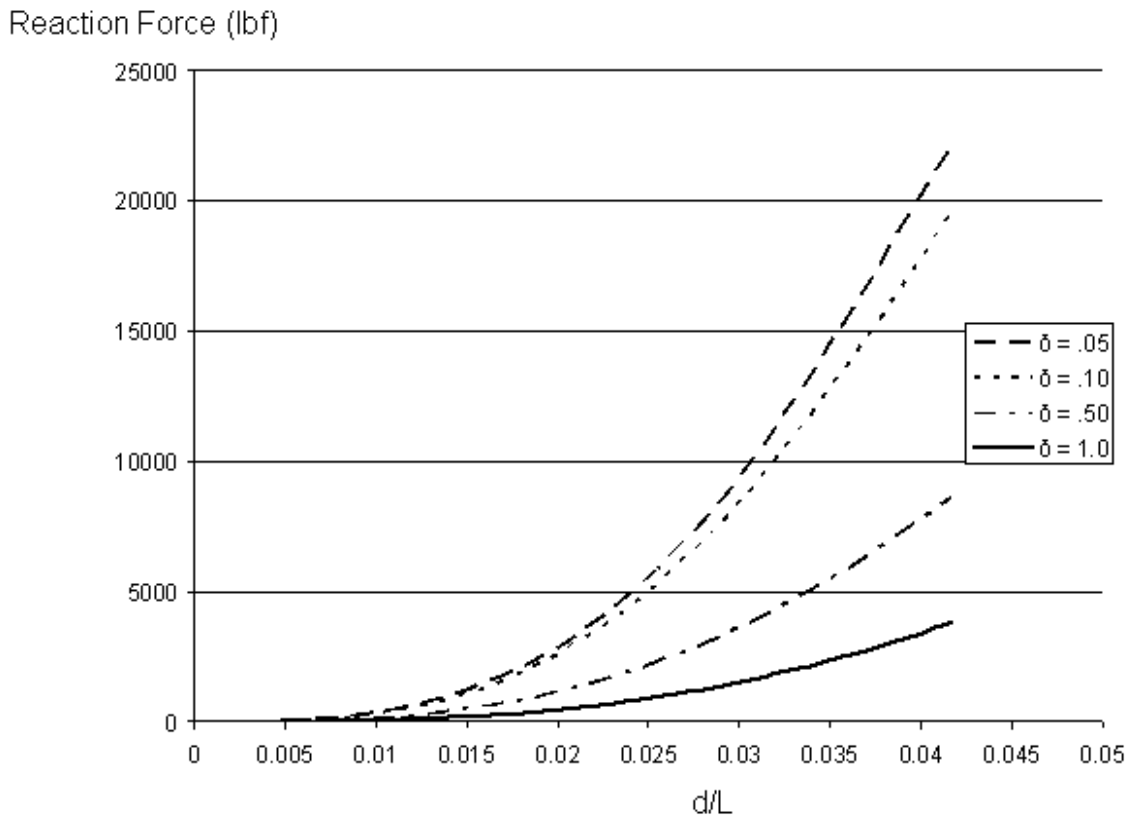

Figure 2.28. Reaction force vs thickness for various values of initial out-of-plane distance for a curved panel

This chapter has detailed the results of a common stiffening method applied to thermal shell structures. The results have revealed that care must be used when placing stiffening material in a thermal environment as very non-intuitive consequences may occur. While these results have focused on increasing thickness, the addition of stiffeners such as I-beams or T-beams can be viewed as increases in material thickness at discrete locations and hence must also be integrated into a thermal stress design with caution.

More modern semi-analytical treatments of buckling and out-of-plane deformation of panels and beams have been studied in [**37**], [**38**], [**39**], [**40**], and [**41**]. The literature review revealed that after the mid 1970's very little work focused on isotropic materials. Composite material formulations dominated the literature for roughly 20

years while very recent work has focused on functionally-graded materials that allow very rapid (approaching continuous) material changes based on the *local* desired properties. It is the author's opinion that the particular revelations regarding the thickness parameter that are the focus of much of this chapter were not produced earlier due to two factors. Firstly, from a design standpoint, the solution to thermally constrained structures is to permit expansion so the necessity of stiffening was avoided. Secondly, when the focus of the research community turned toward composite structures, the stiffness of the panel could now be influenced by a multitude of material properties. To stiffen a particular panel, attention was focused on the reduced stiffnesses of individual layers of the composite [**42**] as opposed to a simple increase in cross section.

2.5. Chapter Summary

In this chapter we have detailed the inherent difficulties associated with thermoelastic design. Many of the traditional design concepts that designers are familiar and comfortable with in a purely mechanically-loaded setting are highly non-optimal when applied to structures whose response is due to thermal energy input. Several examples of common aerospace structures were presented to demonstrate the non-intuitive nature of stiffening strucures subjected to elevated temperature. The entire concept of stiffening must be perceived differently in this environment. Typically, when a designer intends to stiffen a failing part, the intention is to reduce the damage at that location by adding material. The conclusions in this chapter reveal that *stiffening* thin shells in a thermal environment by adding material to the damage location can actually increase the rate of damage. Therefore, to refer to this process as stiffening is a misnomer. Because thermally-loaded structures in essence provide their own loading through material expansion, the addition of material must

be approached cautiously. For additional material to provide a beneficial outcome, it must participate in the reaction of the original loading more than it contributes to additional load in the vicinity of the critical design region. The other major concern that was investigated in this chapter was the additional load that is reacted at the idealized boundary conditions. While in this work, the boundaries are assumed both clamped and simply-supported, in reality, sub- and surrounding structure provide the constraint. When additional material is added to prevent damage or for restoration of a damaged component, additional load is introduced and will be reacted by the surrounding structure. This additional load must be managed and therefore provides an upper bound on what is possible from a stiffening approach.

CHAPTER 3

Topology Optimization

3.1. Overview

Topology optimization of continuum structures has been an area of active research for more than a decade. The topology optimization formulation seeks to determine the optimal distribution of material and void within an initial design region. To prevent the trivial solution for a stiffness objective (i.e., no void regions), a resource constraint on the volume of material is generally enforced. Topology optimization is distinguished from both sizing and shape optimization in that the "layout" of the structure is unknown a priori. In fact, the structural layout is the computed quantity.

A sizing optimization problem commonly has as its design variables, parameters such as thickness, area, or moment of area of a structural member. Sizing optimization has the most straightforward implementation and has numerous analytical solutions [**43**]. Sizing optimization has been incorporated in several structural mechanics codes – two of which are ASTROS [**44**] and GENESIS [**45**].

Increasing in level of complexity, shape optimization involves the determination of the boundary of a structure or structural member. Variational calculus provides a framework for analytical solutions to shape optimization problems (e.g., the brachistochrone function [**46**]). In a finite element or boundary element formulation, the boundary node locations are commonly taken as design variables [**47**]. Other variants parameterize the boundary by a conveniently chosen basis of B-splines [**48**] or structural frequency mode shapes obtained from a former analysis. While shape optimization provides the designer with greater flexibility than simple sizing, the locations

of material and void are necessarily specified by the designer at the preliminary design stage which limits the possible topologies generated.

A plethora of various methods have appeared in the literature which address the topology optimization . Since the topology problem can be formulated as a combinatorial optimization problem with each material point potentially having a value of 0 (void) or 1 (material), genetic algorithms (GA's) [**49**] and [**50**] and heuristic methods [**51**] have been used to determine global optima. Combinatorial (or zeroth order) methods which do not require gradient information are somewhat limited with respect to problem size and will not be pursued in this work. The most popular methods are based on gradient search algorithms (also known as mathematical programming methods). These gradient search methods can be further subdivided based on how the discrete design variable is treated. The discrete problem can be transformed to a continuous representation by either introducing a microscopically composite material using the homogenization method [**52**] or employing an interpolation based on the Simplified Isotropic Material with Penalization (SIMP) method [**53**]. In contrast, other methods such as the evolutionary structural optimization (ESO) method [**54**], more directly address the discrete variable problem by removing elements from the finite element mesh. One relatively new approach which does not require a discrete to continuous transformation is the Level Set Method [**55**]. This method embeds a series of macroscopic holes in a topological domain. These embedded boundaries can move and resize based on the solution to a "Hamilton-Jacobi-type" equation [**56**].

In the following sections, previous work in the area of topology optimization will be detailed. The subsequent summaries are by no means exhaustive but provide a general overview of the subject areas along with references for the interested reader to gain further insight.

3.2. The Homogenization Method

Early work in topology optimization was first introduced by Bendsoe and Kikuchi [**57**] within the framework of the method of homogenization. The homgenization method is an analytical technique that facilitates the analysis of heterogeneous materials by determining equivalent macro-scale material properties (which can be used in structural analysis software) from periodic micro-scale features. The reader is referred to texts on asymptotic perturbation techniques for a thorough treatment of the subject of homogenization [**58**], [**59**], [**60**] and [**61**].

This early work is more appropriately viewed as an "inverse" homogenization process. In the solution to the traditional homogenization problem, the microstructure is given and the task is to determine the "homogenized" properties whereas the methodology employed in [**57**] determines the microstructure based on the desired macroscopic response. Although the homogenization method is a technique that permits multiple constituents and is very general with respect to the complexity of the micro-scale features (e.g., this technique is applied to complex three-dimensional composite weaves with multiple constituents), the approach taken in [**57**] introduces a two constituent model consisting of (i) a single homogeneous material model with (ii) micro-scale voids. The topology optimization problem is then defined by seeking the optimal porosity of such a porous medium using a desired condition of optimality. The porosity is related to geometric characteristics by introducing a square micro-scale pattern of length a along with an orientation angle θ (Figure 3.1). The density $\mu(x)$ of the body Ω is given locally by $1 - a^2$. Both the square characteristic length and the orientation angle are treated as design variables. Typically, a finite element mesh is used to discretize the domain. Each finite element can contain single values of a and θ or sub-discretization of each element can be carried out for finer grain

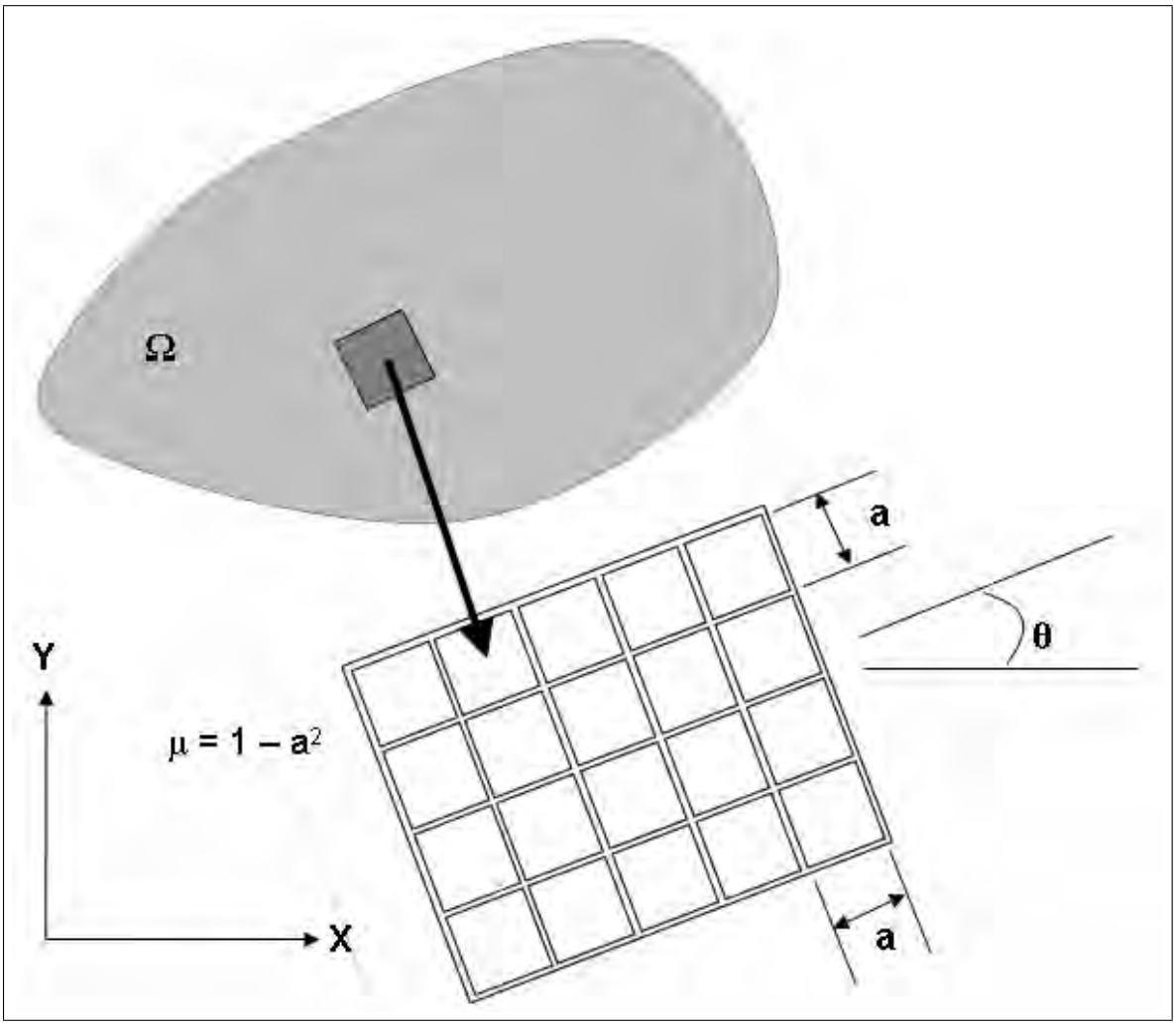

Figure 3.1. Variable definitions for homogenization model

structures. Note that anisotropic structures are possible since the orientation angle θ is included in the formulation.

One of the early problems with homogenization was that solutions suffered from a numerical instability known as checkerboarding. Checkerboarding is primarily associated with linear, 4-node elements and can be suppressed (but not totally eliminated) by using higher-order elements as shown in [**62**]. Checkerboarding in a topology design is evidenced by alternating solid-void combinations which justify the name. Figure 3.2 provides an example of this phenomena. In addition to the use of higher-order elements, other methods have been developed which penalize these

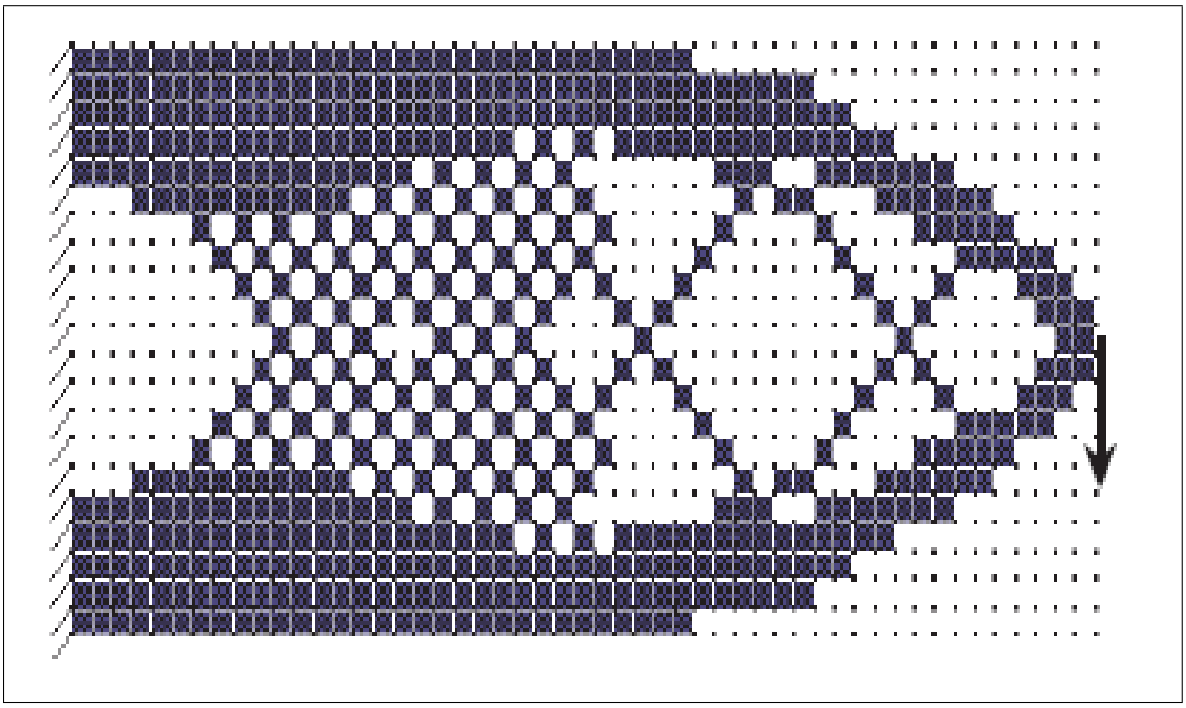

Figure 3.2. Tip-loaded cantilever beam with severe checkerboarding instability.

checkerboard patterns by, for example, placing a constraint on the perimeter of the problem [**63**]. This constraint allows some control over internal boundaries (or holes) that are generated. The most thorough theoretical foundation for checkerboard occurrence is found in Jog and Haber [**64**]. Checkerboarding also occurs in the mixed finite element formuation where two-field problems are solved on a common mesh. For example, a solution to Stoke's flow where both pressure and velocity are sought on a common mesh with identical shape functions produces alternating pressures in adjacent elements. Babuska and Brezzi [**65**] first identified this pathology and proposed a sufficiency condition on the interpolation (or shape) functions for the pressure field to alleviate the checkerboarding phenomena. The proof requires that the two fields form a min-max saddlepoint problem and while checkerboarding in the topology setting does not satisfy this condition, numerical experiments have proven successful when applying the Babuska-Brezzi condition.

3.3. Solid Isotropic Material with Penalization (SIMP)

Another method which relaxes the '0-1' design space is the "solid isotropic material with penalization" (or SIMP) method. One of the primary advantages of the SIMP method is its conceptual simplicity [**66**] and [**67**]. The SIMP method allows intermediate densities to exist in a domain as opposed to the all or nothing approach of material or void. In the typical SIMP approach, material properties are assumed constant within each finite element used to discretize the design domain (although this assumption is not essential to the development) with the design variables being the element "densities". This density field variable does not have to represent the true mass density of the material. Instead it can be a user-defined field variable that is used simply as a multiplier to adjust the modulus. The material properties are modeled to be proportional to the relative density raised to a power. For example, the fourth-order elasticity tensor is given by Eq. 3.1,

$$E_{ijkl}(x) = \left(\frac{\rho(x)}{\rho^0(x)}\right)^p E^0_{ijkl}(x) \tag{3.1}$$

where E_{ijkl} is the scaled value of the elasticity tensor field, E^0_{ijkl} is the initial value of the elasticity tensor, ρ is the density, ρ^0 is the initial density and p an integer power. The effect of the exponent p is to penalize intermediate densities (Figure 3.3). Since intermediate densities are permitted in this method, a penalization of intermediate densities is necessary to prevent so-called "grey" designs from evolving as they are not manufacturable from a two-constituent (material or void) model. The problem with penalizing intermediate densities is that the difficulties associated with the '0-1' problem (e.g., checkerboarding) return as the penalty becomes large. In Figure 3.3, we can see that as the exponent increases, fewer and fewer intermediate modulus ratio values are possible. The value of p is typically chosen to be approximately three. To

circumvent the problems associated with the '0-1' highly penalized behavior and still arrive at designs which contain very little intermediate density, the value of p can be chosen small initially and increased as the optimization proceeds. This approach is known as a continuation method [**68**]. The power-law based approach to topology optimization has been widely applied to problems with multiple constraints, multiple physics and multiple materials. In fact, all (to the author's knowledge) commercial topology optimization codes include a SIMP implementation. This method is chosen primarily for its ease of implementation into a finite element framework. However, the close association of the SIMP topology optimization method with the finite element discretization also limits the topologies generated and can cause mesh dependency issues which much be addressed through filtering techniques [**69**], [**70**] and [**71**].

3.4. Level Set Method

The most recent technique for addressing the structural topology optimization problem is known as the level set model. This model combines level set methods [**72**] and a mathematical programming method for optimization. The level set method uses implicit, moving boundaries for topology optimization. The structural boundaries are viewed as moving during the optimization process. Interior boundaries (or holes) may merge with each other or with the exterior boundary and new holes may be created.

A level set model specifies a surface in an implicit form as an iso-surface of a scalar function, $\Phi : \mathbb{R}^3 \longrightarrow \mathbb{R}$, embedded in 3D, i.e.,

$$S = \{x : \Phi(x) = k\} \tag{3.2}$$

where k is the iso-value and is arbitrary, and x is a point in space on the iso-surface Φ. x is the set of points in $\mathbb{R}^3$ that composes the k^{th} iso-surface of Φ. The embedded Φ can be specified in any specific form, e.g., as a regular sampling on a rectilinear

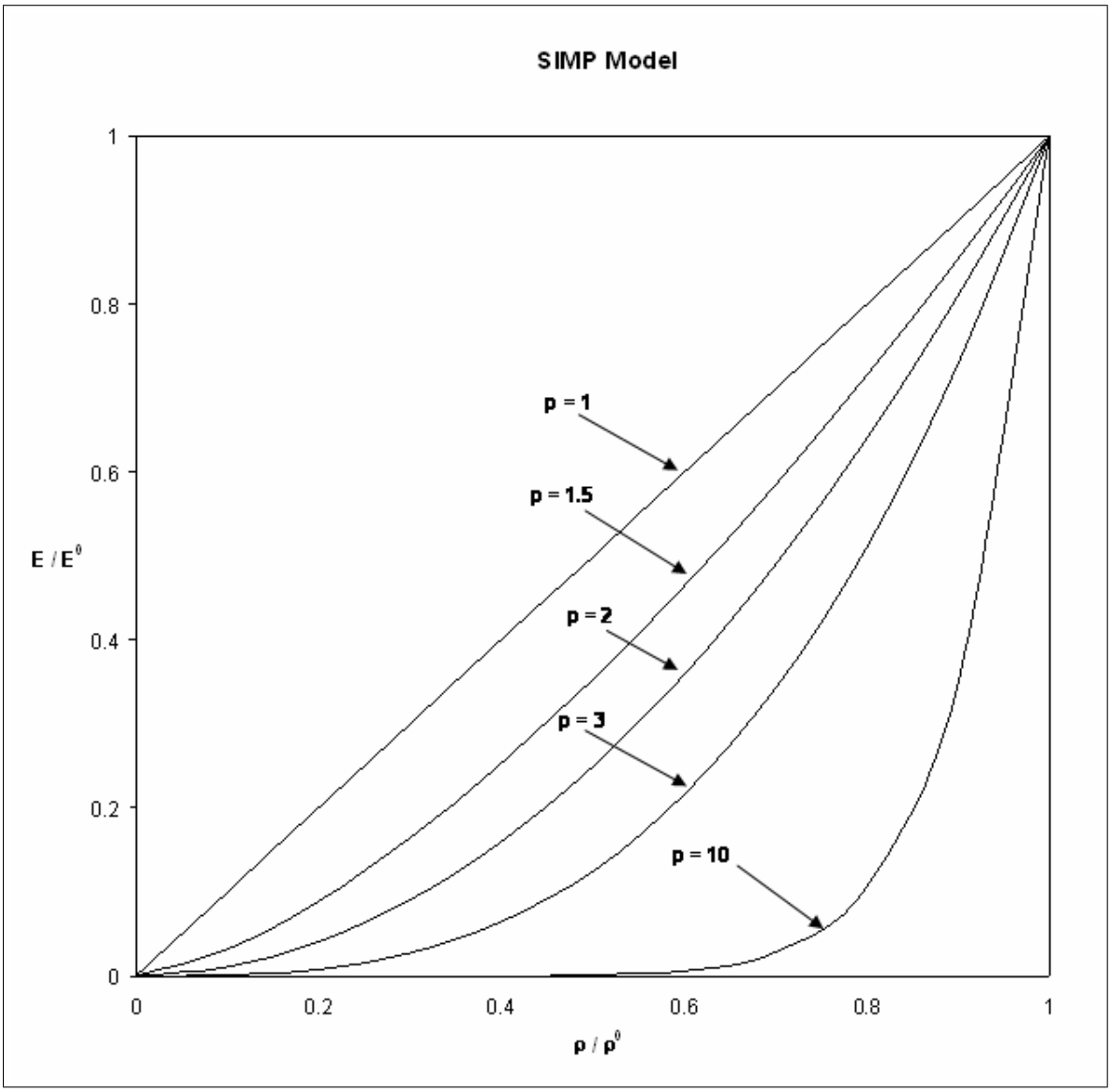

Figure 3.3. Effect of SIMP penalty parameter

grid. A process of structural optimization can be described by letting the level set function dynamically change in time. Thus, the dynamic model is expressed as

$$S(t) = \{x(t) : \Phi(x(t), t) = k \tag{3.3}$$

Upon differentiation of Eq. 3.3 with respect to time, a "Hamilton-Jacobi-type" equation results

$$\frac{\partial \Phi\left(x,t\right)}{\partial t} + \nabla \Phi\left(x,t\right) \frac{dx}{dt} = 0 \tag{3.4}$$

In this dynamic level set model, the structural optimization process can be viewed as follows. Let $\frac{dx}{dt}$ be the movement of a point on a surface driven by the objective of the optimization, such that it can be expressed in terms of the position of x and the geometry of the surface at that point. Then, the optimal structural boundary is expressed as a solution of a partial differential equation on Φ:

$$\frac{\partial \Phi(x,t)}{\partial t} = -\nabla \Phi(x,t) \frac{dx}{dt} \equiv -\nabla \Phi(x,t) \cdot \Gamma(x,\Phi) \tag{3.5}$$

where $\Gamma(x,\Phi)$ denotes the "speed vector" of the level set surface, which depends on the optimization objective. This approach is very similar to that used in shape optimization. In fact, the reference here to "speed vector" is analogously called the design velocity vector in shape optimization and refers to the nodal boundary movement of a model discretized by a finite element mesh [**73**]. Figure 3.4 illustrates the use of the level set method to generate an optimized structure. The objective function represented by the optimization is minimal compliance.

The level set method has some obvious advantages over other topology generating algorithms. Since the boundaries move to represent the structure, the '0-1' nature of the problem is removed. This eliminates the difficulties associated with homogenization and SIMP methods with regard to numerical ill-conditioning of regions with "small" density. Another advantage is the black/white nature of the final design. Regions of intermediate density are no longer problematic and do not require a postiori filtering techniques.

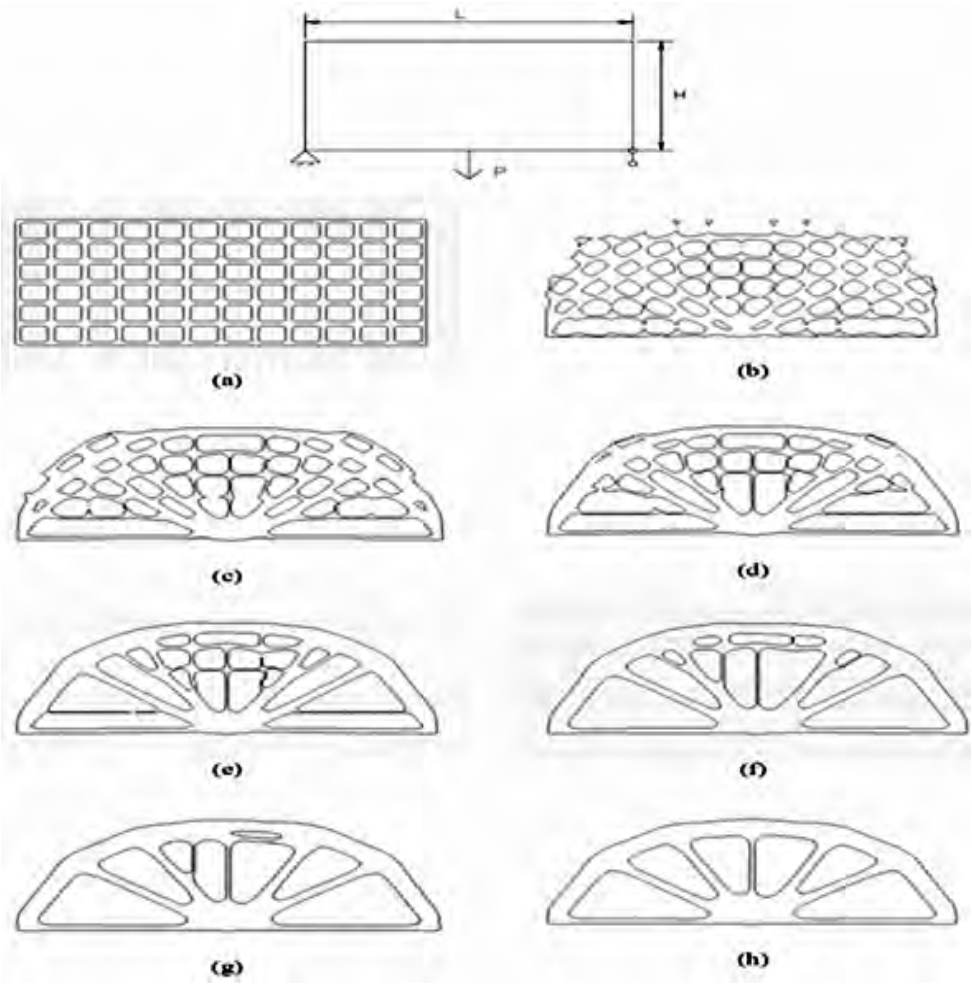

Figure 3.4. Minimum compliance example for level set method [**72**]

The topologies generated by the level set method are somewhat restricted by the choice of the initial boundary unlike that of competing methods. The method also suffers from potential degradation in mesh quality due to large changes in the domain boundary. Mesh smoothing methods are required to maintain proper element aspect ratios. Similar algorithms have routinely been employed in shape optimization. In fact, the nature of the level set method associates it more closely with shape optimization methods than with previously established topology optimization methods. A satisfactory level set formulation for nonlinear response has yet to be developed and is an active area of research.

3.5. Evolutionary Structural Optimization (ESO)

The Evolutionary Structural Optimization (ESO) method for topology optimization was first introduced in 1993 in [**74**]. The genesis for the method has its origins in the well-known optimality criteria concept in structural optimization known as "fully-stressed design." A fully stressed design (FSD) is defined as one in which each point in the body is fully utilized with respect to stress allowables[**75**]. In application, the FSD method usually takes the form of driving the structure toward a uniform stress state. To accomplish the objective, inefficient material is slowly removed from the body over many iterations for the given loading. This slow removal of material substantiates the "evolution" reference in the method title, i.e., the structure "evolves" toward an "optimal" configuration.

There are obvious similarities between the SIMP and ESO methods. In the SIMP method, inefficient material is, in essence, removed by adjusting the modulus downward. In the ESO method, a more discrete methodology is employed which literally removes the inefficient material. Just as the SIMP method is closely tied to the finite element method with regard to material discretization, so is the ESO method. Therefore, inefficient elements are removed from the initial structure generating internal surfaces.

The ESO method is similar to the aforementioned methods in that a design domain is chosen large enough to cover the area of the final design. The design domain is discretized by a fine mesh of finite elements. Loads and boundary conditions are applied and a stress analysis is performed. The stress response is interrogated comparing the lowly stressed regions to the rest of the structure. An appropriate rejection criterion is chosen and is used to remove inefficient material, i.e., elements.

An average stress value is computed for each element using the components of the stress tensor. For this purpose the von Mises stress has been one of the most widely

used criteria for materials with isotropic response. At the end of each finite element analysis, all the elements which satisfy the following condition are deleted from the model.

$$\frac{\boldsymbol{\sigma}_e^{vm}}{\boldsymbol{\sigma}_{\max}^{vm}} < RR_i \tag{3.6}$$

where RR_i is the current *rejection ratio* (RR).

Finite element analyses and subsequent element removal are continued using the same value of RR_i until the process reaches steady state. Steady state in this context is identified with the iteration where no elements are removed. At this stage an *evolutionary rate* (ER) is introduced and added to the rejection ratio, i.e.,

$$RR_{i+1} = RR_i + ER, \qquad i = 0, 1, 2, 3, \ldots \tag{3.7}$$

With this increased rejection ratio, the cycle of analysis and removal is repeated until a new steady state is reached.

The evolutionary process continues until an "optimal" design is reached. In practice, it is difficult to achieve a design where each material point is stressed to full strength. Therefore, a cutoff percentage is typically specified which terminates the process when, for example, all elemental stresses are within 10% of the maximum. Another widely used approach to termination is to specify a volume constraint which becomes active after the "kth" iteration.

The ESO method is considered a heuristic method which correctly implies that ESO is not as mathematically founded as competing methods. Convergence has yet to be proven for the general formulation, however, the remarkable agreement between ESO and other methods suggest that a theoretical basis exists. A first attempt to investigate the theoretical aspects of the ESO method is given in [**76**]. In spite of the

infancy of the theoretical foundation, the ease with which the ESO formulation can be incorporated into a commercial finite element code makes it a formidable tool for design optimization.

Checkerboarding does occur in ESO designs similar to highly penalized SIMP models. A scheme to suppress these unwanted topologies is presented in [**77**]. The method replaces the raw elemental stress response from the analysis with an averaged value based on neighboring element values.

3.6. Formulations

In this section, the formulations for topology optimization applications specific to solid mechanics will be presented. While topology optimization is not limited to structural applications, the overwhelming majority of work has been in this area. The scope of this section begins very broadly eventually narrowing to the topic of nonlinear thermoelastic applications.

3.6.1. Minimum Compliance Design

When a topology optimization problem is formulated, a design objective must be chosen. A seemingly obvious choice is to minimize volume subject to local stress constraints on each finite element. While this objective/constraint combination has been pursued in the literature, a fully satisfactory, robust formulation has yet to be accomplished [**78**]. Having a local stress constraint on each element destroys the efficiency of the widely used adjoint sensitivity method. The adjoint method can accomodate a large number of design variables very efficiently, but its advantages are diminished as the number of response equations increases. Another consideration when attempting to apply local stress constraints is the limit state value. If we specify that the von-Mises stress, σ_{vm}^{k}, in element k should remain less than some

value (e.g, yield stress, σ_y),

$$\sigma_{vm}^k < \sigma_y \tag{3.8}$$

as the optimization proceeds, the density of each element will undoubtedly change. The question arises as to what value of σ_y should be used for these intermediate densities. The so-called "singularity" problem associated with stress constraints requires special consideration in topology optimization [**78**]. The design space defined by the constraint equations suffers from an "irregularity" that produces degenerated appendices in which the Slater condition does not hold. The result of this pathology renders algorithms based on Kuhn-Tucker conditions ill-equipped to locate the optima. Mild success in this area has been achieved by prescribing stress constraints over regions of the model (groups of elements) which converts the local stress constraints to a global quantity and renders the design space more amenable to conventional optimization methods. By not being able to address the stress issue directly, there is no guarantee that an "optimal" topology will be a useful structural design. The study of stress constraints remains a very active area of research as the solution to this problem would make the critical connection between topology optimization and robust structures.

An objective function which does not suffer from the pathologies of the stress objective while producing useful structures is given by the compliance. Minimization of compliance subject to a volume constraint is the most widely used topology optimization formulation in literature. For linear elastic structures, the minimum compliance formulation takes the following form where the objective is to determine the stiffness tensor $E_{ijkl}(x)$ as a field variable over the entire domain, Ω. Introducing

the energy bilinear form:

$$a(u,v) = \int_{\Omega} E_{ijkl}(x)\,\varepsilon_{ij}(u)\,\varepsilon_{kl}(v)\;\; d\Omega \tag{3.9}$$

with linearized strains

$$\varepsilon_{ij}(u) = \frac{1}{2}\left(\frac{\partial u_i}{\partial x_j} + \frac{\partial uj}{\partial xi}\right) \tag{3.10}$$

and the load linear form

$$l(u) = \int_{\Omega} b\; u\; d\Omega \;+\; \int_{\Gamma_T} t\; u\; ds \tag{3.11}$$

the minimum compliance or maximum global stiffness problem is given by

$$\begin{aligned} &\min_{u \epsilon U, E}\; l(u) \\ s.t. \quad &: \quad a_E(u,v) = l(v), \qquad\qquad for\ all\ v\ \epsilon\ U \end{aligned} \tag{3.12}$$

The equilibrium equation is expressed in weak form with U denoting the space of kinematically admissible displacement fields, b, the body forces and t, the tractions on the prescribed traction portion of the boundary, Γ_T. The subscript E in the bilinear form denotes the dependence on the stiffness tensor.

If the domain of the bilinear form is discretized into a finite element mesh with appropriate basis functions, the familiar finite element statement of equilibrium is given by

$$[K]\;\{u\} = \{f\} \tag{3.13}$$

where $[K]$ is the global stiffness matrix, $\{u\}$ is the vector of nodal displacements, and $\{f\}$ is the nodal force vector. Also in discretized form, the compliance is the nodal

force vector multiplied by the nodal displacements,

$$l(u) = \{f\}^T \{u\} \tag{3.14}$$

Combining equations 3.13 and 3.14, the compliance is given by

$$l(u) = ([K]\ \{u\})^T \{u\} \tag{3.15}$$

$$= \{u\}^T [K]^T \{u\} \tag{3.16}$$

The reader familiar with strain energy concepts will recognize equation 3.16 as two times the strain energy of a linear elastic structure provided the stiffness matrix is symmetric. Therefore, minimization of strain energy ensures minimum compliance (or maximum stiffness) of a linear elastic structure.

3.6.2. Linear Thermoelasticity

The first work which addressed the minimum compliance problem for thermoelastic structures was the journal article by Rodrigues, et. al. [**79**]. The development presented in this paper extended the material-based formulation presented by Bendsøe and Kikuchi [**57**], to include the effect of temperature differential. The material effective (homogenized) properties for both the elastic moduli and the thermal expansion coefficient are computed using the homogenization method. The mathematical statement of the compliance objective is given by

$$\min_{(0 \le \mu(\boldsymbol{x}) \le 1,\ \theta(\boldsymbol{x})} \left\{ \int_\Omega \boldsymbol{b} \cdot \boldsymbol{u}\ d\Omega + \int_\Omega \boldsymbol{\beta}^H(\mu,\theta)\boldsymbol{\varepsilon}(\boldsymbol{u})\Delta T\ d\Omega + \int_\Gamma \boldsymbol{t} \cdot \boldsymbol{u}\ d\Gamma \right\} \tag{3.17}$$

subjected to the isoperimetric constraint on volume,

$$\int_\Omega \mu(\boldsymbol{x})\ d\Omega \le \bar{V} \tag{3.18}$$

assuming the constitutive law of linear thermoelasticity,

$$\boldsymbol{\sigma} = \boldsymbol{E}^H \boldsymbol{\varepsilon}(\boldsymbol{u}) - \boldsymbol{\beta}^H \Delta T \tag{3.19}$$

where $\boldsymbol{E}^H(\mu, \theta)$ is the homogenized fourth-order elasticity tensor, $\boldsymbol{\alpha}^H(\mu, \theta)$ the second-order, diagonal, homogenized thermal expansion coefficient tensor, $\boldsymbol{\beta}^H(\mu, \theta) = \boldsymbol{E}^H(\mu, \theta)\boldsymbol{\alpha}^H(\mu, \theta)$, and $\boldsymbol{u}$ is the solution of the equilibrium equation, in weak form,

$$\int_\Omega \boldsymbol{E}^H(\mu, \theta)\boldsymbol{\varepsilon}(\boldsymbol{u})\boldsymbol{\varepsilon}(\boldsymbol{w}) - \boldsymbol{\beta}^H(\mu, \theta)\boldsymbol{\varepsilon}(\boldsymbol{u})\Delta T - \boldsymbol{b} \cdot \boldsymbol{u} \, d\Omega - \int_\Gamma \boldsymbol{t} \cdot \boldsymbol{u} \, d\Gamma = 0, \tag{3.20}$$

$$\forall \quad \boldsymbol{w} \text{ admissible}$$

The equations in this section are combined into a single Lagrangian equation which facilitates the derivation of the optimality conditions. These equations are then solved numerically to arrive at optimal topologies.

It should be noticed that for structural problems in thermoelasticity, the work done by the loads includes the contribution from the thermal expansion terms (Eq. 3.17) and is explicitly dependent on the design via the thermal property tensor, $\boldsymbol{\beta}^H$. One implication of this compliance definition is, as the temperature increases, the optimal structure may fail to use all available material, (i.e., the volume constraint will be inactive). Rodriguez, et. al. demonstrates this fact with a combined thermo-mechanically loaded two-dimensional example problem. The inital design domain (Figure 3.5) and the resulting topologies are shown for a constant mechanical loading and $\Delta T = 0$ (Figure 3.6) and $\Delta T = 1^\circ$ using 4-noded elements (Figure 3.7). The results of using higher-order elements (9-noded) are are shown in Figure 3.8. In the figures below, the darker areas indicate fixed regions. For the mechanical-only loading, the volume constraint is active providing the most material to resist the displacement in the direction of loading. In Figure 3.7 we see that supports are

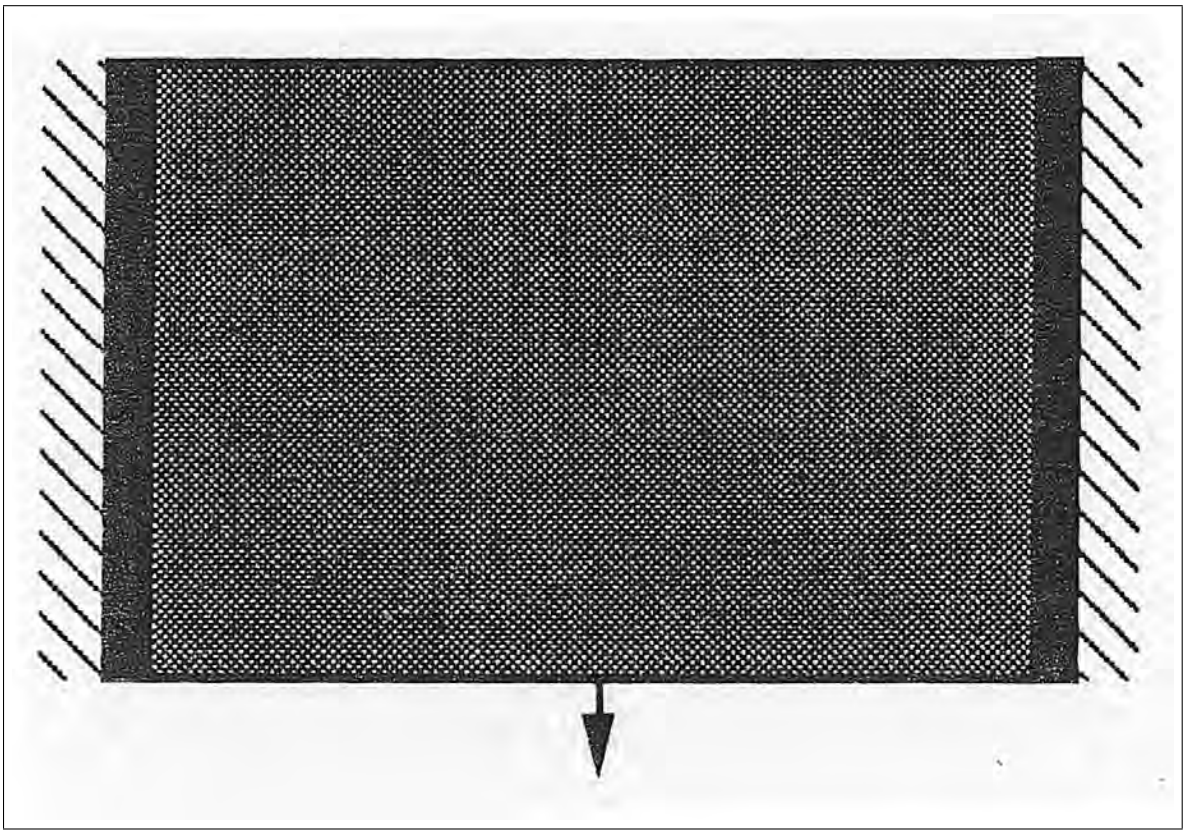

Figure 3.5. Initial design domain thermoelastic example [**79**]

beginning to form which, when heated, help to resist the mechanical loading. While the volume constraint is still active for this small temperature increase, an indication is inferred by the topology that further increases in temperature could result in a situation where additional material would actually increase the compliance. The authors use both four-noded as well as nine-noded elements for the study. The well-known checkerboard pathology is revealed in the four-noded mesh (Figure 3.7). These instabilities can be successfully suppressed through filtering techniques as mentioned earlier in this chapter. The nine-noded elements do not suffer from this numerical instability (Figure 3.8).

As the temperature is increased to $\Delta T = 4°C$, the resulting topology is shown in Figure 3.9. The final volume for this topology is less than what is available to the optimizer through the constraint. The supports which resist the mechanical load are

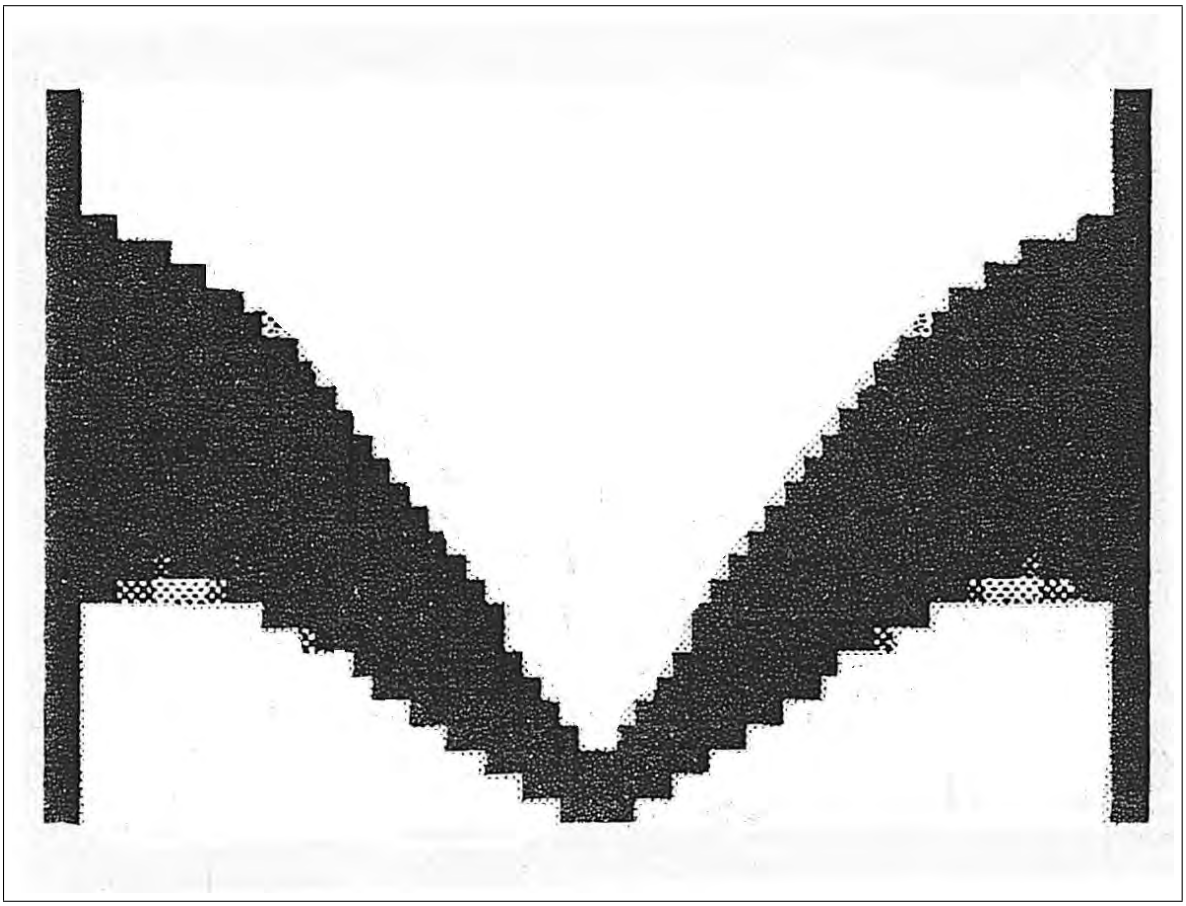

Figure 3.6. Optimal topology for Rodriguez, et. al [**79**] example where $\Delta T = 0°$.

very pronounced in this case. By adjusting the volume constraint, a condition could be achieved where the displacement corresponding to the applied load is zero. This is very similar to the results for topological material design where a three-constituent model can be constructed with a *negative* coefficient of thermal expansion [**80**]. The final point to be made from the work in [**79**] is in the definition of compliance used. If the continuum body was fully constrained, the displacement would vanish and hence the compliance would be zero. Alternatively, if the body were free to expand without constraint, the compliance would be quite large since the thermal compliance term is comprised of the total strain tensor, $\boldsymbol{\varepsilon}(\boldsymbol{u})$. Therefore, in thermally loaded structures, a compliance function like that in 3.17, seems diametrically opposed to our ultimate

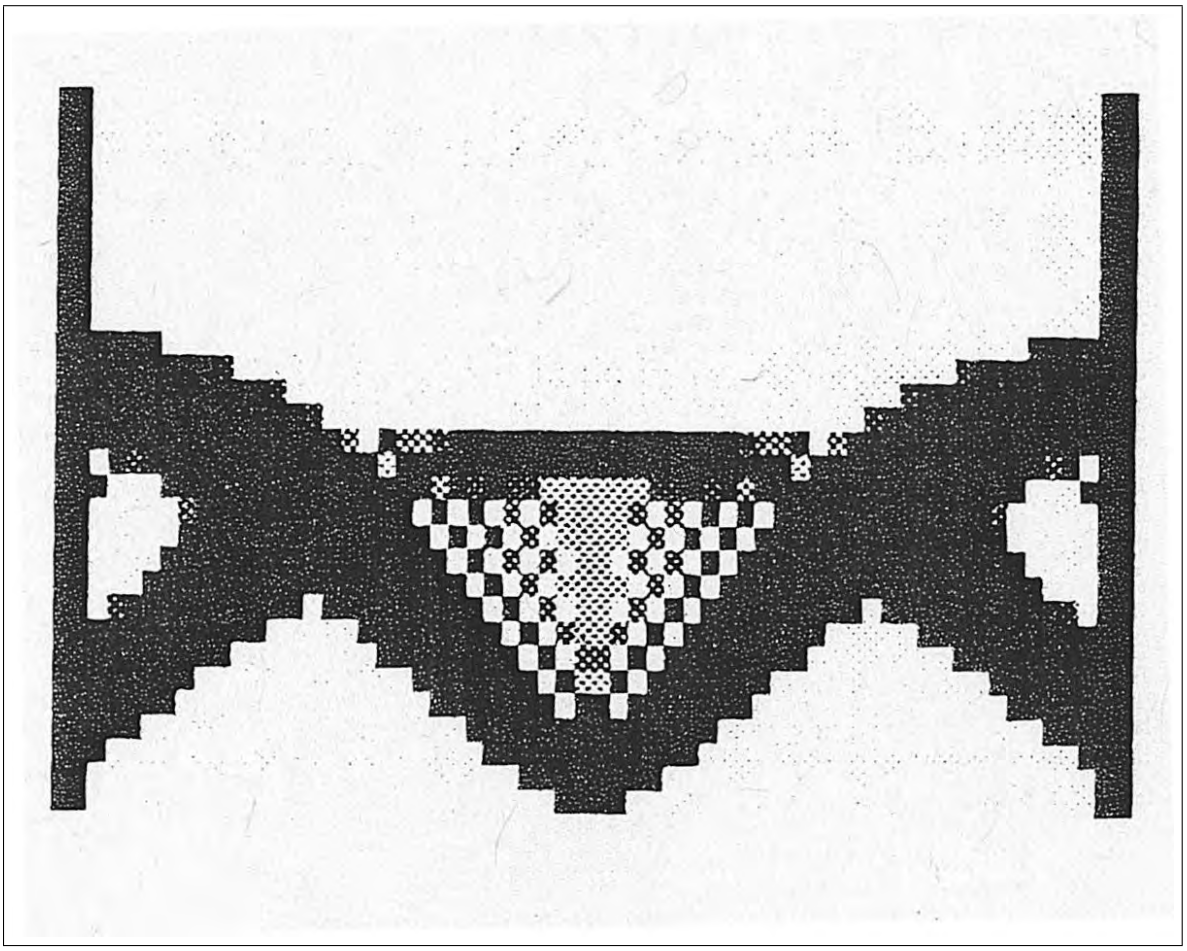

Figure 3.7. Optimal topology for Rodriguez, et. al [**79**] example where $\Delta T = 1^\circ$ using 4-noded elements

desire to produce low stress designs. If the volume constraint for the mechanical-only situation were relaxed to allow more material to resist the load, the stresses will tend to decrease. Since the volume constraint for the $\Delta T = 4^\circ$ case is not active, increasing the constraint will have no effect on the topology and will not decrease stress values. The use of total strain in the objective function definition eliminates the relationship between compliance and strain energy.

The ESO method has also been applied in the area of linear thermoelasticity. In [**81**], Li, et. al. address displacement minimization of thermoelastic structures. Since compliance is a global measure of displacement, the minimum compliance formulation is very similar to the minimization of a particular displacement in a structure. Instead

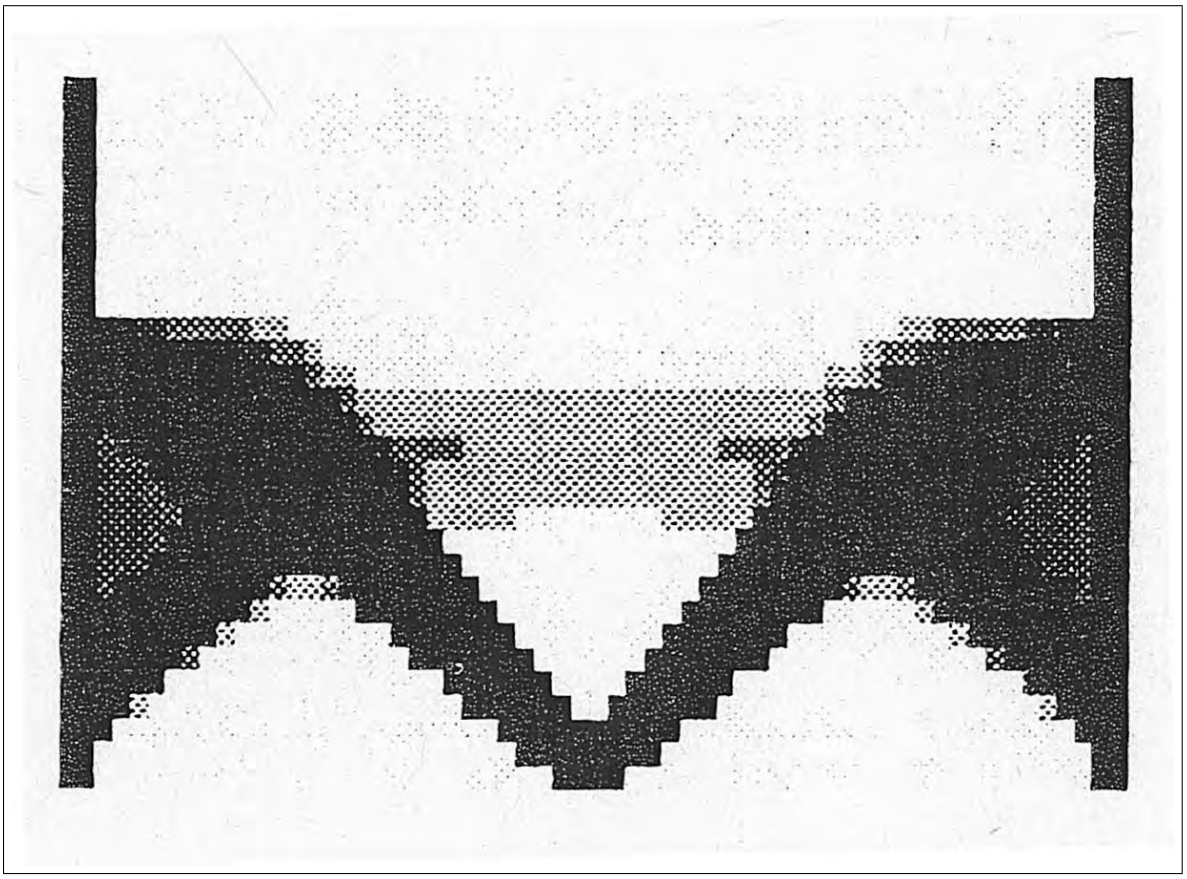

Figure 3.8. Optimal topology for Rodriguez, et. al [**79**] example where $\Delta T = 1^{\circ}$ using 9-noded elements.

of "hard" removal of elements, a sensitivity number is computed for each element and the thickness of elements with the smallest value of sensitivity are adjusted downward.

Suppose that the thickness of the i^{th} element is changed from some old thickness t to a lower thickness $(t - \Delta t)$. Since the global stiffness matrix depends on the thickness of each element, an accompanying change in the stiffness matrix is given by

$$\Delta \hat{\boldsymbol{K}}_i = \hat{\boldsymbol{K}}_i(t - \Delta t) - \hat{\boldsymbol{K}}_i(t) \tag{3.21}$$

where $\hat{\boldsymbol{K}}_i(t)$ and $\hat{\boldsymbol{K}}_i(t - \Delta t)$ are the extended stiffness matrices of the i^{th} element for the old thickness t and the new thickness $(t - \Delta t)$, respectively. The effects of element resizing on the mechanical loading $\boldsymbol{f}_{me}$ are negligible. This assumption is reasonable

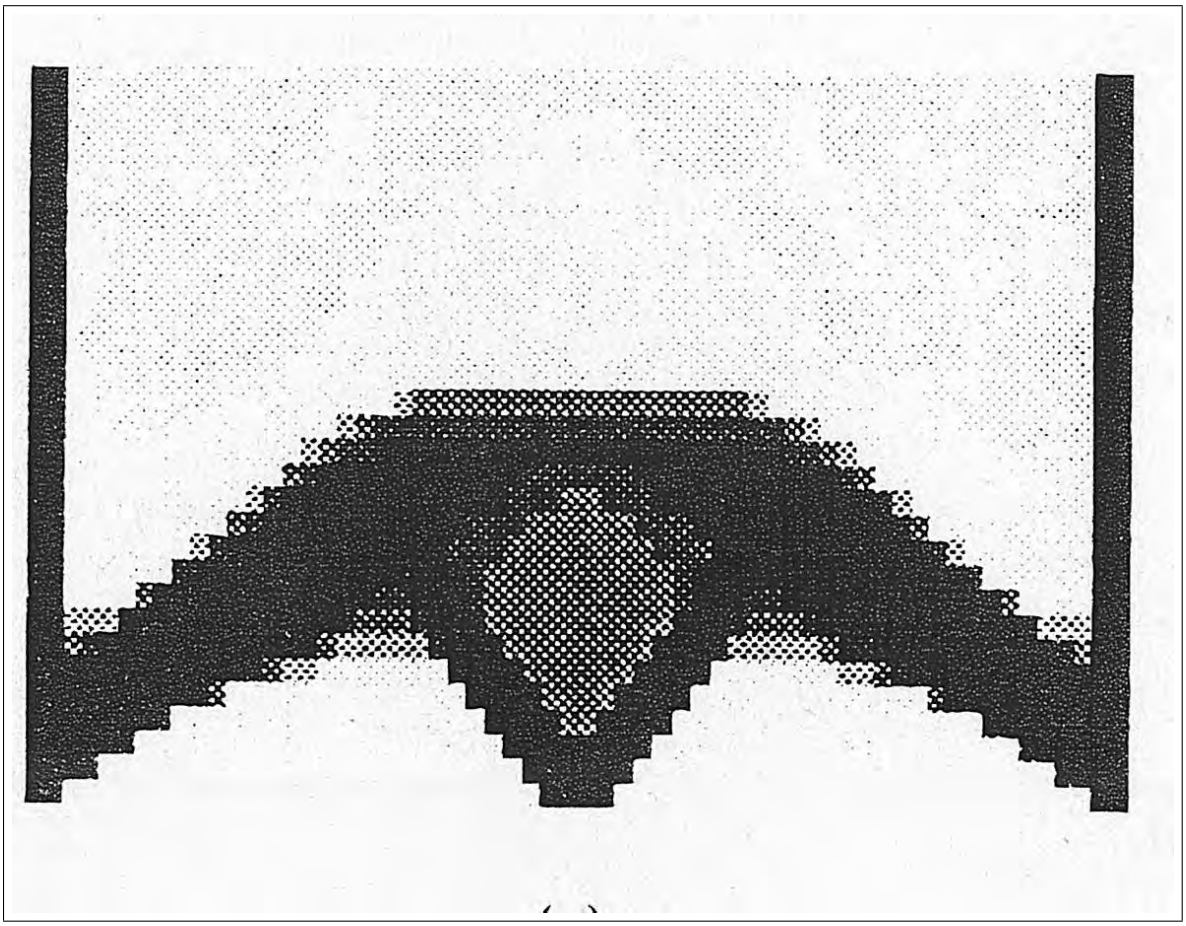

Figure 3.9. Optimal topology for Rodriguez, et. al [**79**] example where $\Delta T = 4^{\circ}$ using 4-noded elements.

for "dead" loads which are not design dependent. The change in displacement vector can be determined by considering equilibrium, pre- and post- thickness change. These equations are

$$\boldsymbol{K}\ \boldsymbol{u} = \boldsymbol{f}_{me} + \boldsymbol{f}_{th} \tag{3.22}$$

before the thickness change, and

$$(\boldsymbol{K} + \boldsymbol{\Delta}\hat{\boldsymbol{K}}_i)\ (\boldsymbol{u} + \Delta\boldsymbol{u}) = (\boldsymbol{f}_{me} + \Delta\boldsymbol{f}_{me}) + (\boldsymbol{f}_{th} + \Delta\boldsymbol{f}_{th}) \tag{3.23}$$

after the thickness change where $\boldsymbol{f}_{me}$ and $\boldsymbol{f}_{th}$ denote the mechanical and thermal loads, $\Delta\boldsymbol{f}_{me}(=0)$ and $\Delta\boldsymbol{f}_{th}$ denote the changes in mechanical and thermal loads, respectively. By subtracting Eq. 3.22 from Eq. 3.23 and ignoring higher order terms, the first order change in displacement vector is given by

$$\Delta\boldsymbol{u} = \boldsymbol{K}^{-1}(\Delta\boldsymbol{f}_{th} - \Delta\hat{\boldsymbol{K}}_i\boldsymbol{u}) \tag{3.24}$$

To find the change in a given j^{th} displacement component u_j, a virtual mechanical load vector $\boldsymbol{f}_j$ is introduced, in which the j^{th} component is equal to one and all others are equal to zero. Taking the scalar product of Eq. 3.24 with the transpose of $\boldsymbol{f}_j$, the change Δu_j in the specified j^{th} displacement component due to the thickness change in the i^{th} element is determined as

$$\begin{aligned} \Delta u_j &= \boldsymbol{f}_j^T \cdot \Delta\boldsymbol{u} = \boldsymbol{f}_j^T \cdot \boldsymbol{K}^{-1}(\Delta\boldsymbol{f}_{th} - \Delta\hat{\boldsymbol{K}}_i\boldsymbol{u}) \\ &= \boldsymbol{u}_j^T \cdot \Delta\boldsymbol{f}_{th} - \boldsymbol{u}_j^T \cdot \Delta\hat{\boldsymbol{K}}_i\ \boldsymbol{u} \end{aligned} \tag{3.25}$$

where $\boldsymbol{u}_j$ is the displacement solution of the virtual system $\boldsymbol{K}\ \boldsymbol{u} = \boldsymbol{f}_j$. The reader familiar with the adjoint sensitivity method will see the similarity between the "virtual" load and the pseudo-load of the adjoint approach. Since Eq. 3.25 is a scalar value, the calculations may be computed at the element level. For the i^{th} element,

$$\Delta u_j = \boldsymbol{u}_{ij}^T \cdot \Delta\boldsymbol{f}_{i,th} - \boldsymbol{u}_j^T \cdot \Delta\boldsymbol{K}_i\ \boldsymbol{u}_i \tag{3.26}$$

where $\Delta\boldsymbol{K}_i$ denotes the change in element stiffness matrix due to its respective thickness change, $\boldsymbol{u}_i$ and $\boldsymbol{u}_{ij}$ represent, respectively, the entries from global solution vectors

$\boldsymbol{u}$ and $\boldsymbol{u}_j$ which are related to the i^{th} element, while

$$\Delta \boldsymbol{f}_{i,th} = \boldsymbol{f}_{i,th}(t - \Delta t) - \boldsymbol{f}_{i,th}(t) = \int_{A_i} \boldsymbol{B}^T \boldsymbol{D}\ \alpha \begin{Bmatrix} 1 \\ 1 \\ 0 \end{Bmatrix} (T - T_{ref})(-\Delta t)\ dA_i \tag{3.27}$$

is the change in the corresponding element's equivalent thermal nodal force subjected to a given temperature difference $\Delta T = (T - T_{ref})$ [**82**]. Substituting Eq. 3.27 into Eq. 3.26, we arrive at the displacement sensititivity number of the thermoelastic structure.

Li, et. al. points out in this article that the thermoelastic sensitivity number can take on positive or negative values, which implies that the displacement components u_j may increase or decrease when there is a change in the thickness of element i. The example problem used to demonstrate the method is very similar to that used in [**79**]. The resulting structure also demonstrates the same characteristics as those found in [**79**]. Figure 3.10 shows the resulting structure from an initial design domain similar to Figure 3.5. Another interesting result is revealed by the plot of volume ratio verses displacement (Figure 3.11). Note the minimum value of volume ratio on the curve. This point corresponds to a displacement which is nearly zero. Any increase in the volume will only increase the displacement (or compliance) of the system. Again, this process does not address the stress in the structure.

Li et. al. produced another article which features the ESO technique applied to thermoelastic structures [**83**]. Because structures rarely operate at a single temperature, this article develops an approach to multiple temperature load cases. In this development, the traditional ESO approach is used which eliminates elements based on a von-Mises stress criterion driving the design toward a fully-stressed design. Both mechanical and thermal loads are applied to a two-dimensional design

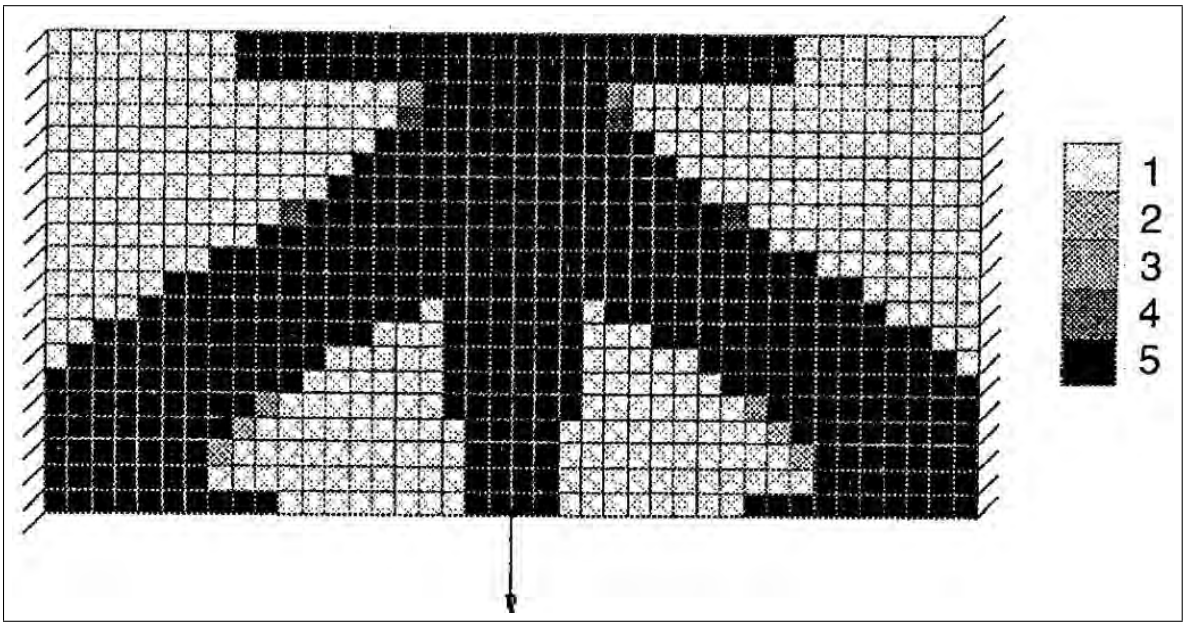

Figure 3.10. Optimized thickness design for displacement minimization (V/Vo=54.7%) [**81**].

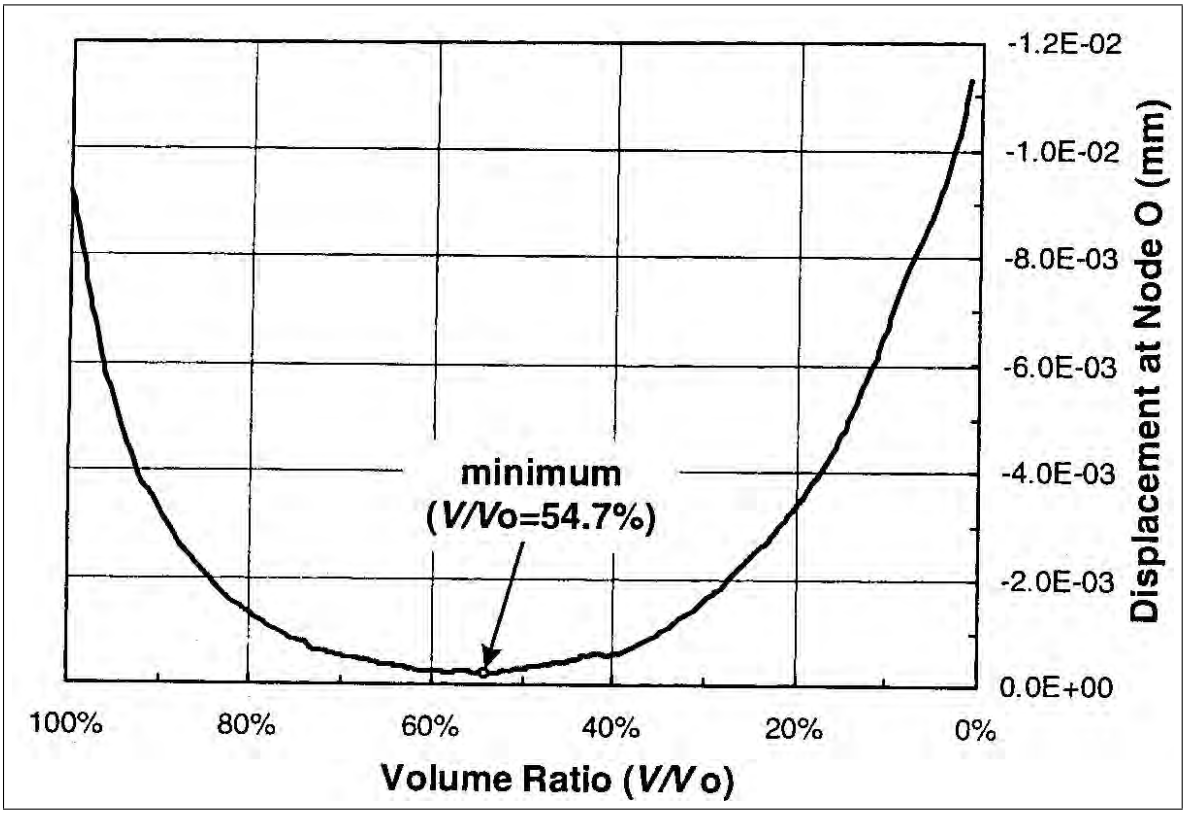

Figure 3.11. Evolution history of displacement vs volume ratio [**81**].

domain, again similar to that used in [**79**]. The structures generated are also very similar to the optimized shapes found in the minimum compliance designs of [**79**]. This is not surprising as the equivalence between the ESO stress criterion and minimum compliance was established in [**84**]. The concept of *fully*-stressed design should not be confused with necessarily producing *low* stressed designs. Removing lowly stressed elements does produce efficient designs where very little underutilized material remains. However, as material is removed from a mechanically-loaded structure, the stress will typically increase as a simple appeal to $\sigma = P/A$, with diminishing A, reveals. The fact that the temperature load takes the form of a design dependency is not mentioned in the article. No consideration in the objective function is given to the fact that thermal stress will be relieved if expansion is allowed.

3.6.3. Nonlinear Thermoelasticity

Linear elasticity has been, by far, the area to which topology optimization has been most applied. This formulation makes up the foundation of virtually all commercially available topology codes. The obvious reason for this focus is the relative infancy of the topology method when compared with other optimization techniques. So as not to convolute the results of the various topology methods, the simplest response was chosen, i.e., linear elasticity, as the demonstration tool.

More recent developments have moved beyond the linear elastic model and have addressed the topology optimization of nonlinear elastic structures [**71**] and [**85**]. In [**71**], Bruns and Tortorelli solve the minimum compliance objective with a volume constraint for small strain but allow for large displacement. The authors compare the results from both linear and nonlinear topology optimization. Their findings indicate that while the compliances between the two approaches were similar, the resulting topologies were different.

The first work to address nonlinear thermoelasticity was by Jog [**86**]. Jog's formulation is similar to the SIMP method in which a "density" variable is introduced to transform the problem from one of integer programming to a continuous variable over the domain. The variable is penalized to remove intermediate densities. Jog also introduces a perimeter constraint to eliminate the tendency toward checkerboarding. Jog makes very precise definitions of the equations of motion and energy. These strong forms of the equations are reproduced from earlier work in linear thermoelasticity [**87**]. Jog also generalizes the compliance definition given in [**79**]. His topology optimization statement combines the compliance of the mechanical loading and the thermal loading through a simple additive equation. Jog, similar to Rodriguez et. al. [**79**], uses the total strain, (albeit the Green's strain due to the nonlinear formulation), to define the thermal compliance contribution. He summizes that this objective will *not* lead necessarily to lower stress designs due to the non-proportionality between stress and strain. The author concludes that, under combined thermo-mechanical loading, a different performance functional would have to be used in order to have a more even (magnitude-wise) stress distribution in the structure.

3.6.4. Coupled Heat Transfer and Minimum Compliance

Up to this point, we have examined topology optimizations where the temperature field has been treated as a known or given distribution that is independent of the topology changes that take place. In many real life scenarios, a heat flux may be prescribed on a boundary along with convection and radiation conditions also prescribed on various portions of the domain. Therefore, only a small number of cases lend themselves to treating the temperature field as independent of the topology with the primary exception being that of uniform temperature. As the topology changes,

the conduction path for heat must also change. A limited number of publications have demonstrated the advantages of considering both phenomena in a coupled fashion.

In [**88**], Cho et.al. compute adjoint sensitivities for the coupled field equations and apply these sensitivities to the topology optimization problem. The objective function used for the structural part of the problem is the familar compliance functional. Similar to previous works, the total strain value is used to construct the functional. Therefore, a similar disconnect is observed between minimal compliance and stress reduction. By including heat transfer mechanisms, a secondary possibility exists for reducing the compliance function. If the average temperature in the domain is reduced, then expansion effects are also reduced resulting in lower compliance. This effect is observed in the topologies generated in this article. A cooling, convective boundary condition is prescribed on a portion of the design domain. The topology evolves in such a manner as to conduct heat towards the heat sink, thereby reducing the average temperature in the structure and the compliance. This formulation is given in terms of linear responses for both the temperature and the displacement. However, incorporating large deformation would not alter the trends of the process.

3.6.5. Compliant Mechanisms

While thermoelastic topology design has been applied to the design of structures as detailed above, thermally actuated devices have also been an active area of research. Generating mechanisms that *displace* in a specified manner in response to thermal energy is, in some sense, the opposite objective of a structure designed to minimize compliance. This area of research has shown particular promise in the area of MEMS (microelectromechanical systems). Sigmund's two part monograph which analyzes single [**89**] and two-material [**90**] systems provides a thorough treatment of thermally-actuated compliant mechanisms. Two figures are taken from this article

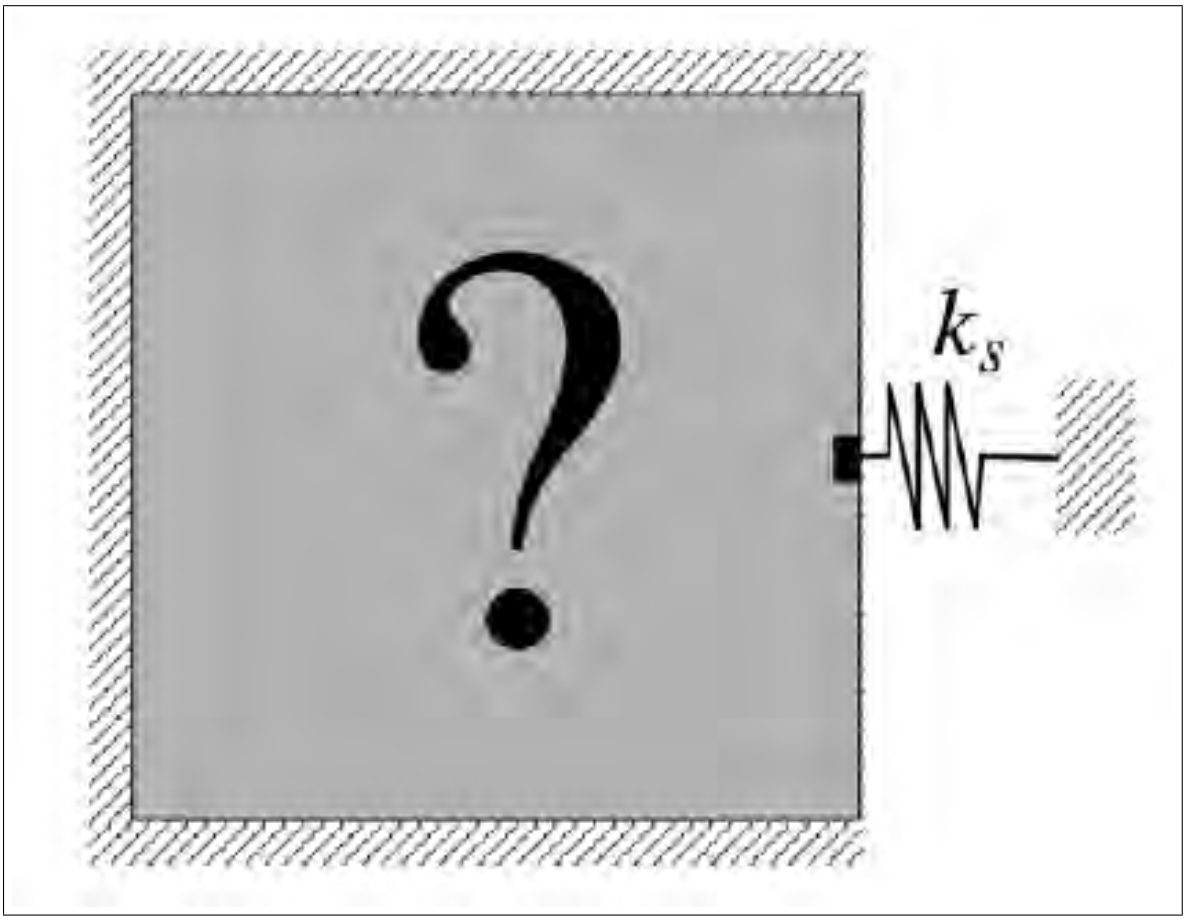

Figure 3.12. Design domain for a compliant thermal actuator mechanism [**89**].

that demonstrate the problem formulation. Figure 3.12 shows the design domain where the desired objective is to maximize the work done against the spring. The results of the optimization are shown in Figure 3.13 for various values of spring stiffness. For small spring stiffnesses the work objective is maximized by producing a mechanism that generates large displacement. As the spring stiffness increases, the mechanism exchanges the large gain in displacement for mechanical advantage neede to displace the heavier spring.

The example presented above is based on a constant temperature application. One of the more creative applications of a thermally-actuated mechanism involves the response to a transient thermal field. In [**91**], Li et. al. apply a transient

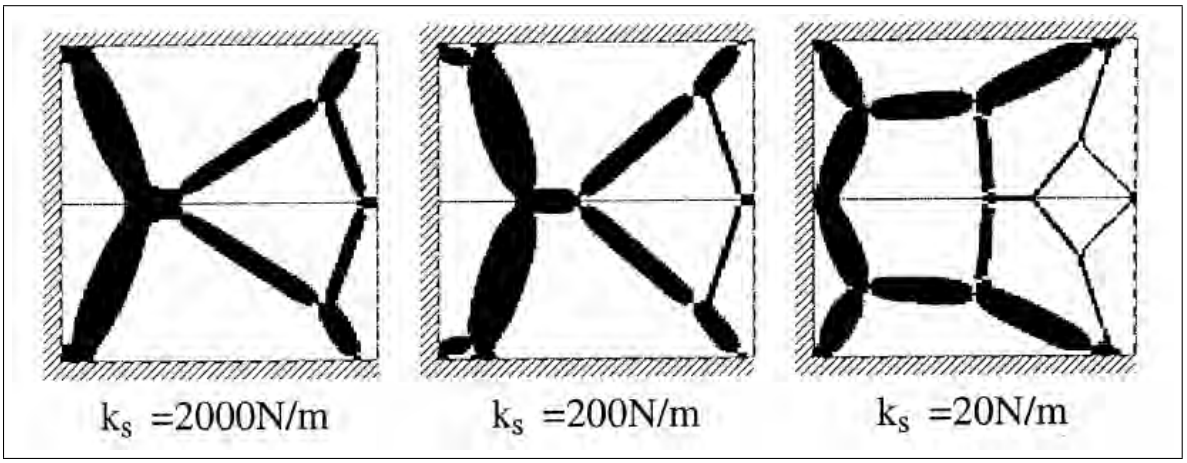

Figure 3.13. Optimized topologies for various output spring stiffnesses [**89**].

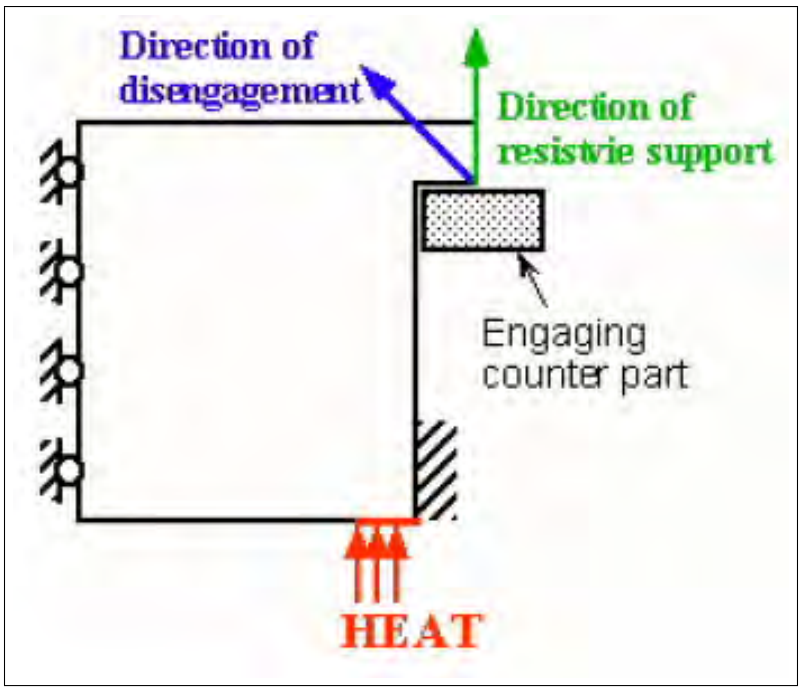

Figure 3.14. Load and design domain of thermal snap-fit mechanism [**91**].

thermal field to a design domain to generate a snap-fit mechansim. In Figure 3.14 the desired action of the mechanism is specified. The snap-fit mechanism is designed to disengage when a specified transient thermal field is applied at the location shown in the figure. The resulting topology is shown in Figure 3.15. Since the design could be exposed to an elevated temperature in its working environment, care is taken to

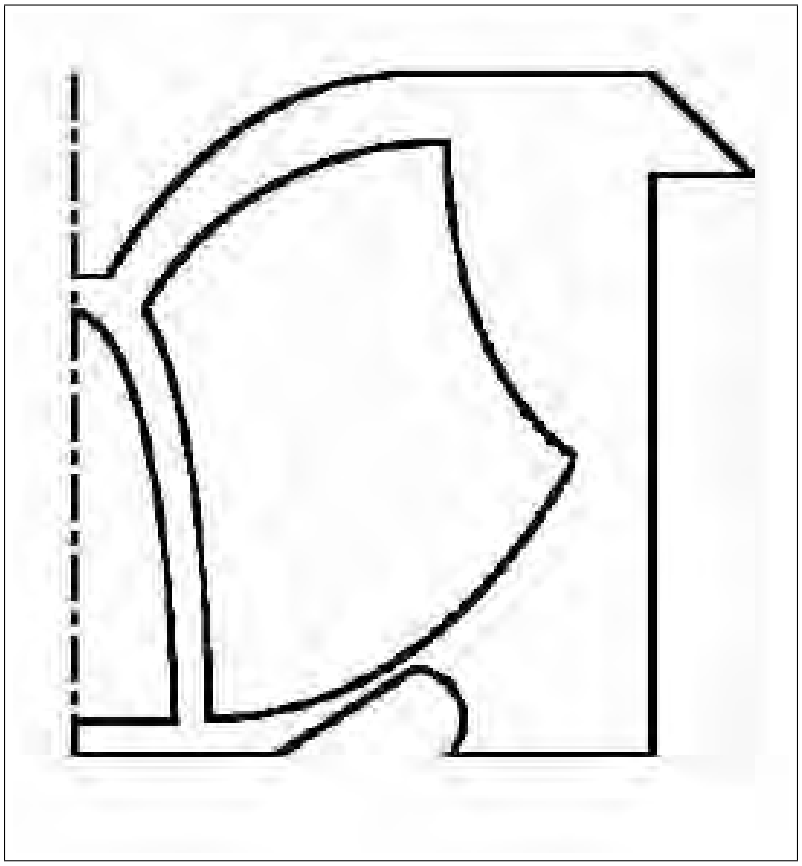

Figure 3.15. Result for snap-fit thermal transient actuator[**91**].

ensure that disengagement only occurs if a specific heat flux is applied to a specific location for a given amount of time.

This section demonstrates that the possibilities for topology optimization are far reaching and are only limited by the designers creativity in applying the techniques to new and innovative problems.

3.6.6. Frequency Maximization

The response of a structure to time-varying loads has long been a concern from a design standpoint. If the structure will be subjected to dynamic inputs in its working environment, consideration should be given to ensure that the natural frequencies of the structure do not coincide with an excitation frequency as this resonant condition

can result in large amplitude oscillations. Topology optimization, with its inherent capability for design variation, is ideally suited for frequency optimization. The problem formulation takes the following form (Eq. 3.28)

$$
\begin{aligned}
(3.28) \qquad & \max_{\rho} \left\{ \lambda_{\min} = \min_{i=1,\ldots,N_{dof}} \lambda_i \right\} \\
& s.t. \quad : \quad (\boldsymbol{K} - \lambda_i \boldsymbol{M})\ \boldsymbol{\Phi}_i = \mathbf{0}, \quad i = 1, \ldots, N_{dof} \\
\sum_{e=1}^{N} v_e \rho_e \quad & \leq \quad V, \quad 0 < \rho_{\min} \leq \rho_e \leq 1, \qquad e = 1, \ldots N
\end{aligned}
$$

where $\boldsymbol{K}$ and $\boldsymbol{M}$ represent the stiffness and mass matrices, respectively and $\boldsymbol{\Phi}_i$ is the eigenvector associated with ith eigenvalue. In practice, only the first few modes are of interest (˜10) in determining the dynamic response. One important observation with regard to the frequency optimization problem (Eq. 3.28) is the existence of a trivial solution. As stated, (Eq. 3.28) will attain an infinite frequency by removing the entire structure. Hence, the eigenvalue formulation is primarily used to reinforce an existing structure with regions that are fixed (or non-designable) due to other problem constraints.

Homogenization, SIMP and ESO have all been successfully applied to frequency optimization. One difficulty that arises when the optimizer is attemping to drive a freqency to a target value is the phenomena known as mode-switching [**54**]. This phenomena manifests itself when (as the name implies) a mode shape that was originally associated with a large eigenvalue exchanges with an initially low frequency mode shape. This phenomena causes problems for the optimizer as the *active* constraint can be switching at each iteration. Variants of the formulation have been developed which place an additional constraint on eigenvalue separation to eliminate the problematic condition from occuring [**92**].

3.7. Summary

The intent of this chapter was to provide the reader with enough information to appreciate previous efforts in topology optimization of thermo-elastic structures. The body of work in this area is relatively sparse as most topological designs address the mechanically-loaded situation. We have shown the most common objective function, compliance, is not a good objective when attempting to stiffen structure that is failing due to thermally-induced loads. A satisfying approach which can stiffen curved or flat panels without unduly supplying load to the boundary has yet to be developed. In the next chapter an approach to this end is proposed.

CHAPTER 4

SIMP Approach to Stiffening of Thermally-Loaded Curved Shells

4.1. Introduction

In this chapter a simple but effective procedure for developing topology designs in constrained thermal environments will be presented. As was demonstrated in Chapter 2, the trade space that develops when attempting to alleviate high edge stresses in thermally-loaded shallow shells is one of tensile stress reduction verses increased load into supporting structure. A conventional approach to failures resulting from out-of-plane bending would appear to require the addition of structural members with large moments of inertia. Typical structural members of this variety include I- or T-shaped beams. In a loading scenario in which the loads are independent of the structure, this approach has proven successful in many applications. However, when the loading becomes dependent on the structure, as is the case in a thermal environment, the effect of the stiffener on the load must be considered.

Stresses in thin, thermally-loaded shells result primarily from the inhibition of thermal expansion. Due to the skin's inability to expand sufficiently against the stiff boundaries, out-of-plane deformation results either through buckling (for a flat plate) or through bowing in the case of an initially curved panel. Two approaches can be taken to diminish the tensile stresses in the panel. The first approach involves the addition of stiffeners large enough to provide motion at the stiff boundaries. This approach essentially forces expansion of the boundary creating additional space for the expansion of the skin with little or no resistance. Structural members designed

for bending are not necessary since the primary load being carried is compression (provided buckling is inhibited). In this scenario, the skin will be virtually load and stress free. The newly-added structural members support the load and the thin skin simply follows the large stuctural members as they expand. The difficulty with this approach is obtaining accurate information regarding the stiffness of the boundary. As was demonstrated in Chapter 2, the additional force resulting from stiffening the skin varies widely depending on the boundary stiffness. If model inaccuracies and assumptions predict a softer boundary than actually exist in the structure, loads into the boundary as well as stresses in the stiffened shell will be underpredicted. If the structure is placed back in service, failures in adjacent structure and/or the original panel could result. So while this approach can produce satisfactory designs, it requires a high level of fidelity in the model. A model to produce this level of predictive capability would require experimental validation of the boundary stiffnesses at each location where the skin is attached to sub- and surrounding structure.

The second approach and the one followed in this work is to provide just enough out-of-plane stiffening to enable the skin to carry greater compressive load without resorting to excessive out-of-plane deformation. Since the material will be placed in such a manner as to prohibit only transverse deflection, a minimal increase in load is expected from the expansion of the additional, stiffening structure. As was demonstrated in Chapter 3, the minimum compliance topology formulation for structures whose primary loads are due to thermal expansion does not ensure lower stresses as the volume constraint is relaxed. While this behavior is intuitive and observed in structures whose function is to support mechanical loads, increasing volume in a thermal stress problem can actually increase compliance. And since thermal expansion effects are related to the volume of the material, as volume increases so too does the potential for larger stresses and reaction loads. To circumvent the problematic issues

associated with topology optimization of thermal structures, an attempt will be made to apply a *mechanical* load to induce a similar deformation as that of the damaging thermal loading. One well-documented *deficiency* in the topology optimization of structures [**85**] occurs when the structure is optimized for a single load case. In the case of minimum compliance, the structure will be stiffened in the direction of the single case loading at the expense of other potential loading directions. In fact, for the case of nonlinear optimized structures, the structure can actually collapse if the load direction remains the same but the magnitude is changed [**93**]. For thermally-loaded shell structures where the objectives are to reduce out-of-plane deformation while limiting load into adjacent structure, the single-load case *deficiency* becomes a valuable *asset* of the methodology.

4.2. Problem Definition

Two models are used to demonstrate this approach. The first model is a singly-curved, shallow titanium shell with clamped edges on all sides. While any real structure will have finite boundary stiffness, as shown in Chapter 2, the fixed assumption provides a useful metric for comparison of alternative stiffening approaches. The shell is subjected to a uniform temperature increase. Material properties of titanium 6-2-4-2 are taken from the Aerospace Structural Mechanics Handbook [**28**] and capture the temperature dependence of both Young's modulus and the coefficient of thermal expansion. Figure 4.1 details the geometry and boundary conditions of the shell structure. The ABAQUS finite element package is used model the nonlinear static response of the shell. Since the maximum usable temperature of this alloy is approximately $1000^{\circ}F$, a $900^{\circ}F$ temperature change above the reference temperature of $70^{\circ}F$ is used to demonstrate the largest stresses that one would expect in operation. The radius of curvature is 144 inches and the baseline shell thickness is 0.160

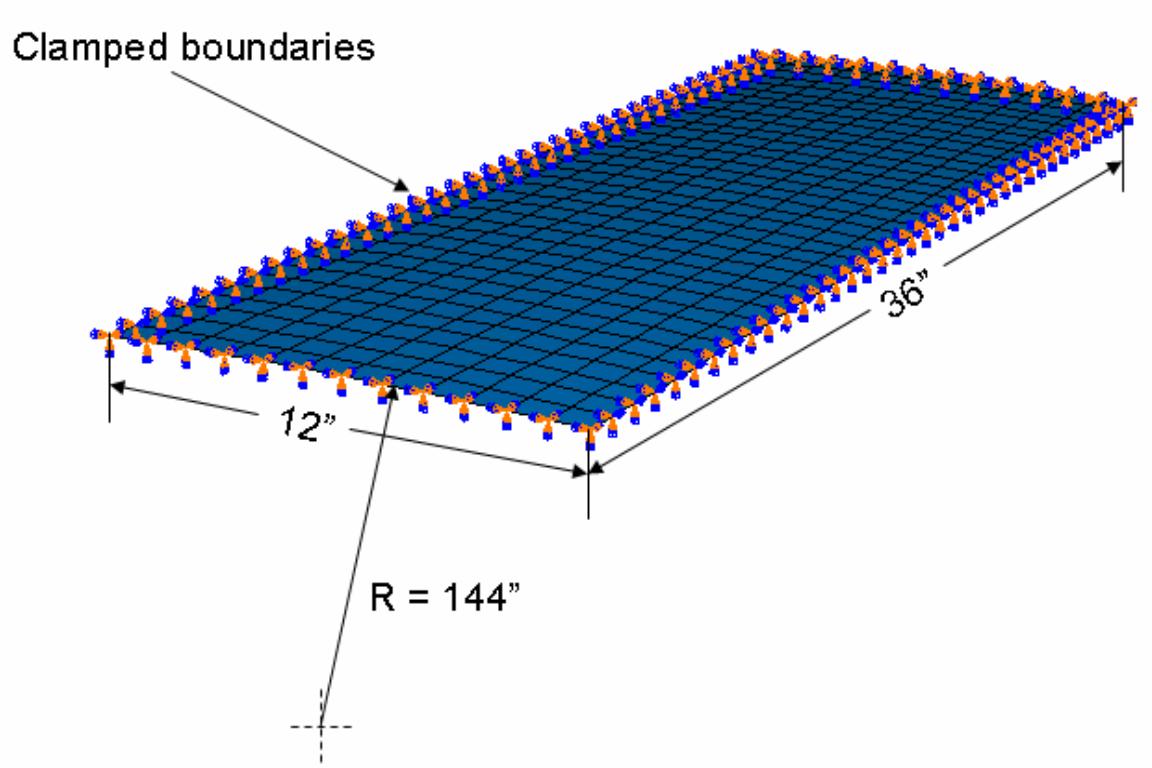

Figure 4.1. Initial geometry of curved shell with clamped boundary.

inches justifiying the finite element shell assumption. These dimensions are inspired from the EEWS application mentioned in the introductory chapter.

The second model is a two-dimensional plane idealization of the three-dimensional shell (Figure 4.2). This model allows the focus to be placed on the edge stresses and permits two-dimensional topology optimization. Since the primary stresses are bending induced, *second-order* triangular elements are used to capture the response. The dimensions of the shell model are maintained except for the 36 inch depth. A reference control point is used to more easily monitor reaction force and moment. Constraint equations are used to enforce the clamped conditions from the reference point to the faces of the elements on both ends of the planar model.

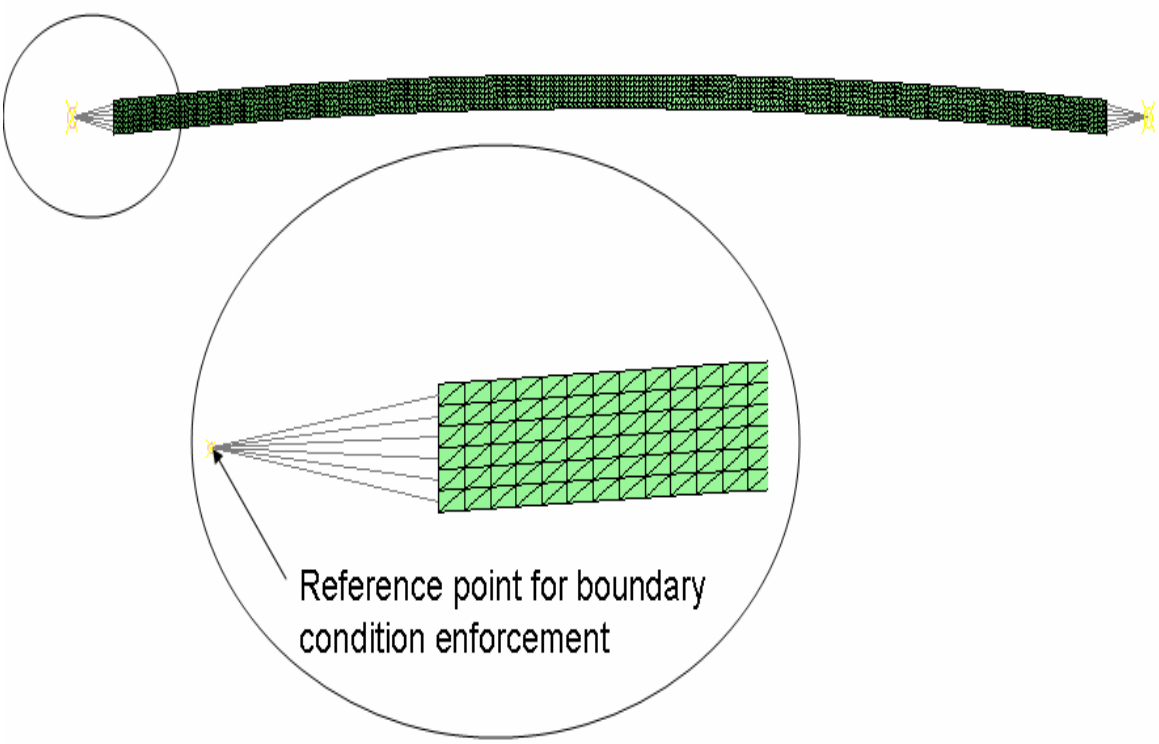

Figure 4.2. Curved plane stress model of constrained skin.

4.3. Bowing or Buckling?

A large portion of Chapter 2 was devoted to analyzing post-buckling of initially flat plates or bowing of initially curved shells. Both of these scenarios induce large tensile stresses at the clamped boundary on the side opposite the deformation. In this section the deformation and stress will be analyzed for an initially curved shell responding to thermal energy for (i) nonlinear geometric bowing and (ii) nonlinear post-buckled response. As shown in Cook, et. al., [**94**] buckling occurs when strain energy stored in membrane compression is exchanged for bending energy. The value of strain energy remains constant but the resulting equilibrium configuration can be vastly different.

In Figure 4.3 we see the nonlinear geometric response of the curved shell to the uniform temperature field. The contours represent maximum principal stress on the

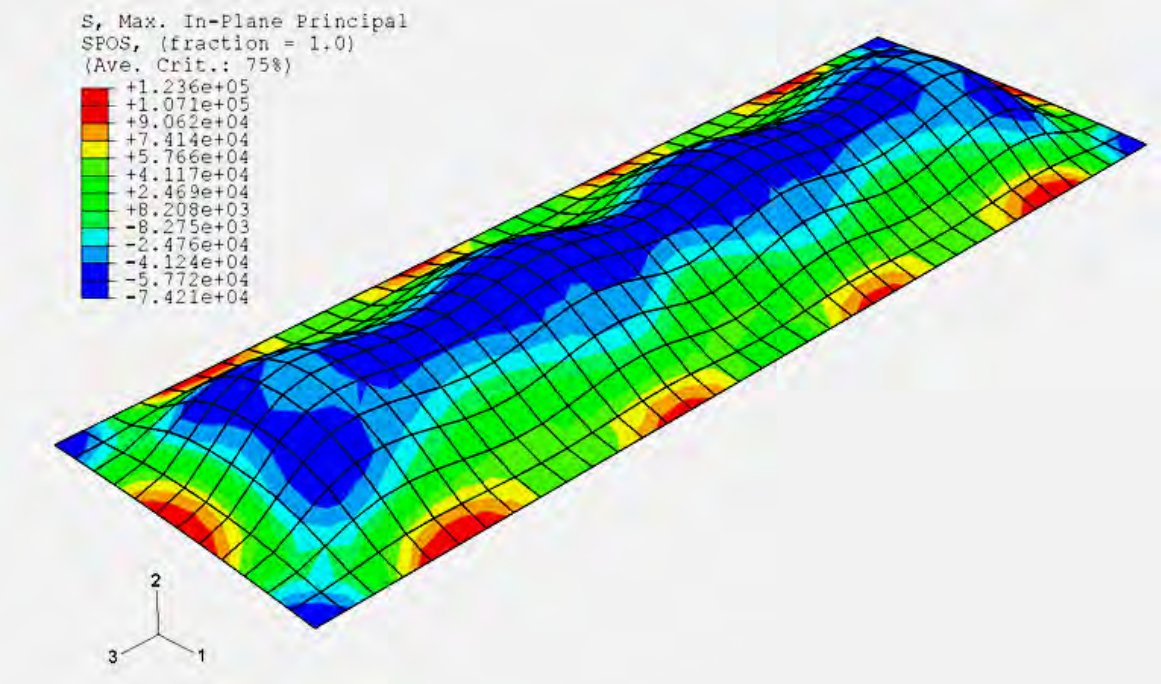

Figure 4.3. Nonlinear stress response of thermally-loaded shell with clamped edges.

bottom (underside) of the shell. Notice the locations of maximum stress occur at the fixed boundaries. This location is consistent with damage found in operation of the EEWS as discussed in the introductory chapter. A linear buckling analysis is performed to determine an estimate of the buckling mode shapes and temperatures. The first four modes are shown in Figure 4.4. The lowest buckling temperature corresponds to the first mode and is given by $258.45°F$. To gain a better estimate of the buckling temperature, the shell is loaded to a temperature just below this linear buckling temperature and another linear buckling analysis is performed. This procedure ensures that all geometric nonlinearity is included in the linear buckling estimate. Cook et. al. [**94**] outlines this procedure in detail. When the shell is heated to a temperature 5% below the original buckling estimate using a nonlinear static procedure and a linear buckling analysis is performed about this new configuration, the buckling temperatures increases to $470.87°F$. In fact, it appears that buckling

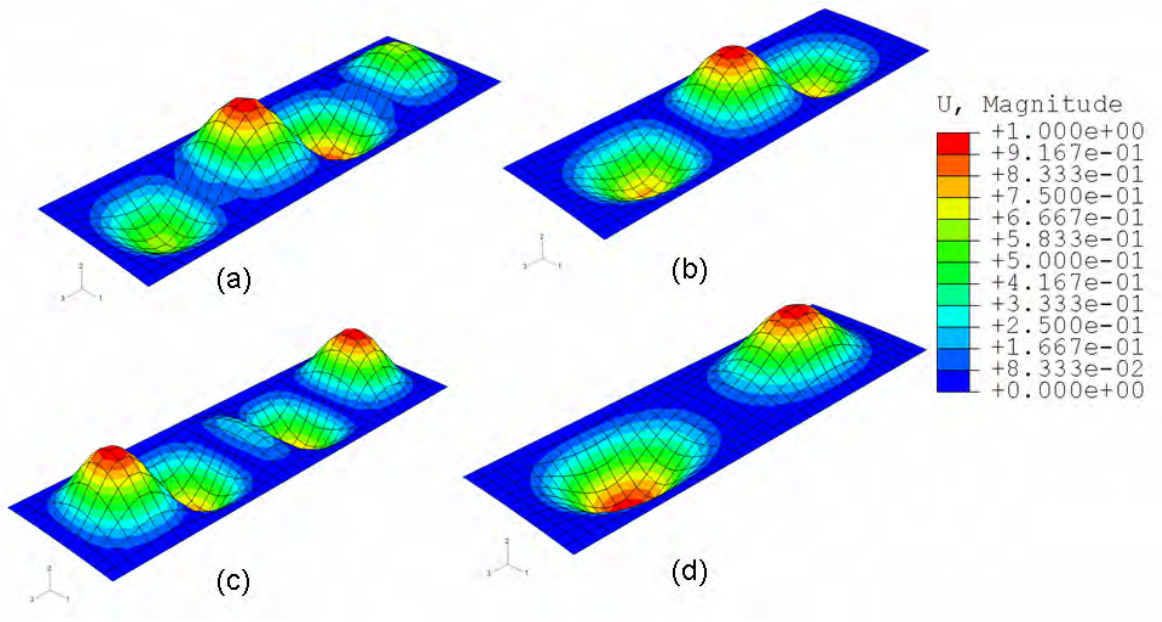

Figure 4.4. First four buckling of thermally-loaded shell (a) $(\Delta T)_c$ =188.45 °F; (b) $(\Delta T)_c$ =188.72 °F; (c) $(\Delta T)_c$ =208.69 °F; (d) $(\Delta T)_c$ =213.07 °F

is not a possible equililbrium state as the predicted buckling temperatures eventually reaches values well above the operating temperature of the material.

While buckling is unlikely in this scenario, the stress state of the post-buckled shell is computed for comparison with the simpler, nonlinear, unbuckled state. To arrive at possible post-buckled configurations, the undeformed shell is seeded with imperfections corresponding to the linear buckling mode shapes. Each imperfection is scaled such that the magnitude of the imperfection is 25% of the thickness of the shell (in this case 0.04 inches). Figure 4.5 shows the stress results of the analysis. Again, the contours represent maximum principal stress. While the deformation state does differ slightly from Figure 4.3, the maximum stress locations also occur at the clamped boundary and are within 2% in magnitude.

The debate over whether the out-of-plane deformation is due to nonlinear deformation and/or buckling is essentially a moot point from a stiffening perspective. Whether the panel is buckling or not has little impact on the deformation or damage

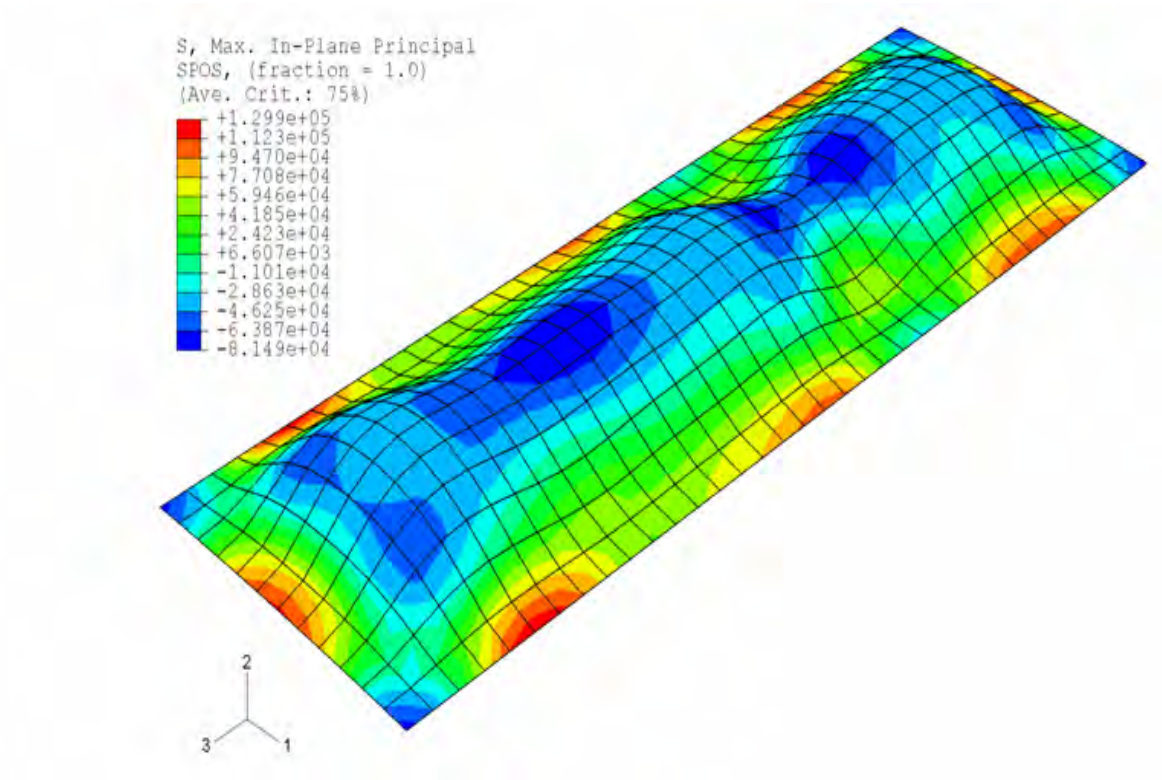

Figure 4.5. Post-buckled, nonlinear stress response of thermally-loaded shell with clamped edges.

location. If buckling were prevented, nonlinear out-of-plane deformation would continue to produce potentially damaging stresses. The observant reader will notice that the stresses shown above are exceedingly high. In fact, plasticity should be included in the modeling process to accurately capture the correct stress response. Since the purpose of this work is stress reduction, the elastic model provides a reasonable metric for comparision of alternatives.

4.4. Strip Model

In order to focus this study to the edge stresses, reaction loads and moments, the plane model (Figure 4.2) is used to approximate the response of the shell model (Figure 4.3). The stress and displacement results of the plane strain model are given in Figure 4.6. This model allows the trade space between reaction loads and bending

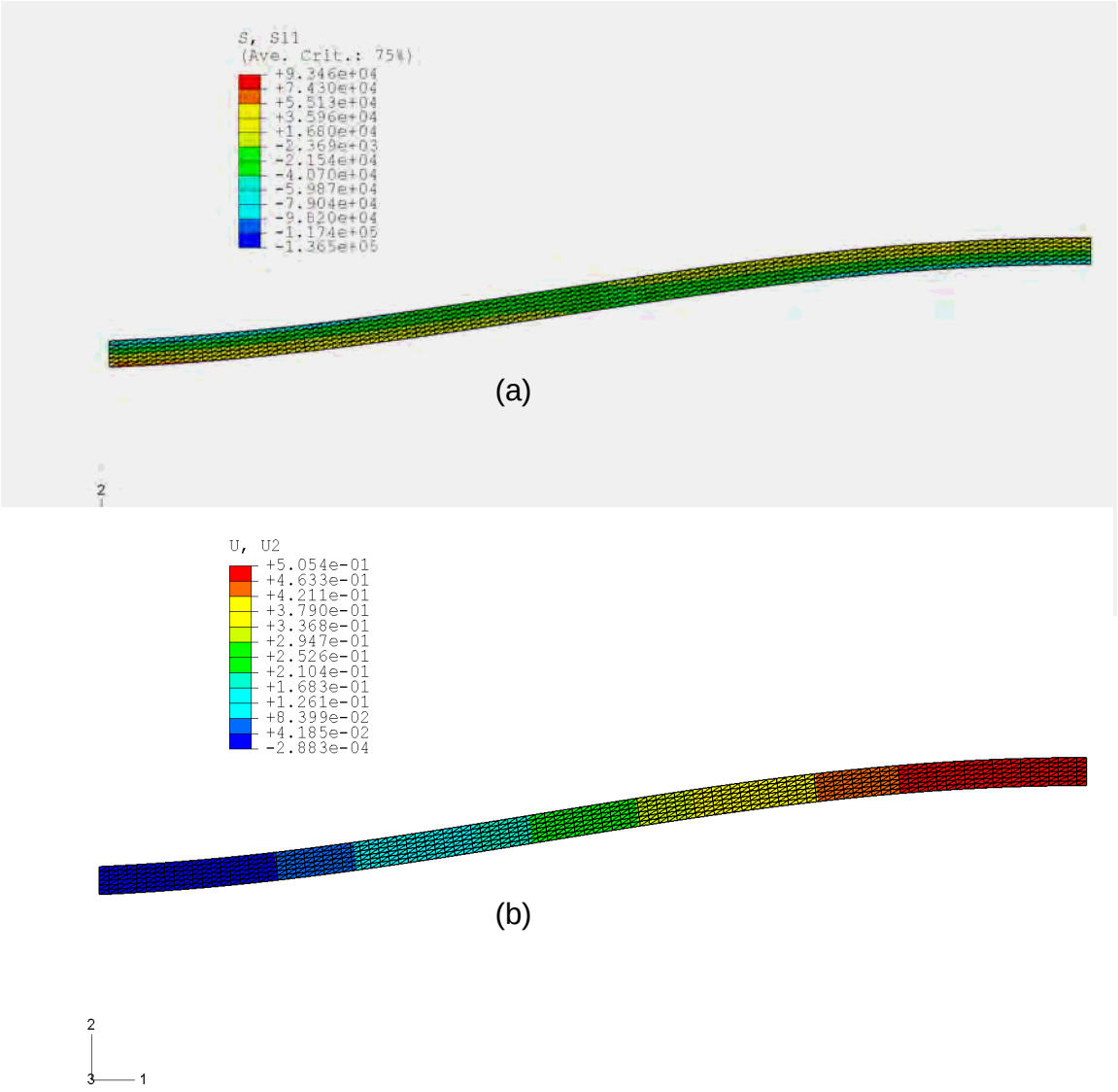

Figure 4.6. Half of plane strain model of (a) axial stress and (b) out-of-plane displacement.

stresses to be analyzed without convolution with three-dimensional effects. As mentioned earlier in this work, a trade space exists between the damaging stresses that exist at the clamped boundary and the loads reacted by the boundary. Graphically, the Venn diagram shown in Figure 4.7 illustrates the two opposing objectives and their intersection. In an attempt to establish a reasonable upper bound on the efficiency of a stiffening approach, the following exercise was carried out. The plane strain

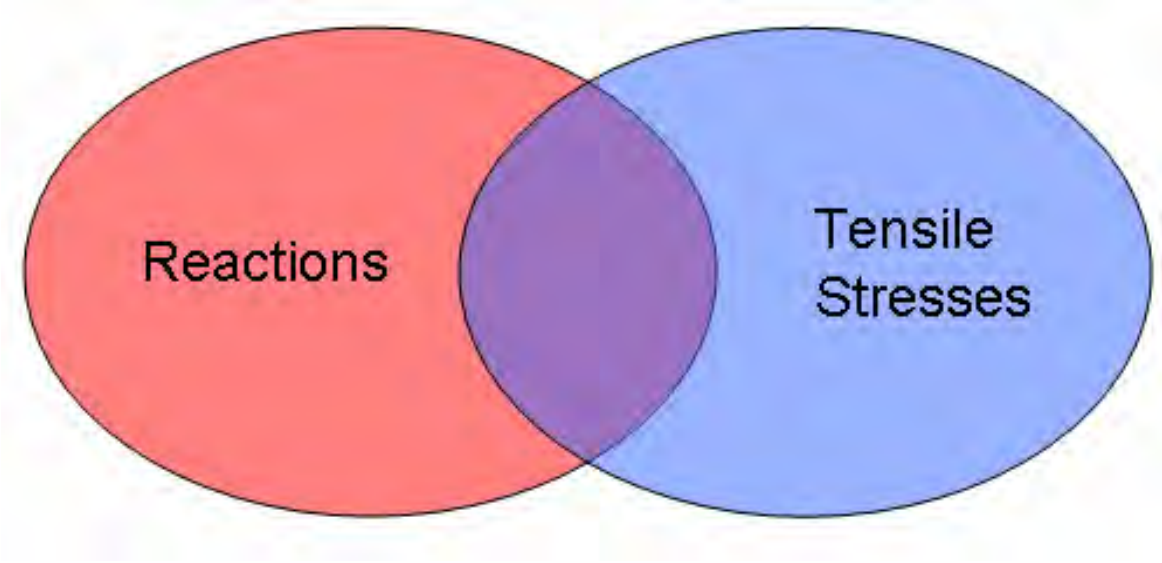

Figure 4.7. Venn diagram of design space intersection between axial stress and reaction force.

model was subjected to the thermal load and permitted to reach the final deformed shape (Figure 4.6). In a secondary analysis, boundary conditions were prescribed at each node of the model on a trajectory that would return structure to the undeformed configuration. This enforced displacement field is denoted by $U_{prescribed}$ in Figure 4.8. Notice that for a maximum tensile stress of 50 ksi, the necessary change in displacement is approximately $1/10^{th}$ of an inch. The objective of this exercise is to monitor the stresses, forces and moments as the out-of-plane deformation was suppressed by a process that required no stiffener. Hence, there would be no additional material to expand and provide additional load to the boundary. This mental exercise, while being impossible to implement in practice, does offer a reasonable metric for comparison between different options that would limit the undesired deformation. Figures 4.9, 4.10 and 4.11 present the axial stress, reaction force and reaction moment, respectively, as a function of the ficticious, prescribed displacement. The arrows denote the loading time sequence. From the diagrams, we see that to achieve a 50 ksi stress, the minimal reaction load increase factor is 5.

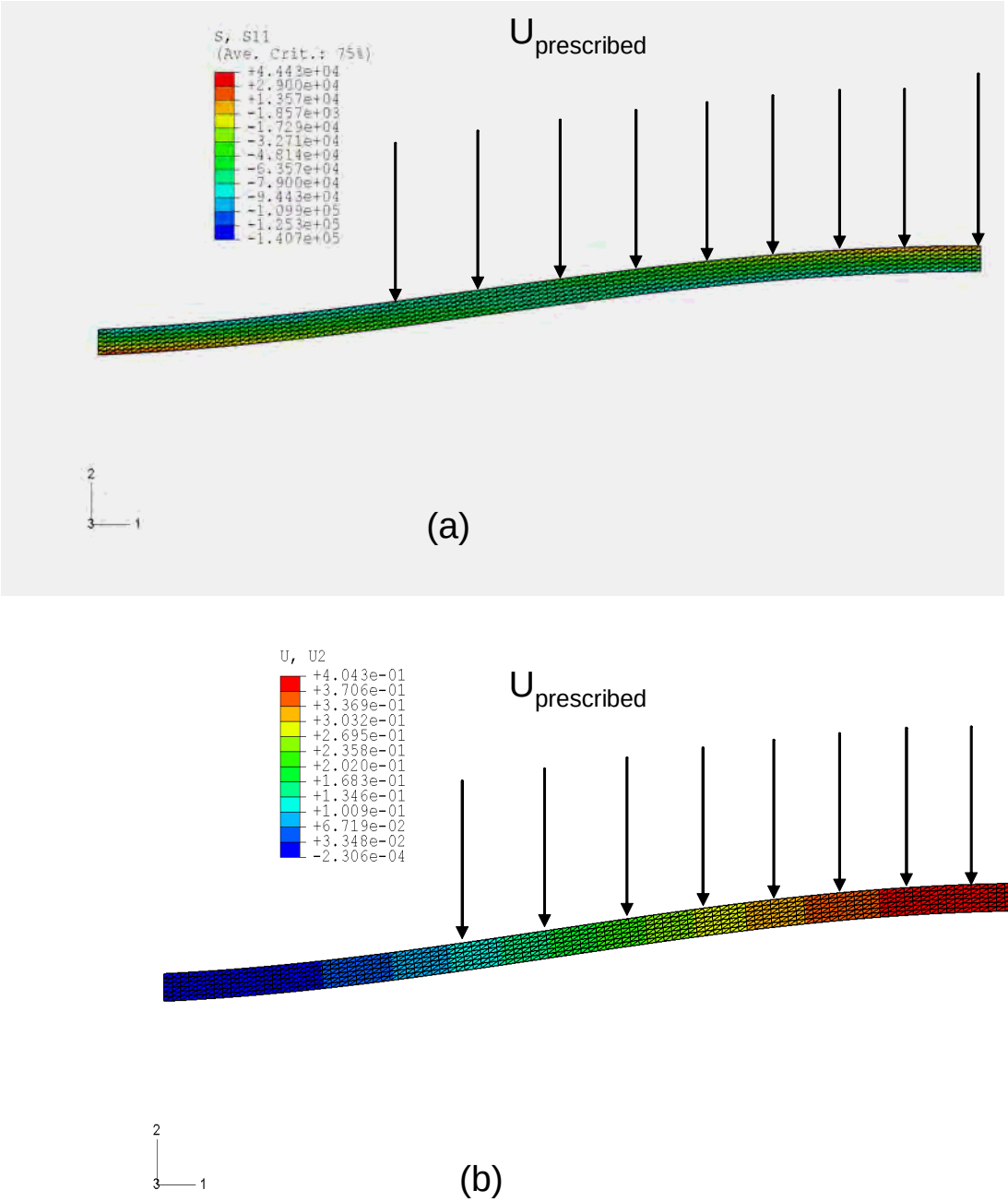

Figure 4.8. Half of plane strain model of (a) axial stress and (b) out-of-plane displacement with enforced boundary condition $U_{prescribed}$.

4.5. Conventional Stiffening

To demonstrate some of the inadequecies associated with applying conventional stiffening methods to the thermally-loaded shell strip, a combination of a doubler

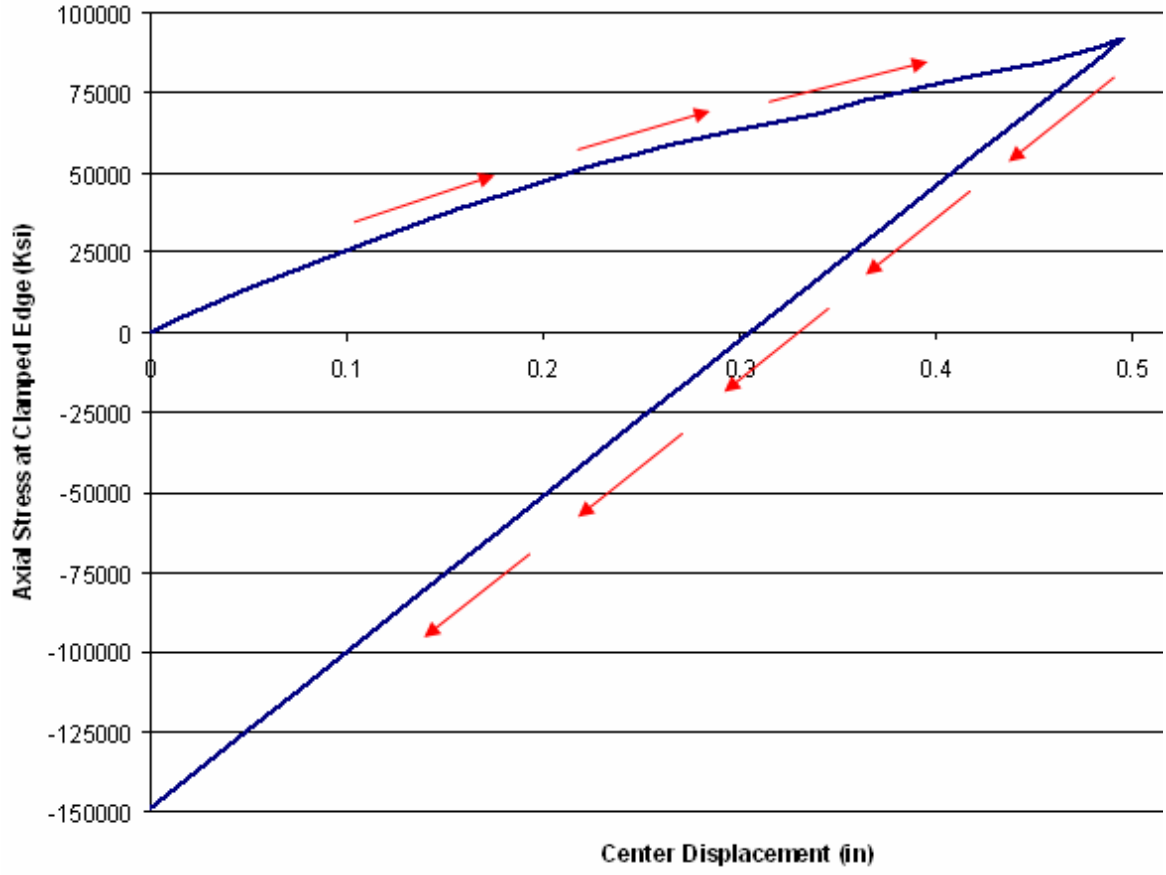

Figure 4.9. Axial stress vs out-of-plane displacement for plane strain model.

(double skin thickness) and T-stiffeners are applied to the shell. This design was motivated from an actual on-aircraft repair concept. The thermal load was applied assuming fixed boundaries and the results are shown in Figure 4.12. We see that the stresses are only reduced in the regions where the stiffeners are placed. In reality, the success of a stiffening concept such as this would require that the I-beams produce motion at the boundary allowing the expansion of the skin. The problem with this concept is the additional load that is transfered to surrounding structure. Without quantitative information regarding the stiffness of the boundary, it is difficult, if not impossible, to determine the loads reacted by the boundary. In the introduction of this chapter, two methods were outlined to reduce the thermal stresses. This

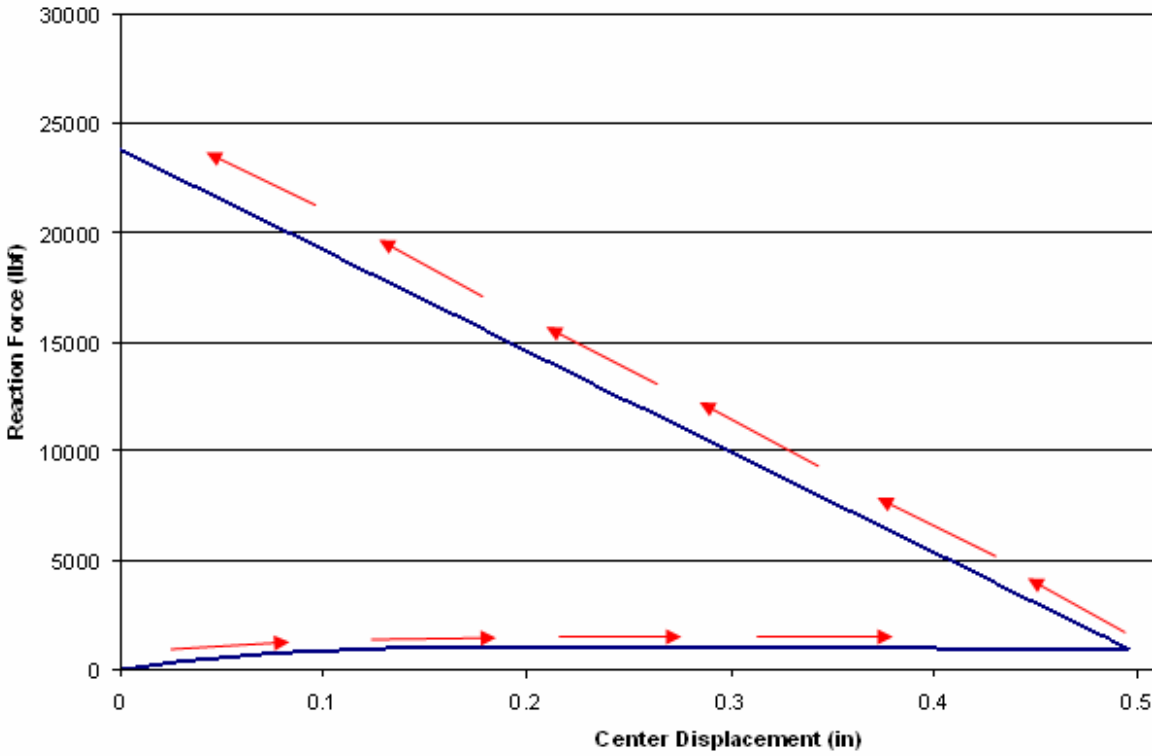

Figure 4.10. Reaction force vs out-of-plane displacement for plane strain model.

approach corresponds to the first method mentioned which attempts to expand the boundaries of the panel to accomodate the skin expansion.

4.6. Topology Optimization of Thermally-loaded Curved Shells

4.6.1. Thermal Loads

The first attempt to generate a useful structure in the elevated temperature environment using topology optimization did not prove constructive. A SIMP formulation was used and thermal loads were applied to the design domain shown in Figure 4.13 A minimum compliance objective was sought with a volume constraint permitting the final structure to use 30% of the original volume. The model is comprised of two parts. The first is the shell strip which is specified to be a fixed region and no material removal is allowed. The second part is the designable area underneath the shell which

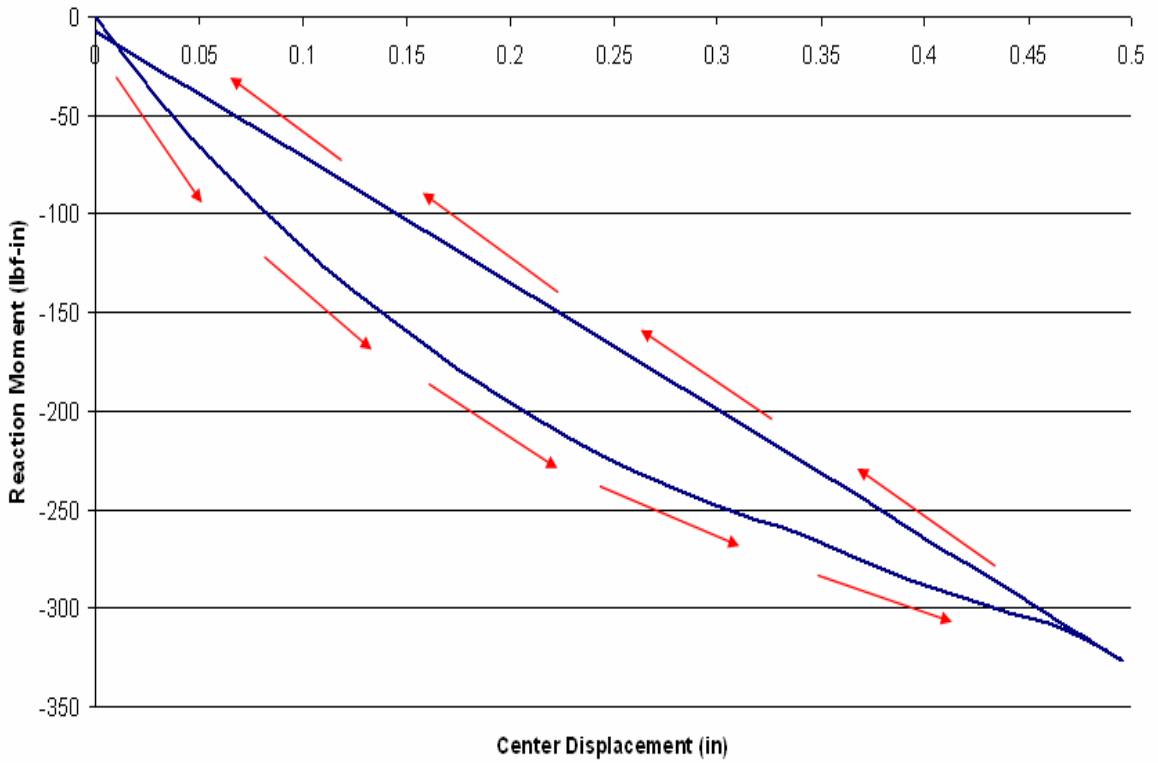

Figure 4.11. Reaction moment vs out-of-plane displacement for plane strain model.

represents the topology design region. The resulting structure is shown in Figure 4.14. The process was repeated for a volume fraction of .15 and is shown in Figure 4.15. The same problems with this formuation that have been well documented in this work are also present in this result. Notice how all the material congregates at the interface of the shell strip. Since the minimum compliance formulation employs the total strain, and the boundary conditions at each end of the strip are fixed, all the material desires to be aligned with the boundary condition to prevent in-plane expansion and a resulting small compliance. As was shown in Chapter 2, placing material as extra thickness is not an efficient means of eliminating edge stresses when boundary loads are a concern. However, from the study of curved panels, it was observed that, with enough thickness addition, the tensile stresses could be reduced. The reaction forces, on the other hand, will always increase as material is added to

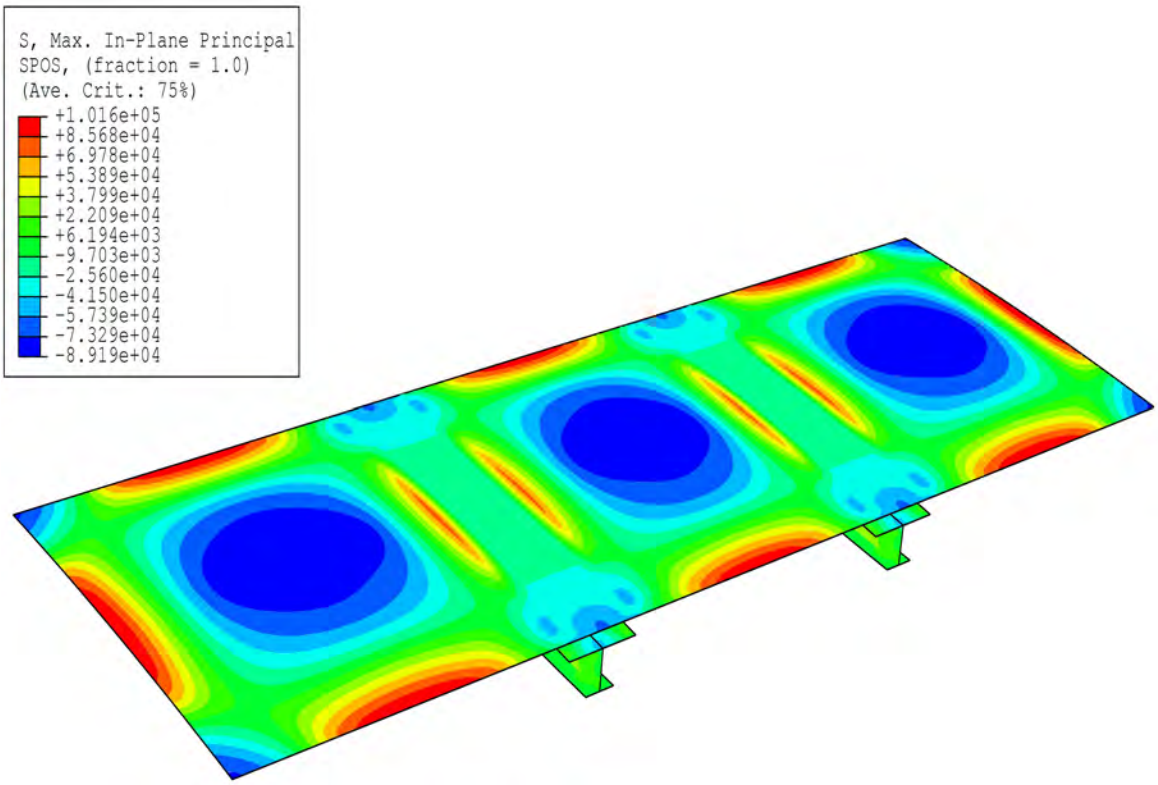

Figure 4.12. Curved shell stiffened with conventional off-the-shelf stiffeners.

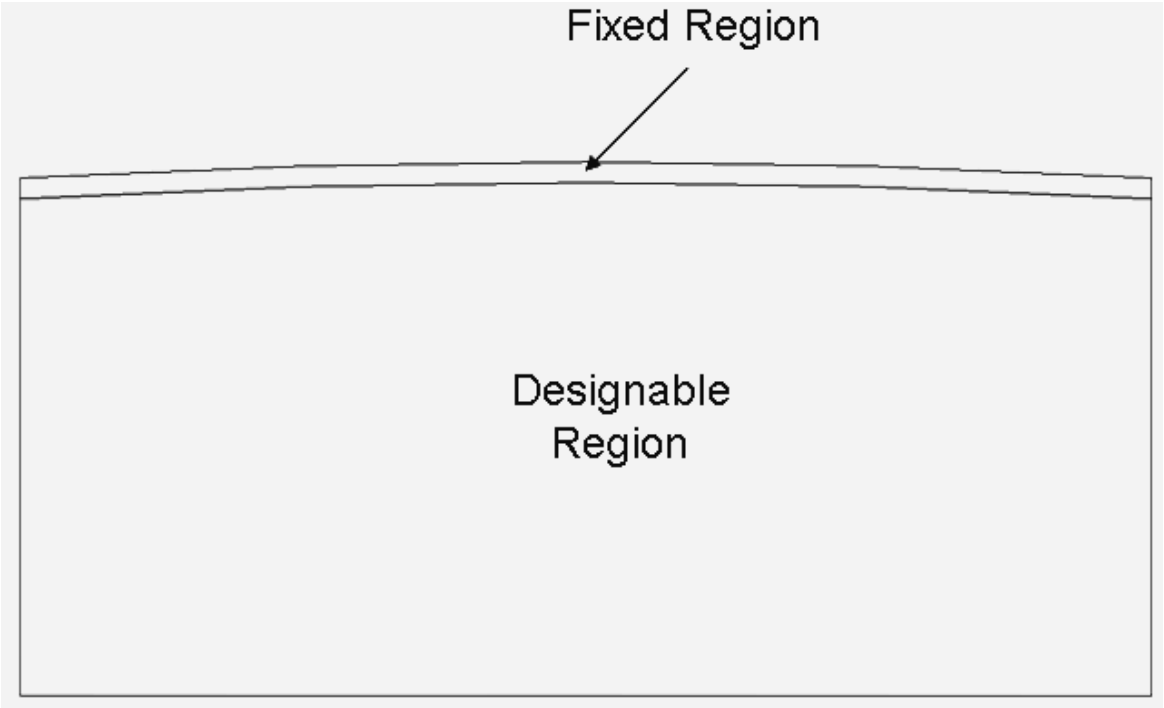

Figure 4.13. Initial design domain featuring fixed and designable regions.

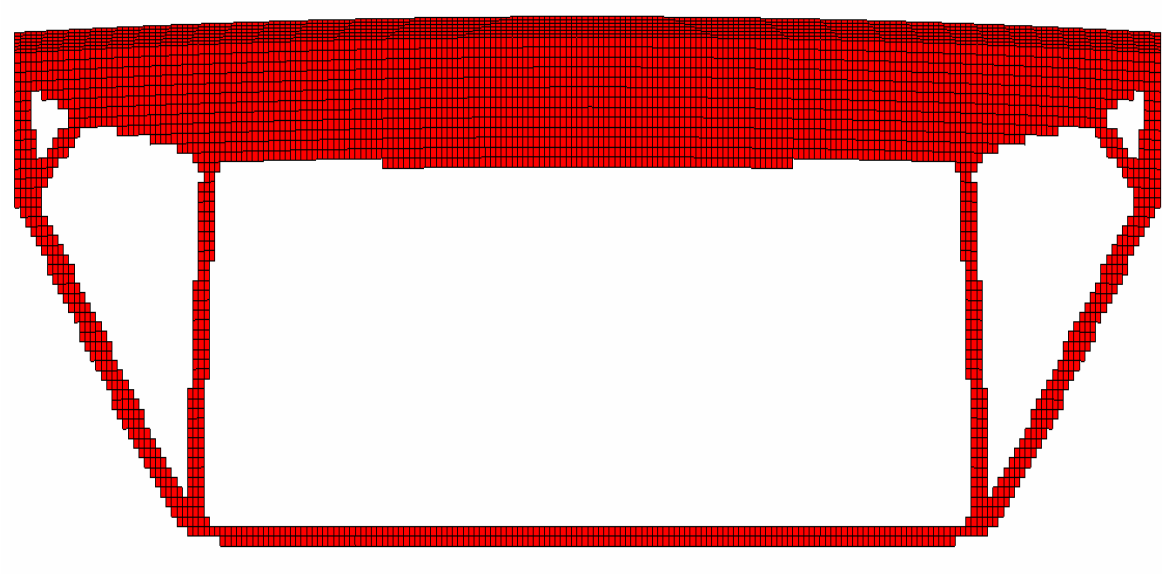

Figure 4.14. Minimum compliance topology for thermal load of $900°F$ and volume constraint of 30% of original volume.

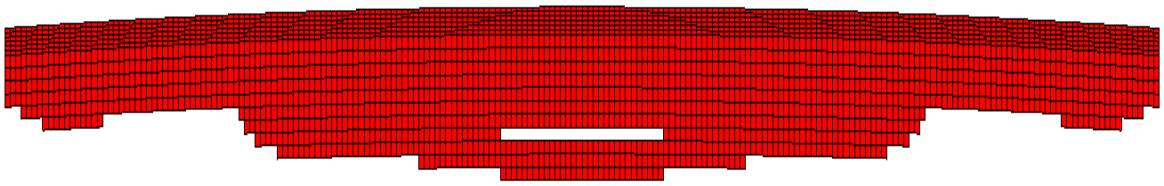

Figure 4.15. Minimum compliance topology for thermal load of $900°F$ and volume constraint of 15% of original volume.

this location creating an opportunity for failures in other locations outside the shell structure.

4.6.2. Mechanical Loads

The next approach to generating stiffening structure that limits the out-of-plane deformation while also restricting the additional load into the boundary, is to apply mechanical loads to the initial design domain (Figure 4.16) that produce the troublesome deformed configuration of the *thermal* loading. To this end, a series of transverse loads of magnitude 10 lb_f each are applied to the upper surface of the

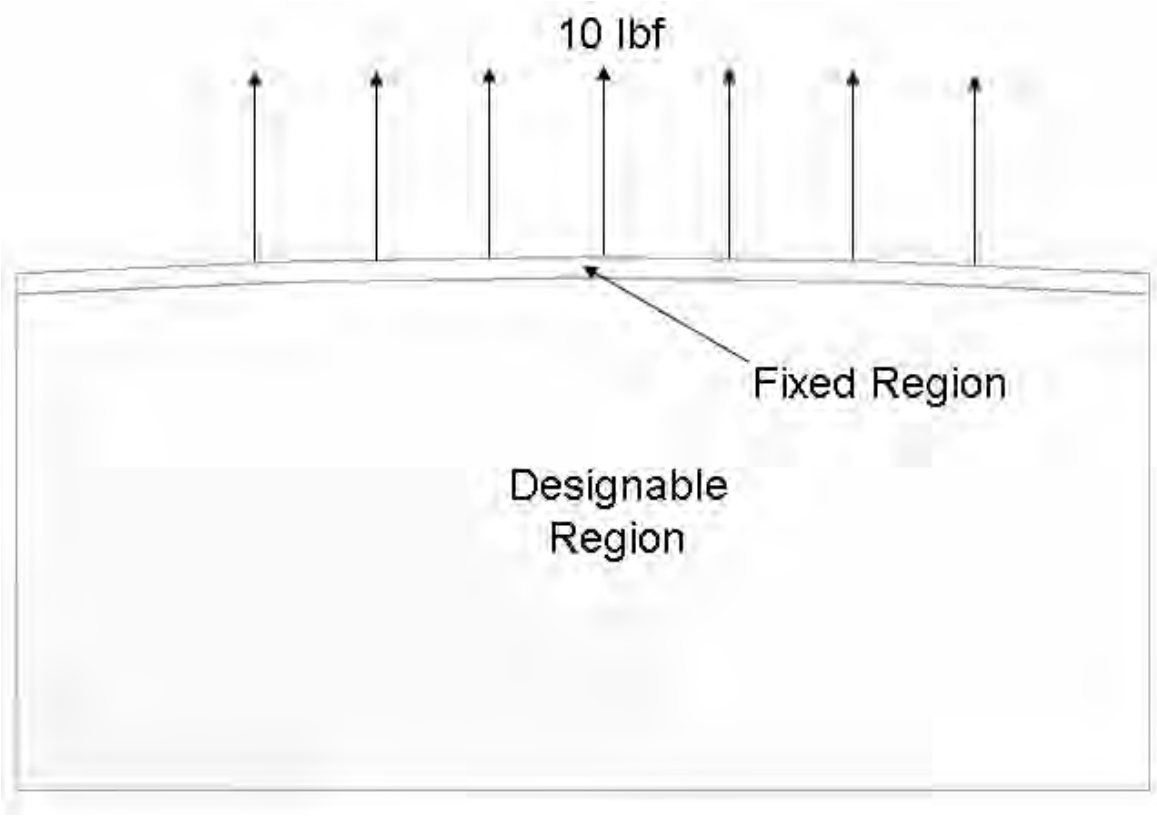

Figure 4.16. Initial design domain with mechanically-loaded out-of-plane concentrated forces.

shell strip. This loading activates the strain energy due to bending. Since a minimum compliance objective is equivalent to minimizing strain energy, the structure will evolve to reduce this out-of-plane deflection. As discussed in the introduction to this chapter, one additional consequence of developing a topology based on a single load case, is the high compliance that the structure demonstrates in response to dissimilar loadings. The results of this loading for volume fractions of .30 and .15 are shown in Figures 4.17 and 4.18, respectively. One can see from Figures 4.17 and 4.18 that the resulting structure will have little resistance to loads applied in the plane of the strip. Consequently, if the structure cannot resist compressive load, its ability to impart load in this direction through thermal expansion is also limited. The reaction force and moment comparisons for each derived configuration can be found

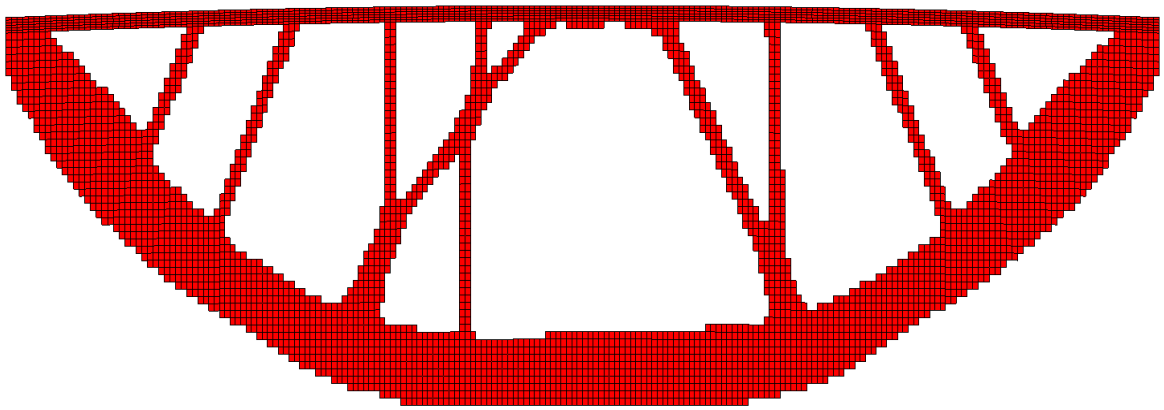

Figure 4.17. Stiffener generated from mechanical loading with minimum compliance objective and 30% volume constraint.

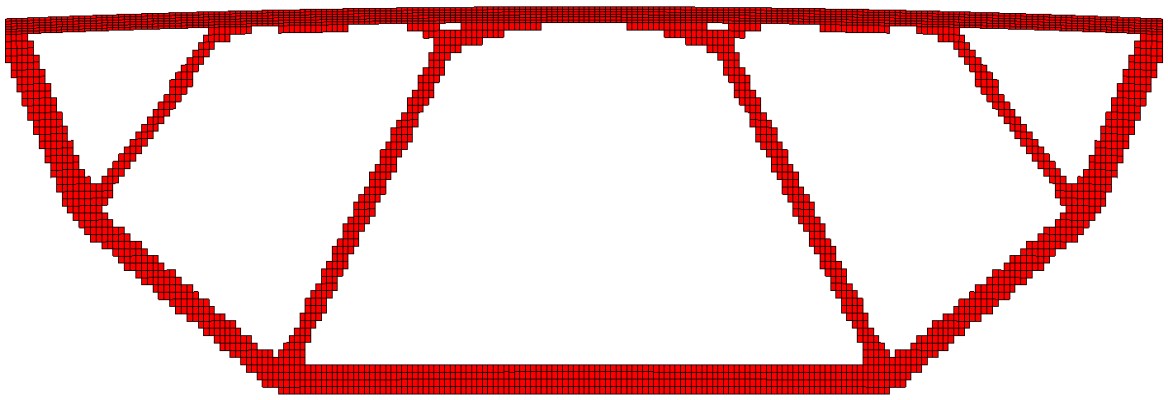

Figure 4.18. Stiffener generated from mechanical loading with minimum compliance objective and 15% volume constraint.

in Figures 4.19 and 4.20 where the thermal load is applied to each topology. The two graphs demonstrate the true feasibility of this topology approach. The desired characteristic of compliance in the in-plane direction has been achieved. One obvious difference between the topologies generated from the mechanical loading and those generated from the thermal loading is the multiple-connectedness of the two domains. The mechanically-loaded topologies generate holes in-line with the fixed boundaries. This characteristic allows thermal expansion to take place internally. This is in contrast to the simply-connected nature of the thermally-derived domains which when heated have very little ability for thermal expansion to take place internally. This

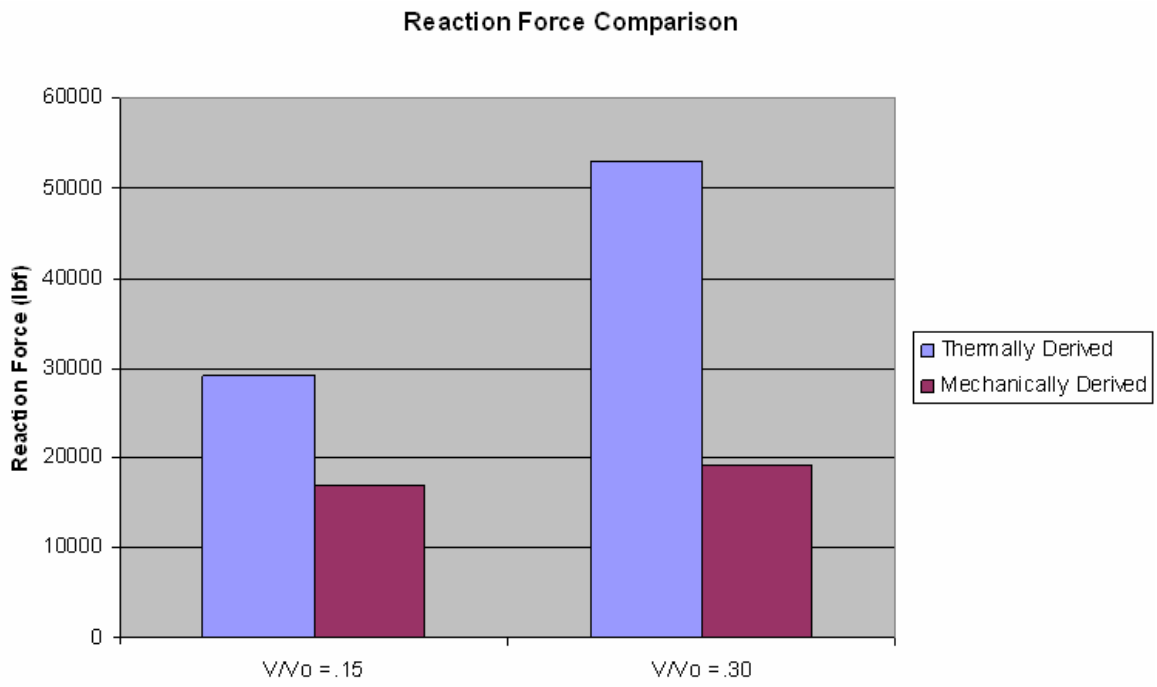

Figure 4.19. Reaction force comparisons for thermally and mechanically derived stiffeners for two volume ratios.

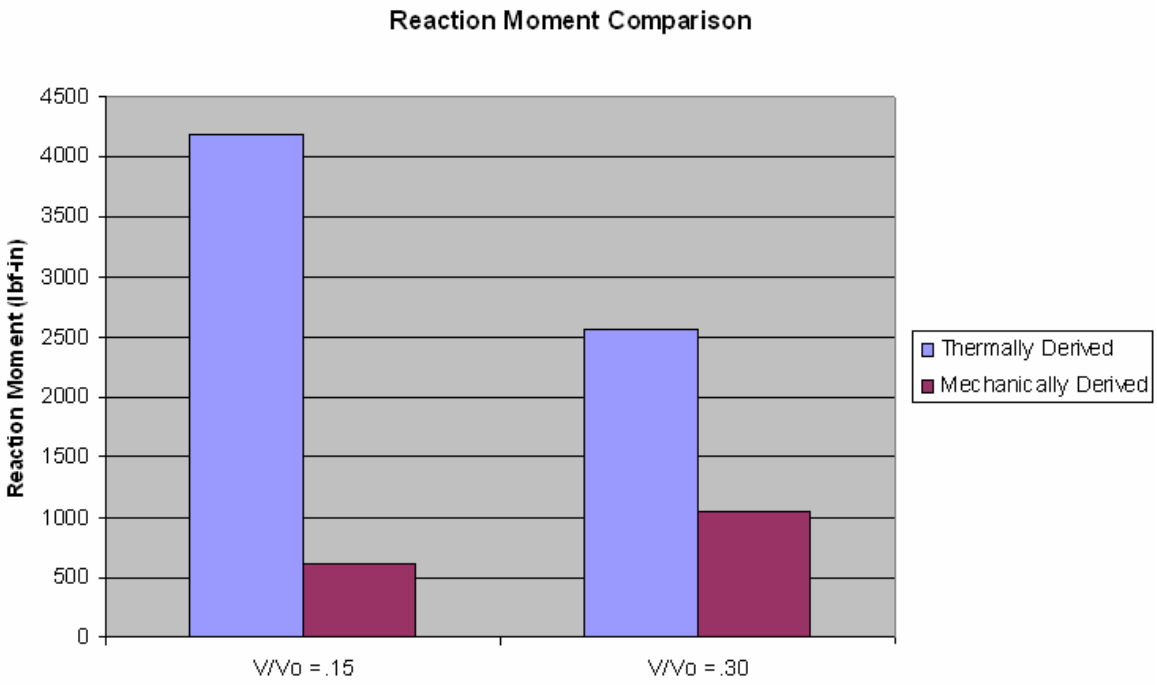

Figure 4.20. Reaction moment comparisons for thermally and mechanically derived stiffeners for two volume ratios.

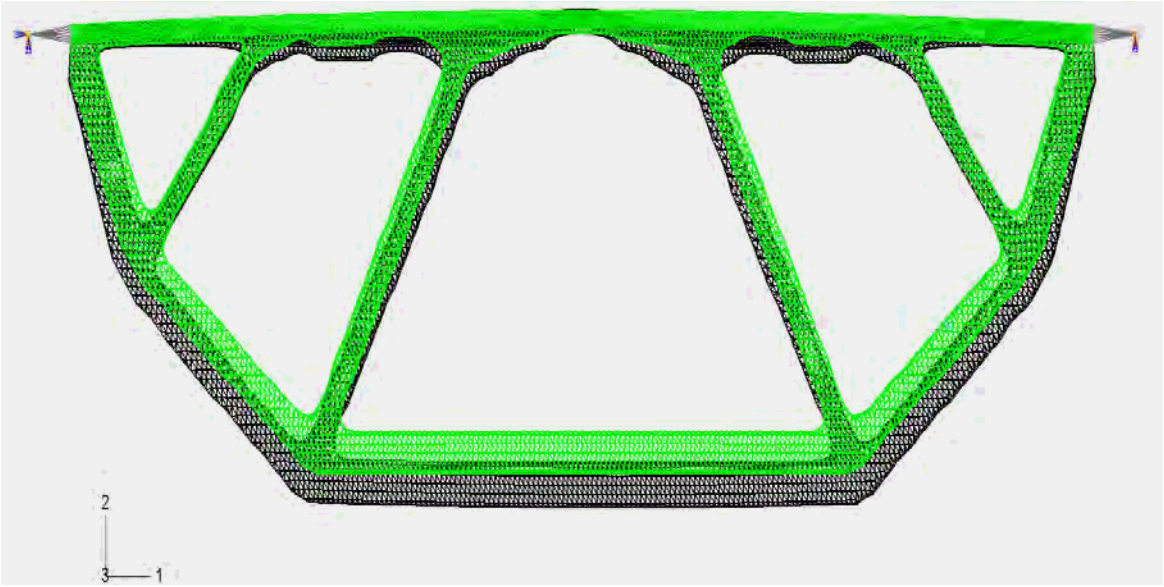

Figure 4.21. Deformed and undeformed configurations for mechanically-derived stiffener subjected to thermal loading.

forces all the attempted thermal expansion to be reacted at the boundary and accounts for the larger reactions found in the study. The next step is to determine if the mechanically-derived stiffener does indeed reduce the deflection of the curved skin thus lowering the edge bending stresses.

Since the low volume, mechanically-derived stiffener was the best from a reaction load and moment perspective, it is chosen as the potential candidate for the design solution. If we analyze this stiffener subjected to the thermal loading, Figure 4.21 shows the undeformed (green) and deformed (white) configurations. A scale factor of five is used to make viewing both configurations possible. Notice how the deformation of the stiffener takes place opposite the in-plane direction. This expansion lowers the possible magnitudes of loads into the boundary. The associated stress contours are shown in Figure 4.22. The maximum principal stress is used as the stress measure since this is the best representation of axial stress for the multi-member body. The maximum axial stress in the skin is only 24 ksi, well below any value that would result in cracking damage. In fact, the stiffener performed the task of eliminating

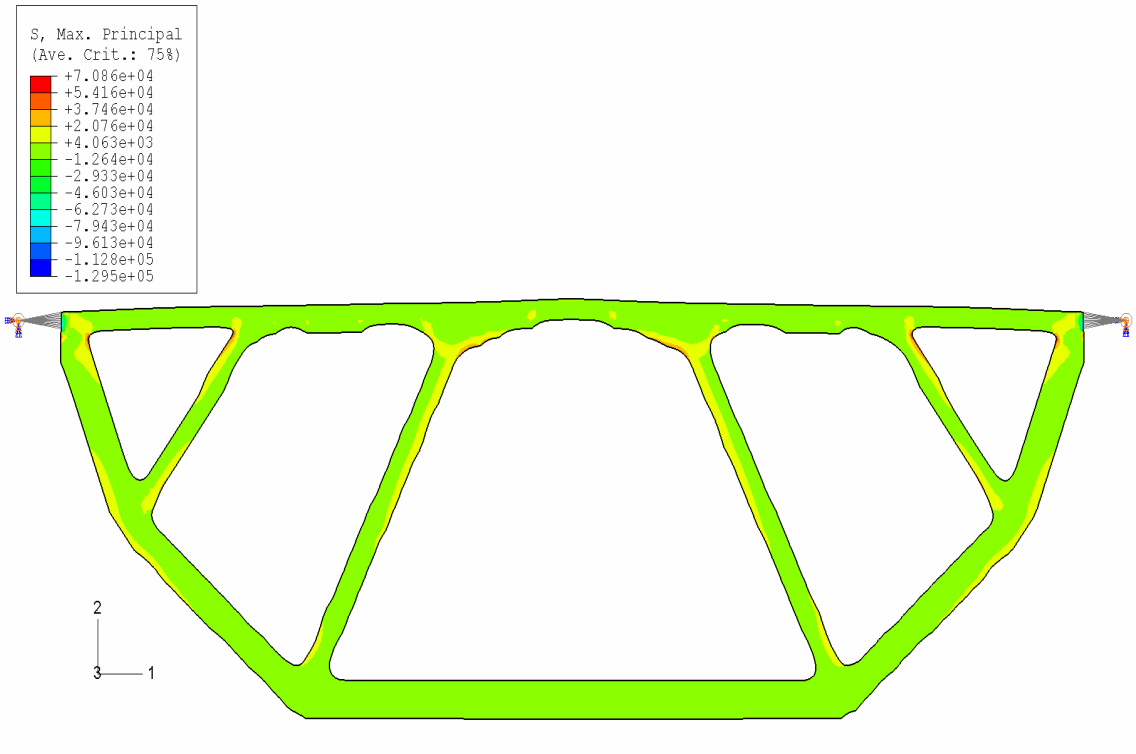

Figure 4.22. Principal stress contours for mechanically-derived stiffener-skin combination.

out-of-plane deformation so well that the thicknesses of the support structure could be reduced to allow more deflection and less load and/or moment reaction. If we compare the axial stress in the skin with the prescribed displacement lower bound of the previous section, we see that the to obtain this value of axial stress would result in a reaction force of 7800 lb_f. The reaction force in the mechanically-derived stiffener is 13,400 lb_f which results in a factor of 1.72. The moment reaction of the mechanically-derived stiffener is 612 in-lb_f while the lower bound is given by 225 in-lb_f, a factor of 2.27. When compared with the thermally-derived stiffener, these values seem very reasonable. In fact, the thermally-derived stiffener resembles most conventional stiffening methods. For example the addition of a doubler sheet and an I-beam reacts similarly to this type of approach.

4.7. Conclusions

In this chapter, a simple method for developing structure which can be used to stiffen a curved shell in a thermally-loaded environment was developed. While the treatment of topology optimization codes is lacking with respect to thermal loadings, all commercial topology codes can be employed to derive a structure that will perform well in a thermal environment. By applying mechanical loads in the problematic direction, structures are evolved which have the property of compliance in dissimilar loading directions. When stiffening a thermally-loaded shell structure that is failing prematurely, the first and most important objective is to do no harm. By generating a family of designs that, by their construction, limit the load into surrounding structure, this objective is accomplished.

The methodology presented in this section could obviously be improved through shape and/or sizing optimization. An objective which attempts to minimize a least squares error between the desired displacement of the skin and the displacement resulting from the optimization could be tailored to produce even more optimal solutions. With topology establishing the property connectivity, many, more traditional approaches are possible. Another concept which could be employed to amplify the pull-down effect of the stiffener is material grading. If, for example, a two material system were permitted, one consisting of titanium (low CTE) and another consisting of Inconel (high CTE), the response of the stiffener could be tailored to produce the desired displacement of the skin. Topology optimization will continue to be an active area of reasearch as it pertains to thermally-loaded structures.

CHAPTER 5

Multi-objective Evolutionary Structural Optimization Using Combined Static/Dynamic Control Parameters for Design of Thermal Protection Systems

In the previous chapter the focus was on a very particular geometry (i.e., curved, clamped shells). In this chapter, a general three-dimensional domain is chosen to demonstrate the applicability of topology optimization methods to a generic thermal protection system. Exterior thermal protection systems (TPS) are responsible for protecting a spacecraft's structural components from degradation due to elevated temperatures that result from atomospheric effects that accompany re-entry. The requirements for a successful thermal protection system should involve a prescription for maximum thermal stress as well as minimum natural frequency. During launch conditions, tremendous vibrational loads are generated from engine noise as a result of multi-stage to orbit propulsion systems as anyone who has attended a space shuttle launch can attest. Unlike typical vibration suppression approaches where care is taken to ensure that the fundamental frequency of the structure is lower or higher than the loading frequency, to alleviate damaging cycles in an acoustic environment, a lower bound on frequency must be specified. The content of the noise contains multiple frequencies and is referred to as wide-band random noise. Typical ranges for frequency are 0 to 2000 Hz. However, for excitation frequencies above 1000 Hz, the strain levels are small enough that damage accumulation is not a major concern. Due to a transient temperature profile and discrete attachments, thermal stress is also a concern. Thus in the design of TPS, both maximum thermal stress

and minimum natural frequency should be considered due to the combined thermo-acoustic environment inherent in high-speed vehicles. In this work, a multi-objective structural optimization method for three-dimensional acreage TPS design is developed using an Evolutionary Structural Optimization (ESO) algorithm. A static control parameter, employed to find the optimum in minimum thermal stress design (in the von-Mises sense), is modified to simultaneously address the irregular mode-switching phenomenon, as well as improvement in the modal stiffness in dynamic analysis. Two objectives are optimized simultaneously; namely, the maximization of fundamental natural frequency and the minimization of maximum thermal stress. The proposed modified control parameter is demonstrated on the design of a metallic TPS using the method of weighted objectives. The results are then compared with the conventional ESO sensitivity approach. This work concludes by applying the methodology which makes use of both topology and shape optimization in the design of an acreage TPS.

5.1. Nomenclature

$\{f\}$ = global nodal force vector

$\{Fr\}$ = external force vector for the r^{th} natural mode

$[K]$ = global stiffness matrix

$[M]$ = global mass matrix

n = number of degrees-of-freedom

N = total number of degrees-of-freedom

P = correlation factor

$R_{j,i}$ = ratio between $\sigma_{j,l}^{vm}$ and $\sigma_{j,\max}^{vm}$

S_l^{multi} = multi-objective control parameter for the l^{th} element

W_j = j^{th} criterion weighting factor

$\{x\}$ = global nodal displacement vector

$\{\ddot{x}\}$ = global nodal acceleration vector

$\sigma_{j,l}^{vm}$ = j^{th} von-Mises stress for the l^{th} element

α = parameter for element removal

ω = natural frequency

$\{\Phi\}$ = natural mode

$\{\varepsilon\}$ = modal displacement vector

$\|\cdot\|$ = L^2 norm

5.2. Introduction

The primary challenges that must be addressed to enable lower-cost access to space are weight, reusability, and ease of maintenance. The current methodology for the design of space and high speed air vehicles is to construct a low-temperature load bearing structure and then apply a thermal protective layer (also known as a Thermal Protection System (TPS)) whose sole purpose is to shield the low temperature structure. A successful TPS will not only perform its primary function of maintaining the underlying vehicle structure within acceptable temperature limits, but must also be durable, operable, cost effective, and lightweight. By construction, TPS is parasitic with respect to weight. In many situations, the themal insulation layer is added after the vehicle is sized for structural loads. Typically, the insulation is attached in such a manner as to permit thermal expansion. When following this "loose" attachment approach, care must be taken ensure that the random noise from the engines does not excessively excite the thermal protection system. Current research efforts in “hot” structures have investigated the feasibility of using advanced structural material systems that can function as load bearing structure at elevated temperature. While hot structures will be important in the future for space and high-speed air vehicle applications, parasitic TPS remains an enabling technology for many current applications particularly in the area of re-entry where the heat load is entirely transient. This work represents a hybrid approach in-between a true "hot" structure where flight load and stagnation pressures are reacted as internal loads and a purely, parasitic TPS where all thermal stress is relieved by expansion joints. In this work, no attempt is made to apply external flight loads to the thermal protection system, however, thermal stresses will result as a "hard" attachment approach is investigated. By attaching the TPS directly to the low-temperature substructure, satisfaction of the frequency constraint will be more easily attainable.

Existing thermal protection systems consist of various types of materials distributed over the spacecraft. Thermal insulators used as TPS are comprised of many material systems including felt blankets, ceramic blankets and tiles, carbon-carbon leading edges, as well as high temperature metallics. Metallic TPS has some obvious advantages along with several disadvantages. On the plus side, the nature and response of metals is well understood. Furthermore, the durability and fracture toughness of metals are typically much greater than that of ceramics. Two important disadvantages of metallic systems are weight and temperature capability. This work attempts to mitigate the weight penalty through minimization.

Metallic thermal protection systems for spacecraft operating in an extreme thermal-acoustic environment is of significant importance [**95**]. Design considerations for thermal and acoustic loading conditions tend to be diametrically opposed to one another. So called *floating* or compliant designs tend to reduce thermal stresses, whereas stiffer designs increase natural frequency and are not as easily excited by wide-band random engine noise. To address the TPS design efficiently, optimization methods are essential from both the standpoint of identifying a potentially small feasible region as well as driving toward low weight designs.

Traditional structural topology optimization methods, such as the density-based method, [**66**], the Homogenization method [**57**] and [**96**], and the Evolutionary Structural Optimization (ESO) method [**54**] and [**97**] are applicable to multi-objective optimization of static or dynamic (modal) problems. A meaningful multi-objective optimization formulation is composed of conflicting objectives in which a compromised, "best" solution is sought. Hence, multi-objective optimization is the generation of designs that achieve optimal performance with consideration given to multiple criteria [**98**] and [**99**]. Optimization solutions of this nature are known as *Pareto* optima

[**99**] and [**100**]. Pareto optima do not produce unique solutions, but rather families of solutions [**101**].

The formulation presented in this chapter incorporates a multi-objective optimization formulation into the traditional ESO algorithm using the weighted objectives technique. The ESO method developed by Xie and Steven is based on the principal that slow removal of inefficient material from a structure *evolves* the structure toward an optimum [**54**]. The ESO procedure addresses the '0-1' problem described in Chapter 3 more directly than other topology methods. The *relaxation* that is utilized to render the '0-1' problem well-posed is the small number of elements that are removed at each iteration. While no proof currently exists, intuitively, the element removal process in the ESO method can be thought of analogously with the continuation methods used in the SIMP topology approach. Recalling from Chapter 3 that continuation is achieved by slowly increasing the penalty exponent to approximate the '0-1' problem at the end of the optimization process.

Traditional ESO procedures do not address the mode-switching phenomenon that is common in three-dimensional dynamic problems. Mode-switching is a phenomenon whereby the ordering of natural modes is altered along with structural modification. The phenomenon often occurs between the natural mode of interest and the neighboring, orthogonal natural modes. The natural frequency of interest and the modal stiffness are drastically affected, resulting in convergence difficulties and/or non-optimal configurations. In two-dimensional structures, Xie and his colleagues achieved success in preventing this pathology by maintaining a prescribed separation between frequencies [**102**]. This method, however, is not applicable to three-dimensional structures in which the phenomenon occurs unpredictably during design iterations. In addition, as the number of elements eliminated becomes large relative to the initial design domain, a sudden drop in the natural frequency of interest is observed. This

is a direct result of the modal stiffness decrease associated with the current level of element removal. The ESO method and the associated dynamic sensitivity number [**54**] fail to consider modal stiffness directly. Consequently, these problems make it harder for the ESO method to determine the Pareto optimum in the multi-objective optimization [**97**] that contains dynamic characteristics.

In the next section, control parameters for static and dynamic analysis based on von-Mises stress are formulated. Section 4 presents the details of the multi-objective optimization technique. The evolutionary optimization algorithm is described in Section 5. In section 6, two relevant metallic TPS models with different load cases are presented to demonstrate the applicability of the ESO method with the novel control parameter.

5.3. Sensitivity Analysis

Like most structural optimization methods, many iterations are required for convergence and the ESO procedure is no exception. Therefore, it is important that the element removal process be efficient and accurate so that the objective is obtained as quickly as possible. In this section, two control parameters (called sensitivity numbers [**54**]), both of which are based on static analyses, are proposed as requisites for element removal. The static control parameter follows the typical ESO approach, whereas the modified static control parameter is newly developed and address the shortcomings of modal stiffness reduction and mode-switching phenomenon in natural frequency optimization.

5.3.1. Control parameter for Static Analysis

To avoid direct consideration of each component of the stress tensor, an average stress value is assigned to each element. The most common stress measure for this purpose

in isotropic materials is the von-Mises stress. The von-Mises stress σ_l^{vm} of the l^{th} element for a three-dimensional structure is defined as

(5.1)
$$\sigma_l^{vm} = \frac{1}{\sqrt{2}}\sqrt{(\sigma_{x,l} - \sigma_{y,l})^2 + (\sigma_{y,l} - \sigma_{z,l})^2 + (\sigma_{z,l} - \sigma_{x,l})^2 + 6(\tau_{xy,l}^2 + \tau_{yz,l}^2 + \tau_{zx,l}^2)}$$

Here, $\sigma_{x,l}$, $\sigma_{y,l}$, and $\sigma_{z,l}$ are normal stresses of the l^{th} element in the x, y, and z directions, respectively, and $\tau_{xy,l}$, $\tau_{yz,l}$, and $\tau_{zx,l}$ are the shear stresses action on the l^{th} element.

Consistent with the ESO algorithm, excessive stress or strain is assumed to be a dependable indicator of structural failure, and a lowly stressed element in the structure is assumed to be under-utilized. Ideally, the stress in every part of a structure should be near the same, safe level. By gradually removing material with low stress, the stress level in the next iterate becomes more uniform. By equating the von-Mises stress with the static control parameter, a prescribed number of elements with the smallest static control parameter are removed so that the increase in the maximum von-Mises stress is minimized. As eluded to in Chapters 3 and 4, the removal process must be modified when the stresses are a result of thermal fields [**30**].

5.3.2. Control parameter for Dynamic Analysis

The dynamic control parameter in the ESO method [**54**], [**102**] is derived from the Rayleigh quotient and is based on the natural mode of interest. This control parameter only estimates change in the natural frequency of interest. No *direct* consideration is given to the modal stiffness. Also, when mode-switching occurs in the optimization process, the dynamic control parameter based on the Rayleigh quotient fluctuates dramatically due to the the natural mode of interest being exchanged for

another mode. These effects render the modal stiffness very small, bringing about drastic changes in the natural frequency of interest when a large number of elements are eliminated from the structure over many iterative steps.

To address the shortcomings of the traditional ESO method, a static control parameter using von-Mises stress is developed, which gives direct consideration to the modal stiffness as a substitute for the conventional dynamic control parameter based on the Rayleigh quotient. In addition, this static control parameter is modified so that consideration is given to adjacent natural modes, as well as the natural mode of interest thus preventing a rapid change in the characteristic of the control parameter.

The derivation of the modified *static* control parameter for dynamics is as follows. The familiar equation of motion for an undamped system is given by

$$[M]\{\ddot{x}\} + [K]\{x\} = \{f\} \tag{5.2}$$

where $[M]$ and $[K]$ are the global mass and stiffness matrix, respectively, and $\{x\}$ and $\{f\}$ are the global nodal displacement and nodal force vectors, respectively. The displacement in the spatial coordinates of Eq. 5.2 can also be expressed using the modal coordinates by

$$\{x\} = \varepsilon_1\{\Phi_1\} + \varepsilon_2\{\Phi_2\} + \cdots + \varepsilon_N\{\Phi_N\} \tag{5.3}$$

where N is the total number of degrees of freedom, and $\{\Phi\}$ and $\{\varepsilon\}$ represent natural modes and modal displacements, respectively.

Using Eq. 5.3 and the property of generalized orthogonality, the response in the spatial coordinates is given by

$$\{x\} = \sum_{r=1}^{N} \frac{\{\Phi_r\}\{\Phi_r\}^T\{F\}}{-\omega^2 m_r + k_r} e^{j\omega t} \tag{5.4}$$

where ω is the natural frequency, $\{\Phi_r\}^T[M]\{\Phi_r\} = m_r = 1$, $\{\Phi_r\}^T[K]\{\Phi_r\} = k_r$, and $\{f\} = \{F\}\ e^{j\omega t}$.

In this method, the displacement of each nodal point is computed by appealing to the concept of a virtual static displacement for each mode shape. The virtual static displacements are chosen to be the eigenvectors of the modal analysis. The displacement for each mode shape is arrived at by assuming $\omega = 0$. The absolute value of the displacement is given by

$$\begin{aligned} \{x\} &= \sum_{r=1}^{N} \frac{\{\Phi_r\}\{\Phi_r\}^T\{F\}}{k_r} \\ &= \{\Phi\}[k_r]^{-1}\{\Phi\}^T\{F\} \end{aligned} \tag{5.5}$$

Note that $[k_r] = \text{diag}(k_1, \cdots, k_N)$. From Eq. 5.5, $[k_r]^{-1}[\Phi]^T\{F\}$ identifies a modal displacement vector due to the external force vector $\{F\}$. The natural mode $\{\Phi_r\}$ can be treated as a response (displacement) by applying the external force whose modal displacement is *1* for the r^{th} mode and 0 for all other modes. Regarding $\{F_r\}$ as the external force satisfying this condition, $\{F_r\}$ is easily obtained by the relationship the displacement - external force relationship given in Eq. 5.6

$$\{F_r\} = [K]\{\Phi_r\} \tag{5.6}$$

In general, the magnitude of the external force will vary from mode to mode, with higher natural modes requiring larger external forces due to the complexity of the

higher mode shapes. This tendency is exploited in the development of a novel control parameter which simultaneously considers all frequencies of interest. This hypothesis uses relative force magnitudes as a surrogate for "closeness" of natural frequencies. The nodal force vectors are scaled such that large nodal forces (corresponding to complicated mode shapes) are reduced by the factor $(\|F_i\| / \|F_r\|)^P$. Thus, $\{F_r\}_{new}$ is given by Eq. 5.7

$$\{F_r\}_{new} = \left(\frac{\|F_i\|}{\|F_r\|}\right)^P \{F_r\} \tag{5.7}$$

Here, subscript i shows the order of interest, $(0 < \ i \ << N)$. Exponent P, which adjusts the magnitude of the scaling factor between the i^{th} natural mode and the r^{th} natural mode, is the correlation factor (typically $P = 1$). A larger value of P emphasizes the relative importance of the natural mode of interest. Taking advantage of linearity, the same scaling may be used for the response.

$$\{\Phi_r\}_{new} = \left(\frac{\|F_i\|}{\|F_r\|}\right)^P \{\Phi_r\} \tag{5.8}$$

These scaled eigenvectors, $\{\Phi_r\}_{new}$, are then applied as static displacement fields.

Using Eqs. 5.1 and 5.8, a series of von-Mises stresses for each element are obtained corresponding to the i^{th} through n^{th} natural modes. Each natural mode is treated as a displacement vector, and the corresponding stress components for each natural mode are obtained via the strain-displacement and constitutive relations. Finally, for each finite element, the maximum von-Mises stress value among the i^{th} through n^{th} natural modes is selected as the new dynamic control parameter. Symbolically,

this process is expressed by Eq. 5.9.

$$\sigma_l^{vm} = \max\left\langle \sigma_{i,l}^{vm}, \sigma_{i+1,l}^{vm}, \sigma_{i+2,l}^{vm}, \cdots, \sigma_{n,l}^{vm} \right\rangle \qquad (0 < i << n,\ n < N) \tag{5.9}$$

Since Eq. 5.9 considers not only the i^{th} natural frequency, but also neighboring natural frequencies, a smooth change in natural frequency is possible even if mode-switching occurs in the iterative process. For example, when other natural frequencies are much higher than the i^{th} natural frequency, only the maximum von-Mises stress of the i^{th} natural mode is selected for each finite element because $\left(\frac{\|F_i\|}{\|F_r\|}\right)^P$ for all competing natural modes is small ($<< 1$). On the other hand, as the neighboring natural frequencies approach that of the i^{th} natural frequency during the iterative process, neighboring natural modes are also considered (i.e., $\left(\frac{\|F_i\|}{\|F_r\|}\right)^P \approx 1$). Note that the necessity of considering lower frequencies than the i^{th} natural frequency with respect to mode switching is not crucial as this rarely occurs in most practical scenarios.

Since the proposed dynamic control parameter is derived using the von-Mises stress, a chosen number of elements with the smallest von-Mises stresses are eliminated from the mesh. These elements represent the most inefficient material in the structural domain. Hence, the dynamic control parameter has been recast as a familiar ESO static optimization problem.

5.4. Multi-Objective Optimization Technique

Using the method of weighted objectives, the static-dynamic multi-objective problem is converted to a single-objective problem. That is, the control parameter for the static characteristic in Eq. 5.1 and the control parameter for the dynamic characteristic in Eq. 5.9 are combined together to form a new single criterion:

$$F_l^{multi} = W_1 R_{1,l} + W_2 R_{2,l} = \sum_{j=1}^{2} W_j R_{j,l} \tag{5.10}$$

where F_l^{multi} is the mult-objective function that determines element removal for each element l. W_j is the j^{th} criterion weighting factor with constraints $0 \leq W_j \leq 1$ and $\sum_{j=1}^{2} W_j = 1$. $R_{j,l} = \sigma_{j,l}^{vm} / \sigma_{j,\max}^{vm}$ is the ratio of the j^{th} criterion control parameter, $\sigma_{j,l}^{vm}$ for the l^{th} element, to the maximum value of the j^{th} criterion control parameter $\sigma_{j,\max}^{vm}$. Since both control parameters possess an associated von-Mises stress, a prescribed number of elements with the smallest F_l^{multi} are removed so that both characteristics are improved simultaneously (identical to the conventional ESO method for statics).

5.5. Evolutionary Structural Optimization Algorithm

The weighted objectives ESO algorithm for simultaneous stress and fundamental frequency consideration is implemented as follows:

(1) Discretize the structure using a fine mesh of finite elements.

(2) Solve the linear static analysis problem under thermal loads (or mechanical loads).

(3) Calculate the von Mises stress by using Eq. 5.1.

(4) Solve the eigenvalue problem.

(5) Calculate the von Mises stress by using Eq. 5.9.

(6) Combine the two control parameters by using Eq. 5.10.

(7) Remove several elements from the current structure that have relatively small contributions.

(8) Repeat steps 2 to 7 until the weight of the structure reaches some predetermined value.

In the traditional ESO procedure, element removal is controlled by the rejection ratio (RR). During the iterative process, the rejection ratio is gradually increased by an evolutionary rate (ER) [**54**]. The rejection ratio is obtained by comparing the

relative values of the control parameter with the model maximum. For mechanically-loaded structures, the maximum value of the reference criterion does not decrease during the evolutionary process. This results in threshold levels steadily increasing as material is removed. Conversely, for cases involving thermal stress, the maximum stress level can actually *decrease* as the evolutionary process converges [**30**]. This is due to the fact that thermal loads act as body forces in the domain. If a given element is removed which contributed more stress *to* its neighbors than it reacted *from* its neighbors, the maximum stress levels can decrease. For this reason, a new rejection ratio is defined, RR_{new} , such that a percentage α of the original domain of elements are removed which contribute the least to the objective F^{multi} function. Note that α should be chosen sufficiently small to ensure smooth evolutions between two iterations. Typical values of α are 1~2%.

5.6. Thermal Protection System Design

Because the TPS composes the external surface of a spacecraft, several requirements must be satisfied to design a TPS for all environments experienced by the vehicle:

- In order to minimize operational costs, a TPS should be as lightweight as possible while maintaining acceptable stiffness and high natural frequency.
- A TPS panel is utilized to protect the spacecraft from heat, while a frame structure may be attached to prevent fluttering due to aerodynamic and/or acoustic loading. If required, a honeycomb sandwich can be affixed to the plate if the spacecraft encounters a maximum surface temperature for an extended period of time.
- A long support connecting the plate to the fuselage is recommended to decrease heat transfer to the fuselage. This construction provides for extra

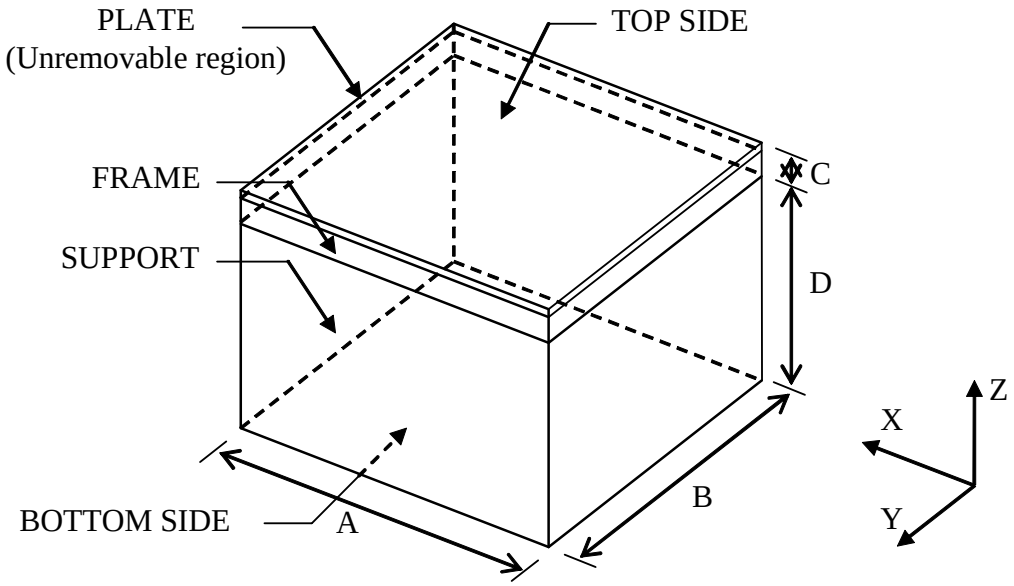

Figure 5.1. An initial metallic TPS.

volume of insulation to be placed in the cavity, and facilitates the generation of novel attachment by ESO (or other topology) methods.

- The maximum thermal stress in the TPS is required to remain below yield strength to avoid plastic deformation.

In this section, two relevant TPS models with different initial conditions are presented to demonstrate the effectiveness of the ESO method with the proposed control parameter. An efficient means for designing a TPS is shown for various requirements by employing the proposed control parameter. The initial TPS design is shown in Fig. 5.1. Inconel alloy 693 is utilized because of its excellent resistance to metal dusting and high temperature corrosion, as well as for its favorable fabrication and joining properties [**103**]. The TPS models are discretized with hexahedron isoparametric linear elements for finite element analysis, and the p-version of the linear finite element method with Guyan reduction is applied to enhance the accuracy of the analysis and reduce computational effort [**104**]. Structural characteristic matrices with more

degrees of freedom are generated, although the sizes of the matrices are identical to those obtained with the h-version finite element method. For both examples, α, a parameter for the element removal, as shown in the previous section, is set at 1%, and in Eq. 5.9 n is set to 10.

5.6.1. Example 1: TPS Model with External Forces

The conventional ESO method and the new ESO method with the proposed control parameter are both applied to a TPS model with a mechanical load case. The TPS model, which has the dimensions of A=0.5 m, B=0.45 m, C=0.03 m, and D=0.27 m, as shown in Fig. 5.1, is loaded at room temperature, with a Young's modulus of 196 GPa, a material density of 7770 kg/m3, and a Poisson's ratio of 0.32. The model is meshed with 0.05 m x 0.05 m x 0.03 m rectangular isoparametric elements with fixity prescribed on the bottom side. External tractions of magnitude 10 N in the x-direction are applied to each nodal point on the top side. The elements identified with the external force, which include those in the plate-frame region, are set as unremovable elements. The region shown as BOTTOM SIDE have a prescribed boundary condition of zero displacement in all directions. This unremovable region renders the evolutionary process unstable in the conventional ESO method as adjacent regions with high modal mass are eliminated without consideration of the modal stiffness.

The optimization problem is to minimize the maximum von-Mises stress and to maximize the fundamental natural frequency while reducing the TPS weight. These two objectives are applied as weighted objectives as shown in Eq. 5.10. The relationship between maximum von-Mises stress and the fundamental natural frequency is investigated by varying both weighting factors and volume reduction.

Figure 5.2 shows the comparison between the fundamental natural frequency and

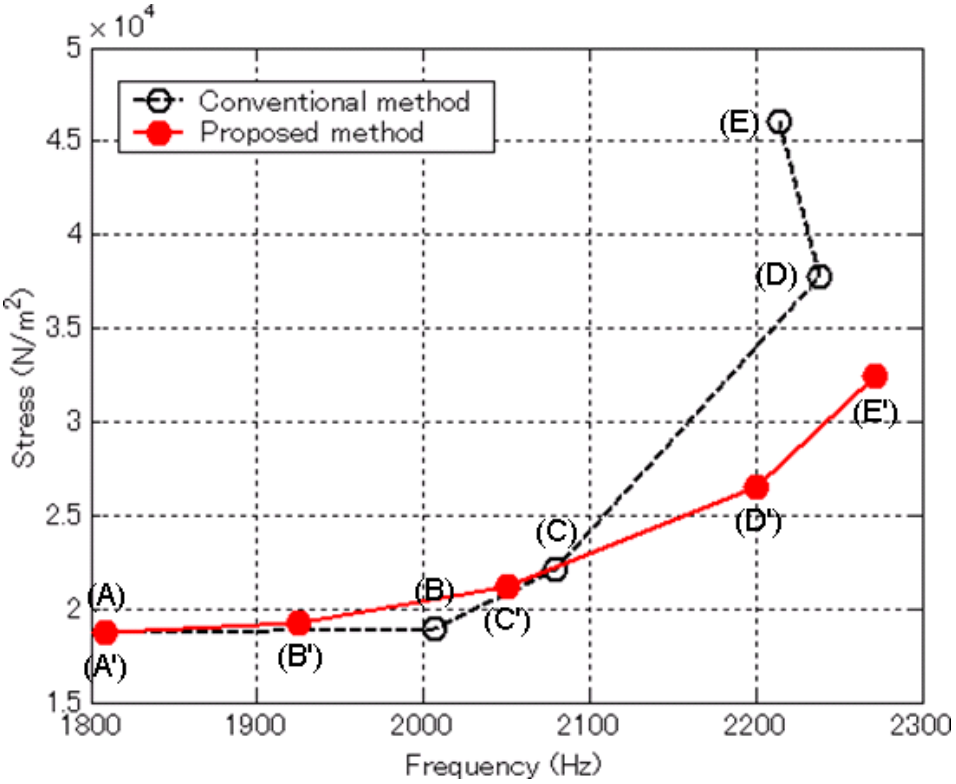

(a) 20% volume reduction

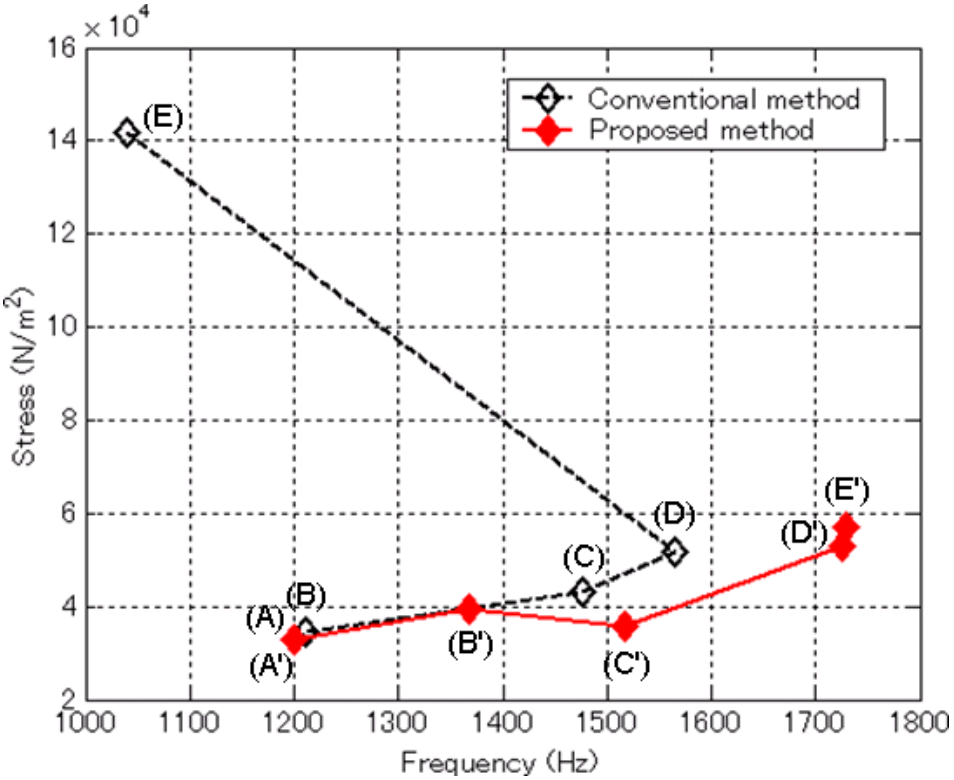

(b) 50% volume reduction

Figure 5.2. Relationship between fundamental frequency and maximum stress.

the maximum von-Mises stress for volume reductions of 20 and 50%. The plots provide results for both the conventional ESO [**97**] and the proposed method. The weighting factor for the dynamic characteristic ($W_{dynamic}$) and the weighting factor for the static characteristic (W_{static}) for each point in Fig. 5.2 are as follows:

(A) and (A'): $W_{dynamic} : W_{static} = 0.0{:}1.0$,

(B) and (B'): $W_{dynamic} : W_{static} = 0.2{:}0.8$,

(C) and (C') $W_{dynamic} : W_{static} = 0.5{:}0.5$,

(D) and (D') $W_{dynamic} : W_{static} = 0.8{:}0.2$,

(E) and (E') $W_{dynamic} : W_{static} = 1.0{:}0.0$.

Points of (A)-(E) and (A')-(E') are results from the conventional and the proposed method, respectively.

In the proposed method, it is observed that each objective is improved by increasing its respective weighting factor (e.g. both the fundamental natural frequency and the maximum von Mises stress increase when the dynamic weighting factor is increased and the static weighting factor is decreased). Because the proposed method applied to the modified static control parameter directly considers the mode-switching phenomenon and the modal stiffness, smooth changes are observed in the static and dynamic characteristics even as a large number of elements are removed as the interation count becomes large. It is shown that any improvement in one criterion requires a tradeoff in the other, revealing a clear Pareto solution (or a Pareto curve).

Unlike the proposed method, a desirable solution is not obtained in the conventional method. As shown in Fig. 5.2, the maximum von- Mises stresses obtained with the conventional method are higher than those obtained from the proposed method with increasing $W_{dynamic}$. Even though the conventional method addresses the relative ratio between modal stiffness and modal mass, the deficiency arises from no *direct* consideration of modal stiffness. In addition, the fundamental natural frequencies at

$W_{dynamic}$:W_{static} =1.0:0.0 are decreased by this lack of modal stiffness as well as the changing control parameter characteristics due to mode-switching. Determining the trend of the Pareto solution with volume reduction is extremely difficult. However, in constrast to the conventional method, the proposed control parameter can be used to design an optimum structure as a large number of elements are eliminated through many iterations and yet provide constructive dynamic modification.

5.6.2. Example 2: TPS Model with Thermal Loading

When a spacecraft re-enters the atmosphere from Low Earth Orbit (LEO), the tremendous heat fluxes generated produce a non-uniform, transient temperature distribution in the metallic TPS. Since most metallics demonstate temperature dependence, the thermal (thermal conductivity and specific heat) and mechanical (Young's modulus and coefficient of thermal expansion) properties will vary with temperature in the TPS. This temperature dependence in the thermal problem results in nonlinearity and necessitates an iterative solution technique.

For the second example, a transient thermal profile is applied to the initial TPS model in Fig. 5.1. The (void) space inside the TPS and the vertical surface boundaries (with the exception of the surface of the plate) are treated as insulated. The plate temperature (T_{plate}) on the top side varies according to a temperature profile, as shown in [**105**]. In this method, the temperature is simply represented as $T_{plate} = 1.2540t + 200$ C when ($t < 500$ $sec.$), and $T_{plate} = 827$ C when ($t \geq 500$ $sec.$), regardless of the elimination of elements from the structure. This assumption is a severe restriction. In the true structure, convection and radiation play major roles in the transfer of energy. For instance, to address the internal radiative heat transfer that will occur as material is removed, an efficient method for constructing view factors during the iterative process would be needed. Since the purpose of this work

was to develop an ESO method for simultaneous consideration of thermal stress and frequency, prescribed temperature boundary conditions were used to ensure tractability.

A numerical time integration scheme,[**106**] similar to Newmark's method, is used to solve the following transient heat transfer problem

$$(5.11)\quad (\frac{1}{\Delta t}[M_t]+\beta[K_t])\{T_{i+1}\} = [\frac{1}{\Delta t}[M_t]-(1-\beta)[K_t]]\{T_i\}+(1-\beta)\{F_i\}+\beta\{F_{i+1}\}$$

where $[M_t]$ is the consistent mass matrix; $[K_t]$ is the thermal conductivity matrix; $\{F_i\}$ is the thermal force vector created from heat sources (or heat sinks), heat fluxes, and convective boundary conditions; Δt is the time step; β is an integration parameter set to 0.5 (Crank-Nicolson rule); and $\{T_i\}$ & $\{T_{i+1}\}$are the nodal temperatures at time t_i and t_{i+1}, respectively. To reduce the computational time of the transient analysis, only the tendency of the temperature profile at t = 1500 sec is evaluated by assuming that $[M_t]$ and $[K_t]$ are constant with time as thermal conductivities ($K_{xx} = K_{yy} = K_{zz}$ = 20 W/(m-C)), density (ρ=7770 kg/m^3), and specific heat (c =530 J/(kg-C)) are treated as temperature-independent variables. A constant timestep of Δt =10 sec. is considered. The initial temperature distribution $\{T_o\}$ for each iterative process is assumed to be a linear profile through the thickness with 127 C on the top side and 27 C on the bottom side.

5.6.2.1. Applicability of the Proposed Control Parameter to a Transient Thermal Profile. Both conventional and proposed methods are compared to demonstrate the applicability of the proposed control parameter for topology optimization of a TPS with a non-uniform temperature profile. The TPS model has dimensions A=0.48 m, B=0.42 m, C=0.03m, and D is intentionally set 0.27 m longer than typical TPS structures [**107**] to reduce thermal stress in the fixed regions at the bottom side (interface to low-temperature material). The plate and frame regions are treated as

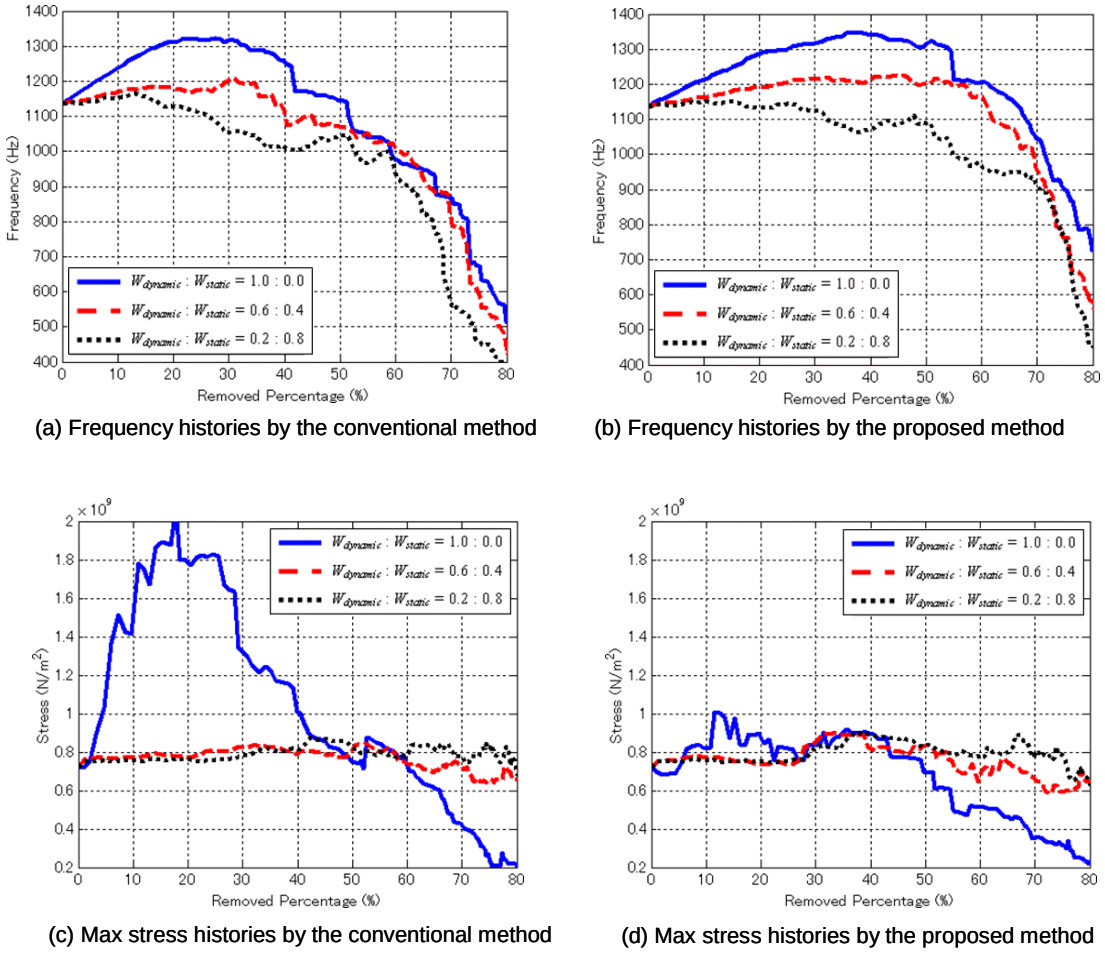

(a) Frequency histories by the conventional method

(b) Frequency histories by the proposed method

(c) Max stress histories by the conventional method

(d) Max stress histories by the proposed method

Figure 5.3. Evolutionary histories of the fundamental natural frequencies and the maximum thermal stress.

unremovable. The model is divided into 0.03 m x 0.03 m x 0.03 m regular hexahedron isoparametric elements, and the 0.06 m x 0.06 m bottom corner regions are considered fixed. The coefficient of thermal expansion and Young's modulus are considered as functions of temperature [**103**]. Similar to Example 1, the weighted objectives method considers both the maximum thermal stress and the fundamental natural frequency as both the weighting factors and volume reduction percentages are varied.

Figure 5.3 shows the change in fundamental frequencies and maximum thermal

stresses as weighting factors and sensitivities are varied. Both methods show improvement in fundamental frequencies as the weighting factors for dynamics are increased, identical to the mechanical load case. In general, when a structure is over-designed, (e.g., when a structure consists of more elements than needed), the fundamental natural frequency can be increased by removing inefficient elements. However, when the stiffness of the structure becomes small, the fundamental natural frequency is decreased. In Fig. 5.3, as a large number of elements are removed from the structure over many iterations, the proposed method keeps the fundamental natural frequencies much higher than that obtained from the conventional method, even though no inertia consideration is inherent in the proposed control parameter. Conversely, the results using the conventional control parameter show that the fundamental natural frequency decreases quickly due to (1) the small modal stiffness in the connecting region between the assumed fixity and the plate-frame region and (2) the characteristic change in the control parameter due to the discontinuous change in the natural modes (i.e., mode-switching).

The analysis of the change in the maximum thermal stress reveals considerably different behavior when compared with that of the mechanical load case. If we examine the maximum stress histories, it is obvious that very little stress reduction takes place when the static parameter dominates. This is not surprising as the elements being removed are some of the lowest stressed. In the conventional method, the minimization of the maximum thermal stress can be obtained by applying a large weighting factor for the static control parameter in the early stages of the volume reduction. As the volume removal percentage increases, the maximum thermal stress that results from dynamic considerations alone becomes less than the maximum thermal stress that results from static considerations alone. These seemingly inconsistent results are, in fact, a revelation similar to the findings of Chapter 4. Just as activating stiffness in

a direction orthogonal to the in-plane direction to minimize in-plane load, was shown to be a successful approach to minimize boundary loads (Chapter 4), when the modal stiffness is biased toward the out-of-plane direction (i.e., bending of the top plate), stress reduction occurs. The von-Mises stress measure does not distinguish between tension or compression. When the optimizer is removing material for all modes except the out-of-plane direction, the other frequencies are being reduced. Granted they are still higher than the mode of interest, but they will approach the bending mode in the limit. The modal stiffness in these other orthgonal modes correspond to static stiffness as well. Hence, this effect renders the structure less equipped to support high compression loads (or reaction forces) for the in-plane directions. As the volume reduction proceeds, to maintain high frequency, the material is focused on suppressing bending in the un-removeable plate region. By focusing material in such a manner, the stiffness is focused directly into the out-of-plane bending mode at the expense of the other modes. Since no mechanical boundary condition constrains the thermal expansion of the TPS in the Z-direction, thermal stress is relieved as frequency remains high even for large values of volume reduction.

Figure 5.4 shows resulting models close to 900 Hz in fundamental natural frequency by both the conventional and proposed methods. Each model is developed using solely dynamic considerations, that is, $W_{dynamic} : W_{static} = 1.0 : 0.0$. The fundamental natural frequency, maximum stress, and the number of elements result in 933.6 Hz, 0.523 GPa, and 740 (155.2 kg) using the conventional method, and 906.8 Hz, 0.330 GPa, and 568 (119.2 kg) by the proposed method. The main difference between the two resulting topologies is the location of the elements that are adjacent to the plate-frame region: one is located towards the center of the plate-frame region, and the other is located towards the edges of the plate-frame region. The conclusion

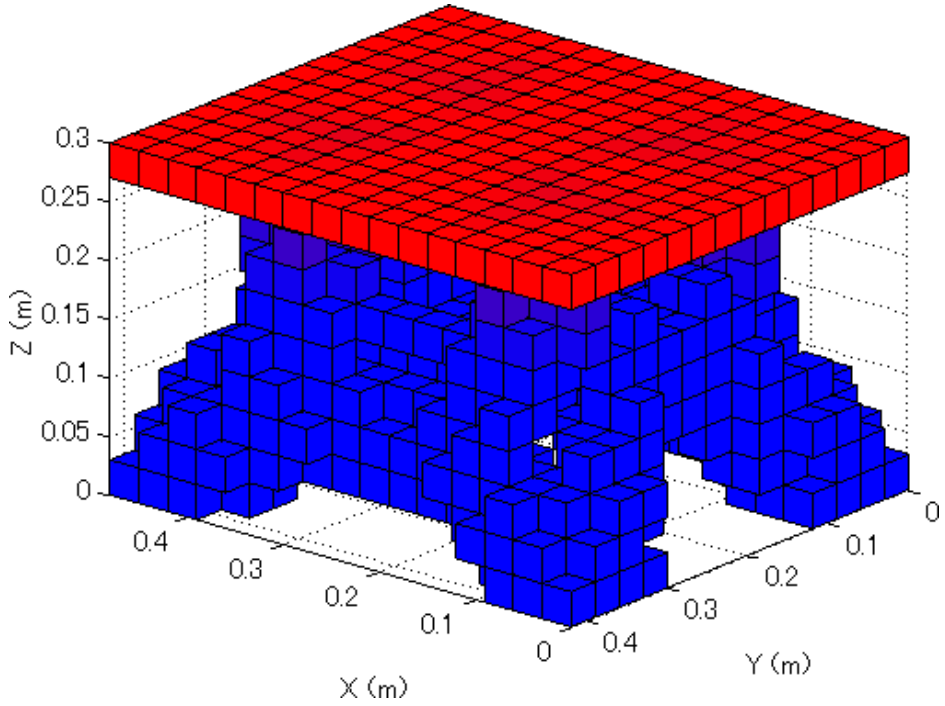

(a) Modified TPS model by the conventional method

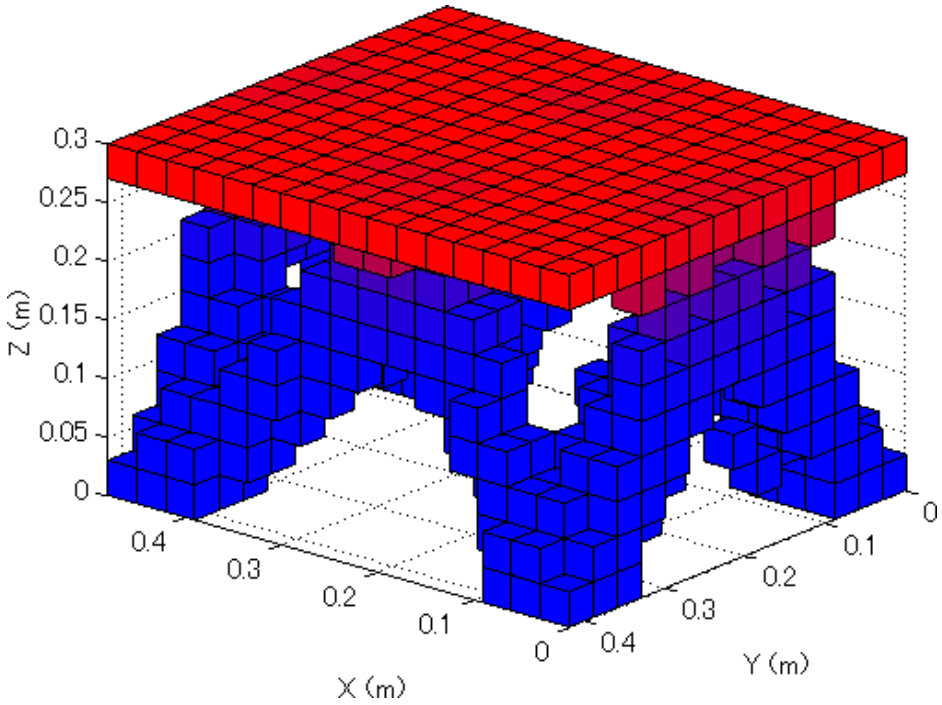

(b) Modified TPS model by the proposed method

Figure 5.4. Resultant TPS models with 900 Hz fundamental natural frequency

to be drawn from this study is the proposed method is superior to the conventional method in both maintaining high fundamental frequency and reducing thermal stress.

From the above results, the ESO method with the proposed control parameter can be used to design a lightweight TPS model with a high fundamental natural frequency and a low maximum thermal stress. Using the assumption that only conduction affects the support region, a practical TPS design is developed by using $W_{dynamic} : W_{static} = 1.0 : 0.0$ in the next section.

5.6.2.2. Detailed TPS Design with Thermal Transient Profile. In contrast to the static case, the convergence of the eigenvalue maximization problem presents a more daunting task. In an evolutionary procedure that requires a large number of element removals over many iterations, the ordering of natural modes may be altered by selection of the initial geometry. Considering the initial geometry as an input, considerable variations in structural characteristics (i.e. neighboring natural frequencies, weight of the structure, etc.) can result. Therefore, appealing to the topology results of the previous section (Fig. 5.4 (b)), the initial TPS model is chosen to be that of Fig. 5.4 (b) with a slight modification. Element removal is only permitted on the inside of the structure, as shown in Fig. 5.5. A *shape* optimization method based on the ESO technique (called 'nibbling ESO [**54**]) is applied to the support region to avoid the checkerboard pattern that occurred in Fig. 5.4 (b). That is, only the structural boundaries in the Z direction between Layer 1 and Layer 10 (with the exception of the unremovable Layer 0 region) are removed from the model. The frame region, as well as the support region, are designed to reduce the TPS weight. Using the proposed method, the objectives take the following form:

Minimize TPS weight

subject to

(1) maximization of the fundamental natural frequency ($f_1 \geq 900\ Hz$)

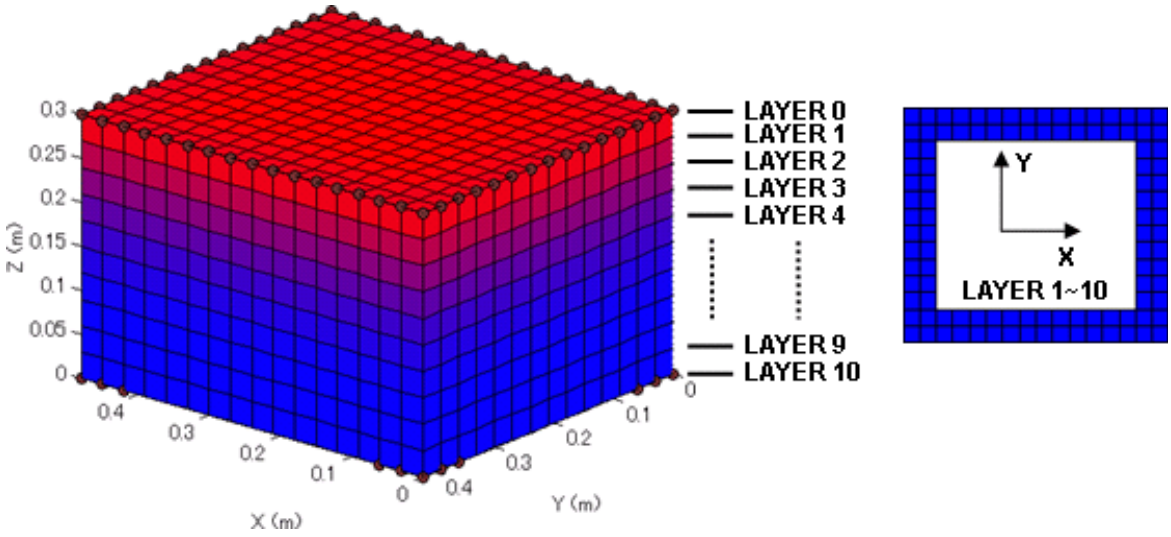

Figure 5.5. Initial model for designing TPS support

(2) minimization of the maximum thermal stress below yield strength ($\sigma_{\max} \leq$ 0.3 GPa)

In early iterations, the fundamental natural mode is the bending mode of the support region. The elements of the frame are eliminated to improve the dynamic characteristics of the support. The local bending mode of the thin top plate becomes the lowest mode of the structure. If the original model is too coarse or too much material is removed at each iteration, the plate may not satisfy the frequency constraint and could result in undesirable flutter or acoustic excitation. Because the top layer of the TPS is unremovable, the problem becomes a multi-scale phenomenon. Inefficient material remains in the base but the optimization algorithm's focus is the low frequency of the plate. Therefore, to address the problem efficiently, the design optimizations for the support region and the frame region are conducted separately.

TPS Support Design. In the support design, the boundary condtions and mesh size are identical to the previous section for the initial model in Fig. 5.5. However, additional fixed regions are established at the edges of the plate to prevent a local mode from occurring in the unremovable region due to dynamic considerations. By

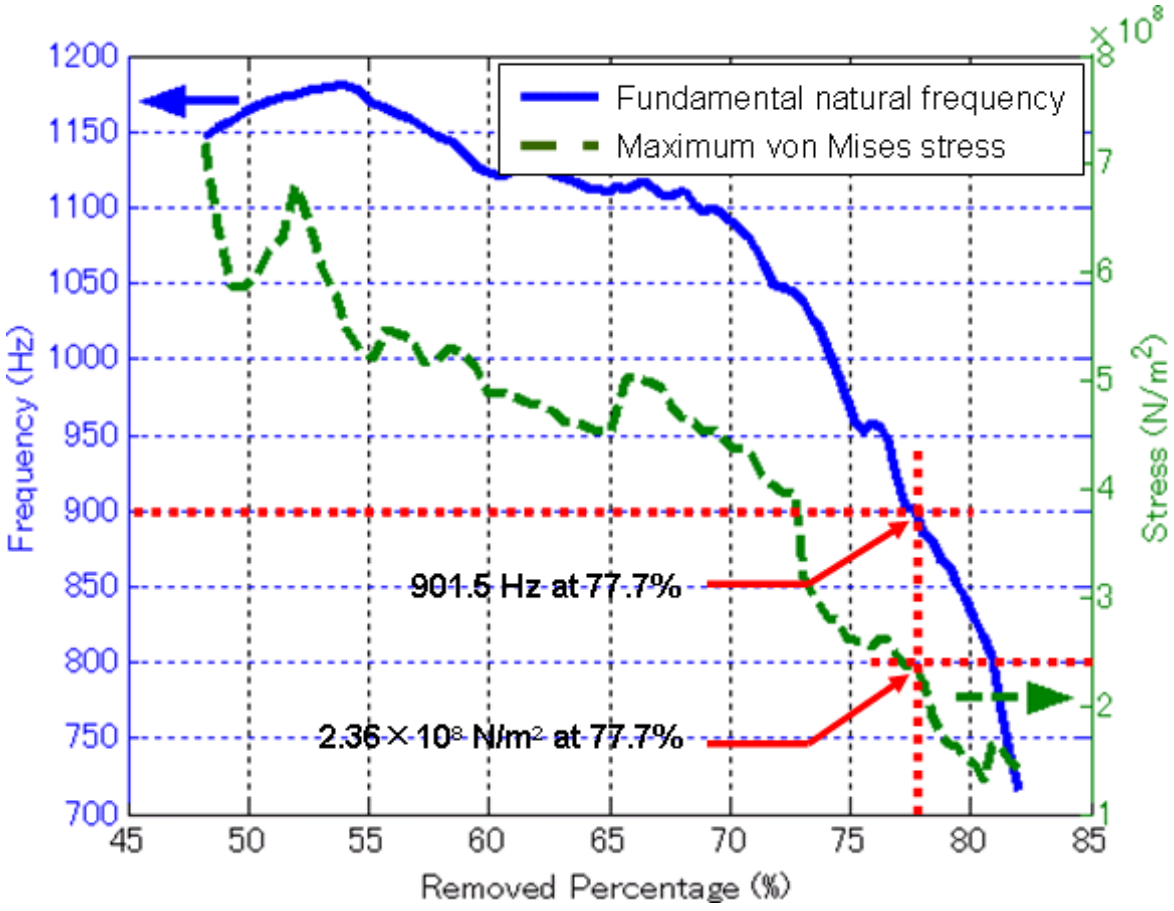

Figure 5.6. Evolutionary histories for TPS support design.

choosing additional stiffnesses of $[k_X, k_Y, k_Z] = [0,\ 0,\ 10^8]$ (N/m), the local mode of the unremovable region will not represent the lowest frequency in the structure to allow the optimizer to focus on the support. Figure 5.6 shows the change in the fundamental natural frequency and the maximum thermal stress as a function of volume reduction. For this case, the structure at 77.7% volume removal is the most lightweight that satisfies the two constraints (Fig. 5.7). Analyzing the TPS with the imposed stiffnesses removed results in a frequency of 871.9 Hz which is slightly less than the 900 Hz target. This is obviously due to the increase in modal mass of the unremovable plate region. However, from an application perspective, producing a design in which the stress is less than the Mises yield criterion along with a frequency of nearly 872 Hz should be considered a success.

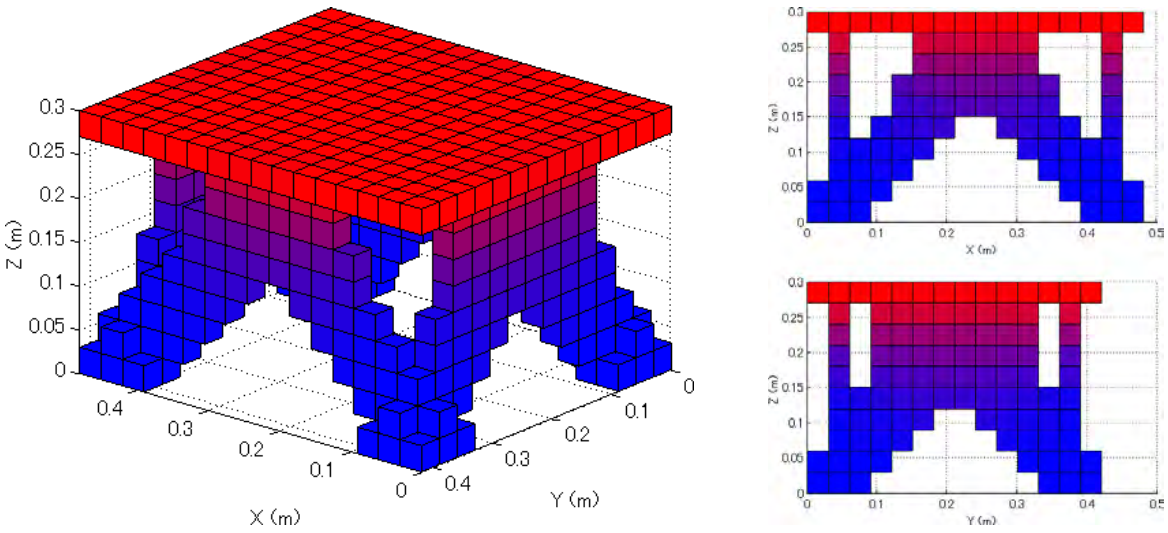

Figure 5.7. Optimum TPS support

TPS Frame Design. To continue improvement in the modified TPS model in Fig. 5.7, attention is focused on modifying the frame independently to achieve the 900 Hz objective. By observation, the potential exists to increase the natural frequency by adjusting the frame design since the elements in the frame region possess large modal mass being located at the extreme of the domain. The modal stiffness of the frame-plate combination will, by construction, be considered when using the proposed control parameter. The plate and frame regions are remeshed using two element sizes, 0.03 m x 0.03 m x 0.007 m in the frame and 0.03 m x 0.03 m x 0.002 m in the plate. The plate is considered as only the first layer of the plate-frame combination. Hence, it has a thickness of 0.002 m. The four corners at the bottom of the support region are assumed fixed as in the previous example. Shape optimization is applied by eliminating elements from the bottom surface of the frame toward the upper skin (or plate) to produce manufacturable designs as was accomplished in the support design. Because the maximum thermal stress exists in the support region, no thermal stress analysis is applied. The spatially varying temperatures are, however, used to adjust material properties to proper values.

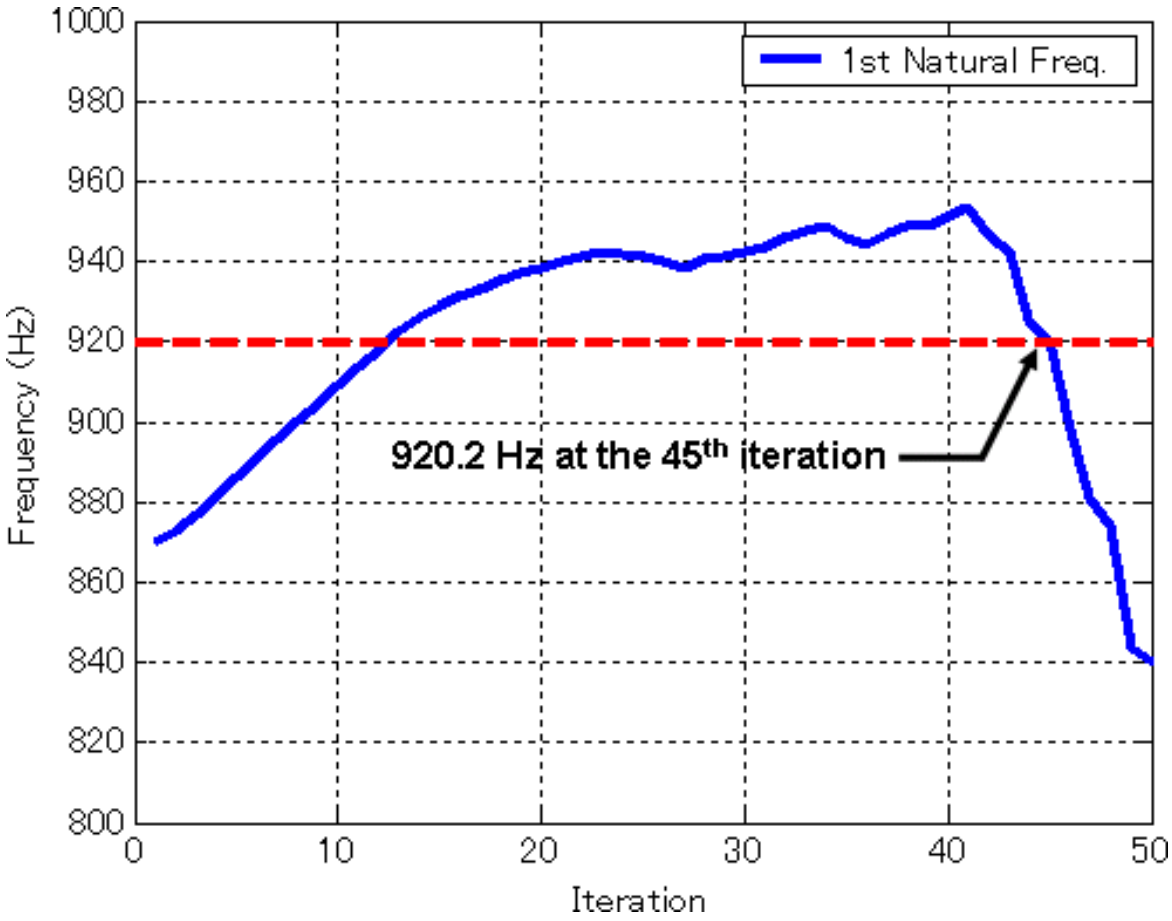

Figure 5.8. Evolutionary history of the fundamental natural frequency for TPS frame design.

Figure 5.8 shows the evolutionary history of the fundamental natural frequency due to modifications in the frame region. Up to the 41^{st} iteration, the fundamental frequency increases because excessive modal mass is removed from the frame. Notice that the frequency drops off drastically at this point due to the modal stiffness reduction owing to the lack of elements in the frame region, although excessive modal mass remains. In the frame design, the modified TPS model satisfies the frequency constraint at the 45th iteration, and has a fundamental natural frequency of 920.2 Hz.

Finally, a transient heat transfer analysis is applied to the TPS model at the 45^{th} iteration to obtain the exact solution. In this case, the model has a fundamental

natural frequency of 919.8 Hz, the maximum thermal stress of 0.228 GPa, and 816 elements (76.50 kg), which consist of 224 elements (3.13 kg) in the plate, 316 elements (15.47 kg) in the frame, and 276 elements (57.90 kg) in the support region. The fundamental natural frequency is reduced slightly by the change of the material properties, and the maximum thermal stress is also reduced slightly by the volume reduction of the frame. The final modified TPS model and the cross-section of the frame-plate are shown in Fig. 5.9. To prevent flutter or acoustic excitation of the plate, the frame elements provide reinforcement at the plate center even though these elements have high modal mass about the natural mode of the plate.

5.7. Summary Remarks

In this chapter, a multi-objective optimization problem for the thermal stress and the fundamental natural frequency was conducted to generate a lightweight TPS model using Evolutionary Structural Optimization (ESO). Two objectives were optimized simultaneously, namely, the maximization of the fundamental natural frequency and the minimization of the maximum thermal stress, through efficient volume reduction. Specifically, the modified static control parameter based on simple static analyses is newly proposed and addresses the frequency response of stand-off TPS designs. Comparisons between the conventional ESO and proposed control parameter have demonstrated that the novel control parameter is successful in preventing several problems. While the proposed control parameter ignores inertia terms in the equation of motion, both the mode-switching phenomenon and direct consideration of modal stiffness are successfully addressed. Additionally, the technology was demonstrated in the successful design of a metallic thermal protection system. In

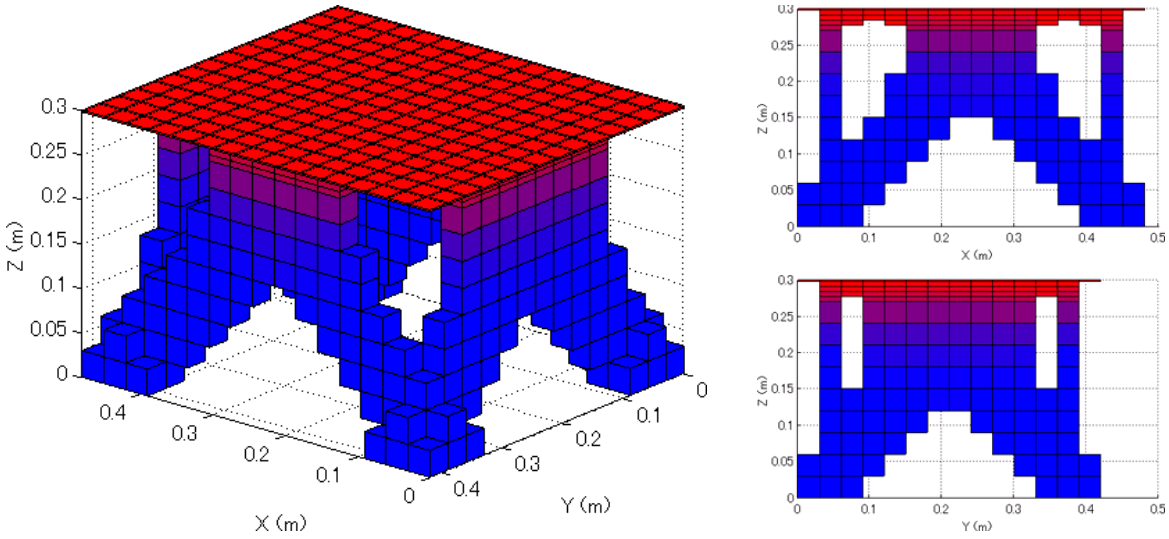

(a) Optimum TPS model

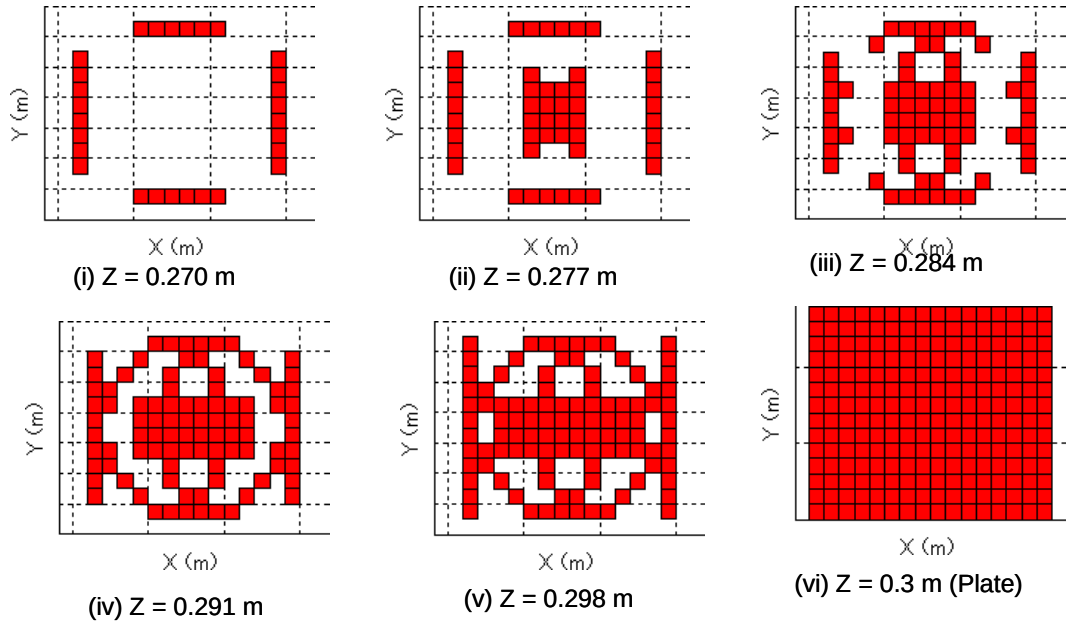

(b) Cross-section in the plate-frame region

Figure 5.9. Optimum TPS model including heat transfer effects.

future work, consideration will be given to more realistic thermal conditions. Inclusion of convection and radiation as well as a maximum temperature constraint could potentially result in new and innovative designs.

CHAPTER 6

Summary and Future Work

6.1. Summary

In this work, the design of thermal structures using topology optimization is explored. The primary motivation for this work rests in the design of low-observable, engine exhaust-washed structures. Embedded engines require a surface on which to expel exhaust gases. This protective covering must survive the thermal stresses while performing its function of shielding the lower temperature substructure from the extreme thermal environment. Of particular concern is the out-of-plane deformation of the thin covering. Conventional stiffening methods are demonstrated to be problematic as tremendous additional loads into sub and surrounding structure can occur. The non-intuitive nature of stiffening thin panels (both flat and curved) in a thermal environment are explored in detail. The findings reveal that adding to the thickness of a panel will not only increase load into surrounding structure, but can also *increase* the maximum tensile stress in the panel.

The Simple Isotropic Material with Penalization (or SIMP) minimum compliance topology optimization is applied to the thermally-loaded problem and found be highly non-optimal as material is distributed close to the original thickness of the panel. However, a minimum compliance formulation is presented which applies mechanical loads in such a way as to activate stiffness only in the out-of-plane direction. This formulation renders the design incapable of producing large loads in the in-plane

direction when heated. The bridge-type stiffening structures generated share a common characteristic in that internal thermal expansion can occur, limiting the reaction load.

A novel ESO control parameter is developed to address both stiffness and frequency simultaneously. Mises stress and fundamental frequency are combined in a weighted objective formulation while volume is reduced to achieve acceptability in both responses. Similar to the exhaust-washed structure, a generic, metallic thermal protection system is designed. A non-uniform temperature profile is applied to the structure and a successful evolutionary design is achieved with von-Mises stress less than yield and first fundamental frequency above 900 Hz. The novel control parameter addresses two major concerns in frequency optimization. The first remedies the three-dimensional effect where the mode of interest exchanges with a different mode which is much lower after structural modification. The second pathology that is mitigated is the inadequacy of previous ESO frequency optimization schemes to directly address modal stiffness. The newly-derived control parameter achieves this end. The ESO method applied to TPS design demonstrates the same characteristics as the SIMP formulation in that lower stress (or lower reaction force) designs are achieved when only frequency optimization is the goal and that frequency corresponds to an out-of-plane mode.

6.2. Adjoint Topology Formulation for Direct Consideration of Load-Stress Trade Space

While the two topology optimization formulations given above produce reasonable designs and extend the knowledge base of thermoelastic topology optimization, a more direct approach to reducing stress and limiting reaction load is needed. The

procedure presented in Chapter 4 does limit the load into the boundary by construction, but further methods (shape and sizing optimization) are required to satisfy a stress objective. The ESO method presented in Chapter 5 limits the von-Mises stress (and hence the reaction load) to some degree but no direct prescription is made. In this section, a methodology will be presented which directly exposes the stress-load trade space and no restriction is made regarding the linearity of the analysis.

This development follows closely to that presented in [**108**] with the inclusion of the thermal expansion effects. The nonlinear thermo-elastic boundary value problem is initially posed in the strong form. A reformulation of the problem statement into the weak form provides a convenient transistion to the finite element discretization. A residual equation is presented which is solved by the Newton-Raphson nonlinear simultaneous equation solver. And finally, an implementation scheme for incorporating this capability into the commerical code ABAQUS via a user-defined element (UEL) is discussed.

6.2.1. Thermoelastic Boundary Value Problem

Using the construct for a Lagrangian, material-based formulation as found in [**34**], a material point $\boldsymbol{\chi}$ is located by the position vector $\boldsymbol{X}$ in the undeformed configuration $\boldsymbol{\Omega}_o$ of the body. Kinematically, the body experiences a displacement field $u(\boldsymbol{X})$ which results in the mapping $f : \boldsymbol{X} \longrightarrow \boldsymbol{x}$ where $\boldsymbol{x}$ is the position vector in the current configuration $\boldsymbol{\Omega}$ of the body. The total strain $\boldsymbol{E}$ is defined through the deformation gradient $\boldsymbol{F}$,

$$\boldsymbol{F}(\boldsymbol{X}) = \boldsymbol{I} + \boldsymbol{\nabla} \boldsymbol{u}(\boldsymbol{X}) \tag{6.1}$$

$$\boldsymbol{E}(\boldsymbol{X}) = \frac{1}{2}\left(\boldsymbol{\nabla u}(\boldsymbol{X}) + \boldsymbol{\nabla u}^T(\boldsymbol{X}) + \boldsymbol{\nabla u}^T(\boldsymbol{X})\,\boldsymbol{\nabla u}(\boldsymbol{X})\right) \tag{6.2}$$

Since thermal expansion effects will be included, we must differentiate between the total strain and the mechanical strain $\boldsymbol{E}_{mech}$ as the mechanical strain is the appropriate strain measure for constitutive equation. The total strain is comprised of both $\boldsymbol{E}_{mech}$ (Eq. 6.3) and the thermal strain $\boldsymbol{E}_{th}$

$$\boldsymbol{E}_{mech} = \boldsymbol{E} - \boldsymbol{E}_{th} \tag{6.3}$$

with the thermal strain given by Eq. 6.4

$$\boldsymbol{E}_{th}(\boldsymbol{X}) = \alpha \triangle T(\boldsymbol{X})\boldsymbol{I} \tag{6.4}$$

The coefficient of thermal expansion, α, can in general be a function of the spatially-varying temperature difference, $\triangle T(\boldsymbol{X})$. The temperature difference field, $\triangle T(\boldsymbol{X})$, is measured relative to a reference temperature, $\triangle T(\boldsymbol{X}) = T(\boldsymbol{X}) - T_{ref}$.

If we assume that inertial effects are negligible (which may not be the case if thermal transients are large), the system response is treated as quasi-static; therefore, the strong forms of local linear and angular momentum balance are respectively given by

$$\begin{aligned} \operatorname{div}\left(\boldsymbol{F}(\boldsymbol{X})\boldsymbol{T}_o(\boldsymbol{X})\right) + \boldsymbol{b}_0(\boldsymbol{X}) &= \boldsymbol{0} \qquad (6.5) \\ \boldsymbol{T}_o(\boldsymbol{X}) &= \boldsymbol{T}_o^T(\boldsymbol{X}) \qquad (6.6) \end{aligned}$$

where $\boldsymbol{T}_o(\boldsymbol{X})$ is the symmetric 2^{nd} Piola-Kirchhoff stress tensor and $\boldsymbol{b}_0(\boldsymbol{X})$ is the body force vector defined per unit original (undeformed) volume.

A hyperelastic material response is assumed which implies path independence of the material response. The hyperelastic assumption also guarantees that the stress response can be derived from a strain energy $e(\boldsymbol{X}) = \widetilde{e}(\boldsymbol{E}_{mech}(\boldsymbol{X}), \boldsymbol{X})$ defined on the undeformed configuration. The 2^{nd} Piola-Kirchhoff stress tensor $\boldsymbol{T}_o(\boldsymbol{X})$ is the derivative of the strain energy $\widetilde{e}$ with respect to the mechanical strain tensor $\boldsymbol{E}_{mech}(\boldsymbol{X})$,i.e. $\boldsymbol{T}_o(\boldsymbol{X}) = \frac{\partial \widetilde{e}}{\partial \boldsymbol{E}_{mech}}$. In this work, the materials considered are high temperature, isotropic metallic alloys, and it follows that small strains may be assumed while the structure may undergo large displacements. The hyperelastic material model introduced is adequate to describe the material behavior, i.e.

$$\widetilde{e} = \frac{\nu E}{2\,(1+\nu)(1-2\nu)}\boldsymbol{tr}(\boldsymbol{E}_{mech})^2 + \frac{E}{2(1+\nu)}\boldsymbol{tr}(\boldsymbol{E}_{mech}^2) \tag{6.7}$$

$$\boldsymbol{T}_o = \frac{\partial \widetilde{e}}{\partial \boldsymbol{E}_{mech}} = \boldsymbol{C}\boldsymbol{E}_{mech} \tag{6.8}$$

where the elasticity tensor $\boldsymbol{C}$ depends on two material parameters, Young's modulus E and Poisson's ratio ν. These material constants should be familiar to the reader as they define the familiar Hooke's law for a linear isotropic material. Experimental results have shown Young's modulus to be a decreasing function of temperature for most engineering materials. Therefore, if the range of operating temperatures is significant, E should include the temperature dependence.

A boundary value problem definition is incomplete without specification of boundary conditions. Displacement and surface traction boundary conditions are prescribed as $\boldsymbol{u}^P$ and $\boldsymbol{t}^P$ on the complementary boundaries $\boldsymbol{A}_0^u$ and $\boldsymbol{A}_0^t$ of the undeformed configuration. The essential and natural boundary conditions are given by

$$\boldsymbol{u}(\boldsymbol{X}) = \boldsymbol{u}^p(\boldsymbol{X}) \qquad \boldsymbol{X} \,\boldsymbol{\epsilon}\, \boldsymbol{A}_0^{\boldsymbol{u}} \tag{6.9}$$

$$\boldsymbol{F}(\boldsymbol{X})\boldsymbol{T}_{\boldsymbol{0}}(\boldsymbol{X})\boldsymbol{n}_{\boldsymbol{0}}(\boldsymbol{X}) = \boldsymbol{t}^p(\boldsymbol{X}) \qquad \boldsymbol{X} \,\boldsymbol{\epsilon}\, \boldsymbol{A}_0^{\boldsymbol{t}} \tag{6.10}$$

The solution to the boundary value problem is known once the displacement field is determined.

6.2.2. Weak Formulation

The thermoelastic boundary value problem is recast into an equivalent variational (or weak) form. The familiar weak form is generated by multiplying both the equilibrium Eq. 6.5 and the natural (traction) boundary condition (Eq. 6.10) by a weight function $\boldsymbol{v}$ and integrating over the appropriate domains. Satisfaction of the essential boundary conditions is ensured by restricting $\boldsymbol{u}$ and $\boldsymbol{v}$ to the set of kinematically admissible displacements. Conservation of angular momentum (Eq. 6.6) is ensured by the proper choice of material constitutive law. After integration by parts and an application of the divergence theorem, a residual equation is formed by the equivalent weak form.

$$g(\boldsymbol{u}) = 0 = -\int_{\Omega_0} \nabla \boldsymbol{v} \cdot (\boldsymbol{F}\,\boldsymbol{T}_0)\, dv_0 + \int_{\Omega_0} \boldsymbol{v} \cdot \boldsymbol{b}_0 dv_0 + \int_{\boldsymbol{A}_0^{\boldsymbol{t}}} \boldsymbol{v} \cdot \boldsymbol{t}^{\boldsymbol{p}} da_0 \tag{6.11}$$

The constitutive equation (Eq. 6.8), the strain-displacement relation (Eq. 6.2), and the mechanical strain (Eq. 6.3) are substituted into Eq. 6.11.

$$\begin{aligned} g(\boldsymbol{u}) &= 0 = -\int_{\Omega_0} \nabla \boldsymbol{v} \cdot (\boldsymbol{F}\boldsymbol{C}\,(\boldsymbol{E} - \boldsymbol{E}_{th}))\, dv_0 + \int_{\Omega_0} \boldsymbol{v} \cdot \boldsymbol{b}_0 dv_0 + \int_{\boldsymbol{A}_0^{\boldsymbol{t}}} \boldsymbol{v} \cdot \boldsymbol{t}^{\boldsymbol{p}} da_0 \\ &= 0 = -\int_{\Omega_0} \nabla \boldsymbol{v} \cdot (\boldsymbol{F}(\boldsymbol{C}\boldsymbol{E}))dv_0 + \int_{\Omega_0} \nabla \boldsymbol{v} \cdot (\boldsymbol{F}\,(\boldsymbol{C}\boldsymbol{E}_{th}))\, dv_0 + \\ &\quad \int_{\Omega_0} \boldsymbol{v} \cdot \boldsymbol{b}_0 dv_0 + \int_{\boldsymbol{A}_0^{\boldsymbol{t}}} \boldsymbol{v} \cdot \boldsymbol{t}^{\boldsymbol{p}} da_0 \end{aligned} \tag{6.12}$$

One important observation should be noted in Eq. 6.12 is the resemblence of the thermal stress work to a body force. In fact, the thermal-elasic equations are identical to the elastic relations with the work of the thermal stress included as a volume

integral over the reference volume. The solution of the responses are found by discretizing the domain and applying the Galerkin finite element method.

The system version of the Newton-Raphson nonlinear equation solver is used to solve the nonlinear algebraic finite element equations. The Newton-Raphson solver is characterized by second-order convergence and the formation of a tangent matrix which is used in subsequent design sensitivity analysis. The nonlinlear finite element equation $\boldsymbol{G}$, expressed as a function of the nodal response vector $\boldsymbol{U}$, is given in residual form by

$$\boldsymbol{G}(\boldsymbol{U}) = \boldsymbol{0} \tag{6.13}$$

The development of the Newton-Raphson method follows from a first-order Taylor series expansion of Eq. 6.13. The expansion is performed about the current solution $\boldsymbol{U}_i$

$$\boldsymbol{G}(\boldsymbol{U}_{i+1}) \approx \boldsymbol{G}(\boldsymbol{U}_i) + \frac{\boldsymbol{DG}}{\boldsymbol{DU}}(\boldsymbol{U}_i)\,\delta\boldsymbol{U} = \boldsymbol{0} \tag{6.14}$$

where $\boldsymbol{\delta U} = \boldsymbol{U}_{i+1} - \boldsymbol{U}_i$ represents the update to the response vector. Rearrangement of Eq. 6.14 gives the familiar finite element form

$$\boldsymbol{K_T}(\boldsymbol{U}_i)\,\boldsymbol{\delta U} = \boldsymbol{G}(\boldsymbol{U}_i) \tag{6.15}$$

where $\boldsymbol{K_T}(\boldsymbol{U}_i) \equiv -\frac{\boldsymbol{DG}}{\boldsymbol{DU}}(\boldsymbol{U}_i)$ is the tangent (stiffness) matrix. Iterative is continued until either (or both) the magnitudes of the residual and response update is less than a specified value.

6.2.3. Finite Element Formulation

For solution expediency, the residual finite element equations are decomposed into internal and external force vectors,

$$\boldsymbol{G}(\boldsymbol{U}) = \boldsymbol{0} = \boldsymbol{S}(\boldsymbol{U}) + \boldsymbol{F} \tag{6.16}$$

where

$$\boldsymbol{S} = -\int_{\Omega_0} \nabla \boldsymbol{v} \cdot (\boldsymbol{F}\,\boldsymbol{T}_0)\, dv_0 \tag{6.17}$$

is the *virtual* work of the internal force vector and

$$\boldsymbol{F} = \int_{\Omega_0} \nabla \boldsymbol{v} \cdot (\boldsymbol{F}\,(\boldsymbol{C}\boldsymbol{E}_{th}))\, dv_0 + \int_{\Omega_0} \boldsymbol{v} \cdot \boldsymbol{b}_0 dv_0 + \int_{\boldsymbol{A}_0^{\boldsymbol{t}}} \boldsymbol{v} \cdot \boldsymbol{t}^{\boldsymbol{p}} da_0 \tag{6.18}$$

is the *virtual* work done by the external forces. The displacement vector is partitioned into an unknown free displacement vector $\boldsymbol{U}^f$ and a known prescribed displacement vector $\boldsymbol{U}^p$. In explicit vector form,

$$\boldsymbol{U} = \begin{Bmatrix} \boldsymbol{U}^f \\ \boldsymbol{U}^p \end{Bmatrix} \tag{6.19}$$

Since only the free degrees of freedom will be solved, it is convenient to partition the residual equation into $\boldsymbol{G^f}$ and $\boldsymbol{G^p}$ vectors as

$$\boldsymbol{G}\left(\boldsymbol{U}^p, \boldsymbol{U}^f\right) = \begin{Bmatrix} \boldsymbol{G}^f\left(\boldsymbol{U}^p, \boldsymbol{U}^f\right) \\ \boldsymbol{G}^p\left(\boldsymbol{U}^p, \boldsymbol{U}^f\right) \end{Bmatrix} = \begin{Bmatrix} \boldsymbol{S}^f\left(\boldsymbol{U}^p, \boldsymbol{U}^f\right) \\ \boldsymbol{S}^p\left(\boldsymbol{U}^p, \boldsymbol{U}^f\right) \end{Bmatrix} + \begin{Bmatrix} \boldsymbol{P} \\ \boldsymbol{R} \end{Bmatrix} = \boldsymbol{0} \tag{6.20}$$

where $\boldsymbol{P}$ and $\boldsymbol{R}$ are the applied and reaction force vectors, respectively. In this development, $\boldsymbol{P}$ will be independent of the displacement response, however, the thermal loading will depend on the design.

The nonlinear equation $\boldsymbol{G^f}$ is solved for the unknown free displacement vector $\boldsymbol{U}^f$ using the Newton-Raphson method. The tangent stiffness matrix in terms of the solution variables is given by

$$\boldsymbol{K_T} = -\frac{\partial \boldsymbol{G}^f}{\partial \boldsymbol{U}^f}\left(\boldsymbol{U}^p, \boldsymbol{U}^f\right) \tag{6.21}$$

In finite element parlance, the computation or *recovery* of the unknown reaction forces can be accomplished by appealing to the second residual in Eq. 6.20 after the solution of $\boldsymbol{U^f}$ is obtained.

6.2.4. Topology Optimization

The topology optimization problem is stated as

$$\begin{aligned} &\min && \boldsymbol{\Theta}_o(\mathbf{d}) \\ &\textit{subject to} && \boldsymbol{\Theta}_i(\mathbf{d}) \leq \mathbf{0} \\ & && \underline{\mathrm{d}}_j \leq d_j \leq \bar{d}_j \end{aligned} \tag{6.22}$$

where $\boldsymbol{\Theta}_o$ is the objective function, $\boldsymbol{\Theta}_i$ $(i = 1, \ldots)$ are the inequality or equality constraints and d_j $(j = 1, \ldots)$ are the design variables that are bounded above and below by $\underline{\mathrm{d}}_j$ and $\bar{d}_j$. The design variable in this scenario is taken as a density variable defined over each element. To ensure a mesh independent design, a filter should be employed.

6.2.5. Adjoint Sensitivity Analysis

As discussed previously in Chapters 3 and 4, the design variables typically consist of a density measure defined over each element. The most common implementation employs a single element density variable over each element. Therefore, the number

of design variables equals the number of elements. Since the problem under consideration is nonlinear, many iterations will be required for solution and subsequent convergence. Hence a premium is placed on efficient sensitivity computation.

For systems with large numbers of design variables but few objective and constraint equations are most efficiently solved by applying the adjoint sensitivity method [**43**] The adjoint formulation for the topology problem is constructed by augmenting the objective function with the constraint equations via Lagrange multipliers (Eq. 6.23).

$$\hat{\mathbf{\Theta}}_k(\mathbf{d}) = \mathbf{\Theta}_k(\mathbf{U}^P(\mathbf{d}), \mathbf{U}^f(\mathbf{d}), \mathbf{R}(\mathbf{d}), \mathbf{d}) + \boldsymbol{\lambda}^f \cdot \mathbf{G}^f(\mathbf{U}^P(\mathbf{d}), \mathbf{U}^f(\mathbf{d}), \mathbf{d}) + \boldsymbol{\lambda}^f \cdot (\mathbf{S}^P(\mathbf{U}^P(\mathbf{d}), \mathbf{U}^f(\mathbf{d}), \mathbf{d}) + \mathbf{R}(\mathbf{d})) \tag{6.23}$$

The sensitivities are computed by differentiating Eq. 6.23 with respect to the design variables $\mathbf{d}$. The result is manipulated such that the coefficients of the response sensititivies are equated to zero. The enforcement of this side condition results in the adjoint problem. The Lagrange multipliers are obtained by solving the adjoint problem for each objective and constraint equation. This process can be very efficient if the decomposed tangent stiffness matrix is available. Assuming this case, the adjoint solution is obtained by a simple back substitution.

For the case of a clamped, curved panel subjected to thermal loading, the objective consists of matching the deformed displacement field to a prescribed field with a more benign tensile stress response. A single constraint that captures the increase in force at the clamped boundary would provide the correct trade space.

6.2.6. ABAQUS Implementation

To implement this formulation in the commercial package ABAQUS, a user-defined element (UEL) would be necessary. The user would be required to implement the necessary shape functions and solution residuals desired by the ABAQUS solver. This step is necessary because the sensitivity arrays would need to be defined in the UEL so that at the end of the analysis, the adjoint problem could be solved by treating them as additional load cases. By using the load case feature in ABAQUS, the nonlinear problem would not require multiple solutions. While the tangent stiffness is not directly available to the user, the implementation outlined would possess the desired efficiency.

References

[1] Earl A. Thornton, editor. *Aerospace Thermal Structures and Materials for a New Era*. American Institute of Aeronatics and Astronautics, Inc., 1995.

[2] Shaeffer, Tuley, and Knott. *Radar Cross Section*. SciTech Publishing, 2004.

[3] J. Goodman, R.V. Kohn, and L. Reyna. Numerical study of a relaxed variational problem from optimal design. *Computer Methods in Applied Mechanics and Engineering*, (57):107–127, 1986.

[4] Thomas Borrvall and Joakim Petersson. Topology optimization of fluids in stokes flow. *International Journal for Numerical Methods in Fluids*, 41(1):77–107, 2002.

[5] O. Sigmund. Topology optimization in multiphysics problems. In *AIAA/USAF/NASA/ISSMO Symposium on Multidisciplinary Analysis and Optimization*, St. Louis, MO, September 1998.

[6] B.A. Boley and J.H. Weiner. *Theory of Thermal Stresses*. John Wiley and Sons, Inc., 1960.

[7] B.E. Gatewood. *Thermal Stresses*. McGraw-Hill Book Company, Inc., 1957.

[8] R.P. Hallion. *Supersonic Flight, The Story of the Bell X-1 and Douglas D-558*. Macmillan, New York, 1972.

[9] Jay Miller. *The X-Planes, X-1 to X-29*. Specialty Press, Marine on St. Croix, MN, 1983.

[10] N.J. Hoff. High temperature effects in aircraft structures. *Applied Mechanics Reviews*, 8(11):453–456, 1955.

[11] W.H. Stillwell. X-15 research results with selected bibliography. *NASA SP-60*, 1955.

[12] Earl A. Thornton. Thermal buckling of plates and shells. *Applied Mechanics Reviews*, 46(10):485–506, October 1993.

[13] S. Timoshenko and J.S. Gere. *Theory of Elastic Stability*. McGraw-Hill, 1961.

[14] Jon Lee. Displacment and strain statistics of thermally buckled plates. In *AIAA/ASME/ASCE/AHS/ASC Structures, Structural Dynamics, and Materials Conference*, volume 3, St. Louis, MO, April 1999.

[15] M.L. Gossard, P. Seide, and W.M. Roberts. *Thermal Buckling of Plates*. NACA TN 2771, 1952.

[16] MW Wilcox and LE Clemmer. Large deflection analysis of heated plates. *Journal of the Engineering Mechanics Division, Proc ASCE*, 20:165–189, 1964.

[17] Theodore Tauchert. Thermally induced flexure, buckling and vibration of plates. *Applied Mechanics Reviews*, 44(8):347–360, August 1991.

[18] P.M. Naghdi. On the theory of thin elastic shells. *Quarterly of Applied Mathematics*, 14:369–380, 1957.

[19] J.L. Ericksen and C. Truesdell. Exact theory of stress and strain in rods and shells. *Archive for Rational Mechanics and Analysis*, 1:295–323, 1958.

[20] J.L. Sanders. Nonlinear theories for thin shells. *Quarterly of Applied Mathematics*, 21:21–36, 1963.

[21] H. Kraus. *Thin Elastic Shells*. Wiley, 1967.

[22] D.O. Brush and B.O. Almroth. *Buckling of Bars, Plates, and Shells*. McGraw-Hill, New York, 1975.

[23] Henry L. Langhaar. *Energy Methods in Applied Mechanics*. Robert E. Krieger Publishing Company, Malabar, FL, 1989.

[24] N.J. Hoff. Thermal buckling of supersonic wing panels. *Journal of Aeronautical Sciences*, 23:1019–1028, 1956.

[25] N.J. Hoff. Buckling of a thin-walled circular cylindrical shell heated along an axial strip. *Journal of Applied Mechanics*, 31:253–258, 1964.

[26] N.J. Hoff. A nonlinear model study of the thermal buckling of thin elastic shells. *Journal of Applied Mechanics*, 32:71–75, 1965.

[27] M.A. Mahayni. Thermal buckling of shallow shells. *International Journal of Solids and Structures*, 2:167–180, 1966.

[28] J. Wolf and W.F. Brown. Aerospace structual metals handbook. Technical Report AFML-TR-68-115, Air Force Materials Lab, 1974.

[29] O.C. Zienkiewicz and R.L. Taylor. *The Finite Element Method, Vol 1: Basic Formulation and Linear Problems*. McGraw-Hill Book Company (UK) Limited, London, 1989.

[30] Li Shirong and Cheng Changjun. Analysis of thermal post-buckling of heated elastic rods. *Applied Mathematics and Mechanics*, 21:133–140, 2000.

[31] Li Shirong, You-He Zhou, and Xiaojing Zheng. Thermal post-buckling of a heated elastic rod with pinned-fixed ends. *Journal of Thermal Stresses*, 25:45–56, 2002.

[32] M.A. Vaz and R.F. Solano. Postbuckling analysis of slender elastic rods subjected to uniform thermal loads. *Journal of Thermal Stresses*, 26:847–860, 2003.

[33] M.A. Vaz and R.F. Solano. Thermal postbuckling of slender elastic rods with hinged ends constrained by a linear spring. *Journal of Thermal Stresses*, 27:367–380, 2004.

[34] Morton E. Gurtin. *An Introduction to Continuum Mechanics*. Academic Press, 1981.

[35] William H. Press, Brian P. Flannery, Saul A. Teukolsky, and William T. Vetterling. *Numerical Recipes - The Art of Scientific Computing*. Cambridge University Press, New York, 1989.

[36] Warren C. Young. *Roark's Formulas for Stress and Strain,Sixth Edition*. McGraw-Hill, Inc, 1989.

[37] J. Yang, K.M. Liew, Y.F. Wu, and S. Kitipornchai. Thermo-mechanical postbuckling of fgm cylindrical panels with tempertature-dependent properties. *Solids and Structures*, 43:307–324, 2006.

[38] A. Rastgo, H. Shafie, and A. Allahverdizadeh. Instability of curved beams made of functionally graded material under thermal loading. *International Journal of Mechanics and Materials in Design*, 2:117–128, 2005.

[39] Jon Lee. Effects of temperature-dependent physical properties on the response of thermally postbuckled plates. *Journal of Thermal Stresses*, 24:1117–1135, 2001.

[40] J. Woo, S.A. Meguid, and K.M. Liew. Thermomechanical postbuckling analysis of functionally graded plates and shallow cylindrical shells. *Acta Mechanica*, 165:99–115, 2003.

[41] J. Woo and S.A. Meguid. Nonlinear analysis of functionally graded plates and shallow shells. *Solids and Structures*, 38:7409–7421, 2001.

[42] J.W. Whitney. *Structural Analysis of Laminated Anisotropic Plates*. Technomic Publishing Company, Inc., 1987.

[43] Raphael T. Haftka and Zafer Gurdal. *Elements of Structural Optimization, 3rd edition*. Kluwer Academic Publishers, The Netherlands, 1991.

[44] Universal Analytics, Inc, Torrance, CA. *Astros User's Reference Manual for Volume 20*, 20 edition, 1999.

[45] Vanderplaats Research and Development, Inc., Colorado Springs, CO. *Genesis Structural Optimization Software, Version 7.3 User's Manual*, 7.3 edition, 2003.

[46] Charles Fox. *An Introduction to the Calculus of Variations*. Dover Publications, New York, 1987.

[47] S. Zhang and A.D. Belegundu. A systematic approach for generating velocity fields in shape optimization. *Structural and Multidisciplinary Optimization*, 5:84–94, 1992.

[48] Carl De Boor. *A Practical Guide to Splines*. Springer, New York, 2001.

[49] D. Goldberg. *Genetic Algorithms in Search, Optimization, and Machine Learning*. Addison-Wesley, Reading, MA, 1989.

[50] M.J. Jakiela. Continuum structural topology design with genetic algorithms. *Computational Methods in Applied Mechanics and Engineering*, 186:339–356, 2000.

[51] Karim Hamza, Haitham Mahmoud, and Kazuhiro Saitou. Design optimization of n-shaped roof trusses using reactive taboo search. *Applied Soft Computing*, 3:221–235, 2003.

[52] S. Ghosh, K. Lee, and S. Moorthy. Multiple scale analysis of heterogeneous elastic structures using homogenization theory and voronoi cell finite element method. *International Journal of Solids and Structures*, 32:27–62, 1995.

[53] M.P. Bendsoe and O. Sigmund. Material interpolation schemes in topology optimization. *Archives of Applied Mechanics*, 69:635–654, 1999.

[54] Y.M. Xie and G.P. Steven. *Evolutionary Structural Optimization*. Springer-Verlag London Limited, 1997.

[55] M.Y. Wang, X.M. Wang, and D.M. Guo. A level set method for structural topology optimization. *Computer Methods in Applied Mechanics and Engineering*, 192:227–246, 2003.

[56] S. Osher and J.A. Sethian. Front propogating with curvature-dependent speed: Algorithms based on hamilton-jacobi formulations. *Journal of Computational Physics*, 79:12–49, 1988.

[57] M. Bendsoe and N. Kikuchi. Generating optimal topologies in structural design using a homogenization method. *Comp. Meth. Appl. Mech. Eng.*, 71:197–224, 1988.

[58] A.H. Nayfeh. *Introduction to Perturbation Techniques*. John Wiley and Sons, Inc., 1993.

[59] Milton Van Dyke. *Perturbation Methods in Fluid Mechanics*. The Parabolic Press, 1975.

[60] A.H. Nayfeh. *Problems in Perturbations*. John Wiley and Sons, Inc., 1985.

[61] E.J. Hinch. *Perturbation Methods*. Cambridge University Press, 1991.

[62] O. Sigmund and J. Petersson. Numerical instabilities in topology optimization: A survey on procedures dealing with checkerboards, mesh-dependecies and local minima. *Structural Optimization*, 16:68–75, 1998.

[63] R.B. Haber, C.S. Jog, and M.P. Bendsoe. New approach to variable-topology shape design using a constraint on perimeter. *Structural Optimization*, 11:1–12, 1996.

[64] C.S. Jog and R.B. Haber. Stability of finite element models for distributed parameter optimization and topology design. *Computer Methods in Applied Mechanics and Engineering*, 130:203–226, 1996.

[65] F. Brezzi and M. Fortin. *Mixed and Hybrid Finite Element Methods*. Springer Verlag, New York, 1991.

[66] M.P. Bendsoe. Optimal shape design as a material distribution problem. *Structural Optimization*, 1:193–202, 1989.

[67] R. J. Yang and C.-H. Chuang. Optimal topology design using linear programming. *Computers and Structures*, 52:265–276, 1994.

[68] M. Stolpe and K. Svanberg. On the trajectories of penalization methods for topology optimization. *Structural and Multidisciplinary Optimization*, 21:128–139, 2001.

[69] J. Petersson and O. Sigmund. Slope constrained topology optimization. *International Journal for Numerical Methods in Engineering*, 41:1417–1434, 1998.

[70] T. Borrvall. Topology optimization of elastic continua using restriction. *Archives of Computational Methods in Engineering*, 8:351–385, 2001.

[71] Tyler Bruns and Daniel Tortorelli. Topology optimization of non-linear elastic structures and compliant mechanisms. *Computer Methods in Applied Mechanics and Engineering*, 190:3443–3459, 2001.

[72] S. Osher and J.A. Sethian. Fronts propogating with curvature-dependent speed: Algorithms based on hamilton-jacobi formulations. *Journal of Computation Physics*, 79:12–49, 1988.

[73] J.H. Choi, R.C. Penmetsa, and R.V. Grandhi. Shape optimization of the cavitator for a supercavitating torpedo. *Stuctural and Multidisciplinary Optimization*, 29:159–167, 2004.

[74] Y.M. Xie and G.P. Steven. A simple evolutionary procedure for structural optimization. *Computers and Structures*, 49:885–896, 1993.

[75] Geir A. Gunnlaugsson and John B. Martin. Optimality conditions for fully stressed designs. *SIAM Journal of Applied Mathematics*, 25:474–482, 1973.

[76] Pasi Tanskanen. The evolutionary structural optimization method: theoretical aspects. *Computer methods in applied mechanics and engineering*, 191:5485–5498, 2002.

[77] Q. Li, G.P. Steven, and Y.M. Xie. A simple checkerboard suppression algorithm for evolutionary structural optimization. *Structural and Multidisciplinary Optimization*, 22:230–239, 2001.

[78] G.D. Cheng and Z. Jiang. Study on topology optimization with stress constraints. *Engineering Optimization*, 20:129–148, 1992.

[79] H.C. Rodrigues and P. Fernandes. A material based model for topology optimization of thermoelastic structures. *International Journal for Numerical Methods in Engineering*, 38:1951–1965, 1995.

[80] O. Sigmund and S. Torquato. Design of materials with extreme thermal expansion using a three-phase topology optimization method. *Journal of the Mechanics and Physics of Solids*, 45:1037–1067, 1997.

[81] Qing Li, Grant P. Steven, and Y.M. Xie. Displacement minimization of thermoelastic structures by evolutionary thickness design. *Computer Methods in Applied Mechanics and Engineering*, 179:361–378, 1999.

[82] K.J. Bathe. *Finite Element Procedures in Engineering Analysis*. Prentice-Hall, NJ, 1982.

[83] Q. Li, G.P. Steven, and Y.M. Xie. Thermoelastic topology optimization for problems with varying temperature fields. *Journal of Thermal Stresses*, 24:347–366, 2001.

[84] Q. Li, G.P. Steven, and Y.M. Xie. On equivalence between stress criterion and stiffness criterion in evolutionary structural optimization. *Structural Optimization*, 18:67–73, 1999.

[85] T. Buhl, C.B.W. Pedersen, and O. Sigmund. Stiffness design of geometrically non-linear structures using topology optimization. *Structural and Multidisciplinary Optimization*, 19:93–104, 2000.

[86] C.S. Jog. Distributed-parameter optimization and topology design for nonlinear thermoelasticity. *Computer Methods in Applied Mechanics and Engineering*, 132:117–134, 1996.

[87] D.E. Carlson. *Linear thermoelasticity, in: S. Flugge, ed., Handbuch Der Physik, Volume VIa/2*. Springer, Berlin, 1972.

[88] Seonho Cho and Jae-Yeon Choi. Efficient topology optimization of thermoelasticity problems using coupled field adjoint sensitivity analysis method. *Finite Elements in Analysis and Design*, 41:1481–1495, 2005.

[89] O. Sigmund. Design of multiphysics actuators using topology optimization - part i: One-material structures. *Computer methods in applied mechanics and engineering*, 190:6577–6604, 2001.

[90] O. Sigmund. Design of multiphysics actuators using topology optimization - part ii: One-material structures. *Computer methods in applied mechanics and engineering*, 190:6605–6627, 2001.

[91] Ying Li, Kazuhiro Saitou, and Noboru Kikuchi. Topology optimization of thermally actuated compliant mechanisms considering time-transient effect. *Finite Elements in Analysis and Design*, 40:1317–1331, 2004.

[92] R.V. Grandhi. Structural optimization with frequency constraints - a review. *AIAA J.*, 31:2296–2303, 1993.

[93] M.P. Bendsoe and O. Sigmund. *Topology Optimization - Theory, Methods and Applications*. Springer-Verlag, New York, 2003.

[94] R.D. Cook, David S. Malkus, and Michael E. Plesha. *Concepts and Applications of Finite Element Analysis*. John Wiley and Sons, 1989.

[95] R.C. Penmetsa, R.V. Grandhi, and M.A. Haney. Topology optimization for evolutionary design of thermal protection system. *AIAA Journal of Spacecraft and Rockets*, submitted 2004.

[96] Z.D. Ma, N. Kikuchi, and H.C. Chang. Topological design for vibrating structures. *Computer Methods in Applied Mechanics and Engineering*, 121:259–280, 1995.

[97] K.A. Proos, G.P. Steven, O.M. Querin, and Y.M. Xie. Multicriterion evolutionary structural optimization using global criterion methods. *AIAA Journal*, 39:2006–2012, 2001.

[98] R.V. Grandhi, G. Bharatram, and V.B. Venkayya. Multiobjective optimization of large scale structures. *AIAA Journal*, 31:1329–1337, 1993.

[99] D.G. Carmichael. Computation of pareto optima in structural design. *International Journal for Numerical Methods in Engineering*, 15:925–952, 1980.

[100] I. Das and J.E. Dennis. A closer look at drawbacks of minimizing weighted sums of objectives for pareto set generation on multicriteria optimization problems. *Structural Optimization*, 14:63–69, 1997.

[101] J. Pietrzak. Pareto optimum tests. *Computers and Structures*, 71:35–42, 1999.

[102] Y.M. Xie and G.P. Steven. Evolutionary structural optimization for dynamics problems. *Computers and Structures*, 58:1067–1073, 1996.

[103] *Inconel alloy 693 - Excellent Resistance to Metal Dusting and High Temperature Corrosion,*. http://www.specialmetals.com/documents/Inconel, 2005.

[104] W.Y. Kim, T. Nakahara, and M. Okuma. An evolutionary optimization method for designing three-dimensional structures. *Transactions of Japan Society for Computational Engineering and Science*, 5:25–31, 2003.

[105] M.L. Blosser. *Thermal Protection Systems for Reusable Launch Vehicles*. 14th Annual Thermal and Fluids Analysis Workshop, 2003.

[106] D.L. Logan. *A First Course in the Finite Element Method-3rd ed*. Brooks/Cole: USA, 2000.

[107] M.L. Blosser, C.J. Martin, K. Daryabeigi, and C.C. Poteet. *Reusable Metallic Thermal Protection Systems Development*. Third European Workshop on Thermal Protection Systems, Noordwijk, The Netherlands, March 25-27, 1988.

[108] Tyler Eilert Bruns. *Topology Optimization of Nonlinear Elastic Structures and Compliant Mechanics*. PhD thesis, University of Illinois, 2001.